

Doctoral thesis

Doctoral theses at NTNU, 2021:279

Even Thingstad

Collective effects in low-dimensional systems with coupled quasiparticles

NTNU
Norwegian University of Science and Technology
Thesis for the Degree of
Philosophiae Doctor
Faculty of Natural Sciences
Department of Physics



Norwegian University of
Science and Technology

Even Thingstad

Collective effects in low-dimensional systems with coupled quasiparticles

Thesis for the Degree of Philosophiae Doctor

Trondheim, September 2021

Norwegian University of Science and Technology
Faculty of Natural Sciences
Department of Physics

NTNU

Norwegian University of Science and Technology

Thesis for the Degree of Philosophiae Doctor

Faculty of Natural Sciences

Department of Physics

© Even Thingstad

ISBN 978-82-326-5820-6 (printed ver.)

ISBN 978-82-326-5514-4 (electronic ver.)

ISSN 1503-8181 (printed ver.)

ISSN 2703-8084 (online ver.)

Doctoral theses at NTNU, 2021:279

Printed by NTNU Grafisk senter

Abstract

Many of the most fascinating and challenging phenomena in condensed matter physics occur in systems with coupling between quasiparticles of different nature. This thesis is concerned with the study of collective effects which may occur due to coupling between electrons, magnons, and phonons in various two-dimensional systems, and is based on four research papers.

In the first paper, we examine a spin model analog of the Haldane model which has a topologically non-trivial magnon band structure. We discuss the effect of coupling the topological magnons to phonons, and suggest signatures both in the transverse magnon spin Hall conductivity and through exotic magnon-polaron edge states.

In the second paper, we use a tight binding approach to model electron-phonon coupling in graphene, and study possible phonon-mediated superconductivity in doped graphene using a detailed model for the effective phonon-mediated electron-electron interaction.

In the third paper, we provide a revealing physical picture for the eigenexcitations of the quantum antiferromagnet, and discuss the implications of this in various physical settings. Amongst others, we emphasize that coupling asymmetrically to the two sublattices of the antiferromagnet through an uncompensated interface may enhance the effective coupling strength to the antiferromagnetic magnons.

In the fourth paper, we discuss superconductivity mediated by antiferromagnetic magnons in a heterostructure of a normal metal coupled to antiferromagnetic insulators. We find that sublattice coupling asymmetry plays an important role in determining the pairing symmetry of the superconducting phase. Using Eliashberg theory instead of BCS theory, we furthermore demonstrate the importance of a proper treatment of the frequency dependence of the effective pairing interaction for magnon-mediated superconductivity.

Preface

This thesis is submitted in partial fulfillment of the requirements for the degree of Philosophiae Doctor at the Norwegian University of Science and Technology (NTNU) in Trondheim, Norway. The work presented in this thesis has been conducted at the Department of Physics from August 2017 until June 2021 under the supervision of Professor Asle Sudbø, while Professor Jacob Linder has been co-supervisor. I have been affiliated with the research centre Quspin. During these years, I have also been enrolled in the PhD program of the Department of Physics, and completed 30 ECTS credits of coursework. In addition, I have completed teaching duties corresponding to one year, which have consisted of teaching the course TFY4210 Quantum Theory of Many-Particle Systems, as well as teaching student labs. The work has been funded by the Faculty of Natural Sciences at NTNU and the Research Council of Norway through Grant Number 262633 “Center of Excellence on Quantum Spintronics”.

The core of this thesis are the four research papers enclosed in the back. In addition, the thesis consists of introductory chapters on the broader topics these papers are concerned with through a discussion of magnetism, topology, phonons, and superconductivity in Chapters 2-5, while more specialized discussions are given in Chapters 6-8, where I try to introduce the themes and some of the results in the papers without going into excessive detail.

One of the best feelings I know, is the feeling of solving a puzzle or understanding something new after thinking about it for a long time. During four years as a PhD candidate, I have been fortunate to have that feeling a number of times. I hope this thesis can help you to understand something new, have a new idea, or view something from a new angle.

Acknowledgements

I started my PhD four years ago. Those four years have passed so quickly that it is easy to forget how much that has happened and how much that has changed over the course of the years. I started out hardly knowing anything or anyone. I made friends, and saw friends move to different cities and countries. Some projects just worked, and in some, I got tangled up in completely unexpected problems. There has been hard work. There has been ups and downs. But in the end, being a PhD candidate and working together with others to understand the world we live in slightly better, is simply a enormous privilege.

First of all, I would like to thank my supervisor Asle Sudbø. You have been there throughout all those years. You have always encouraged me, confided in me, and shared your deep and sparkling enthusiasm. Thank you for your bottomless support. Being your PhD student has been an absolute pleasure. Thank you, Asle.

I would also like to thank my collaborators on the research papers in this thesis. Thank you to Akashdeep Kamra for fruitful collaborations, countless discussions, and for always offering your help and advice. I am truly grateful for getting the chance to work closely with Eirik Erlandsen. That has been rewarding, inspiring, and above all, very enjoyable. Thank you to Justin Wells for stimulating discussions and for involving me in the activities of your group, and to Arne Brataas for help and support. I would also like to thank Jacob Linder for serving as my co-supervisor.

I am very happy to have worked in a sizeable research environment like Quspin, with many great colleagues and friends to discuss physics with. I have greatly appreciated being able to come to you with questions, to ask for help, all the enlightening discussions, and your best efforts in explaining me what you are working on. Yet, special thanks go to the people I have been working the closest with; to Henning, Håvard, Nicolay, Bjørnulf, Niels Henrik, and Kristian, as well as my current office mates Vasil and Marion.

Thank you also to Håkon, Anna Cecilie, and Johannes for our joint work and numerous enjoyable discussions.

More than anything, however, I am grateful for getting to know the people I have shared these years at Quspin with. I have thoroughly enjoyed lunches, hikes, dinners, travels, barbeques, celebrations, late evenings, going swimming, watching movies, playing games, volleyball, and taking ice cream breaks with you. Thinking back at those joyous moments reminds me of how fortunate I am to have made so many great friends during these last four years. It is hard to express how much you have meant to me.

Finally, I would like to thank my family. You will probably never be able to understand the equations and half of the words in this thesis, but you do know how much I have invested in it. Thank you for everything we have shared. Thank you for always being there.

Publications

Paper 1:

E. Thingstad, A. Kamra, A. Brataas, and A. Sudbø,
Chiral Phonon Transport Induced by Topological Magnons,
Physical Review Letters **122**, 107201 (2019) [1].

Paper 2:

E. Thingstad, A. Kamra, J.W. Wells, and A. Sudbø,
Phonon-mediated superconductivity in doped monolayer materials,
Physical Review B **101**, 214513 (2020) [2].

Paper 3:

A. Kamra, E. Thingstad, G. Rastelli, R.A. Duine, A. Brataas, W. Belzig,
and A. Sudbø,
Antiferromagnetic magnons as highly squeezed Fock states underlying quantum correlations,
Physical Review B **100**, 174407 (2019) [3].

Paper 4:

E. Thingstad, E. Erlandsen, and A. Sudbø,
Eliashberg study of superconductivity induced by interfacial coupling to anti-ferromagnets,
Preprint, arXiv:2105.02235 (2021) [4].
Accepted in Physical Review B.

My contributions to the papers

In Paper 1, I carried out all analytical and numerical calculations, and wrote major parts of the first draft of the manuscript. In Paper 2, I performed all analytical and numerical calculations, and wrote the first draft of the manuscript. In Paper 3, I discussed the ideas and the results in the paper through frequent meetings with the first author, and contributed to the revision of the paper. In Paper 4, I performed the numerical and analytical calculations and wrote the first draft of the manuscript in close collaboration with the second author, and we contributed equally to the paper.

Contents

1	Introduction	1
2	Magnetism	3
2.1	Spin models	4
2.2	Magnons	5
2.3	Antiferromagnetic magnons	8
2.4	Dzyaloshinskii-Moriya interaction	13
3	Topology	17
3.1	Hall conductivity and Berry curvature	19
3.2	The Haldane model	26
3.3	Bulk-boundary correspondence	31
3.4	Topological bosonic systems	37
4	Phonons	39
4.1	Force constant models	40
4.2	Electron-phonon coupling	43
4.3	Magnetoelastic coupling	50
5	Superconductivity	55
5.1	BCS theory	56
5.2	Eliashberg theory	71
5.3	Spin-fluctuation mechanism	88
6	Topological magnons	93
6.1	Hall conductivities	94
6.2	A magnon Haldane model	99
6.3	Topological magnons coupled to phonons	102
6.4	Further developments	108

7 Graphene superconductivity	111
7.1 Electronic properties of graphene	112
7.2 Phonons and electron-phonon coupling	114
7.3 Superconductivity in graphene	118
8 Magnon-mediated superconductivity	123
8.1 Squeezed antiferromagnetic magnons	124
8.2 Heterostructure model system	128
8.3 Processes and Eliashberg theory	129
8.4 Phase diagram and results	134
8.5 Discussion	138
9 Conclusion	141
A Currents and Hall conductivities	143
B Dimensionless electron-phonon coupling	153
Bibliography	154
Publications	175

Chapter 1

Introduction

Imagine taking two ice cubes out of the freezer, and placing one on top of a piece of wood and one on top of an equally shaped piece of aluminium. Which of the two ice cubes melts first?

Being able to answer the above question correctly may help you staying cold on a hot summer day. Understanding why is one of the great achievements of 20th century physics.

The explanations of seemingly simple everyday phenomena like the one above can be thought of as pyramid shaped. The simple answer to the question is that the ice cube on the piece of aluminium melts first because aluminium is a better conductor of heat than wood. Climbing one step down the pyramid, however, we may ask why aluminium is a better conductor of heat than wood. A proper explanation of this ultimately requires quantum mechanics, the Pauli principle, band theory, screening, and a fundamental understanding of the basic quantum degrees of freedom describing the solid state.

In simple terms, the solid state can be thought of as being described by a small number of the basic degrees of freedom. First, a solid consists of ions organized in a periodic structure, and these ions may vibrate around their equilibrium lattice positions. Second, electrons in the solid may either be bound to ions or move rather freely around. Finally, both ions and electrons have the quantum property of spin. Understanding the behaviour of these three degrees of freedom is at the heart of condensed matter physics.

Condensed matter physics allows us to understand why aluminium is a better conductor of electricity than wood, why electron spins may all align in a ferromagnet, and why phonons and not electrons dominate the transport

of heat in insulators.

Some of the most fascinating, surprising, and confusing phenomena in condensed matter physics occur, however, when the basic degrees of freedom are allowed to interact with each other. Cooling the piece of aluminium down to 1.2 K, it becomes superconducting due to interaction between the electrons and vibrations of the lattice [5]. Fluctuations of spins explain resistance minima in the Kondo effect [6], and seem to play an important role in the superconductivity of heavy fermion compounds and high- T_c cuprates [7].

Phenomena due to coupling between the fundamental degrees of freedom are also of great technological utility. For instance, superconductors are used to generate large magnetic fields in MRI scanners, and coupling between electron currents and the magnetization of ferromagnetic domains can be used to read a hard drive through the giant magnetoresistance effect [8].

In this thesis, we study collective effects arising due to the coupling between electrons, magnons, and phonons in low-dimensional quantum systems. In Paper [1], we discuss the coupling of topological magnons in a magnetic system to the quantum excitations of the lattice called phonons. The resulting excitations are superpositions of lattice vibrations and spin flips, and we discuss how this affects the notion of topology in the system. In Paper [2], we discuss how the coupling between lattice vibrations and electrons may give rise to superconductivity in graphene. In Paper [3], we provide a physical picture for the magnetic excitations in an antiferromagnet. Building on this, we complete the triangle in Paper [4], and use an Eliashberg theory framework to discuss how coupling between electrons in a normal metal and magnons in an adjacent antiferromagnet may give rise to superconductivity.

The thesis can be thought of as consisting of two parts. First, in chapters 2 to 5, we introduce the basic condensed matter phenomena and formalisms used in the research papers through separate chapters on magnetism, topology, phonons, and superconductivity. Second, in the chapters 6, 7, and 8, we bring these phenomena together, and provide an introduction to the papers and their main results.

Paper [1] is discussed in Chapter 6, and is based on material introduced in the introductory chapters on magnetism, topology and phonons.

Paper [2] is discussed in Chapter 7, building on material introduced in the introductory chapters on phonons and superconductivity.

Papers [3] and [4] are discussed in Chapter 8. The discussion of Paper [3] is based on material introduced in the chapter on magnetism, while the discussion of Paper [4] in addition builds on material introduced in the chapter on superconductivity.

Chapter 2

Magnetism

Unlike most condensed matter phenomena, the phenomenon of magnetism is truly ancient, and its discovery dates thousands of years back. Yet, a proper understanding of magnetism must be built on quantum mechanics and condensed matter physics. Historically, the study of magnetism is also intimately connected with the development of the modern understanding of phase transitions, including concepts such as spontaneous symmetry breaking and the Berezinskii-Kosterlitz-Thouless phase transition [9].

Today, magnetism is a rich and varied topic. Fundamental research is performed along a multitude of directions for a multitude of reasons. Within spintronics, magnetic systems are investigated as possible platforms for low dissipation data storage and manipulation [10], while magnetic fluctuations are also studied in the pursuit of a theory for the poorly understood high-temperature superconductors [11–13]. Furthermore, magnetic systems may host strongly correlated and massively degenerate phases of fundamental interest [14, 15], and magnetic systems continue to function as working platform to study novel phase transitions which cannot be understood within existing paradigms of phase transitions [16–18].

In this chapter, we will primarily be discussing magnetism within the context of magnetically ordered insulators. In Sec. 2.1, we introduce the basic description for such systems. In Sec. 2.2, we introduce the concept of a magnon in ferromagnetic systems. In Sec. 2.3, we generalize the concept to antiferromagnetically ordered systems, and this will be particularly relevant for Papers [3, 4]. Finally, in Sec. 2.4, we discuss the Dzyaloshinskii-Moriya interaction, which plays an important role in Paper [1].

2.1 Spin models

We consider a set of quantum spins $\{\mathbf{S}_i\}$ with spin quantum number S localized on lattice sites labelled by i on some lattice. A spin model can then be specified by a Hamiltonian on the form

$$H = \sum_i h_i^1(\mathbf{S}_i) + \sum_{ij} h_{ij}^2(\mathbf{S}_i, \mathbf{S}_j) + \sum_{ijk} h_{ijk}^3(\mathbf{S}_i, \mathbf{S}_j, \mathbf{S}_k) + \dots, \quad (2.1)$$

where the various terms correspond to a single spin contribution h_i^1 , two-spin-interactions h_{ij}^2 , and so on. This quantum Hamiltonian dictates the ground state of the system, along with its excitations and thermodynamics.

In the research discussed in this thesis, we encounter spin models which mainly consist of terms on the form

$$H = \sum_{i,j} J_{ij} \mathbf{S}_i \cdot \mathbf{S}_j - K \sum_i (S_i^z)^2 - B \sum_i S_i^z. \quad (2.2)$$

Here, $K \geq 0$ is an easy-axis anisotropy, B represents a homogeneous magnetic field, and J_{ij} is the exchange interaction strength between spins on lattice sites i and j . We will only be considering spin models where J_{ij} is non-zero only for nearest and next-to-nearest neighbours on the lattice, and denote the nearest neighbour exchange coupling by J_1 , and the next-to-nearest neighbour exchange coupling by J_2 . Furthermore, we will be considering spin models on the square and the honeycomb lattice, which are so-called bipartite lattices¹. Thus, they can be separated into two sublattices denoted by A and B , as shown in Fig. 2.1 (a) and (b).

In the above model, the easy axis anisotropy tends to favour spins pointing along direction \hat{z} in spin space. Depending on the sign of the exchange interaction, the exchange coupling between the spins \mathbf{S}_i and \mathbf{S}_j tends to favour them pointing along the same direction when $J_{ij} < 0$, and in opposite directions when $J_{ij} > 0$. Assuming the nearest neighbour interaction J_1 to dominate, we therefore expect ferromagnetic order when $J_1 < 0$, and antiferromagnetic order on bipartite lattices when $J_1 > 0$, as illustrated in Fig. 2.1 (c) and (d).

Since a general model on the form in Eq. (2.1) contains a macroscopic number of interacting spins, deducing the ground state and its excitations

¹To define the notion of bipartite, we may think of a lattice as a set of points, where we have defined a set of “neighbours” for each of the points. The lattice is then bipartite if the set of lattice points can be split into two disjoint sets such that each lattice site in one set only has “neighbours” in the other set. Such a separation is possible for the square lattice and the honeycomb lattice (if we assume that two lattice points are “neighbours” when their distance is as short as it gets), but not the triangular lattice.

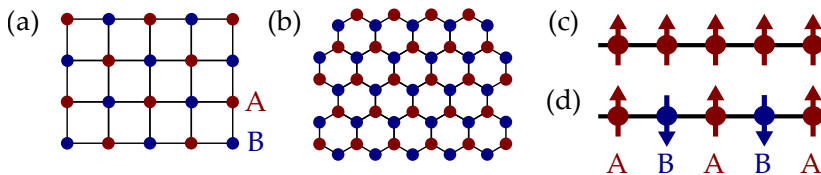


Figure 2.1: Lattices and magnetic order. (a) The square lattice is bipartite since it can be split into two sublattices. (b) Honeycomb lattice. (c) Each lattice site in a spin model is associated with a quantum spin. Loosely speaking, the system has ferromagnetic order when all spins are pointing in the same direction. (d) Antiferromagnetic order with spins on the two sublattices pointing in opposite directions.

is in general not a trivial task. Therefore, several techniques have been developed to analyze the behaviour of spin models.

The arguably most basic is known as linear spin wave theory, and applies to the situation where the ground state has long-range magnetic order, and there are only small fluctuations around this order. For low temperatures, this allows us to restrict our analysis to a low-energy subspace consisting of states with few spin flips on top of the ordered state. We will be reviewing this in the next section.

We also mention, however, a few techniques beyond linear spin wave theory. A technique which does not depend on any particular magnetic order is the introduction of Schwinger bosons or Schwinger fermions [19], which can be combined with mean field or saddle point approaches. Furthermore, in one-dimensional systems [20] and certain two-dimensional systems [21], it may be useful to map the spin system to a set of fermions using the Jordan-Wigner transformation. Finally, a path integral representation for the spin system allows for various field theory techniques and gauge field theory descriptions [19, 22]. In one dimension, certain properties can sometimes even be calculated analytically using a so-called Bethe Ansatz [23].

2.2 Magnons

To introduce the concept of a magnon, we consider a ferromagnetic spin model, which we assume to take the form in Eq. (2.2).

For simplicity, we assume that $J_{ij} = J_1 < 0$ when i and j are nearest neighbours, and zero otherwise. One may then show that the ground state of the system is the ferromagnetically aligned state, where every spin is in the

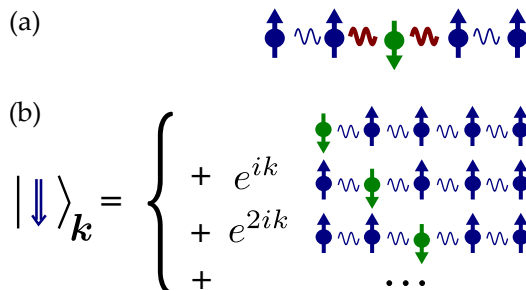


Figure 2.2: (a) A spin flip in a ferromagnet costs a significant amount of energy due to the antiparallel alignment of neighbouring spins. (b) Magnons are delocalized spin flips.

state with magnetic quantum number S with respect to the spin quantization axis $B\hat{z}$ [23]².

In our research, we are specifically interested in the excitations on top of this state. The conceptually simplest excitation we can make is the flip of a spin on a given site, as shown in Fig. 2.2 (a). However, this excitation costs a significant energy of order $|J_1|$, as the spin is no longer parallel with its neighbours. An excitation with lower energy is instead obtained by delocalizing the spin flip, creating a superposition of spin flips at different lattice sites, as shown in Fig. 2.2 (b). Such delocalized spin flips are referred to as magnons.

The elementary excitations on top of the ground state in a condensed matter system can often be represented in terms of bosons through bosonization techniques. In line with the low energy behaviour we expect, we therefore want our bosons to represent delocalized spin flips. This can be achieved through the so-called Holstein-Primakoff representation [23–25]

$$S_i^+ = \sqrt{2S - a_i^\dagger a_i} a_i \quad (2.3)$$

$$S_i^- = a_i^\dagger \sqrt{2S - a_i^\dagger a_i} \quad (2.4)$$

$$S_i^z = S - a_i^\dagger a_i, \quad (2.5)$$

where the boson operators a_i, a_i^\dagger represent local changes in the magnetic spin

²To be more specific, one may show that each term in the Hamiltonian takes on its minimum possible value in that state, and thus, the ferromagnetic state must be the ground state of the system [23].

quantum number along the quantization axis \hat{z} . One may show that the S -operators satisfy spin commutation relations when the a -operators satisfy boson commutation relations, and vice versa.

In line with the qualitative reasoning above, we assume that the number of spin flips in the system remains small, so that the ferromagnetic insulator is close to being perfectly magnetically ordered. Up to quadratic order in the boson operators in the Hamiltonian, we may then use the linearized Holstein-Primakoff transformation

$$S_i^+ = \sqrt{2S}a_i \quad (2.6)$$

$$S_i^- = \sqrt{2S}a_i^\dagger \quad (2.7)$$

$$S_i^z = S - a_i^\dagger a_i. \quad (2.8)$$

From the local spin flip bosons, one may construct delocalized spin flip operators through the Fourier transform

$$a_{\mathbf{q}\kappa} = \frac{1}{\sqrt{N}} \sum_n e^{-i\mathbf{q}\cdot(\mathbf{x}_n + \boldsymbol{\tau}_\kappa)} a_{n\kappa}, \quad (2.9)$$

where $a_{n\kappa}$ annihilates a spin flip on the lattice site at position $\mathbf{x}_n + \boldsymbol{\tau}_\kappa$ for atom κ in unit cell n , and where N is the number of unit cells in the system.

Within linear spin wave theory, one may then derive the excitation spectrum of the quantum ferromagnet on the two-dimensional square lattice to show that the Hamiltonian takes the diagonalized form

$$H = \sum_{\mathbf{q}} \omega_{\mathbf{q}} a_{\mathbf{q}}^\dagger a_{\mathbf{q}}, \quad (2.10)$$

with magnon excitation spectrum

$$\omega_{\mathbf{q}} = 2KS + BS + 2|J_1|S(2 - \cos q_x - \cos q_y), \quad (2.11)$$

and where we have set the lattice constant a to 1.

The spin model considered above is symmetric with respect to spin rotations around the spin space \hat{z} -direction. This symmetry can be broken by adding another easy axis anisotropy $\sum_i K_x (S_i^x)^2$ or considering an in-plane exchange coupling anisotropy. In addition to terms on the form $a_{\mathbf{q}}^\dagger a_{\mathbf{q}}$, we then generate terms on the forms $a_{\mathbf{q}}^\dagger a_{-\mathbf{q}}^\dagger$ and $a_{\mathbf{q}} a_{-\mathbf{q}}$. In that case, the Hamiltonian can be diagonalized using a Bogoliubov transformation, as discussed in further detail in the next section.

2.3 Antiferromagnetic magnons

In the antiferromagnetic Heisenberg model, we expect there to be antiferromagnetic order, where the spins are on average pointing in opposite directions on the two sublattices A and B of a bipartite lattice. The linear spin-wave theory above can easily be generalized also to these systems. In Papers [3] and [4] we make use of the excitations on top of the ground state of an antiferromagnet, and we will be discussing these excitations in the following.

Our starting point is the Hamiltonian

$$H = \sum_{i,j} J_{ij} \mathbf{S}_i \cdot \mathbf{S}_j - K \sum_i (S_i^z)^2, \quad (2.12)$$

where we let $J_1 \geq 0$, $K > 0$, and consider a square lattice. The classical ground state is the so-called Néel state, where neighbouring spins on the two sublattices of the system are pointing in opposite directions along the spin quantization axis \hat{z} .

As one may easily check, however, this Néel state is not an energy eigenstate of the quantum spin Hamiltonian, and it can therefore also not be the ground state. Yet, since we do expect antiferromagnetic order in the ground state, we assume that the system can still be understood in terms of a small number of spin flip excitations on top of the Néel state.

Therefore, we again introduce the linearized Holstein-Primakoff representation. Denoting the spin flips on the lattice sites $i \in A$ and $j \in B$ by a_i and b_j , we have [23]

$$S_{i \in A}^+ = \sqrt{2S} a_i \quad S_{i \in A}^- = \sqrt{2S} a_i^\dagger \quad S_{i \in A}^z = S - a_i^\dagger a_i \quad (2.13a)$$

$$S_{j \in B}^+ = \sqrt{2S} b_j^\dagger \quad S_{j \in B}^- = \sqrt{2S} b_j \quad S_{j \in B}^z = -S + b_j^\dagger b_j. \quad (2.13b)$$

In terms of the local spin flips bosons, the spin Hamiltonian then takes the form

$$H = 2S(z_1 J_1 - z_2 J_2 + K) \sum_i (a_i^\dagger a_i + b_i^\dagger b_i) + 2z_1 J_1 S \sum_{\langle ij \rangle} (a_i b_j + a_i^\dagger b_j^\dagger) + 2z_2 J_2 S \sum_{\langle\langle ij \rangle\rangle} (a_i^\dagger a_j + b_i^\dagger b_j), \quad (2.14)$$

consisting of an onsite energy term, a term describing the simultaneous creation or annihilation of sublattice magnons on neighbouring lattice sites, and a next-to-nearest neighbour magnon hopping term.

Since the system is translationally invariant when we assume periodic boundary conditions, we introduce the Fourier transform to diagonalize the system. As before, we therefore introduce Fourier transformed boson operators $a_{\mathbf{q}}$ and $b_{\mathbf{q}}$ through the transformation

$$a_i = \frac{1}{\sqrt{N}} \sum_{\mathbf{q}} e^{i\mathbf{q}\cdot\mathbf{x}_i} a_{\mathbf{q}} \quad (2.15)$$

$$b_i = \frac{1}{\sqrt{N}} \sum_{\mathbf{q}} e^{i\mathbf{q}\cdot\mathbf{x}_i} b_{\mathbf{q}}. \quad (2.16)$$

With spins oriented in opposite directions on the two sublattices, the periodicity of the system is enhanced with respect to the square lattice, and the number of atoms in the basis is doubled by introducing different operators a and b on the two sublattices. To preserve the number of degrees of freedom in the system, the Brillouin zone is therefore reduced, and the momenta \mathbf{q} run over the so-called reduced Brillouin zone indicated in orange in Fig. 2.3 (d).

Furthermore, we also introduce the Fourier transforms of the nearest and next-to-nearest neighbour interactions through

$$\gamma_{\mathbf{q}} = \frac{1}{z_1} \sum_{\boldsymbol{\delta}_1} e^{i\mathbf{q}\cdot\boldsymbol{\delta}_1} \quad \tilde{\gamma}_{\mathbf{q}} = \frac{1}{z_2} \sum_{\boldsymbol{\delta}_2} e^{i\mathbf{q}\cdot\boldsymbol{\delta}_2}, \quad (2.17)$$

where the sums run over the sets of nearest- and next-to-nearest neighbour vectors $\boldsymbol{\delta}_1$ and $\boldsymbol{\delta}_2$, and z_1 and z_2 are the number of vectors in these sets. The Hamiltonian then takes the form

$$H = \sum_{\mathbf{q}} C_{\mathbf{q}} (a_{\mathbf{q}}^{\dagger} a_{\mathbf{q}} + b_{-\mathbf{q}}^{\dagger} b_{-\mathbf{q}}) + D_{\mathbf{q}} (a_{\mathbf{q}} b_{-\mathbf{q}} + a_{\mathbf{q}}^{\dagger} b_{-\mathbf{q}}^{\dagger}), \quad (2.18)$$

where we have introduced coefficients

$$C_{\mathbf{q}} = 2z_1 J_1 S - 2z_2 J_2 S (1 - \tilde{\gamma}_{\mathbf{q}}) + 2KS \quad (2.19)$$

$$D_{\mathbf{q}} = 2z_1 J_1 S \gamma_{\mathbf{q}}. \quad (2.20)$$

The Hamiltonian thus consists of two kinds of terms. The first term, which is proportional to $C_{\mathbf{q}}$, corresponds to an energy cost associated with the creation of the excitations described by the boson operators $a_{\mathbf{q}}$ and $b_{\mathbf{q}}$. This term conserves the boson number. In contrast, the second term couples sectors of the Hilbert space which do not have the same number of bosons. A quantity which is however conserved, is

$$N_{\mathbf{q}} = a_{\mathbf{q}}^{\dagger} a_{\mathbf{q}} - b_{-\mathbf{q}}^{\dagger} b_{-\mathbf{q}}. \quad (2.21)$$

It can be thought of as a momentum resolved Néel order parameter. Thus, we may separate our Hilbert space into sectors with different values for $N_{\mathbf{q}}$ for each momentum \mathbf{q} , and diagonalize the Hamiltonian separately within each sector. This can be achieved through the Bogoliubov transform³

$$a_{\mathbf{q}} = u_{\mathbf{q}} \alpha_{\mathbf{q}} + v_{\mathbf{q}} \beta_{-\mathbf{q}}^{\dagger} \quad (2.22a)$$

$$b_{-\mathbf{q}}^{\dagger} = u_{\mathbf{q}} \beta_{-\mathbf{q}}^{\dagger} + v_{\mathbf{q}} \alpha_{\mathbf{q}}, \quad (2.22b)$$

with some coefficients $u_{\mathbf{q}}$ and $v_{\mathbf{q}}$ ⁴. As one may easily show by solving for $\alpha_{\mathbf{q}}$ and $\beta_{-\mathbf{q}}^{\dagger}$ above, the inverse transformation is given by

$$\alpha_{\mathbf{q}} = u_{\mathbf{q}} a_{\mathbf{q}} - v_{\mathbf{q}} b_{-\mathbf{q}}^{\dagger} \quad (2.23a)$$

$$\beta_{-\mathbf{q}}^{\dagger} = u_{\mathbf{q}} b_{-\mathbf{q}}^{\dagger} - v_{\mathbf{q}} a_{\mathbf{q}}. \quad (2.23b)$$

Since we want the new operators $\alpha_{\mathbf{q}}$ and $\beta_{\mathbf{q}}$ to satisfy boson commutation relations, the coefficients $u_{\mathbf{q}}$ and $v_{\mathbf{q}}$ have to satisfy the hyperbolic constraint

$$u_{\mathbf{q}}^2 - v_{\mathbf{q}}^2 = 1. \quad (2.24)$$

The so-called coherence factors $u_{\mathbf{q}}$ and $v_{\mathbf{q}}$ can therefore be expressed as

$$u_{\mathbf{q}} = \cosh \theta_{\mathbf{q}} \quad v_{\mathbf{q}} = \sinh \theta_{\mathbf{q}}. \quad (2.25)$$

We may now choose the hyperbolic angle $\theta_{\mathbf{q}}$ so that the Hamiltonian is diagonalized. One may show that this corresponds to the choice

$$\theta_{\mathbf{q}} = -\frac{1}{2} \tanh^{-1} \left(\frac{D_{\mathbf{q}}}{C_{\mathbf{q}}} \right) = -\frac{1}{2} \tanh^{-1} \left(\frac{z_1 J_1 \gamma_{\mathbf{q}}}{z_1 J_1 + K - z_2 J_2 (1 - \tilde{\gamma}_{\mathbf{q}})} \right), \quad (2.26)$$

and that the Hamiltonian then takes the form

$$H = E_0 + \sum_{\mathbf{q}} \omega_{\mathbf{q}} (\alpha_{\mathbf{q}}^{\dagger} \alpha_{\mathbf{q}} + \beta_{\mathbf{q}}^{\dagger} \beta_{\mathbf{q}}), \quad (2.27)$$

³More generally a Bogoliubov transform allows the diagonalization of a quadratic Hamiltonian with any number of coupled bosonic modes, where the boson number is not necessarily conserved [26–29].

⁴The Bogoliubov transform given here has been defined according to Paper [4]. We notice that the parameter $v_{\mathbf{q}}$ in Paper [3] has been defined with a relative sign difference.

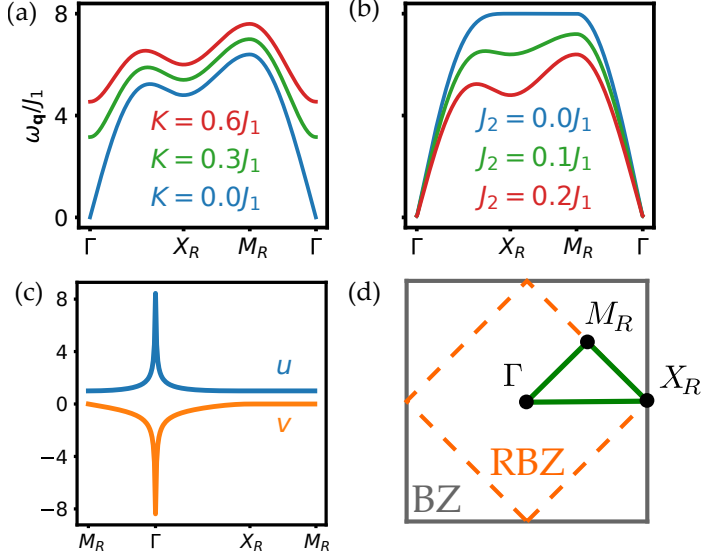


Figure 2.3: (a) Magnon spectra along high-symmetry path in (d) for various K . (b) Magnon spectra for various J_2 . (c) Coherence factors $u_{\mathbf{q}}$ and $v_{\mathbf{q}}$. (d) Brillouin zone (BZ) and reduced Brillouin zone (RBZ) with high symmetry path and points.

where E_0 is a constant and the excitation spectrum $\omega_{\mathbf{q}}$ is given by

$$\omega_{\mathbf{q}} = \sqrt{C_{\mathbf{q}}^2 - D_{\mathbf{q}}^2}. \quad (2.28)$$

Inserting the explicit expressions for $C_{\mathbf{q}}$ and $D_{\mathbf{q}}$, we have

$$\omega_{\mathbf{q}} = 2S\sqrt{[z_1J_1 - z_2J_2(1 - \tilde{\gamma}_{\mathbf{q}}) + K]^2 - (z_1J_1\gamma_{\mathbf{q}})^2}. \quad (2.29)$$

The spectrum is shown for various easy axis anisotropies K with $J_2 = 0$ in Fig. 2.3 (a), and for various J_2 with a small easy axis anisotropy $K/J_1 = 10^{-4}$ in Fig. 2.3 (b).

Any state can be constructed from the Néel state by superimposing states with multiple spin flips. Since the mode $a_{\mathbf{q}}$ only couples to the mode $b_{-\mathbf{q}}$ and the quantity $N_{\mathbf{q}}$ is conserved, it should therefore be possible to write the ground state on the form

$$|GS\rangle = \prod_{\mathbf{q}} f_{\mathbf{q}}(a_{\mathbf{q}}^{\dagger} b_{-\mathbf{q}}^{\dagger})|0\rangle \quad (2.30)$$

where $f_{\mathbf{q}}$ is a function of the creation operators, and $|0\rangle$ the Néel state, corresponding to the vacuum state for the sublattice magnon operators $a_{\mathbf{q}}$ and $b_{\mathbf{q}}$. Since the eigenoperators $\alpha_{\mathbf{q}}$ and $\beta_{\mathbf{q}}$ represent eigenexcitations, the ground state in the system is clearly the state without any α - or β -excitations. Thus, the ground state should satisfy

$$\alpha_{\mathbf{q}}|GS\rangle = \beta_{\mathbf{q}}|GS\rangle = 0. \quad (2.31)$$

These conditions can be used to derive differential equations⁵ for the function $f_{\mathbf{q}}$, which are easily solved to give

$$f_{\mathbf{q}}(a_{\mathbf{q}}^{\dagger}b_{-\mathbf{q}}^{\dagger}) = \frac{1}{\mathcal{N}} \exp\left(\frac{v_{\mathbf{q}}}{u_{\mathbf{q}}} a_{\mathbf{q}}^{\dagger}b_{-\mathbf{q}}^{\dagger}\right). \quad (2.32)$$

Calculating the ground state inner product to fix the normalization constant⁶, one then finds the normalized ground state

$$|GS\rangle = \sum_{n=0}^{\infty} \prod_{\mathbf{q}} \left(\frac{\tanh^n \theta_{\mathbf{q}}}{\cosh \theta_{\mathbf{q}}}\right) \frac{(a_{\mathbf{q}}^{\dagger})^n (b_{-\mathbf{q}}^{\dagger})^n}{n!} |0\rangle = \sum_n \prod_{\mathbf{q}} P_n(\mathbf{q}) |n, n\rangle_{\mathbf{q}} \quad (2.33)$$

where $|n_A, n_B\rangle_{\mathbf{q}}$ is the state with n_A delocalized spin flips with momentum \mathbf{q} on the sublattice A and n_B delocalized spin flips at momentum $-\mathbf{q}$ on sublattice B . The weight $P_n(\mathbf{q})$ is given by

$$P_n(\mathbf{q}) = \left(\frac{\tanh^n \theta_{\mathbf{q}}}{\cosh \theta_{\mathbf{q}}}\right). \quad (2.34)$$

For small $\theta_{\mathbf{q}}$, the weight $P_n(\mathbf{q})$ of the states with a large number $n_{\mathbf{q}}$ of pairs of spin flips on the two sublattices in the above superposition is small. When $\mathbf{q} \rightarrow 0$ and $K/z_1 J_1$ is small, however, $|\theta_{\mathbf{q}}|$ approaches 1, and the ground state has significant weight also for states with a large number of spin flips. At the same time, the magnitude of the coherence factors can be approximated by

$$|u_{\mathbf{q} \rightarrow 0}| \approx |v_{\mathbf{q} \rightarrow 0}| \sim (z_1 J_1 / K)^{1/4}, \quad (2.35)$$

⁵This is achieved by utilizing that $[a, f(a^{\dagger})] = f'(a)$ for a function f depending only on a^{\dagger} and not a .

⁶The result can for instance be shown by Taylor expanding the two exponentials in the inner product and utilizing $a^n (a^{\dagger})^n |0\rangle = n!$.

which becomes large for small easy axis anisotropies⁷. This is also shown in Fig. 2.3 (c), which shows the coherence factors $u_{\mathbf{q}}$ and $v_{\mathbf{q}}$ along a high symmetry path for $K = 10^{-4}J_1$. This observation becomes important when we discuss squeezed magnons and magnon-mediated superconductivity in Chapter 8.

2.4 Dzyaloshinskii-Moriya interaction

So far, we have considered a restricted class of spin interactions, namely ferromagnetic or antiferromagnetic exchange couplings on the form $J\mathbf{S}_i \cdot \mathbf{S}_j$, and an easy-axis anisotropy on the form $K(S_i^z)^2$. In general, there may of course also be more exotic two-spin interactions. In addition to anisotropic versions of the exchange interaction, we may have a so-called Dzyaloshinskii-Moriya or antisymmetric exchange interaction between two spins, and we will be considering a model with such an interaction in Paper [1].

A Dzyaloshinskii-Moriya interaction between two spins \mathbf{S}_i and \mathbf{S}_j is an interaction on the form

$$H_{ij}^{DMI} = \mathbf{D}_{ij} \cdot (\mathbf{S}_i \times \mathbf{S}_j), \quad (2.36)$$

where \mathbf{D}_{ij} is a vector which determines both the interaction strength $D_{ij} = |\mathbf{D}_{ij}|$ and the direction of the interaction. The Dzyaloshinskii-Moriya interaction typically occurs due to the presence of spin-orbit coupling in an underlying electronic system. In the following, we discuss two examples of this.

In Mott insulators, the antiferromagnetic exchange interaction can be obtained through second order perturbation theory based on a Hubbard model with hopping parameter t_{ij} and onsite repulsion u to produce exchange interaction $J_{ij} \propto |t_{ij}|^2/u$. By assuming that there are in addition spin flip hoppings proportional to s_{ij} in the Hubbard model originating from spin orbit coupling, a similar procedure produces a Dzyaloshinskii-Moriya interaction $D_{ij} \propto t_{ij}s_{ij}/u$ [30, 31].

Similarly, in systems of localized spins with itinerant electrons, the localized spins interact through an RKKY exchange interaction mediated by the electrons. If the electrons are spin-orbit coupled, a similar mechanism produces a Dzyaloshinskii-Moriya interaction linear in the spin orbit coupling strength [32].

⁷The fact that this may actually happen is a consequence of the hyperbolic nature of the constraint in Eq. (2.24), which contrary to the corresponding constraint for a unitary transformation does not constrain the absolute values of the matrix elements $u_{\mathbf{q}}$ and $v_{\mathbf{q}}$.

To understand qualitatively how the Dzyaloshinskii-Moriya interaction affects the ground state of a spin model, we may use classical considerations. When the spin cross product $\mathbf{S}_i \times \mathbf{S}_j$ is aligned oppositely with \mathbf{D}_{ij} and the spins are orthogonal, the energy associated with the Dzyaloshinskii-Moriya interaction is minimal. The Dzyaloshinskii-Moriya interaction therefore favours spin textures where the spins are no longer collinear, and that may cause various spiral or skyrmion phases.

To see why, we may consider a pair of spins at lattice sites i and j which are interacting through a ferromagnetic exchange interaction and a Dzyaloshinskii-Moriya interaction, so that

$$H_{ij} = -J\mathbf{S}_i \cdot \mathbf{S}_j + D\hat{z} \cdot (\mathbf{S}_i \times \mathbf{S}_j) - h(S_i^z + S_j^z), \quad (2.37)$$

where we have assumed the Dzyaloshinskii-Moriya interaction to be oriented along the \hat{z} -direction. In terms of spin raising and lowering operators, the pair Hamiltonian can then be written

$$H_{ij} = -JS_i^z S_j^z - \frac{V}{2}(e^{-i\phi} S_i^+ S_j^- + e^{+i\phi} S_i^- S_j^+) - h(S_i^z + S_j^z), \quad (2.38)$$

where $V = \sqrt{J^2 + D^2}$ and $\phi = \arctan D/J$. To analyze it further, one may rotate one of the spin coordinate systems around the \hat{z} -axis relative to the other by introducing the rotated spins

$$\tilde{S}_i^\pm = e^{i\theta_i S^z} S^\pm e^{-i\theta_i S^z} = e^{\pm i\theta_i} S_i^\pm, \quad (2.39)$$

where the last equality can be shown by utilizing the Baker-Hausdorff-Campbell lemma [33]. By choosing $\theta_i = 0$ and $\theta_j = \phi$, one may then eliminate the phase ϕ in the Hamiltonian to produce the effective model

$$H_{ij} = -J\tilde{S}_i^z \tilde{S}_j^z - V(\tilde{S}_i^x \tilde{S}_j^x + \tilde{S}_i^y \tilde{S}_j^y) - h(\tilde{S}_i^z + \tilde{S}_j^z). \quad (2.40)$$

If we first consider $h = 0$, the classical ground state simply consists of ferromagnetically ordered spins in the xy -plane. In the original coordinates, this corresponds to a state where one of the spins is rotated with respect to the other.

Turning on the magnetic field, we expect that the two spins will eventually align along the \hat{z} -direction. Then, the Dzyaloshinskii-Moriya interaction does not affect the ground state energy of the pair Hamiltonian, but it will affect the excitations, and in Paper [1], we will see that a particular Dzyaloshinskii-Moriya interaction plays an essential role in generating a topologically non-trivial magnon band structure on a honeycomb lattice.

Let us now go beyond the simple two-spin model, and think of a one-dimensional spin chain with neighbouring spins interacting according to the above pair Hamiltonian in the absence of a magnetic field. The classical ground state is therefore a spin spiral where the spins in the chain are aligned along a position dependent quantization axis which rotates with a fixed angle ϕ for every step we move along the chain.

Depending on the lattice and the pattern of the Dzyaloshinskii-Moriya vectors \mathbf{D}_{ij} , it may in higher dimensions not be possible to minimize all the pair Hamiltonians at the same time. This makes the spin model frustrated, and it may consequently host exotic phases and excitations [34, 35].

Chapter 3

Topology

An informal investigation of the abstracts in the condensed matter section of the preprint server arXiv in May 2021 indicated that roughly 20 % of the abstracts contain the word “topology” in some form. The concept grew popular through the classification of electronic band structures to explain the integer quantum Hall effect. Nowadays, however, the usage has exploded. The concept is applied to describe the ground states and excitations of magnetic systems [36], superfluids [37], superconductors [38], and lattices [39], while major technology companies invest millions and millions of dollars to realize topological quantum computation [40].

With such a broad range of applications in physics, one may suspect that the core concept is very general. Indeed, the concept itself comes from mathematics, where the notion of a topological space is defined with great mathematical rigour [41]. To the physicist, it is simpler and more useful to think of topology as the qualitative study and classification of continuous mappings. To make this statement less abstract, we consider two examples in the following.

Consider first a chain of XY spins with periodic boundary conditions. The orientation of an XY spin can be specified by an angle $\theta \in [0, 2\pi)$. Let us furthermore assume that we have a continuum of these spins. The configuration of the spin chain can then be specified through the function $\theta(x)$, where $x \in [0, L)$ is the position of a given spin, and we have $\theta(0) = \theta(L)$. We now also require the mapping $x \mapsto \theta(x)$ to be continuous. The domain of the mapping can be considered equivalent (homeomorphic) to a unit circle, which we denote by S_1 . Since the target space is also a unit circle, configurations in the system can be represented by the various continuous

mappings $S_1 \rightarrow S_1$. This illustrates that a spin configuration can be thought of as a mapping [42].

Furthermore, from this simple example, it is also clear that the various mappings can be organized into various classes according to their winding number. If we think of a continuous mapping $x \mapsto \theta(x)$, it is clear that since $\theta(L) = \theta(0)$, the angle θ can only complete an integer number of complete turns. This number is known as the “winding number” of the mapping, and can be expressed as

$$w = \int_0^L dx \theta'(x), \quad (3.1)$$

where $\theta'(x)$ is the derivative of $\theta(x)$ with respect to its argument. We notice that although the winding number is a global property describing the mapping as a whole, it can be calculated by summing over the instantaneous local changes in the angle. Furthermore, mappings with different topological invariants cannot continuously be deformed into each other, and the winding number therefore introduces a non-trivial equivalence relation between mappings [24, 42].

As a second example, we consider the electronic states of a quantum system with translational invariance. Assume we have M different energy levels $E_n(\mathbf{k})$ and eigenstates $\psi_n(\mathbf{k})$ associated with the quasimomentum \mathbf{k} , where the quasimomentum \mathbf{k} takes on values in the first Brillouin zone. For simplicity, we consider a two-dimensional system with $M = 2$ energy bands. The physical states of the system can now be represented by points on the Bloch sphere, which is equivalent to the unit sphere S_2 consisting of unit vectors \mathbf{n} . The eigenstates of the system can therefore be thought of as a mapping from the torus to the unit sphere, $\mathcal{T} \rightarrow S_2$, where $\mathbf{k} \mapsto \mathbf{n}(\mathbf{k})$.

Although more challenging to visualize and understand, the topological invariant of this mapping is the so-called skyrmion or wrapping number [42]

$$S = \frac{1}{A_{\mathcal{T}}} \int_{\mathcal{T}} d^2k \mathbf{n} \cdot (\partial_x \mathbf{n} \times \partial_y \mathbf{n}), \quad (3.2)$$

where ∂_μ denotes the partial derivative with respect to k_μ and $A_{\mathcal{T}}$ is the area of the torus. This skyrmion number can be thought of as the number of times the mapping wraps around the unit sphere [22, 42].

The two examples given above represent two of the most common notions of topology used in condensed matter and statistical physics, namely the notions of topological band structures and topological excitations. In this thesis, we will primarily be concerned with the notion of topological band structures.

Based on the above discussion, it should be possible to classify electronic band structures into topologically distinct classes. Yet, for such a classification to be useful, we need to relate it to some physical properties of the system. Historically, the whole concept of the topology of band structures was introduced to explain the quantized levels of conductance in the integer quantum Hall effect [43]. Thus, at our level of understanding, we should expect that Hall conductivities in condensed matter systems are somehow related to topological invariants of the band structure, and that materials can be classified topologically according to their Hall response. Furthermore, as we will see, the topological classification can also be used to understand the presence or absence of edge modes in a system through the so-called bulk-boundary correspondence.

In this chapter, we will be introducing the concept of topology in condensed matter physics. In Sec. 3.1, we discuss the connection between topology and Hall conductivities, while in Sec. 3.2, we introduce the Haldane model as an example of a model containing topologically non-trivial phases. This model will be relevant for Paper [1]. Building on the discussion of the Haldane model, we introduce the bulk-boundary correspondence in Sec. 3.3. Finally, we discuss topological bosonic band structures in Sec. 3.4, while a more detailed discussion of the specific instance of topological magnons is given in Chapter 6.

3.1 Hall conductivity and Berry curvature

The classical Hall effect was discovered in 1879 by Edwin Hall [44], who discovered that when a conductor is placed in a magnetic field $\mathbf{B} = B\hat{z}$, the application of an electric field E_y gives rise to a transverse voltage V_x . We may understand this due to an off-diagonal term σ_{xy} in the conductivity matrix, so that the electric field $\mathbf{E} = E_y\hat{y}$ gives rise to a transverse current. Because of this, a boundary charge builds up and causes a transverse voltage.

In the original discovery, Hall made use of rather small magnetic fields. In the classical picture, this gives rise to large cyclotron orbits, which renders the electron motion essentially classical. Increasing the magnetic fields, the cyclotron orbits shrink, and at sufficiently large magnetic fields, we would expect quantum effects to become important. When von Klitzing and coworkers [43] measured the Hall conductivity at magnetic fields reaching 18 T, the measurements showed plateaus, and the Hall conductivity σ_{xy} took on quantized values

$$\sigma_{xy} = \frac{e^2}{2\pi\hbar}\nu, \quad (3.3)$$

where $\nu \in \mathbb{Z}$ is an integer.

To explain this phenomenon theoretically, we therefore need a quantum mechanical description of the system and a method to calculate Hall conductivities. In the following, we will therefore be discussing currents within a second quantization framework, and how to calculate Hall conductivities using linear response theory. As we will see, this calculation allows us to associate the quantity ν with the so-called Chern number of the bands, which is a topological invariant.

3.1.1 Current operator

We consider a system of spinless electrons described by a tight binding hopping model on a lattice. In the absence of an electromagnetic field, the system can thus be described by a Hamiltonian on the form

$$H = - \sum_{ij} t_{ij} c_i^\dagger c_j, \quad (3.4)$$

where $t_{ij} = t_{ji}^*$ is in general complex. For systems with translational invariance, it is useful to introduce the Fourier representation of the electron creation and annihilation operators through

$$c_{n\alpha} = \frac{1}{\sqrt{N}} \sum_{\mathbf{k}} e^{i\mathbf{k}\cdot\mathbf{x}_n^\alpha} c_{\mathbf{k}\alpha} \quad (3.5)$$

$$c_{n\alpha}^\dagger = \frac{1}{\sqrt{N}} \sum_{\mathbf{k}} e^{-i\mathbf{k}\cdot\mathbf{x}_n^\alpha} c_{\mathbf{k}\alpha}^\dagger, \quad (3.6)$$

where $c_{n\alpha}$ is the annihilation operator for an electron on sublattice α within the Bravais unit cell n , and where \mathbf{x}_n^α is the position of the lattice site, while N is the number of unit cells. The Hamiltonian then takes the form

$$H = \sum_{\mathbf{k}} \sum_{\alpha\beta} h_{\alpha\beta}(\mathbf{k}) c_{\mathbf{k}\alpha}^\dagger c_{\mathbf{k}\beta}. \quad (3.7)$$

This Hamiltonian can be diagonalized by introducing new fermion operators $d_{\mathbf{k}\alpha}$ through the unitary transformation $d_{\mathbf{k}\alpha} = \sum_{\beta} U_{\alpha\beta}(\mathbf{k}) c_{\mathbf{k}\beta}$ to obtain eigenenergies $E_{\mathbf{k}\alpha}$, where α is a band index.

We now aim at deriving a second quantized expression for the current operator in the system. Since the canonical and kinematic momenta are in

general different [45], the current operator j_μ along direction μ in general has two contributions, one paramagnetic and one diamagnetic. The diamagnetic part is simply given in terms of the electron density n_i and the vector potential \mathbf{A}_i on site i . Letting H be the Hamiltonian in the absence of an electromagnetic field, the paramagnetic part can be extracted from the Heisenberg equation of motion [33]

$$e\dot{n}_i = -\frac{ie}{\hbar}[n_i, H] \quad (3.8)$$

by comparing with the continuity equation

$$e\dot{n}_i + \sum_{\delta} j_{i,i+\delta} = 0 \quad (3.9)$$

for the electron charge. Here, $j_{i,i+\delta}$ is the operator corresponding to current flowing from lattice site i to lattice site $i + \delta$. We discuss this in more detail in Appendix A.

We now define a local current density operator

$$\mathbf{j}_i = \frac{1}{V_{\text{uc}}} \sum_j j_{ij} \boldsymbol{\delta}_{ij}, \quad (3.10)$$

where $\boldsymbol{\delta}_{ij}$ is the displacement vector between lattice sites i and j , and V_{uc} is the real space volume of the unit cell. As shown in Appendix A, the Fourier transformed current operator $j_\mu(\mathbf{q} \rightarrow 0)$ then takes the form

$$j_\mu(\mathbf{q} \rightarrow 0) = \left(\frac{1}{V_{\text{uc}} \sqrt{N}} \right) \frac{e}{\hbar} \sum_{\mathbf{k}} \sum_{\alpha\beta} \left(\frac{\partial h_{\alpha\beta}(\mathbf{k})}{\partial k_\mu} \right) c_{\mathbf{k}\alpha}^\dagger c_{\mathbf{k}\beta}. \quad (3.11)$$

Furthermore, we introduce the velocity matrix

$$v_\mu^{\alpha\beta} = \frac{1}{\hbar} \left(\frac{\partial h_{\alpha\beta}(\mathbf{k})}{\partial k_\mu} \right). \quad (3.12)$$

When the matrix $h_{\alpha\beta}$ is diagonal, the result therefore has a very simple interpretation, and can simply be thought of as the number of electrons in a given state multiplied with the group velocity.

3.1.2 Linear response and Berry curvatures

Knowing the second quantized form of the current operators, we are ready to calculate Hall conductivities using linear response theory. We consider a system described by the Hamiltonian in Eq. (3.7), and subject the system

to a time dependent electric field $\mathbf{E}(t) = \mathbf{E}e^{-i\omega t}$, where we eventually let the frequency go to zero. This electric field is incorporated in the theory through the time dependent vector potential

$$\mathbf{A}(t) = \frac{\mathbf{E}}{i\omega}e^{-i\omega t}, \quad (3.13)$$

which is coupled to the electric current in the system through the interaction term

$$H_{\text{em}} = -V_{\text{uc}} \sum_j \mathbf{A}(\mathbf{x}_j) \cdot \mathbf{j}_j. \quad (3.14)$$

Using linear response theory to linear order in the vector potential as discussed in Appendix A, the Hall conductivity can be expressed as [46, 47]

$$\sigma_{xy} = \frac{e^2}{2\pi\hbar} \sum_{\alpha} \int_{\text{BZ}} \frac{d^2k}{2\pi} n_F(E_{\mathbf{k}\alpha}) [1 - n_F(E_{\mathbf{k}\beta})] \mathcal{F}^{\alpha\beta}(\mathbf{k}). \quad (3.15)$$

Here $E_{\mathbf{k}\alpha}$ is the single particle energy of a particle in eigenstate α , and $n_F(E_{\mathbf{k}\alpha})$ is the corresponding Fermi-Dirac distribution. We have furthermore introduced the curvature matrix

$$\mathcal{F}^{\alpha\beta}(\mathbf{k}) = i\hbar^2 \frac{\tilde{v}_x^{\alpha\beta} \tilde{v}_y^{\beta\alpha} - \tilde{v}_y^{\alpha\beta} \tilde{v}_x^{\beta\alpha}}{(E_{\mathbf{k}\alpha} - E_{\mathbf{k}\beta})^2} \quad (3.16)$$

expressed in terms of the velocity matrix elements $\tilde{v}_{\mu}^{\alpha\beta}$ in the band eigenstate basis, which are obtained from the sublattice basis matrix elements $v_{\mu}^{\alpha\beta}$ through

$$\tilde{v}_{\mu}^{\alpha\beta}(\mathbf{k}) = U_{\alpha\rho}^{\dagger}(\mathbf{k}) v_{\mu}^{\rho\sigma}(\mathbf{k}) U_{\sigma\beta}(\mathbf{k}), \quad (3.17)$$

where $U_{\alpha\beta}(\mathbf{k})$ is the unitary transformation which diagonalizes the Hamiltonian.

We now assume that there is an energy gap in the spectrum, and that the chemical potential lies in the middle of the gap. Furthermore, we also assume that the temperature is small compared to the gap. This allows us to replace the Fermi-Dirac distributions above by unity or zero depending on whether the bands lie above or below the Fermi surface. Thus, the Hall conductivity can be written

$$\sigma_{xy} = \frac{e^2}{2\pi\hbar} \sum_{\alpha \text{ filled}} \int_{\text{BZ}} \frac{d^2k}{2\pi} \mathcal{F}^{\alpha}(\mathbf{k}), \quad (3.18)$$

where the sum runs over the filled bands and the band curvature

$$\mathcal{F}^\alpha(\mathbf{k}) = \sum_{\beta \neq \alpha} \mathcal{F}^{\alpha\beta}(\mathbf{k}) \quad (3.19)$$

is obtained by summing over a given row of the curvature matrix.

As also shown in Appendix A, this curvature equals the Berry curvature $\Omega^\alpha(\mathbf{k})$ of band α , which is defined as [46, 48]

$$\Omega^\alpha(\mathbf{k}) \equiv i[\langle \partial_x u_{\mathbf{k}}^\alpha | \partial_y u_{\mathbf{k}}^\alpha \rangle - \langle \partial_y u_{\mathbf{k}}^\alpha | \partial_x u_{\mathbf{k}}^\alpha \rangle]. \quad (3.20)$$

Here, ∂_μ denotes the derivative with respect to k_μ , and we have used the bracket notation $|u_{\mathbf{k}}^\alpha\rangle$ for the column vector α of the matrix $U_{\beta\alpha}(\mathbf{k})$. Integrating the Berry curvature over the Brillouin zone one obtains the so-called Chern number \mathcal{C}^α , so that the Hall conductivity can be expressed

$$\sigma_{xy} = \frac{e^2}{2\pi\hbar} \mathcal{C}, \quad (3.21)$$

where $\mathcal{C} = \sum_{\alpha \text{ filled}} \mathcal{C}^\alpha$ is the Chern number of the filled bands and $e^2/2\pi\hbar$ is the so-called quantum of conductance.

The concepts of Berry phases and Chern numbers in physics were first introduced to describe the adiabatic evolution of the states of quantum Hamiltonians described by parameters which depend on time [48]. Since the system we consider is translationally invariant and momentum is conserved, we may similarly consider the quasimomentum \mathbf{k} as a parameter which can be varied to control the matrix $h(\mathbf{k})$ and its eigenvectors. This allows us to construct a hierarchy of quantities which will prove useful in the following.

For simplicity, we consider a two-dimensional system, so that $\mathbf{k} = (k_x, k_y)$ lives on the torus. One may then define the Berry connection [49]

$$\mathbf{A}^\alpha(\mathbf{k}) = i\langle u_{\mathbf{k}}^\alpha | \nabla_{\mathbf{k}} | u_{\mathbf{k}}^\alpha \rangle. \quad (3.22)$$

Considering some path \mathcal{P} in the Brillouin zone, the Berry phase γ_B is obtained by integrating the Berry connection along the path, so that

$$\gamma_B = \int_{\mathcal{P}} d\mathbf{k} \cdot \mathbf{A}^\alpha(\mathbf{k}). \quad (3.23)$$

Motivated by Stokes' theorem, we may furthermore define the Berry curvature

$$\Omega^\alpha(\mathbf{k}) = (\nabla_{\mathbf{k}} \times \mathbf{A}^\alpha)_z, \quad (3.24)$$

and this definition is completely equivalent with the definition given above in Eq. (3.20). Finally, the Chern number is given by

$$C^\alpha = \int_{\text{BZ}} \frac{d^2k}{2\pi} \Omega^\alpha(\mathbf{k}), \quad (3.25)$$

as already discussed above.

While the skyrmion density $\mathbf{n} \cdot (\partial_x \mathbf{n} \times \partial_y \mathbf{n})$ used to define the wrapping number in Eq. (3.2) can be thought of as the unit sphere area spanned out by the vectors \mathbf{n} corresponding to an infinitesimal area around the point \mathbf{k} in the domain, the Berry curvature $\mathcal{F}^\alpha(\mathbf{k})$ can similarly be thought of as the portion of the Hilbert space spanned out by eigenstates of the Hamiltonian for the momenta around \mathbf{k} .

3.1.3 Quantization of the Chern number

We have now shown that the Hall conductivity is related to a quantity called the Chern number, which we have defined in terms of the eigenstates of the system. At this stage, however, it is not clear what these quantities have to do with topology. In particular, it is not clear yet why the Chern number should only be allowed to take on integer values. This is what we discuss in the following.

The Berry curvature $\mathcal{F}^\alpha(\mathbf{k})$ is a gauge invariant quantity, and is not affected by the gauge transformation [48]

$$|u_{\mathbf{k}}^\alpha\rangle \rightarrow e^{i\zeta(\mathbf{k})} |u_{\mathbf{k}}^\alpha\rangle. \quad (3.26)$$

In contrast, the Berry connection is not gauge invariant, and transforms according to

$$\mathbf{A}^\alpha(\mathbf{k}) \rightarrow \mathbf{A}^\alpha(\mathbf{k}) - \nabla_{\mathbf{k}} \zeta(\mathbf{k}). \quad (3.27)$$

As starting point for our argument, we consider a square Brillouin zone which we denote by D , and a curve \mathcal{P} which encloses a domain $D_1 \subset D$, such that $\mathcal{P} = \partial D_1$. However, since the Brillouin zone has the topology of a torus, the curve \mathcal{P} does not have a well defined inside and outside, so in fact, we could equally well think of the curve \mathcal{P} as enclosing the conjugate domain D_2 , as shown in Fig. 3.1 (a). Considering the integral of the Berry connection around the closed path \mathcal{P} and using Stoke's theorem, we may now write

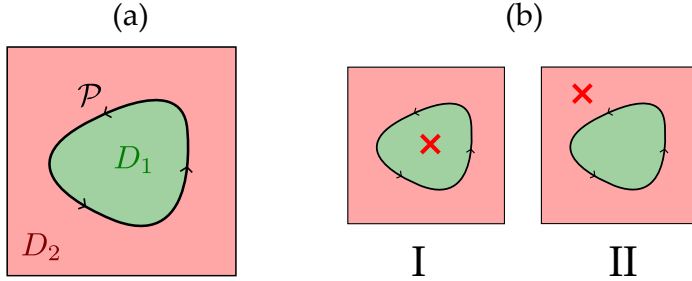


Figure 3.1: (a) Stoke's theorem on a torus. A curve \mathcal{P} enclosing the domain D_1 can equally well be thought of as enclosing D_2 . (b) The location of exceptional points in the topologically non-trivial regime depends on the choice of gauge.

$$\int_{\mathcal{P}} d\mathbf{k} \cdot \mathbf{A}^\alpha(\mathbf{k}) = + \int_{D_1} d^2k \mathcal{F}^\alpha(\mathbf{k}) \quad (3.28a)$$

$$\int_{\mathcal{P}} d\mathbf{k} \cdot \mathbf{A}^\alpha(\mathbf{k}) = - \int_{D_2} d^2k \mathcal{F}^\alpha(\mathbf{k}), \quad (3.28b)$$

where the opposite signs occur because the path \mathcal{P} is oriented in opposite directions with respect to the two domains D_1 and D_2 . By subtracting the second equation from the first, we obtain an integral over the entire domain D . Thus, it may at first glance appear as if the Chern number is always trivial, so that $\mathcal{C}^\alpha = 0$. However, this is not the case, and the reason is subtle. The eigenvectors of the Hamiltonian are associated with arbitrary phases. To be able to calculate the Berry curvature, we need to calculate the derivatives of the eigenstates, and this requires us to fix the phases of the various states (i.e. fix the gauge). However, it may not be possible to do this in a continuous way over the entire Brillouin zone within a single gauge, and we may then have exceptional points, as indicated in Fig. 3.1 (b). By changing the gauge, however, the exceptional point can typically be moved from one domain to the other, and we should then evaluate the two equations in Eq. (3.28) in different gauges which we denote by I and II. Subtracting the the two equations and utilizing that the Berry curvature is a gauge invariant quantity, we then have

$$2\pi\mathcal{C}^\alpha = \int_D d^2k \mathcal{F}^\alpha(\mathbf{k}) = \oint_{\mathcal{P}} d\mathbf{k} \cdot [A_{\text{I}}^\alpha(\mathbf{k}) - A_{\text{II}}^\alpha(\mathbf{k})], \quad (3.29)$$

where $\mathbf{A}_I^\alpha(\mathbf{k})$ and $\mathbf{A}_{II}^\alpha(\mathbf{k})$ are the Berry connections in the two gauges. Assuming that gauge II is obtained from gauge I via a gauge transformation specified by ζ through Eq. (3.26), we then have

$$\oint_{\mathcal{P}} d\mathbf{k} \cdot [\mathbf{A}_I^\alpha(\mathbf{k}) - \mathbf{A}_{II}^\alpha(\mathbf{k})] = \oint_{\mathcal{P}} d\mathbf{k} \cdot \nabla_{\mathbf{k}} \zeta(\mathbf{k}) = 2\pi m, \quad (3.30)$$

where $m \in \mathbb{Z}$ is an integer and we have utilized the uniqueness of the phase factor $\exp(i\zeta(\mathbf{k}))$ upon completing the loop. This proves that \mathcal{C}^α is integer valued. Hence, conductivity is quantized, and the Chern number allows a topological classification of electronic band structures. In experiments, the quantization of conductance has been found to be extremely precise, with a precision down to 10^{-9} [50].

From the above argument, we also realize that the Chern number is always trivial when we can choose a consistent gauge in the entire Brillouin zone. We will be commenting on this in a concrete context when discussing the Haldane model in Sec. 3.2.

An infinitesimally small change in the model through the matrix $h_{\alpha\beta}(\mathbf{k})$ cannot usually change the Chern number significantly, and since the Chern number must be an integer, it therefore cannot change at all. Thus, a dramatic change in the model is needed to change the Chern number. Such a dramatic change is a gap closing. When a gap closes, the involved eigenstates become degenerate, and this makes the otherwise gauge invariant Berry curvature ill defined at the gap closing point, and as opposed to case of the exceptional point discussed above, this problem cannot simply be solved by moving to a different gauge. When a gap opens again, the Chern number may have changed.

3.2 The Haldane model

Both the original discovery of the Hall effect and the discovery of the integer quantum Hall effect were done in systems with a net magnetic field penetrating the sample. However, a net magnetic field is in fact not necessary to give finite Hall conductivities. In systems with broken time reversal symmetry, the band structure itself may provide a finite Hall conductivity. An explicit demonstration of this was provided by Haldane in 1988 [51], who investigated what we today know as the Haldane model.

In Paper [1], we will be studying a spin model with magnon excitations which perfectly mimic the electronic states in the Haldane model. To prepare for this, we will therefore be discussing the Haldane model in an electronic

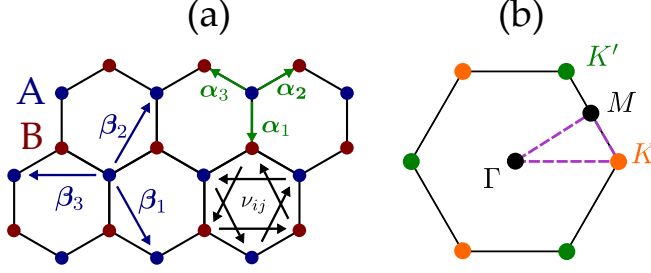


Figure 3.2: (a) Honeycomb lattice with sublattices A and B. Next-to-nearest neighbour hoppings are associated with a phase $\nu_{ij}\phi$, where $\nu_{ij} = \pm 1$ is +1 for hoppings along the arrows and -1 for hoppings against the arrows. (b) The Brillouin zone of the hexagonal lattice with high-symmetry points and a typical high-symmetry path.

context in this section, and also use it to illustrate the main concepts in topological band theory.

The Haldane model is a model describing hopping of electrons between the lattice sites of a honeycomb lattice, as shown in Fig. 3.2. The model is given by [46, 51, 52]

$$H = -t_1 \sum_{\langle ij \rangle} c_i^\dagger c_j - t_2 \sum_{\langle\langle ij \rangle\rangle} e^{i\phi_{ij}} c_i^\dagger c_j + M \sum_i \epsilon_i c_i^\dagger c_i, \quad (3.31)$$

where t_1 is the nearest neighbour hopping amplitude, and where $\epsilon_i = +1$ for $i \in A$ and $\epsilon_i = -1$ for $i \in B$, so that M is the strength of a staggered potential. The special term that was added by Haldane is the next-to-nearest neighbour hopping with amplitude t_2 . In this term, each hopping is associated with a phase $\phi_{ij} = \nu_{ij}\phi$, where the sign $\nu_{ij} = \pm 1$ is chosen according to the pattern in Fig. 3.2 (a). These phases can be thought of as generated by a staggered magnetic field through the unit cell, but where the net magnetic field is still zero.

In his paper introducing the Haldane model, Haldane remarked that “the particular model presented here is unlikely to be directly physically realizable”. Several decades later, it has, in perfect fulfilment of the irony of fate, been realized in ultracold atom systems [53].

3.2.1 Bulk spectrum

To determine the bulk energy spectrum, we introduce the Fourier representation for the fermion creation and annihilation operators. The honeycomb lattice can be thought of as a hexagonal lattice with a two-atomic basis. The lattice sites of the honeycomb lattice are then located at positions \mathbf{x}_n^D , where n is a unit cell index and $D \in \{A, B\}$ a sublattice index. We define the Fourier transform according to

$$c_{nD} = \frac{1}{\sqrt{N_A}} \sum_{\mathbf{k}} e^{i\mathbf{k} \cdot \mathbf{x}_n^D} c_{\mathbf{k}D}, \quad (3.32)$$

where the operator c_{nD} is the electron annihilation operator on the D sublattice in unit cell n . The first Brillouin zone of the hexagonal lattice is shown in Fig. 3.2 (b), and has the shape of a hexagon. The high symmetry points K and K' are inequivalent.

Using the above Fourier transform, the Haldane Hamiltonian takes the form

$$H = \sum_{\mathbf{k}} c_{\mathbf{k}}^\dagger h(\mathbf{k}) c_{\mathbf{k}}, \quad (3.33)$$

where we have introduced electron spinor $c_{\mathbf{k}} = (c_{\mathbf{k}A} \quad c_{\mathbf{k}B})^T$, and the Hamiltonian matrix $h(\mathbf{k})$ is given by

$$h(\mathbf{k}) = \begin{pmatrix} M - 2t_2 \sum_{\beta} \cos(\mathbf{k} \cdot \boldsymbol{\beta} + \phi) & -t_1 \sum_{\alpha} e^{i\mathbf{k} \cdot \boldsymbol{\alpha}} \\ -t_1 \sum_{\alpha} e^{-i\mathbf{k} \cdot \boldsymbol{\alpha}} & -M - 2t_2 \sum_{\beta} \cos(\mathbf{k} \cdot \boldsymbol{\beta} - \phi) \end{pmatrix}, \quad (3.34)$$

where the sums over $\boldsymbol{\alpha}$ and $\boldsymbol{\beta}$ are over the sets of three nearest and next-to-nearest neighbour vectors shown in Fig. 3.2 (a).

Since the matrix is Hermitian, it can also be expressed in terms of Pauli matrices, which form a basis for Hermitian 2×2 matrices. Thus, we may also write

$$h(\mathbf{k}) = d_0(\mathbf{k}) + d_i(\mathbf{k})\sigma_i, \quad (3.35)$$

where σ_i denotes a Pauli matrix, and $i \in \{1, 2, 3\}$. Here, the coefficients

$d_\mu(\mathbf{k})$ are given by

$$d_0(\mathbf{k}) = -2t_2 \cos \phi \sum_{\beta} \cos(\mathbf{k} \cdot \beta) \quad (3.36a)$$

$$d_1(\mathbf{k}) = -t_1 \sum_{\alpha} \cos \mathbf{k} \cdot \alpha \quad (3.36b)$$

$$d_2(\mathbf{k}) = +t_1 \sum_{\alpha} \sin \mathbf{k} \cdot \alpha \quad (3.36c)$$

$$d_3(\mathbf{k}) = M + 2t_2 \sin \phi \sum_{\beta} \sin \mathbf{k} \cdot \beta. \quad (3.36d)$$

The energy spectrum of a Hamiltonian on the given form is known to be

$$E_{\mathbf{k}\pm} = d_0(\mathbf{k}) \pm |\mathbf{d}(\mathbf{k})|, \quad (3.37)$$

where we have introduced the vector $\mathbf{d} = (d_1, d_2, d_3)$. For the Haldane model, this spectrum is shown along a high-symmetry path in Fig. 3.3 for $\phi = \pi/2$ and two different values of M .

The gap in the spectrum is determined solely by the magnitude of the vector \mathbf{d} . Since the two vector components d_1 and d_2 vanish only at the special points K and K' in the Brillouin zone, these are the only two points where the gap can actually close. At these points, the last component d_3 is given by

$$d_3(\pm K) = M \pm 3\sqrt{3}t_2 \sin \phi, \quad (3.38)$$

so that the gap closes at the point $\pm K$ for $M = \mp 3\sqrt{3}t_2 \sin \phi$. As we have already argued, the topological properties of the system can only change under a gap closing. Thus, we suspect that one may draw a phase diagram in the ϕ - M -plane which has the curves defined by setting $d_3 = 0$ as phase boundaries.

3.2.2 Topology

To verify our suspected phase diagram, we need to know the topological invariants within the different regions of the ϕ - M -plane. A simple way to do this, is to calculate the Berry curvature and integrate it numerically over the Brillouin zone to obtain the Chern number.

For Hamiltonians on the form of Eq. (3.35), the Berry curvature can conveniently be calculated using the formula [48]

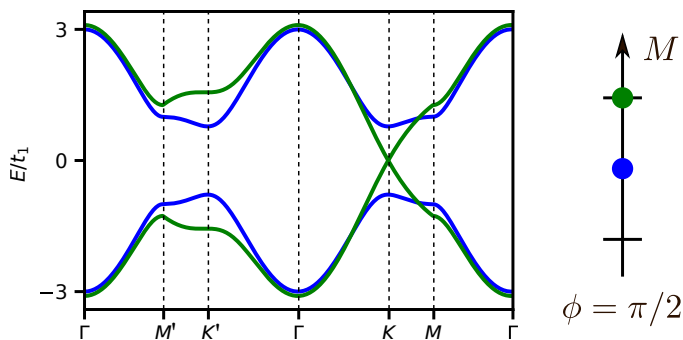


Figure 3.3: Haldane model energy spectrum for $\phi = \pi/2$ and $M = 0$ (blue) and $M = 3\sqrt{3}t_2$ (green), corresponding to the gap closing point.

$$\Omega^\pm = \mp \hat{\mathbf{d}} \cdot (\partial_{k_x} \hat{\mathbf{d}} \times \partial_{k_y} \hat{\mathbf{d}}), \quad (3.39)$$

and the result is shown in Fig. 3.4 (a) for four different parameter choices as indicated in Fig. 3.4 (b). Integrating over the Brillouin zone to obtain the Chern numbers, we obtain the phase diagram in Fig. 3.4 (b), which shows the Chern number of the lowest band in the M - ϕ -plane. There are three phases, where the Chern number takes on the values $\mathcal{C} = 0$ (topologically trivial) and $\mathcal{C} = \pm 1$ (topologically non-trivial). The model transitions between these phases in a so-called topological phase transition when the gap closes. As illustrated in Fig. 3.4 (c), this topological phase transition can be thought of as an exchange of a unit Chern number at the point K .

To understand some aspects of this result, we may consider the Haldane model in the atomic limit $M \rightarrow \pm\infty$. The model is then trivially solvable, and the eigenstates and energies become momentum independent, clearly corresponding to a topologically trivial phase. To calculate the Chern number in the remaining sectors of the phase diagram, one may show that a unit Chern number is transferred between the bands in a gap closing within a low energy effective theory valid close to the gap closing point [46]. We will not be discussing this further here.

Earlier, we remarked that non-zero Chern numbers may only occur when it is not possible to choose a consistent gauge over the entire Brillouin zone. The topologically trivial regime corresponds to $|M| > 3\sqrt{3}t_2 \sin \phi$, and in this regime, $d_3(\mathbf{k}) > 0$ for all \mathbf{k} . In contrast, the topologically non-trivial regime also has a set of momenta \mathbf{k} where $d_3 < 0$. Thus, while the mapping from the torus to the unit sphere spanned out by \mathbf{d} covers the full unit sphere

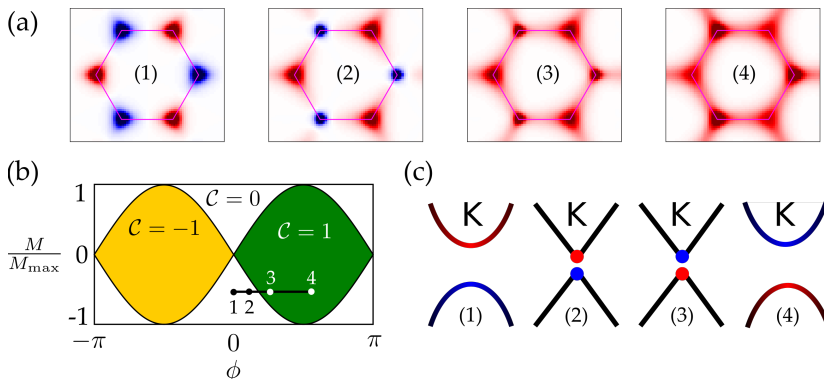


Figure 3.4: (a) Berry curvatures for four different parameter choices (1)-(4) indicated in the Haldane model phase diagram of (b). The Haldane model has topologically trivial ($C = 0$) and non-trivial ($C = \pm 1$) phases. (c) Approaching a topological phase transition, the negative Berry curvature (in blue) becomes more and more peaked around the point K where the gap closes. The bands interchange a unit Chern number in the transition.

in the topologically non-trivial regime, in the topologically trivial regime, it does not.

The eigenstates of the Hamiltonian at a given momentum \mathbf{k} are aligned along the vector $\mathbf{d}(\mathbf{k})$ on the Bloch sphere. However, as discussed in Sec. 8.6 of Ref. [49], there exists no gauge where the mapping from the unit sphere to a spinor ψ representing the eigenstate is continuous over the entire unit sphere. Thus, within any gauge, there always exists a point \mathbf{k} where the mapping $\mathbf{k} \rightarrow \mathbf{d} \rightarrow \psi$ is discontinuous. This represents an exceptional point as discussed in Sec. 3.1.3, and the presence of such an exceptional point gives rise to a non-zero Chern number and non-zero Hall conductivities.

3.3 Bulk-boundary correspondence

So far, we have been considering systems with periodic boundary conditions. In systems of finite size, or which do not have translational invariance, it turns out that topological classification is also intimately connected with the presence or absence of edge modes. The association of bulk properties with the properties on the edge of the system is known as the “bulk-boundary correspondence”.

Simply put, the bulk-boundary correspondence states the following: The interface between two materials characterized by topological invariants ν_1 and ν_2 has a set of $|\nu_1 - \nu_2|$ localized boundary modes.

Thus, when a material undergoes a topological phase transition, this is always associated with the emergence or disappearance of boundary modes at the edges of the material. Remarkably, the bulk-boundary correspondence therefore provides us with a tool to say something about the physics on the edges of a system based only on the physics of the system with periodic boundary conditions.

Proving the bulk-boundary correspondence is not an easy task. In some cases, it can be done based on index theorems in fibre bundle theory [41], but there is no general proof [54]. The bulk-boundary can be checked in multiple systems, where one may show that closing the gap changes the topological invariant, and at the same time introduces edge modes. Proving or justifying the bulk-boundary correspondence convincingly beyond very hand-wavy arguments is however very challenging. The basic problem is that whereas the bulk properties are concerned with infinite systems with translational invariance, the boundary properties can only occur when we explicitly break translational symmetry in the system.

Instead of venturing into mathematical details, we will simply see how the bulk-boundary correspondence unfolds for the Haldane model. We will be doing this through two approaches. First, we break translational invariance in the Haldane model by considering a ribbon geometry, and calculate the band structure numerically. Second, we develop an effective low energy theory in which the boundary modes can be calculated analytically.

3.3.1 Ribbon geometry

Consider a Haldane model on a ribbon geometry, where we consider periodic boundary conditions in the \hat{x} -direction and a finite number of unit cells in the \hat{y} -direction, as shown in Fig. 3.5 (a). Since the system is translationally invariant in the \hat{x} -direction, it is useful to perform a Fourier transform there, but use a real space description in the remaining direction. This can be done through the partial Fourier transform

$$c_{n_x, n_y} = \frac{1}{\sqrt{N_x}} \sum_{k_x} e^{ik_x \hat{x} \cdot \mathbf{x}_n^D} c_{k_x n_y, D}, \quad (3.40)$$

where \mathbf{x}_n^D is the position of the atom on sublattice D in the Bravais lattice cell labelled by $n = (n_x, n_y)$, and N_x is the number of Bravais unit cells in the

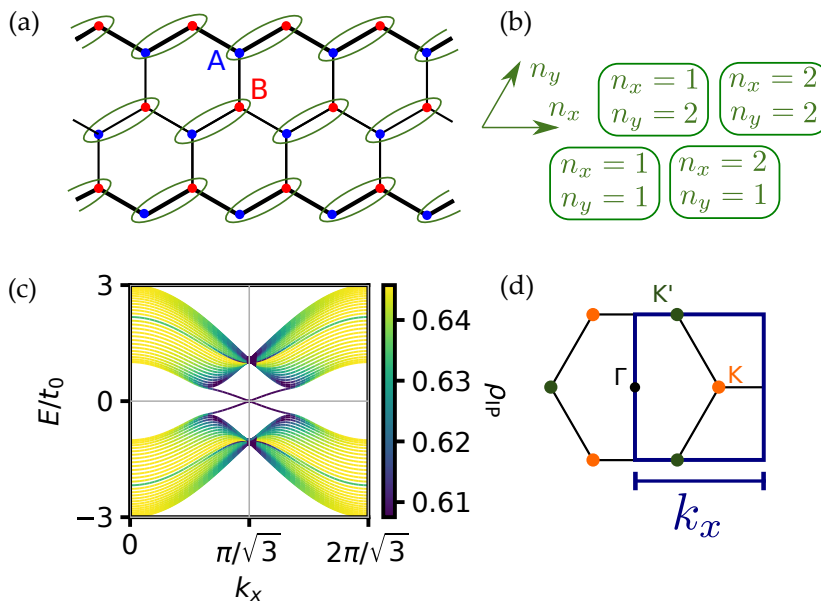


Figure 3.5: Zigzag ribbon geometry spectrum for the Haldane model. (a) Honeycomb ribbon with zigzag edge. Periodic boundary conditions in the horizontal direction and a finite number of layers in the vertical direction. (b) Labelling of unit cells on the honeycomb ribbon. (c) Ribbon geometry spectrum with inverse participation ratio indicated with color. (d) The bulk part of the ribbon spectrum can be thought of as a projection down on the indicated line.

\hat{x} -direction. The operators $c_{k_x n_y, D}$ are our new partially Fourier transformed operators. The surface Brillouin zone is determined by the periodicity in the direction \hat{x} , which is $\sqrt{3}d$ for the zig-zag edge ribbon geometry, where d is the nearest neighbour distance. Thus, the surface Brillouin zone can be chosen as $k_x \in [0, 2\pi/\sqrt{3}d)$.

Introducing this partial Fourier transform in the Hamiltonian of Eq. (3.31) on the ribbon geometry, the Hamiltonian takes the form

$$H = \sum_{k_x} c^\dagger(k_x) h(k_x) c(k_x), \quad (3.41)$$

where $c(k_x)$ now denotes a vector of size $2N_y$ containing the various operators $c_{n_y D}(k_x)$. Similarly, $h(k_x)$ is an $2N_y \times 2N_y$ matrix. Diagonalization

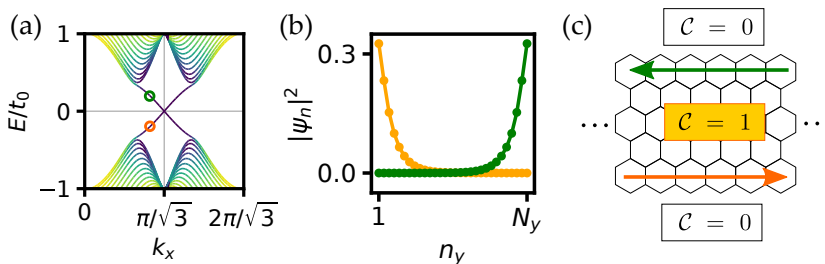


Figure 3.6: Haldane model edge states. (a) Ribbon geometry spectrum in the topologically non-trivial regime with edge modes crossing the gap. (b) Edge state probability amplitudes for the states indicated in (a). The two edge states are localized on opposite edges. (c) Different Chern numbers across the sample edges imply the existence of edge modes.

of this matrix gives the $2N_y$ eigenvalues and eigenvectors corresponding to momentum k_x .

The spectrum that results from this is shown in Fig. 3.5 (c) for parameters $M = 0$ and $\phi = \pi/2$ corresponding to the topologically non-trivial regime. The bands have been colored according to their inverse participation ratio. Assuming that a state in the band structure corresponds to probability amplitudes ψ_i with $i \in \{1, \dots, N\}$, we define the inverse participation ratio as

$$\rho_{\text{IP}} = \frac{1}{N} \left(\sum_i |\psi_i|^4 \right)^{-1}. \quad (3.42)$$

When a set of M amplitudes in the eigenvector are equally probable and the remaining amplitudes are zero, this gives $\rho_{\text{IP}} = M/N$. Thus, a localized edge state would have a vanishing edge participation ratio in the thermodynamic limit $N \rightarrow \infty$, while a delocalized state would have a finite value.

Although the bulk spectrum is gapped (see Fig. 3.3), the spectrum on the ribbon geometry still has states crossing the gap. Since there are no bulk states within this energy range, the states must be edge states, as also indicated by their purple color. This is also shown in Fig. 3.6, where (b) shows the spatial profile of the edge states indicated in (a). From the group velocities of the states, it is furthermore clear that these are chiral edge states, since they are only propagating in the counter-clockwise direction around the sample, as illustrated in Fig. 3.6 (c).

3.3.2 Effective low energy theory

The existence of chiral edge states in the Haldane model can also be demonstrated within an effective low energy theory describing the system [46, 50]. We are interested in the physics close to the situation where the gap closes, and therefore expand the Haldane model Hamiltonian around the points $\pm K$ to obtain the effective low energy theories

$$h(\pm K + \mathbf{q}) = 3t_2 \cos \phi + \frac{3t_1 d}{2} (\pm q_x \sigma_x - q_y \sigma_y) + (M \pm 3\sqrt{3}t_2 \sin \phi) \sigma_z \quad (3.43)$$

describing the electrons close to the two special points $\pm K$. Introducing the velocity $v = 3t_1 d/2$ and the gap parameter $m_{\pm} = M \pm 3\sqrt{3}t_2 \sin \phi$, the two theories can be written

$$h_{\pm}(\mathbf{q}) = v(\pm q_x \sigma_x + q_y \sigma_y) + m_{\pm} \sigma_z, \quad (3.44)$$

where we have disregarded the constant term, which is insignificant because it does not affect the eigenstates of the system. From this low energy effective theory, we may now go back to a real space theory by replacing the momenta according to $q_{\mu} \rightarrow -i\partial_{\mu}$. We are interested in the possible existence of edge modes. We therefore have to consider a system which contains an interface between topologically trivial and non-trivial subsystems. We therefore allow the mass m to depend on the position coordinate y in such a way that $m(y \rightarrow \infty) = m$ and $m(y \rightarrow -\infty) = -m$, as shown in Fig. 3.7. We then have real space theory

$$h^{\pm} = -v(\pm \sigma_x i\partial_x + \sigma_y i\partial_y) + m_{\pm}(y) \sigma_z. \quad (3.45)$$

The above Hamiltonian is separable, as it can be written on the form $h^{\pm} = h_x^{\pm} + h_y^{\pm}$ with Hamiltonians $h_{x,y}^{\pm}$ acting only on the x or y coordinates. Furthermore, the x -dependence is trivial and describes a freely propagating particle. We therefore write the eigenstates of the system on the form

$$|\psi\rangle = e^{iq_x x} [\phi_1(y) \gamma_1 + \phi_2(y) \gamma_2], \quad (3.46)$$

where γ_1 and γ_2 are the two eigenvectors of σ_x with corresponding eigenvalues $\zeta_{1,2} = \pm 1$. These eigenvectors are given by

$$\gamma_1 = \begin{pmatrix} 1 \\ 1 \end{pmatrix} \quad \gamma_2 = \begin{pmatrix} 1 \\ -1 \end{pmatrix}. \quad (3.47)$$

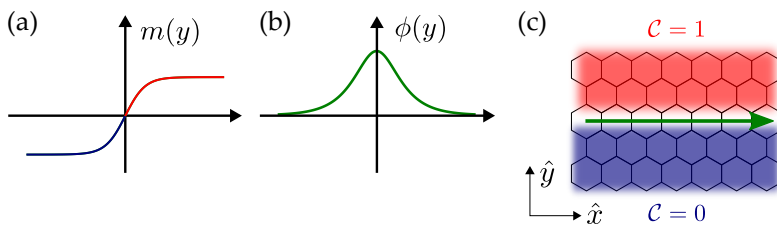


Figure 3.7: Edge states in effective low energy theory. If the effective sublattice asymmetry $m(y)$ changes sign as function of y and takes on values $\pm m$ for $y \rightarrow \pm\infty$, an edge mode eigenstate occurs on the boundary between the two regions. Thus, as shown in (c), two regions in space with different topological invariants have an edge mode travelling in the direction \hat{x} in between.

In the regimes $y \rightarrow \pm\infty$, one may now show that the model has eigenstates on the form $|\psi\rangle \propto e^{i(q_x x + q_y y)}$ with energies $E = \pm\sqrt{v^2(q_x^2 + q_y^2) + m^2}$. These are the bulk eigenstates. However, the model also permits a localized solution on the form

$$|\psi\rangle = e^{iq_x x} \phi_i(y) \gamma_i \quad (3.48)$$

with energy $E_i = \pm\zeta_i v q_x$ originating only from the term h_y^\pm in the Hamiltonian¹. The eigenequations for $\phi_i(y)$ then become

$$[\zeta_i v \partial_y - m_\pm(y)] \phi_i(y) = 0, \quad (3.49)$$

and the solution is

$$\phi_i(y) = \exp\left[\frac{\zeta_i}{v} \int_0^y m_\pm(y') dy'\right]. \quad (3.50)$$

In the limits $y \rightarrow \pm\infty$, this function approaches an exponential. Crucially, however, the wavefunction is normalizable for both $y \rightarrow \infty$ and $y \rightarrow -\infty$ only when $m_\pm(y)$ changes sign. This corresponds exactly to the situation where the material is in different topological phases in the two half planes of the system. Thus, only one of the two eigenvectors $\gamma_{1,2}$ may give a properly normalized edge state. Which of the two this is depends on $\text{sgn } m(y \rightarrow \infty)$,

¹By carrying out the full analysis, one may show that the localized eigenstates of the effective low energy model can always be written on this form, and that the energy contribution from h_y^\pm is always zero.

and determines the direction of propagation along the interface since the energy of the edge mode is $E_i = \pm\zeta_i v k_x$.

If we were to introduce models for the upper and lower half-planes with Chern numbers ± 1 , the effective low energy Hamiltonians corresponding to both valleys would have masses $m_{\pm}(y)$ with a changing sign. Consistent with the bulk-boundary correspondence, we would then get two edge modes.

3.4 Topological bosonic systems

We have seen that the band structure of an electronic system can be viewed as a mapping from the Brillouin zone to the Hilbert space of the model for non-interacting electron systems, which are described by quadratic Hamiltonians. The band structure and diagonalization procedure in such a case does, however, not depend on the fermionic nature of the electrons. We can therefore equally well classify the band structures of bosonic particles and excitations through the topological classification scheme.

As discussed previously, the whole concept of topological band structures was invented to explain quantized Hall conductance, which had not been predicted before it was observed experimentally. Furthermore, the fact that the Hall conductivity in electronic systems is simply proportional to the integer valued Chern number is a consequence of the Pauli principle, as it rests on being able to replace the Fermi-Dirac distributions in Eq. (3.15) with unity or zero. Since bosons obey different statistics, we would not expect bosonic transverse conductivities to be quantized. It is therefore by no means a coincidence that topological band structures were first discussed within an electronic setting.

Recently, however, there has also been significant interest in topological bosonic systems². Topological bosonic band structures can now be realized in a multitude of settings. Ultracold atoms in optical lattices have band structures similar to condensed matter systems which can be engineered to realize topologically non-trivial phases [55–57]. Topology is also used to classify the lattice vibrations and edge modes in acoustical and solid state materials [58–62]. The suggestion and observation of topological photons [63–65] in photon crystals has led to the emergence of topological photonics [66], and in magnetic materials, both magnon and Schwinger boson band structures can become topologically non-trivial [36, 67]. In short, topological band

²By topological bosonic systems, we will be referring to systems with a topologically non-trivial band structure. A spin texture hosting skyrmions can also be considered topological, but this is not what we will be considering.

theory is no longer restricted to electronic systems.

A key question is, however, where we can find topologically non-trivial bosonic band structures. A good place to start, is to think of how topologically non-trivial phases occur in electronic systems. To demonstrate the theoretical possibility of a topologically non-trivial band structure without a net magnetic field, Haldane added the famous next-to-nearest neighbour hopping term breaking time reversal symmetry. Similar symmetry breaking is required to produce bosonic analogs of the Haldane model within the contexts above. In ultracold atom systems, artificial gauge fields can be engineered with astonishing precision using lasers [53]. In acoustic metamaterials, one may use acoustic elements with rotating parts [59, 68], and Coriolis forces originating from rotation of the sample may produce topological phonon band structures [61]. In magnetic systems, topologically non-trivial band structures often occur due to the presence of a Dzyaloshinskii-Moriya interaction originating from spin-orbit coupling [36].

Although there is no quantized conductance in topological bosonic systems, the description of the band structure within the framework of topological band theory may still provide important insights on experimentally accessible observables. Hall conductivities are typically still related to the Berry curvatures of the system, not through the Chern number, but weighted with some Bose distributions. As a consequence, various Hall conductivities may often have a non-trivial dependence with temperature as various energy ranges in the band structure with different Berry curvatures are filled [69, 70]. Furthermore, the connection between topological bulk band structures and the emergence or disappearance of edge modes is independent of particle statistics. Thus, the boundaries of topological bosonic systems may provide channels for edge transport.

Contrary to fermions, bosonic topological edge states may hybridize with other bosonic excitations. In Paper [1], we exploit this in a system of topological magnons coupled to lattice vibrations. We show that the edges may host exotic magnon-polarons composed of chiral edge magnons hybridized with edge phonons. Thus, coupling effects may produce bosonic topological insulators with new and exotic edge states. The mixing may also lead to a chirality in the phonon transport of the system, and we will be discussing this in more detail in Chapter 6.

Chapter 4

Phonons

In the solid state, translational symmetry is broken spontaneously, and the atoms may organize into periodic structures in space, forming crystalline order. However, just like there can be magnetic fluctuations around a magnetically ordered state, there may also be fluctuations around the crystalline order. The basic degree of freedom describing these fluctuations is the deviation of an atom from its equilibrium position. Delocalizing such excitations, we obtain a quantum mechanical description in terms of collective quasiparticles called phonons [71].

Phonons play an important role for material properties such as heat capacity and thermal conductivity [72]. Importantly, however, phonons also play a very important role in condensed matter physics due to their interaction with other degrees of freedom. Most notably, phonons interact with electrons to produce superconductivity in weak coupling superconductors [73]. Lattice distortions may also interact with magnetic degrees of freedom to produce magnetostriction and new exotic magnon-polaron quasiparticles [74], which are excitations of both magnetic and phononic character.

In this Chapter, we will be discussing the aspects of phonons relevant for the research in Papers [1] and [2]. We start by discussing how force constant models can be used to model phonon spectra in Section 4.1. Subsequently, we will be discussing how phonons couple to electrons in Sec. 4.2. This is relevant for Paper [2], where we study the possibility of a superconducting instability in graphene due to a phonon-mediated mechanism. In Sec. 4.3, we will be discussing magneto-elastic coupling. This will be relevant for Paper [1], where we discuss the coupling and hybridization of phonons with topological magnons.

4.1 Force constant models

Phonons are quantum excitations corresponding to lattice vibrations in crystalline solid systems. We assume that the lattice can be considered a Bravais lattice [75] with several atoms in the basis. In their equilibrium configuration, the atoms are then localized at positions $\mathbf{x}_{in} = \mathbf{x}_i + \boldsymbol{\tau}_n$, where \mathbf{x}_i is the position of Bravais lattice site i , and $\boldsymbol{\tau}_n$ is the relative position of atom n inside the Bravais unit cell.

A general model for the solid state must in addition to kinetic terms for electrons and ions in the system contain interactions between the ions, between electrons, and between electrons and ions. To understand the bare phonon properties of the system, however, it usually suffices to consider the interaction between ions in the material, which we assume to take the form

$$H_{\text{ph}} = \sum_{i,n} \frac{(\mathbf{P}_{in})^2}{2M_n} + \frac{1}{2} \sum_{i,j} \sum_{m,n} U(\mathbf{R}_{in} - \mathbf{R}_{jm}), \quad (4.1)$$

where \mathbf{R}_{in} is the position of ion n in the basis of Bravais unit cell i , and which may deviate from the equilibrium position \mathbf{x}_{in} . Furthermore, we let atom n in the basis have mass M_n , and \mathbf{P}_{in} denote its momentum. The form of $U(\boldsymbol{\delta})$ is typically isotropic, and has a minimum at some distance r_0 . Due to homogeneity of space, the interaction between the atoms depends only on the relative displacement of the two atoms.

Assuming the ion displacements \mathbf{u}_{in} from the equilibrium positions are small, we may write $\mathbf{R}_{in} = \mathbf{x}_{in} + \mathbf{u}_{in}$ and Taylor expand the Hamiltonian in small \mathbf{u}_{in} to obtain

$$H_{\text{ph}} = \sum_{i,n} \frac{(\mathbf{P}_{in})^2}{2M_n} + \frac{1}{2} \sum_{i,j} \sum_{mn} \sum_{\mu\nu} \Phi_{\mu\nu}^{nm}(\boldsymbol{\delta}_{ij}^{nm}) u_{in}^\mu u_{jm}^\nu. \quad (4.2)$$

Here, the indices μ, ν denote directions the ions may be displaced in, and for now, we may think of them Cartesian indices, so that $\mu, \nu \in \{x, y, z\}$. Furthermore, $\boldsymbol{\delta}_{ij}^{nm} = \mathbf{x}_{jm} - \mathbf{x}_{in}$ is the vector connecting the equilibrium lattice sites at positions \mathbf{x}_{in} and \mathbf{x}_{jm} . In the above Hamiltonian, we will typically only keep interactions between deviations on lattice sites which are fairly close, but in principle, they can be arbitrarily far apart.

Since the above Hamiltonian is quadratic in momenta and ion deviations from equilibrium, it can be diagonalized. As a first step, we introduce the rescaled coordinates

$$\tilde{\mathbf{u}}_{in} = \sqrt{\mu_n} \mathbf{u}_{in} \quad \tilde{\mathbf{P}}_{in} = \frac{1}{\sqrt{\mu_n}} \mathbf{P}_{in}, \quad (4.3)$$

where we have defined a relative mass μ_n for basis atom n such that $M_n = \mu_n M$ and $M = \prod_m N_b \sqrt{M_m}$, where N_b is the number of atoms in the basis. This rescaling has been chosen such that the canonical commutation relations are preserved, so that

$$[\tilde{u}_{in}^\mu, \tilde{P}_{jm}^\nu] = i\hbar \delta_{ij} \delta_{\mu\nu} \delta_{mn}. \quad (4.4)$$

The idea is that the Hamiltonian then takes the form

$$H_{\text{ph}} = \sum_i \frac{(\tilde{P}_{in})^2}{2M} + \frac{1}{2} \sum_{i,j} \sum_{nm} \sum_{\mu\nu} \frac{1}{\sqrt{\mu_m \mu_n}} \Phi_{\mu\nu}^{nm}(\delta_{ij}^{nm}) \tilde{u}_{in}^\mu \tilde{u}_{jm}^\nu, \quad (4.5)$$

with a kinetic term that is now described by a unit matrix instead of a matrix with different entries along the diagonal. Thus, we may freely perform unitary transformations on the momenta and deviations in the Hamiltonian without having to fear producing off-diagonal kinetic terms.

In the research papers, we are interested in diagonalizing a Hamiltonian on this form on the honeycomb lattice for two different kinds of geometries. First, the bulk spectrum can be obtained by assuming periodic boundary conditions and introducing the Fourier representations

$$\tilde{u}_{in} = \frac{1}{\sqrt{N}} \sum_{\mathbf{q}} e^{i\mathbf{q}\cdot(\mathbf{x}_i + \boldsymbol{\tau}_n)} \tilde{u}_{\mathbf{q}n} \quad (4.6)$$

$$\tilde{P}_{in} = \frac{1}{\sqrt{N}} \sum_{\mathbf{q}} e^{i\mathbf{q}\cdot(\mathbf{x}_i + \boldsymbol{\tau}_n)} \tilde{P}_{\mathbf{q}n}. \quad (4.7)$$

Second, we will be interested in the phonon spectrum on a ribbon geometry, as discussed in Sec. 3.3.1. Then, we may introduce a partial Fourier transform analogous to the transform of Eq. (3.40), which we used to find the edge modes of the Haldane model. In the following, we will be discussing the calculation of the bulk spectrum. The ribbon geometry calculation requires us to work with a far larger number of coupled deviations, but is otherwise perfectly analogous.

Assuming the force constants to satisfy translational symmetry, the Fourier transform renders the Hamiltonian on the form

$$H = \frac{1}{2M} \sum_{n,\mathbf{q}} \tilde{P}_{-\mathbf{q}n} \tilde{P}_{\mathbf{q}n} + \frac{1}{2} \sum_{nm} \sum_{\mu\nu} \sum_{\mathbf{q}} \tilde{u}_{-\mathbf{q}n}^\mu D_{\mu\nu}^{nm}(\mathbf{q}) \tilde{u}_{\mathbf{q}m}^\nu. \quad (4.8)$$

Here, we have introduced the dynamic matrix

$$D_{\mu\nu}^{nm}(\mathbf{q}) = \sum_j \frac{1}{\sqrt{\mu_n \mu_m}} \Phi_{\mu\nu}^{nm}(\boldsymbol{\delta}_j^{nm}) e^{i\mathbf{q} \cdot \tilde{\boldsymbol{\delta}}_j^{nm}}, \quad (4.9)$$

where the sum over j corresponds to a sum over the equilibrium displacements vectors $\boldsymbol{\delta}_j^{nm}$ which lattice sites on sublattice m may have relative to an atom on sublattice n in any Bravais unit cell.

We now combine the deviations \tilde{u}_{qn}^μ corresponding to various Cartesian directions in various atoms in the basis into a spinor $\tilde{\underline{u}}_{\mathbf{q}}$. We then introduce a unitary transform

$$\tilde{\underline{u}}_{\mathbf{q}} = U_{\mathbf{q}} v_{\mathbf{q}} \quad (4.10a)$$

$$\tilde{\underline{P}}_{\mathbf{q}} = U_{\mathbf{q}} Q_{\mathbf{q}}. \quad (4.10b)$$

The unitary transformation preserves canonical commutation relations. Choosing $U_{\mathbf{q}}$ to diagonalize the matrix $D(\mathbf{q})$, the Hamiltonian takes the form

$$H = \frac{1}{2M} \sum_{\mathbf{q}} Q_{-\mathbf{q}}^\lambda Q_{\mathbf{q}}^\lambda + \frac{1}{2} \sum_{\lambda} \sum_{\mathbf{q}} d_{\mathbf{q}}^\lambda v_{-\mathbf{q}}^\lambda v_{\mathbf{q}}^\lambda, \quad (4.11)$$

where the index λ labels the various entries of the deviation and canonical momentum spinors, and $d_{\mathbf{q}}^\lambda$ are the eigenvalues of $D(\mathbf{q})$. We may recognize this as the Hamiltonian for uncoupled harmonic oscillators with eigenfrequencies given by

$$\omega_{\mathbf{q}\lambda} = \sqrt{d_{\mathbf{q}}^\lambda / M}. \quad (4.12)$$

Such a Hamiltonian can be expressed in terms of phonon creation and annihilation operators $a_{\mathbf{q}\lambda}$ and $a_{-\mathbf{q}\lambda}^\dagger$ through [25]

$$v_{\mathbf{q}}^\lambda = \sqrt{\frac{\hbar^2}{2M\hbar\omega_{\mathbf{q}}}} (a_{\mathbf{q}\lambda} + a_{-\mathbf{q}\lambda}^\dagger) \quad (4.13)$$

$$Q_{\mathbf{q}}^\lambda = \sqrt{\frac{\hbar^2}{2M\hbar\omega_{\mathbf{q}}}} i(a_{\mathbf{q}\lambda}^\dagger - a_{-\mathbf{q}\lambda}) \quad (4.14)$$

to obtain the diagonalized phonon Hamiltonian

$$H = \sum_{\mathbf{q}\lambda} \hbar\omega_{\mathbf{q}\lambda} \left(a_{\mathbf{q}\lambda}^\dagger a_{\mathbf{q}\lambda} + \frac{1}{2} \right). \quad (4.15)$$

Assuming the force constants $\Phi_{\mu\nu}^{nm}(\boldsymbol{\delta}_j^{nm})$ are known, the diagonalization procedure is now clear.

Not all of the force constant in the matrix $\Phi_{\mu\nu}^{nm}(\boldsymbol{\delta}_j^{nm})$ are independent. Utilizing the symmetries of the system, it is typically possible to reduce the number of independent force constants significantly. In Papers [1] and [2], we apply a force constant model on the above form to derive the phonon spectra for the out-of-plane and in-plane modes in graphene using nearest neighbour and up to third-nearest-neighbour models. Some details of the symmetry analysis for the in-plane modes are presented in Paper [2].

In principle, the lattice structure, lattice constant, and the force constants can all be determined from ab-initio calculations [76]. Instead, our approach will rather be to adjust the force constants so that the resulting spectrum fits with experimental data [77].

4.2 Electron-phonon coupling

Although phonons are important quasiparticles in their own right, some of the most interesting phenomena in condensed matter physics occur when we allow bosonic quasiparticles such as phonons to interact with electrons. In Paper [2], we discuss phonon-mediated superconductivity, and therefore need to understand electron-phonon coupling, which we will be discussing in the following. Our discussion here will also provide a useful prequel to the discussion of magnon-mediated superconductivity in Paper [4].

The standard electron-phonon interaction is a many-body interaction between electrons and phonons on the form

$$H_{\text{el-ph}} = \sum_{\mathbf{k}\sigma} \sum_{\mathbf{q}\nu} g_{\mathbf{k},\mathbf{k}+\mathbf{q}}^{\eta\eta',\nu} (a_{\mathbf{q}\nu} + a_{-\mathbf{q},\nu}^\dagger) c_{\mathbf{k}+\mathbf{q},\eta'\sigma}^\dagger c_{\mathbf{k},\eta\sigma}, \quad (4.16)$$

and describes the scattering of an electron with spin σ and quasimomentum \mathbf{k} in band η to a state with quasimomentum $\mathbf{k}+\mathbf{q}$ in band η' through absorption of a phonon with momentum \mathbf{q} or emission of a phonon with momentum $-\mathbf{q}$. Here, $g_{\mathbf{k}\mathbf{k}'}^{\eta\eta',\nu}$ is the electron-phonon coupling matrix element. The above form is generic, and to understand electron-phonon coupling in more detail, it is necessary to understand the behaviour of the electron-phonon coupling matrix element with momenta and band and mode indices.

To calculate the electron-phonon coupling matrix element, we therefore need to go to a more elementary description of the system [72, 78–80]. The earliest works on electron-phonon coupling were based on Bloch wave matrix elements [81–83], and this is often referred to as the Bloch approach. An

alternative is the so-called Fröhlich or tight binding approach [84], where it is assumed that electrons follow the ion cores almost adiabatically due to the slow time scale of the ionic motion compared with the electron time scale [85–90]. It has been shown, however, that the two approaches are equivalent up to order $\sqrt{m_e/M}$, where m_e and M are the electronic and ionic masses [91]. Since then, there has also been significant progress in the calculation of electron-phonon coupling using ab-initio approaches based on density functional theory methods [80].

In Paper [2], we will be using a tight binding model to describe the electron-phonon coupling in graphene and to study superconductivity. To illustrate the methodology, we apply it to a square lattice model in the section below.

4.2.1 Modelling the electron-phonon coupling

Consider a system of atoms with a square lattice structure and some free electrons described by the single band tight binding model [79, 92]

$$H = - \sum_{i,j} t_{ij} c_i^\dagger c_j - \mu \sum_i c_i^\dagger c_i. \quad (4.17)$$

Due to the time scale separation of electrons and phonons, we may then think of the hopping matrix element t_{ij} as an almost instantaneous function of the positions of the ions on the lattice [79, 93]. Since the overlap integrals t_{ij} are then functions of the relative positions of lattice sites i, j , we may write $t_{ij} = t(\mathbf{d}_{ij})$, where \mathbf{d}_{ij} is the relative displacement between the atoms at positions $\mathbf{x}_i + \mathbf{u}_i$ and $\mathbf{x}_j + \mathbf{u}_j$. Expanding around the equilibrium displacement $\boldsymbol{\delta}_{ij} = \mathbf{x}_j - \mathbf{x}_i$, we obtain

$$t_{ij}(\mathbf{d}_{ij}) = t_{ij}(\boldsymbol{\delta}_{ij}) + (\mathbf{u}_i - \mathbf{u}_j) \cdot \nabla_{\mathbf{d}} t_{ij}(\mathbf{d}). \quad (4.18)$$

When the system is mirror symmetric with respect to the line connecting the equilibrium lattice sites i and j , we may furthermore write

$$t_{ij}(\mathbf{d}_{ij}) = t_{ij}^0 + \frac{1}{a^2} \gamma_{ij} t_{ij}^0 \boldsymbol{\delta}_{ij} \cdot (\mathbf{u}_i - \mathbf{u}_j), \quad (4.19)$$

where t_{ij}^0 is the hopping integral when the atoms are at their equilibrium positions, a is the lattice constant, and where

$$\gamma_{ij} = - \left(\frac{a^2}{t_{ij}^0 |\boldsymbol{\delta}_{ij}|^2} \right) \boldsymbol{\delta}_{ij} \cdot \nabla_{\mathbf{d}} t_{ij}(\mathbf{d})|_{\mathbf{d}=\boldsymbol{\delta}_{ij}} \quad (4.20)$$

is a dimensionless parameter of order 1, which can be thought of as the logarithmic derivative of the overlap integral with respect to inter-atomic distance.

Assuming we keep only the nearest neighbour contribution, the tight binding electron-phonon coupling then takes the form

$$H_{\text{el-ph}} = -\frac{\gamma t_1}{a^2} \sum_{i, \delta} \boldsymbol{\delta} \cdot (\mathbf{u}_{i+\delta} - \mathbf{u}_i) c_{i+\delta}^\dagger c_i, \quad (4.21)$$

where the sum over $\boldsymbol{\delta}$ now runs over the nearest neighbour vectors.

From this simple expression, it is already clear that the electron-phonon coupling should take the form in Eq. (4.16).

As discussed in the previous section, lattice site deviations can be expressed in terms of the phonons of the system through

$$\mathbf{u}_i = \sqrt{\frac{\hbar^2}{2MN}} \sum_{\mathbf{q}, \nu} e^{i\mathbf{q} \cdot \mathbf{x}_i} \frac{\mathbf{e}_\nu(\mathbf{q})}{\sqrt{\hbar\omega_{\mathbf{q}\nu}}} (a_{\mathbf{q}\nu} + a_{-\mathbf{q}\nu}^\dagger), \quad (4.22)$$

where $\mathbf{e}_\nu(\mathbf{q})$ is the polarization of the phonon mode ν , and would in general correspond to an eigenvector of the matrix $U_{\mathbf{q}}$ introduced to diagonalize the phonon Hamiltonian. Thus, the polarization vector is in general momentum dependent, but for the square lattice, we may simply take $\mathbf{e}_\nu(\mathbf{q})$ to be unit vectors along the three Cartesian directions.

By introducing the Fourier transform also for the fermion operators, the electron-phonon coupling takes the expected form

$$H_{\text{el-ph}} = \sum_{\mathbf{k}\sigma} \sum_{\mathbf{q}\nu} g_{\mathbf{k}, \mathbf{k}+\mathbf{q}}^\nu (a_{\mathbf{q}\nu} + a_{-\mathbf{q}, \nu}^\dagger) c_{\mathbf{k}+\mathbf{q}, \sigma}^\dagger c_{\mathbf{k}\sigma}, \quad (4.23)$$

with electron-phonon coupling matrix element

$$g_{\mathbf{k}, \mathbf{k}+\mathbf{q}}^\nu = -\frac{1}{2} \frac{\gamma t_1}{a} \sqrt{\frac{\hbar^2}{2MN a^2 \hbar\omega_{\mathbf{q}\nu}}} \sum_{\boldsymbol{\delta}} e^{-i(\mathbf{k}+\mathbf{q}) \cdot \boldsymbol{\delta}} (e^{i\mathbf{q} \cdot \boldsymbol{\delta}} - 1) \mathbf{e}_\nu(\mathbf{q}) \cdot \boldsymbol{\delta}. \quad (4.24)$$

Thus, for the square lattice, only longitudinal modes couple to the electrons.

Above, we have introduced the electron-phonon coupling through a lattice model. In the long-wavelength limit $\mathbf{q} \rightarrow 0$, the matrix element reduces to

$$g_{\mathbf{k}, \mathbf{k}+\mathbf{q}}^\nu = -\frac{1}{2} \frac{\gamma t_1}{a} \sqrt{\frac{\hbar^2}{2MN a^2 \hbar\omega_{\mathbf{q}\nu}}} \sum_{\boldsymbol{\delta}} e^{-i\mathbf{k} \cdot \boldsymbol{\delta}} i(\mathbf{q} \cdot \boldsymbol{\delta}) (\mathbf{e}_\nu(\mathbf{q}) \cdot \boldsymbol{\delta}), \quad (4.25)$$

which apart from the insignificant phase factor $e^{i\mathbf{k}\cdot\boldsymbol{\delta}}$ matches the jellium model electron-phonon coupling [6], and where γt_1 plays the role of the deformation potential. Furthermore, the electron-phonon coupling vanishes in the limit $\mathbf{q} \rightarrow 0$ for acoustic modes with $\omega_{\mathbf{q}} \propto |\mathbf{q}|$. Letting ω_D be a characteristic phonon frequency, the characteristic energy scale for the electron-phonon coupling is

$$g_0 = \gamma t_1 \sqrt{\left(\frac{\hbar^2}{2Ma^2}\right)\left(\frac{1}{\hbar\omega_D}\right)}. \quad (4.26)$$

Thus, it can be thought of as the electron energy scale multiplied with the square root of the kinetic energy of an ion inside a box of linear size a divided by the phonon energy scale.

In Paper [2], we generalize the above calculation to systems with two sublattices. The results are very similar, but it is necessary to also incorporate the rotation of the electron basis and the sublattice structure of the phonon polarizations.

4.2.2 Normal state electron-phonon coupling effects

Due to the electron-phonon coupling, the electronic properties of the system are in general affected by the phonons, and vice versa. Since we are primarily interested in whether electron-phonon coupling (and electron-boson coupling in general) may give rise to superconductivity, we are primarily interested in the effect the phonons have on the electrons, and not the other way around. We will be discussing this in the following.

As starting point, we use the model $H = H_{\text{el}} + H_{\text{ph}} + H_{\text{el-ph}}$ with

$$H_{\text{el}} = \sum_{\mathbf{k}\sigma} \xi_{\mathbf{k}} c_{\mathbf{k}\sigma}^\dagger c_{\mathbf{k}\sigma} \quad (4.27a)$$

$$H_{\text{ph}} = \sum_{\mathbf{q}\nu} \omega_{\mathbf{q}\nu} a_{\mathbf{q}\nu}^\dagger a_{\mathbf{q}\nu} \quad (4.27b)$$

$$H_{\text{el-ph}} = \sum_{\mathbf{k}\sigma} \sum_{\mathbf{q}\nu} g_{\mathbf{k},\mathbf{k}+\mathbf{q}}^\nu (a_{\mathbf{q}\nu} + a_{-\mathbf{q},\nu}^\dagger) c_{\mathbf{k}+\mathbf{q}\sigma}^\dagger c_{\mathbf{k}\sigma}, \quad (4.27c)$$

where we assume that the electron spectrum $\xi_{\mathbf{k}} = \epsilon_{\mathbf{k}} - \mu$ and phonon spectra $\omega_{\mathbf{q}\nu}$ for are known, and that we also know the form of the electron-phonon coupling matrix element $g_{\mathbf{k}\mathbf{k}'}^\nu$.

To understand the electronic properties of the system, one may consider the electronic Green's function $G(\mathbf{k}, t)$. This Green's function can be calculated using the Matsubara Green's function technique within many-body

perturbation theory. In Chapter 5 we will be deriving a perturbative expansion for the renormalization of both normal and anomalous correlations. The calculation of normal state effects is similar. In this chapter, we therefore simply outline the procedure and the results to arrive at a qualitative understanding of some of the normal state effects of electron-phonon coupling.

For the electron-phonon interaction as given, one may use many-body perturbation theory to show that the electron Green's function is given by the self-consistent expansion

$$G(\mathbf{k}, i\omega_n) = G^0(\mathbf{k}, i\omega_n) + G^0(\mathbf{k}, i\omega_n)\Sigma(\mathbf{k}, i\omega_n)G(\mathbf{k}, i\omega_n), \quad (4.28)$$

where $G^0(\mathbf{k}, i\omega_n)$ is the non-interacting Matsubara Green's function, and $\Sigma(\mathbf{k}, i\omega_n)$ the self energy. In the following, we keep only the lowest order contribution to the self energy, which can be written [6]

$$\Sigma(\mathbf{k}, z) = \sum_{\mathbf{q}\nu} |g_{\mathbf{k}, \mathbf{k}+\mathbf{q}}^\nu|^2 \left[\frac{1 + n_B(\omega_{\mathbf{q}}) - n_F(\xi_{\mathbf{k}+\mathbf{q}})}{z - (\xi_{\mathbf{k}+\mathbf{q}} + \omega_{\mathbf{q}})} + \frac{n_B(\omega_{\mathbf{q}}) + n_F(\xi_{\mathbf{k}+\mathbf{q}})}{z - (\xi_{\mathbf{k}+\mathbf{q}} - \omega_{\mathbf{q}})} \right]. \quad (4.29)$$

To obtain the retarded Green's function G_R at real frequency ω , we have to evaluate the self-energy Σ at frequency $z = \omega + i\delta$, where $\delta > 0$ is infinitesimal [45]. Decomposing Σ into its real and imaginary parts Σ' and Σ'' , we then obtain the decomposition $\Sigma_R(\mathbf{k}, \omega) = \Sigma'(\mathbf{k}, \omega + i\delta) + i\Sigma''(\mathbf{k}, \omega + i\delta)$. The real frequency Green's function then takes the form

$$G_R(\mathbf{k}, \omega) = \frac{1}{\omega - \xi_{\mathbf{k}} - \Sigma'_R(\mathbf{k}, \omega) - i\Sigma''_R(\mathbf{k}, \omega)}, \quad (4.30)$$

and the spectral function is

$$A(\mathbf{k}, \omega) = -2 \text{Im} G(\mathbf{k}, \omega + i\delta) = -\frac{2\Sigma''_R(\mathbf{k}, \omega)}{[\omega - \xi_{\mathbf{k}} - \Sigma'_R(\mathbf{k}, \omega)]^2 + \Sigma''_R(\mathbf{k}, \omega)^2}. \quad (4.31)$$

This function is peaked at the so-called effective quasiparticle energy $\xi_{\mathbf{k}}^*$, which corresponds to the solution of the equation

$$\xi_{\mathbf{k}}^* = \xi_{\mathbf{k}} + \Sigma'_R(\mathbf{k}, \xi_{\mathbf{k}}^*), \quad (4.32)$$

and is shifted with respect to the bare electron value $\xi_{\mathbf{k}}$.

To understand the effect of renormalization somewhat better, we now assume that the quasiparticle energy shift is small. The spectral function

can then be Taylor expanded around the renormalized quasiparticle energy. Then, it is useful to introduce the mass enhancement parameter

$$\tilde{\lambda}_{\mathbf{k}} = - \left. \frac{d\Sigma'(\mathbf{k}, \omega)}{d\omega} \right|_{\omega=\xi_{\mathbf{k}}^*}. \quad (4.33)$$

Subsequently, the Green's function can be written as

$$G(\mathbf{k}, \omega) = \frac{z_{\mathbf{k}}}{\omega - \xi_{\mathbf{k}}^* - i\Gamma_{\mathbf{k}}^*/2}, \quad (4.34)$$

where we have expanded the real part of the self energy to linear order in $\omega - \xi_{\mathbf{k}}$, but only to zeroth order for the imaginary part. We have here introduced a wave function renormalization factor $z_{\mathbf{k}} = 1/(1 + \tilde{\lambda}_{\mathbf{k}})$ and a quasiparticle decay rate $\Gamma_{\mathbf{k}}^* = 2z_{\mathbf{k}}\Sigma''(\mathbf{k}, \xi_{\mathbf{k}}^*)$.

From the above quantities, we may now derive various electronic properties. First, we consider how renormalization affects the Fermi surface group velocity. From Eq. (4.32), the slope of the renormalized quasiparticle excitation energy is given by

$$\nabla_{\mathbf{k}}\xi_{\mathbf{k}}^* = \nabla_{\mathbf{k}}\xi_{\mathbf{k}} + \nabla_{\mathbf{k}}\Sigma'(\mathbf{k}, \xi_{\mathbf{k}}^*). \quad (4.35)$$

Utilizing that the self energy typically varies much faster with the energy than with the explicit momentum dependence, we may then express the renormalized quasiparticle energy slope as

$$\nabla_{\mathbf{k}}\xi_{\mathbf{k}}^* = \left(\frac{1}{1 + \tilde{\lambda}_{\mathbf{k}}} \right) \nabla_{\mathbf{k}}\xi_{\mathbf{k}} \quad (4.36)$$

where we have used $\nabla_{\mathbf{k}}\Sigma'(\mathbf{k}, \xi_{\mathbf{k}}^*) \approx -\tilde{\lambda}_{\mathbf{k}}\nabla_{\mathbf{k}}\xi_{\mathbf{k}}^*$. Thus, the quasiparticle energy slope velocity is reduced by a factor of $1 + \tilde{\lambda}_{\mathbf{k}}$. This relation also explains the term ‘‘mass enhancement parameter’’, as it corresponds to a mass renormalization $m \rightarrow (1 + \tilde{\lambda})m$ within the free electron gas picture widely adopted to understand the properties of normal metals.

To connect this renormalization with physical observables, we may now calculate the renormalized electronic density of states through

$$N_F^* = \frac{1}{N} \sum_{\mathbf{k}} \delta(\xi_{\mathbf{k}}^*) \approx (1 + \tilde{\lambda})N_F, \quad (4.37)$$

where we for simplicity have assumed that the system is nearly isotropic, so that $\tilde{\lambda}_{\mathbf{k}} \approx \tilde{\lambda}$ is weakly dependent on momentum \mathbf{k} . Since physical properties such as the electronic contribution to the heat capacity and the electrical

resistivity are directly proportional to the density of states [72], the mass enhancement parameter is necessary to explain observed values for these quantities in metals.

4.2.3 Dimensionless electron-phonon coupling strength

The quantity $\tilde{\lambda}_{\mathbf{k}}$ is dimensionless and a measure of how much the slope of the energy spectrum is increased by the electron-phonon coupling. Thus, it also represents a sensible measure of the electron-phonon coupling strength in the system.

However, we may in fact also introduce a whole hierarchy of quantities which say something about the electron-phonon coupling strength. Let us start by introducing the function

$$\alpha^2 F_{\mathbf{k}}(\xi, \Omega) = \sum_{q\nu} |g_{\mathbf{k}, \mathbf{k}+q}^\nu|^2 \delta(\Omega - \omega_{q\nu}) \delta(\xi - \xi_{\mathbf{k}+q}), \quad (4.38)$$

which represents the scattering strength of processes with phonon energy Ω from a state at momentum \mathbf{k} to states on the isoenergy contour corresponding to energy ξ . This function can subsequently be used to define what we will refer to as the state dependent dimensionless electron-phonon coupling strength

$$\lambda_{\mathbf{k}} = \int d\Omega \frac{2}{\Omega} \alpha^2 F(\xi_{\mathbf{k}}, \Omega) = \sum_{\mathbf{k}'\nu} \frac{2}{\omega_{\mathbf{k}-\mathbf{k}',\nu}} |g_{\mathbf{k}\mathbf{k}'}^\nu|^2 \delta(\xi_{\mathbf{k}'} - \xi_{\mathbf{k}}). \quad (4.39)$$

Performing Fermi surface averages, we may introduce the function $\alpha^2 F(\omega)$ given by

$$\alpha^2 F(\omega) = \frac{1}{N_F} \sum_{\mathbf{k}\mathbf{k}'} \sum_{\nu} |g_{\mathbf{k}\mathbf{k}'}^\nu|^2 \delta(\omega - \omega_{\mathbf{k}-\mathbf{k}',\nu}) \delta(\xi_{\mathbf{k}}) \delta(\xi_{\mathbf{k}'}), \quad (4.40)$$

where N_F is the electronic density of states at the Fermi surface. The corresponding dimensionless electron-phonon coupling strength λ is given by

$$\lambda = \frac{1}{N_F} \sum_{\mathbf{k}\mathbf{k}'} \sum_{\nu} \frac{2}{\omega_{\mathbf{k}-\mathbf{k}',\nu}} |g_{\mathbf{k}\mathbf{k}'}^\nu|^2 \delta(\xi_{\mathbf{k}}) \delta(\xi_{\mathbf{k}'}). \quad (4.41)$$

From Eq. (4.38), it then follows that $\alpha^2 F(\omega)$ and λ are related through

$$\lambda = \int d\omega \frac{2}{\omega} \alpha^2 F(\omega). \quad (4.42)$$

In fact, as discussed in Appendix B, it can be shown that when $\alpha^2 F_{\mathbf{k}}(\xi, \omega)$ is weakly dependent on ξ , which is typically the case, the dimensionless electron phonon coupling $\lambda_{\mathbf{k}}$ and the mass enhancement factor $\tilde{\lambda}_{\mathbf{k}}$ introduced in the previous section are approximately equal for momenta on the Fermi surface. Thus, we have $\lambda \approx \tilde{\lambda}$.

In Chapter 5, we will be discussing how electron-phonon coupling may provide an effective interaction between electrons, and scatter electron pairs from $\pm\mathbf{k}$ to $\pm\mathbf{k}'$ through the pair scattering potential

$$V_{\mathbf{k}\mathbf{k}'} = \sum_{\nu} |g_{\mathbf{k}\mathbf{k}'}^{\nu}|^2 \frac{2\omega_{\mathbf{k}-\mathbf{k}',\nu}}{(\xi_{\mathbf{k}} - \xi_{\mathbf{k}'})^2 - \omega_{\mathbf{k}-\mathbf{k}',\nu}^2}. \quad (4.43)$$

Thus, we may also think of the dimensionless electron phonon coupling as $\lambda = -N_F \langle V_{\mathbf{k}\mathbf{k}'} \rangle_{\text{FS}}$, where $\langle V_{\mathbf{k}\mathbf{k}'} \rangle_{\text{FS}}$ is the average of the potential for momenta \mathbf{k}, \mathbf{k}' ranging over the entire Fermi surface. Since superconductivity is known to occur due to pairing because of effective interactions mediated by phonons, we may already now suspect that the quantity λ plays an important role in the description of superconductivity. We will be discussing this in more detail in Chapter 5.

Using various spectroscopic methods such as photoemission spectroscopy and neutron scattering [78], it is possible to map out the spectral function $A(\mathbf{k}, \omega)$. Since the spectral function contains information such as quasiparticle energies and their associated linewidths, one may use these to extract the self energy. This allows experimental determination of the electron-phonon coupling strength [78, 94, 95].

4.3 Magnetoelastic coupling

When the magnetization of a ferromagnetic material is changed, the change in magnetization is associated with a deformation of the material. This is called magnetostriction [96], and indicates that the magnetic and vibrational degrees of freedom are coupled. The effect is known to give rise to an audible sound from transformers [97], which have rapidly changing magnetic fields.

Considering a ferromagnetic insulator, we may similarly expect that the magnetic excitations are coupled to lattice site vibrations. Within the language of collective quantum excitations, this corresponds to a coupling between magnons and phonons. Such an interaction was first studied by Kittel [98, 99], who showed that within a classical model for a system with

magnetic order along the \hat{z} -direction, the magnetoelastic interaction can be written on the form [100]

$$H_{\text{me}}^{3\text{D}} \propto \sum_{\mu\nu} \int d^3r M_\mu M_\nu \left[\frac{\partial u_\mu}{\partial x_\nu} + \frac{\partial u_\nu}{\partial x_\mu} \right], \quad (4.44)$$

where M_μ is the magnetization component along the Cartesian direction μ , and u_μ is the deviation from the equilibrium position. Considering small magnetic fluctuations around the magnetization $M\hat{z}$, the magnetoelastic coupling in a two-dimensional system can be written

$$H_{\text{me}} \propto \int d^2r \left(M_x \frac{\partial u_z}{\partial x} + M_y \frac{\partial u_z}{\partial y} \right), \quad (4.45)$$

where the magnetization along the \hat{z} -direction is assumed to be constant. In a lattice model description where we assume that nearest-neighbour lattices sites are separated by nearest-neighbour vectors $\boldsymbol{\delta}$, the magnetoelastic coupling then takes the form

$$H_{\text{me}} = \kappa \sum_{i,\boldsymbol{\delta}} (\boldsymbol{\delta} \cdot \mathbf{S}_i) (u_{i+\boldsymbol{\delta}}^z - u_i^z), \quad (4.46)$$

with magnetoelastic coupling strength κ . Expressing the spin operators in terms of magnon operators in linear spin wave theory and using the usual second quantized description for the lattice site deviations u_i^z , this magnetoelastic coupling represents a bi-linear magnon-phonon coupling. A more detailed discussion of lattice models for magnetoelastic coupling is given in Ref. [101] from a symmetry point of view.

To understand the basic effect of magnon-phonon coupling in a quantum system, we may use a very simple model describing the coupling of a single magnon mode to a single phonon mode. Thus, we consider a Hamiltonian on the form

$$H = \sum_{\mathbf{q}} \omega_{\mathbf{q}}^{\text{ph}} a_{\mathbf{q}}^\dagger a_{\mathbf{q}} + \sum_{\mathbf{q}} \omega_{\mathbf{q}}^{\text{m}} b_{\mathbf{q}}^\dagger b_{\mathbf{q}} + \sum_{\mathbf{q}} g (a_{\mathbf{q}}^\dagger b_{\mathbf{q}} + b_{\mathbf{q}}^\dagger a_{\mathbf{q}}), \quad (4.47)$$

where $a_{\mathbf{q}}$ is the annihilation operator for a phonon mode with associated phonon spectrum $\omega_{\mathbf{q}}^{\text{ph}}$, and $b_{\mathbf{q}}$ the annihilation operator for a magnon mode with eigenfrequency spectrum $\omega_{\mathbf{q}}^{\text{m}}$. Here, g is a magnon-phonon coupling strength, which we assume to be momentum independent. For simplicity, we will be assuming that the magnon spectrum is constant and that the phonon spectrum is acoustic, so that

$$\omega_{\mathbf{q}}^{\text{ph}} = \omega_0 q/a \quad \omega_{\mathbf{q}}^{\text{m}} = \omega_0, \quad (4.48)$$

with constant magnon energy ω_0 , and where a is a momentum scale which determines the slope of the bare phonon spectrum. The Hamiltonian can then be written on the matrix form

$$H = \sum_{\mathbf{q}} \begin{pmatrix} a_{\mathbf{q}}^{\dagger} & b_{\mathbf{q}}^{\dagger} \end{pmatrix} \begin{pmatrix} \omega_{\mathbf{q}}^{\text{ph}} & g \\ g & \omega_{\mathbf{q}}^{\text{m}} \end{pmatrix} \begin{pmatrix} a_{\mathbf{q}} \\ b_{\mathbf{q}} \end{pmatrix}. \quad (4.49)$$

To diagonalize it, we may introduce a unitary transform $U(\mathbf{q})$ to obtain eigenmodes $d_{\mathbf{q}1}$ and $d_{\mathbf{q}2}$ given by

$$\begin{pmatrix} d_{\mathbf{q}1} \\ d_{\mathbf{q}2} \end{pmatrix} = U(\mathbf{q}) \begin{pmatrix} a_{\mathbf{q}} \\ b_{\mathbf{q}} \end{pmatrix}. \quad (4.50)$$

The resulting eigenvalue spectrum $\omega_{\pm}(\mathbf{q})$ is given by

$$\omega_{\pm} = \frac{1}{2}(\omega_{\mathbf{q}}^{\text{ph}} + \omega_{\mathbf{q}}^{\text{m}}) \pm \sqrt{\left(\frac{\omega_{\mathbf{q}}^{\text{ph}} - \omega_{\mathbf{q}}^{\text{m}}}{2}\right)^2 + g^2}. \quad (4.51)$$

When the two uncoupled excitation spectra cross so that $\omega_{\mathbf{q}}^{\text{ph}} = \omega_{\mathbf{q}}^{\text{m}}$, the energy difference between the two bands is $2|g|$. Thus, the magnon-phonon coupling strength determines the direct gap in the system.

The eigenmodes in the system are in general linear combinations of magnons and phonons. The total phonon content $P_{\pm}(\mathbf{q})$ and magnon content $M_{\pm}(\mathbf{q})$ in each mode can be written

$$P_{\pm}(\mathbf{q}) = |U_{1\pm}(\mathbf{q})|^2 \quad M_{\pm} = |U_{2\pm}(\mathbf{q})|^2, \quad (4.52)$$

where $U_{i\pm}$ is a column in the unitary matrix U and corresponds to the eigenvector with eigenvalue ω_{\pm} . The unitarity of the transformation matrix U gives the relations $P_i + M_i = 1$ and $P_1 + P_2 = M_1 + M_2 = 1$.

Calculating the magnon and phonon content explicitly for the eigenstate with energy ω_{\pm} , we obtain

$$P_{\pm} = \frac{1}{1 + (p_{\pm}^{\pm})^2} \quad M_{\pm} = \frac{1}{1 + (1/p_{\pm}^{\pm})^2}, \quad (4.53)$$

where we have introduced the quantity

$$p_{\mathbf{q}}^{\pm} = \sqrt{1 + \left(\frac{\Delta_{\mathbf{q}}}{|g|}\right)^2} \pm \frac{\Delta_{\mathbf{q}}}{|g|}, \quad (4.54)$$

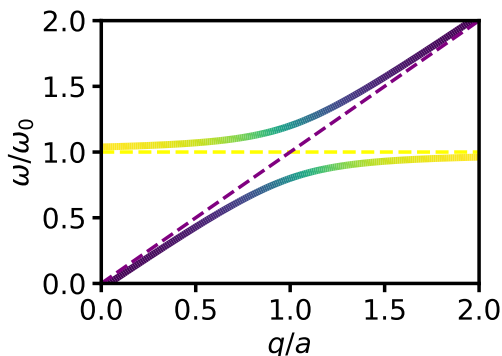


Figure 4.1: Excitation spectrum for hybridized magnons and phonons. The bare spectra are indicated with dashed lines. Colors indicate the magnon content $M_{\pm}(\mathbf{q})$ of each mode, where yellow modes have a predominant magnon character and purple modes a predominant phonon character.

and where $2\Delta_{\mathbf{q}} = \omega_{\mathbf{q}}^{\text{m}} - \omega_{\mathbf{q}}^{\text{ph}}$ is the energy difference of the bare magnon and phonon excitations.

When the energy difference is large compared to the coupling, $p_{\mathbf{q}}^{\pm}$ is large or small depending on the sign of $\Delta_{\mathbf{q}}$. Thus, the excitation is either purely magnon-like or phonon-like. At the crossing point for the uncoupled models, where $\Delta_{\mathbf{q}} = 0$, we have $p_{\mathbf{q}}^{\pm} = 1$, and therefore, $P_{\pm} = M_{\pm} = 1/2$.

The energy spectrum can be plotted as function of momentum, and this is shown in Fig. 4.1, where the bands are colored according to their magnon content $M_{\pm}(\mathbf{q})$, where yellow color corresponds to a magnon-like excitation and purple color to a phonon-like excitation. Whereas the bare phonon and magnon spectra cross at $q = a$, the coupled spectrum instead has an avoided crossing. Close to this avoided crossing, the eigenexcitations are magnon-polarons of hybrid nature [74].

Chapter 5

Superconductivity

The history of superconductivity is packed with surprises. In 1911, it was discovered that the electrical resistivity of mercury drops to zero below a critical temperature [102]. Naturally, this first main characteristic property of the superconducting state was at odds with all existing theories for the low temperature behaviour of resistivity in metals. The magnetic flux expulsion from bulk superconductors known as the Meißner effect was discovered experimentally in 1933 [103], and is the second main characteristic property of the superconducting state. At the time, superconductors were thought of merely as perfect conductors, and solely within the framework of electrodynamics, this property could not be predicted. Only after further experimental leads, Bardeen, Cooper, and Schrieffer were able to identify the basic mechanism causing superconductivity and explain these two main characteristic properties microscopically [104]. With the evolution of BCS theory into Eliashberg theory [105–107], it seemed like most properties of superconductors could be understood within the established theories. This was radically changed with the discovery of superconductivity in heavy fermion compounds [108] and high- T_c cuprates [109]. Challenging established truths about superconductivity, these discoveries placed theorists in zugzwang, and stimulated massive activity on new theories and new mechanisms of superconductivity.

From the above historic examples, it should be clear that the development of theories of superconductivity has always been heavily guided by experiments, and that understanding the microscopic origin of superconductivity is very challenging¹. The magnitude of the challenge can partly be

¹Felix Bloch is known to jokingly have postulated that any theory of superconductivity

explained by the dramatic nature of the superconducting transition, inducing a qualitative change in the system preventing superconductivity from being understood within naive perturbation theory around the free electron gas. Second, the collective and strongly correlated nature of electrons in superconductors makes it tough to understand what the superconducting ground state is.

In this chapter, our main goal is to introduce the main theoretical frameworks which we use to study the possible superconducting instabilities in Papers [2] and [4]. The BCS theory of superconductivity is reviewed in Sec. 5.1, which we apply to investigate the possibility of phonon-mediated superconductivity in graphene in Paper [2]. In Sec. 5.2, we discuss Eliashberg theory, which is used to study the possibility of magnon-mediated superconductivity in heterostructures in Paper [4]. In this chapter, we introduce both BCS theory and Eliashberg theory with a phonon-induced mechanism in mind. In Sec. 5.3, however, we instead discuss the spin fluctuation mechanism of superconductivity which had to be investigated in detail with the discovery of superconductivity in heavy fermion compounds and the cuprates. This provides important background also for the discussion of magnon-mediated superconductivity in Chapter 8 and Paper [4].

5.1 BCS theory

The paper “Theory of Superconductivity” by Bardeen, Cooper, and Schrieffer from 1957 [104] culminated a period of intensive search for a microscopic theory of superconductivity. In addition to providing an explanation for the basic mechanism behind superconductivity and a description of the electronic ground state, the theory was able to explain many of the experimentally observed properties of superconductors. In short, the roughly 30 page long paper provides almost everything we can expect from a proper theory of superconductivity.

BCS theory did not just appear out from nothing. The search for a theory of superconductivity dates back to its very discovery. From the beginning, these models were naturally of classical nature, and phenomenological descriptions were devised based on classical electromagnetism and fluid models [110]. The works culminated with the Ginzburg-Landau description of superconductors [111], which accurately describes the superconducting state, but remains purely phenomenological, and fails to identify a microscopic mechanism and give any description of the microscopic state [112].

is refutable [73].

This much was however clear: Driven by some sort of interaction, the electrons in the superconducting state reorganize from the free electron gas known to describe the normal metal well, and into some other state with different properties. From measurements of the critical magnetic field h_c where superconductivity breaks down, it was furthermore known that the energy gained by such a reorganization was tiny [73].

A crucial lead was discovered in 1950 with the discovery of the isotope effect [113, 114], namely that the critical temperature of an elemental superconductor scales roughly as $T_c \propto M^{-1/2}$ with the isotope mass M of the atoms in the system. Thus, the critical temperature seemed to be related to the motion of the ions. Independently, Fröhlich had suggested that electron-phonon interaction was responsible for superconductivity, and had even derived the isotope effect using perturbation theory [73, 115]. Yet, he soon came to suspect that perturbation theory is not sufficient to understand superconductivity [73]. Importantly, however, Fröhlich demonstrated that electron-phonon coupling could provide an effective attraction between electrons [84].

Previous works using Ginzburg-Landau theory had indicated that superconductivity could be understood due to coherent behaviour of entities with charge $2e$ [112]. Motivated by this, Leon Cooper investigated how a pair of electrons interacting with the Fermi sea would behave [116]. With an attractive interaction close to the Fermi surface motivated by Fröhlich's effective potential [84], he was able to solve a simplified problem exactly. In the process, he showed that the system gained energy by adding a pair of electrons on top of the Fermi surface in a coherent manner. This indicated that the Fermi surface was unstable, and paved the way for the BCS theory of superconductivity.

5.1.1 Formulation of the theory

Based on the newly gained insights, Bardeen, Cooper, and Schrieffer realized that the essential physics in superconductivity is contained in the interaction between pairs of electrons in opposite spin states and with zero net momentum. The starting point for BCS theory is therefore the so-called reduced BCS Hamiltonian

$$H = \sum_{\mathbf{k}\sigma} \xi_{\mathbf{k}} c_{\mathbf{k}\sigma}^\dagger c_{\mathbf{k}\sigma} + \sum_{\mathbf{k}\mathbf{k}'} V_{\mathbf{k}\mathbf{k}'} c_{\mathbf{k}'\uparrow}^\dagger c_{-\mathbf{k}'\downarrow}^\dagger c_{-\mathbf{k}\downarrow} c_{\mathbf{k}\uparrow}, \quad (5.1)$$

which describes the scattering of a pair of electrons with opposite spins at momenta $\pm\mathbf{k}$ and to momenta $\pm\mathbf{k}'$ through a scattering potential $V_{\mathbf{k}\mathbf{k}'}$.

Since other scattering processes take the electrons out of these pair states, we assume them to play a negligible role in the physics.

The effective potential in BCS theory can in principle be due many different mechanisms. In the most paradigmatic explanation of superconductivity, however, the potential is due to electron-phonon coupling. Following Cooper [116], Bardeen, Cooper, and Schrieffer assumed the effective pair scattering potential to take the form

$$V_{\mathbf{k},\mathbf{k}'} = \begin{cases} -u/N & \text{for } |\xi_{\mathbf{k}}|, |\xi_{\mathbf{k}'}| \leq \omega_D \\ 0 & \text{otherwise} \end{cases}, \quad (5.2)$$

where u is a constant attractive potential, N the number of unit cells on the Bravais lattice, and ω_D is a characteristic phonon frequency in the system. We may keep this potential in mind for now, but will be discussing the form of $V_{\mathbf{k}\mathbf{k}'}$ in further detail in Sec. 5.1.4.

In BCS theory, one starts out from the above BCS Hamiltonian, and derives a so-called gap equation. There are several ways to do this. The most standard is to perform a mean field theory expansion around a finite pairing amplitude [6, 112, 117]. Alternately, one may also use a Green's function formalism based on an equation of motion approach for the Green's functions [83, 118, 119], or a saddle point approximation in a functional integral formalism [6, 120]. Remarkably, the reduced BCS Hamiltonian is in fact sufficiently simple that an exact solution exists [73, 117, 121]. In the following, however, we will be outlining the derivation of the gap equation within a mean field approach.

5.1.2 Mean field theory and gap equation

To derive the BCS gap equation, we will be following Ref. [117]. Considering spin singlet pairing, we introduce the mean field parameter $b_{\mathbf{q}} = \langle c_{-\mathbf{q}\downarrow} c_{\mathbf{q}\uparrow} \rangle$, while the more general description allowing also for spin triplet pairing is discussed in Ref. [122] within the BCS approach. Using mean field theory to neglect deviations from the mean field parameter, we obtain

$$H = - \sum_{\mathbf{k}\mathbf{k}'} V_{\mathbf{k}\mathbf{k}'} b_{\mathbf{k}'}^* b_{\mathbf{k}} + \sum_{\mathbf{k}} \xi_{\mathbf{k}} (c_{\mathbf{k}\uparrow}^\dagger c_{\mathbf{k}\uparrow} + c_{-\mathbf{k}\downarrow}^\dagger c_{-\mathbf{k}\downarrow}) + \sum_{\mathbf{k}} (\Delta_{\mathbf{k}}^* c_{-\mathbf{k}\downarrow} c_{\mathbf{k}\uparrow} + \Delta_{\mathbf{k}} c_{\mathbf{k}\uparrow}^\dagger c_{-\mathbf{k}\downarrow}^\dagger), \quad (5.3)$$

where we have introduced the gap parameters

$$\Delta_{\mathbf{k}} = \sum_{\mathbf{k}'} V_{\mathbf{k}'\mathbf{k}} b_{\mathbf{k}'} \quad (5.4)$$

$$\Delta_{\mathbf{k}}^* = \sum_{\mathbf{k}'} V_{\mathbf{k}\mathbf{k}'} b_{\mathbf{k}'}^*. \quad (5.5)$$

Consistent with the notation, these are easily shown to be complex conjugates of each other by utilizing the property $V_{\mathbf{k}\mathbf{k}'}^* = V_{\mathbf{k}'\mathbf{k}}$ which follows from the hermiticity of the reduced BCS Hamiltonian.

By introducing the Nambu spinor $\psi_{\mathbf{k}} = (c_{\mathbf{k}\uparrow}, c_{-\mathbf{k}\downarrow}^\dagger)^T$, the Hamiltonian can be written as

$$H = E_0 + \sum_{\mathbf{k}} \xi_{\mathbf{k}} + \sum_{\mathbf{k}} \psi_{\mathbf{k}}^\dagger h_{\mathbf{k}} \psi_{\mathbf{k}}, \quad (5.6)$$

with matrix $h_{\mathbf{k}}$ given by

$$h_{\mathbf{k}} = \begin{pmatrix} \xi_{\mathbf{k}} & \Delta_{\mathbf{k}} \\ \Delta_{\mathbf{k}}^* & -\xi_{\mathbf{k}} \end{pmatrix}, \quad (5.7)$$

and a constant term E_0 originating from the constant term in Eq. (5.3) and fermionic anticommutation relations.

The Hamiltonian can be diagonalized by a Bogoliubov-Valantin transformation. Introducing a transformation $\gamma_{\mathbf{k}} = (\gamma_{\mathbf{k}\uparrow}, \gamma_{-\mathbf{k}\downarrow}^\dagger)^T = U_{\mathbf{k}} \psi_{\mathbf{k}}$, the new operators in $\gamma_{\mathbf{k}}$ satisfy fermionic anticommutation when $U_{\mathbf{k}}$ is unitary. We may therefore write²

$$\gamma_{\mathbf{k}} = \begin{pmatrix} \gamma_{\mathbf{k}\uparrow} \\ \gamma_{-\mathbf{k}\downarrow}^\dagger \end{pmatrix} = \begin{pmatrix} u_{\mathbf{k}} & -v_{\mathbf{k}}^* \\ v_{\mathbf{k}} & u_{\mathbf{k}}^* \end{pmatrix} \begin{pmatrix} c_{\mathbf{k}\uparrow} \\ c_{-\mathbf{k}\downarrow}^\dagger \end{pmatrix} = U_{\mathbf{k}} \psi_{\mathbf{k}}, \quad (5.8)$$

where the unitarity of $U_{\mathbf{k}}$ imposes $|u_{\mathbf{k}}|^2 + |v_{\mathbf{k}}|^2 = 1$. By computing the eigenvalues of the matrix $h_{\mathbf{k}}$, it is then clear that the diagonalized form of the Hamiltonian is

$$H = E_0 + \sum_{\mathbf{k}} \xi_{\mathbf{k}} + \sum_{\mathbf{k}} \begin{pmatrix} \gamma_{\mathbf{k}\uparrow}^\dagger & \gamma_{-\mathbf{k}\downarrow} \end{pmatrix} \begin{pmatrix} E_{\mathbf{k}} & 0 \\ 0 & -E_{\mathbf{k}} \end{pmatrix} \begin{pmatrix} \gamma_{\mathbf{k}\uparrow} \\ \gamma_{-\mathbf{k}\downarrow}^\dagger \end{pmatrix}, \quad (5.9)$$

and that the excitation spectrum $E_{\mathbf{k}}$ is

$$E_{\mathbf{k}} = \sqrt{\xi_{\mathbf{k}}^2 + |\Delta_{\mathbf{k}}|^2}. \quad (5.10)$$

²The form below is in fact not the only way to introduce fermion operators so that the Hamiltonian is diagonalized. An alternate version is employed in Refs. [112, 123].

Furthermore, by computing the eigenvectors, it follows that this diagonalization is achieved by choosing

$$u_{\mathbf{k}} = \sqrt{\frac{1}{2} \left(1 + \frac{\xi_{\mathbf{k}}}{E_{\mathbf{k}}} \right)} \quad v_{\mathbf{k}} = \sqrt{\frac{1}{2} \left(1 - \frac{\xi_{\mathbf{k}}}{E_{\mathbf{k}}} \right)}. \quad (5.11)$$

Writing out the terms in the Hamiltonian explicitly, we now have

$$H = \tilde{E}_0 + \sum_{\mathbf{k}} E_{\mathbf{k}} (\gamma_{\mathbf{k}\uparrow}^\dagger \gamma_{\mathbf{k}\uparrow} + \gamma_{-\mathbf{k}\downarrow}^\dagger \gamma_{-\mathbf{k}\downarrow}), \quad (5.12)$$

with a ground state energy \tilde{E}_0 depending on the fields $\{b_{\mathbf{k}}\}, \{b_{\mathbf{k}}^*\}$.

To determine the mean field parameter $\Delta_{\mathbf{k}}$, there are two equivalent options. Either, one may minimize the free energy with respect to $\Delta_{\mathbf{k}}$, or one may use the self-consistency equation in Eq. (5.5) to derive an equation for the gap. Irrespective of the chosen approach, we obtain the BCS gap equation

$$\Delta_{\mathbf{k}} = - \sum_{\mathbf{k}'} V_{\mathbf{k}\mathbf{k}'} \chi_{\mathbf{k}'} \Delta_{\mathbf{k}'}, \quad (5.13)$$

where we have introduced susceptibility

$$\chi_{\mathbf{k}} = \frac{1}{2E_{\mathbf{k}}} [1 - n_F(E_{\mathbf{k}})] = \frac{\tanh \beta E_{\mathbf{k}}/2}{2E_{\mathbf{k}}}. \quad (5.14)$$

The key microscopic input in the gap equation is the pair scattering potential $V_{\mathbf{k}\mathbf{k}'}$, which we will be discussing in more detail in the next section. We solve the equation with a simple model for $V_{\mathbf{k}\mathbf{k}'}$ in Sec. 5.1.5, but let us for now try to understand the behaviour of the equation qualitatively.

The gap equation is a non-linear eigenvalue problem whose solutions are eigenvectors $\Delta_{\mathbf{k}}$ of the matrix $M_{\mathbf{k}\mathbf{k}'} = V_{\mathbf{k}\mathbf{k}'} \chi_{\mathbf{k}'}$ corresponding to eigenvalue 1. The eigenvalue problem is non-linear because the matrix $M_{\mathbf{k}\mathbf{k}'}$ depends on $\Delta_{\mathbf{k}}$ itself through the excitation spectrum in $\chi(E_{\mathbf{k}})$. Furthermore, we notice that introducing a gap increases the excitation energy, so that $\chi(E_{\mathbf{k}})$ is always reduced with increasing $|\Delta_{\mathbf{k}}|$.

Start at large temperatures, $\chi_{\mathbf{k}}$ is suppressed, and the largest eigenvalue of $M_{\mathbf{k}\mathbf{k}'}$ is smaller than 1, so that the equation does not have non-zero solutions. At a certain critical temperature T_c , however, the largest eigenvalue of the matrix becomes 1, and we may have solutions with an infinitesimal, yet non-zero gap. Decreasing the temperature further, the gap $\Delta_{\mathbf{k}}$ in the solution of the gap equation grows beyond infinitesimal values to keep the eigenvalue of $M_{\mathbf{k}\mathbf{k}'}$ at 1.

5.1.3 Ground state

From the diagonalized Hamiltonian in Eq. (5.12), it is clear that since the operators γ represent excitations on top of the ground state, the ground state itself is the vacuum state in the basis of the γ -operators. It is not yet clear, however, what the ground state looks like in terms of the original fermion operators. To obtain such a representation, we start by noticing that in a fermionic system, the condition $\gamma|\psi\rangle = 0$ uniquely defines the occupation of the single particle state corresponding to a fermion annihilation operator γ . Thus, the ground state of the mean field BCS Hamiltonian can be uniquely defined by demanding

$$\gamma_{\mathbf{k}\sigma}|\psi_{\text{BCS}}\rangle = 0 \quad \forall \mathbf{k}, \sigma \quad (5.15)$$

for the BCS mean field ground state $|\psi_{\text{BCS}}\rangle$ ³. Since, $(\gamma_{\mathbf{k}\uparrow})^2 = (\gamma_{\mathbf{k}\downarrow})^2 = 0$, the operator $\prod_{\mathbf{k}} \gamma_{\mathbf{k}\uparrow} \gamma_{\mathbf{k}\downarrow}$ acts as projection operator projecting any state down on its ground state component. Since the state $\prod_{\mathbf{k}} \gamma_{\mathbf{k}\uparrow} \gamma_{\mathbf{k}\downarrow} |0_c\rangle$ is non-zero, where $|0_c\rangle$ denotes the vacuum state in the c -operator basis, it must therefore be proportional to the ground state. Thus, it is readily shown that the BCS ground state can be written on the form

$$|\psi_{\text{BCS}}\rangle = \frac{1}{\mathcal{N}} \prod_{\mathbf{k}} (u_{\mathbf{k}} + v_{\mathbf{k}} c_{-\mathbf{k}\downarrow}^\dagger c_{\mathbf{k}\uparrow}^\dagger) |0_c\rangle, \quad (5.16)$$

where \mathcal{N} is a normalization constant. Alternately, one may expand the BCS ground state in terms of the c -operator number states, and derive explicit conditions for the expansion coefficients to show that the ground state takes this form.

5.1.4 Effective phonon-mediated potential

Although BCS theory was developed to describe phonon-mediated superconductivity, the theory itself is completely indifferent to the origin of pair scattering potential, as long as it is attractive. Thus, the effective potential may in principle occur due to phonons, spin fluctuations [125–127], any other boson [128–131], or be of purely electronic origin [132–134]. In the following, we will be discussing how to obtain an effective electron-electron pair scattering potential for a phonon exchange mechanism, but the methods can

³An alternate route to deriving the ground state is given in Ref. [124], and is based on an effective isospin description, where the ground state is obtained by rotating the the ground state for $\Delta_{\mathbf{k}}$ to align it with the direction of the effective magnetic field $\mathbf{n}_{\mathbf{k}}$ given such that $h_{\mathbf{k}} = \mathbf{n}_{\mathbf{k}} \cdot \boldsymbol{\sigma}$.

also be generalized to other boson exchange mechanisms. We thus consider the electron-phonon coupled Hamiltonian

$$H = \sum_{\mathbf{k}\sigma} \xi_{\mathbf{k}} c_{\mathbf{k}\sigma}^\dagger c_{\mathbf{k}\sigma} + \sum_{\mathbf{q}\nu} \omega_{\mathbf{q}\nu} b_{\mathbf{q}\nu}^\dagger b_{\mathbf{q}\nu} + \sum_{\mathbf{q}\nu} \sum_{\mathbf{k}\sigma} g_{\mathbf{k},\mathbf{k}+\mathbf{q}}^\nu (b_{\mathbf{q}\nu} + b_{-\mathbf{q}\nu}^\dagger) c_{\mathbf{k}+\mathbf{q},\sigma}^\dagger c_{\mathbf{k}\sigma}. \quad (5.17)$$

The system consists of electronic and bosonic degrees of freedom which interact through a non-linear interaction. Thus, the electrons in the system affect the phonon system, which again affects the electron system, and so on.

In the BCS Hamiltonian, the bosons do not appear explicitly, and the only trace of their presence is the effective interaction $V_{\mathbf{k}\mathbf{k}'}$. We therefore need a way to decouple the bosons from the electrons, and transform the electron-phonon coupling into an effective electron-electron interaction. This decoupling can be performed through a Schrieffer-Wolff transformation [135–137] as first shown by Fröhlich [84], and we outline the procedure in the following.

Following Ref. [138], we write the Hamiltonian on the form

$$H = H_0 + \eta H_1, \quad (5.18)$$

where H_0 is the non-interacting part of the Hamiltonian describing the free electrons and bosons, H_1 is the electron-phonon interaction, and η is an expansion parameter. The basic idea of the Schrieffer-Wolff transformation is to transform the Hamiltonian through the canonical transformation

$$H \rightarrow H' = e^{-\eta S} H e^{\eta S}, \quad (5.19)$$

which effectively changes the basis of the many-body Hilbert space slightly. Using the Baker-Hausdorff-Campbell lemma [33] and expanding in small η , we then have

$$H' = H_0 + \eta (H_1 + [H_0, S]) + \eta^2 \left([H_1, S] + \frac{1}{2} [[H_0, S], S] \right) + \dots \quad (5.20)$$

Choosing S so that

$$H_1 + [H_0, S] = 0, \quad (5.21)$$

the linear terms in the electron-phonon coupling strength are eliminated. After also utilizing this identity in the second order contribution in η , we are left with $H' = H_0 + H_{\text{eff}}$ and an effective interaction Hamiltonian

$$H_{\text{eff}} = \frac{\eta^2}{2} [H_1, S]. \quad (5.22)$$

Furthermore, it can be shown that an appropriate choice is to write S on the form [138]

$$S = \sum_{\mathbf{k}\sigma} \sum_{\mathbf{q}\nu} g_{\mathbf{k},\mathbf{k}+\mathbf{q}}^\nu (x_{\mathbf{k},\mathbf{q}}^\nu b_{\mathbf{q}\nu} + y_{\mathbf{k},\mathbf{q}}^\nu b_{-\mathbf{q}\nu}^\dagger) c_{\mathbf{k}+\mathbf{q}\sigma}^\dagger c_{\mathbf{k}\sigma}, \quad (5.23)$$

and that choosing the parameters $x_{\mathbf{k},\mathbf{q}}^\nu$ and $y_{\mathbf{k},\mathbf{q}}^\nu$ appropriately, the effective pair interaction becomes

$$V_{\mathbf{k},\mathbf{k}+\mathbf{q}} = \sum_{\nu} |g_{\mathbf{k},\mathbf{k}+\mathbf{q}}^\nu|^2 \frac{2\omega_{\mathbf{q}\nu}}{(\xi_{\mathbf{k}+\mathbf{q}} - \xi_{\mathbf{k}})^2 - \omega_{\mathbf{q}\nu}^2}. \quad (5.24)$$

The above derivation is essentially perturbation theory in the electron-phonon interaction. BCS theory can thus be viewed as a perturbative method to compute the effective potential joining forces with non-perturbative methods to find the ground state of the BCS Hamiltonian [139]. The canonical transformation method can also be generalized to systems with coupling to magnons, as shown in Refs. [140, 141].

Although Fröhlich's canonical transformation is the most standard way to derive the effective potential, it is not the only one. The effective decoupling of the bosonic system can also be performed within a flow equation approach [142, 143]. Remarkably, since the condition in Eq. (5.21) does not uniquely determine the matrix S , this approach gives rise to effective potentials which are on different forms than the Fröhlich effective potential in Eq. (5.24) [142, 144, 145]. However, as the free electron Hamiltonian is also affected by the transformation within this approach, these effective potentials cannot immediately replace the Fröhlich potential.

In a diagrammatic expansion similar to the one we will be considering in the section on Eliashberg theory, the interaction between electrons is mediated by a phonon. Letting $D_R(\mathbf{q}, \omega)$ be the retarded phonon propagator, the effective potential can therefore be thought of as

$$V_{\mathbf{k},\mathbf{k}+\mathbf{q}}^{\text{eff}}(\omega) = \sum_{\nu} |g_{\mathbf{k},\mathbf{k}+\mathbf{q}}^\nu|^2 D_R^\nu(\mathbf{q}, \omega) = \sum_{\nu} |g_{\mathbf{k},\mathbf{k}+\mathbf{q}}^\nu|^2 \frac{2\omega_{\mathbf{q}\nu}}{\omega^2 - \omega_{\mathbf{q}\nu}^2}. \quad (5.25)$$

This is a frequency dependent effective potential, which unlike the effective potential above should not be thought of as an interaction term occurring in the Hamiltonian. Instead, the frequency ω occurs in the diagrammatic expansion for a frequency dependent Green's function, and has to be summed

over. Clearly, the Fröhlich effective potential can be obtained from this effective potential through the replacement $\omega \rightarrow \xi_{\mathbf{k}+\mathbf{q}} - \xi_{\mathbf{k}}$, but the formal basis for this is through the canonical transformation. In BCS theory, one therefore replaces the properly frequency dependent potential with an effective description where, somewhat strangely, the momentum dependence accounts for the frequency dependence.

5.1.5 Morel-Anderson model

The above approaches give rise to detailed effective potentials. In the original BCS paper, however, the approach was to simplify the potential as much as possible while still keeping the main qualitative features. In the Fröhlich potential, the interaction is attractive close to the Fermi surface, while it becomes repulsive for electron energy transfers exceeding the characteristic boson frequency, which acts as resonance frequency and effective cutoff for the attractive part of the potential.

Bardeen Cooper and Schrieffer therefore postulated that superconductivity could be explained with the effective interaction in Eq. (5.2), which is attractive for electrons \mathbf{k} and \mathbf{k}' closer to the Fermi surface than the energy ω_D , and that the potential vanishes otherwise. We will instead consider a somewhat more general potential, where we also include a constant repulsive potential, which we think of as coming primarily from Coulomb repulsion between the electrons. This is known as the Morel-Anderson model [146], and within this model, the effective pair scattering potential is assumed to take the form

$$V_{\mathbf{k},\mathbf{k}'} = \left\{ \begin{array}{ll} (-u + v)/N & \text{for } |\xi_{\mathbf{k}}|, |\xi_{\mathbf{k}'}| \leq \omega_D \\ v/N & \text{for } \omega_D \leq |\xi_{\mathbf{k}}|, |\xi_{\mathbf{k}'}| \leq W \\ 0 & \text{otherwise} \end{array} \right\}, \quad (5.26)$$

where W is the electron bandwidth, u the strength of the attractive potential, and v the strength of the repulsive potential. The potential is illustrated in Fig. 5.1, and the standard BCS potential is regained by letting $v = 0$.

With the standard BCS potential, we need the effective pair scattering potential to be negative on the Fermi surface to be able to find a solution. Thus, we would naively expect that one may only find solutions to the BCS gap equation for $u > v$. However, this is not the case, and we will see why in the following.

Since the potential takes on different values in the two different regions corresponding to electron energies $|\xi_{\mathbf{k}}| < \omega_D$, and $\omega_D < |\xi_{\mathbf{k}}| < W$, we assume that the gap can also be written on the form

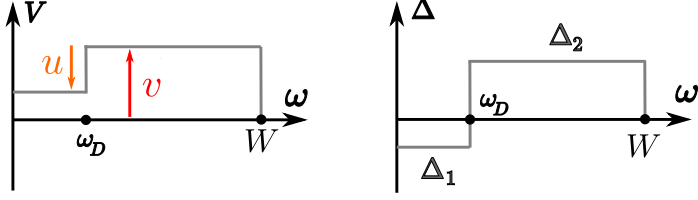


Figure 5.1: Morel-Anderson potential and gap Ansatz.

$$\Delta_{\mathbf{k}} = \begin{cases} \Delta_1 & \text{for } |\xi_{\mathbf{k}}|, |\xi_{\mathbf{k}'}| \leq \omega_D \\ \Delta_2 & \text{for } \omega_D \leq |\xi_{\mathbf{k}}|, |\xi_{\mathbf{k}'}| \leq W \\ 0 & \text{otherwise} \end{cases}, \quad (5.27)$$

as shown in Fig. 5.1. We now insert the given profiles for the gap and the potential into the gap equation. Since the potential $V_{\mathbf{k}\mathbf{k}'}$ and the gap $\Delta_{\mathbf{k}}$ depend on momentum only through the electronic energy $\xi_{\mathbf{k}}$, the gap equation can be written on the form [6, 123]

$$\Delta(\xi) = -D_F \int d\xi' V(\xi, \xi') \chi(\xi') \Delta(\xi'), \quad (5.28)$$

where we have introduced the susceptibility

$$\chi(\xi, \Delta) = \frac{\tanh(\beta\sqrt{\xi^2 + \Delta^2}/2)}{2\sqrt{\xi^2 + \Delta^2}}. \quad (5.29)$$

Separating the integrals over the two regions of the Brillouin zone, we obtain a gap equation

$$\begin{pmatrix} \Delta_1 \\ \Delta_2 \end{pmatrix} = -D_F \begin{pmatrix} (v-u)f_1(\Delta_1) & vf_2(\Delta_2) \\ vf_1(\Delta_1) & vf_2(\Delta_2) \end{pmatrix} \begin{pmatrix} \Delta_1 \\ \Delta_2 \end{pmatrix} \quad (5.30)$$

where we have introduced the functions

$$f_1(\Delta_1) = 2 \int_0^{\omega_D} \chi(\xi, \Delta_1) d\xi \quad (5.31a)$$

$$f_2(\Delta_2) = 2 \int_{\omega_D}^W \chi(\xi, \Delta_2) d\xi. \quad (5.31b)$$

Since a homogeneous linear set of equations can only have non-zero solutions when the determinant vanishes, we may only find non-zero solutions when

$$[1 + D_F(v - u)f_1][1 + D_Fvf_2] - (D_Fv)^2 f_1 f_2 = 0. \quad (5.32)$$

This condition relates $f_1(\Delta_1)$ to $f_2(\Delta_2)$, and solving for $f_1(\Delta_1)$, we obtain

$$f_1(\Delta_1) = \left[D_Fu - \frac{D_Fv}{1 + D_Fvf_2(\Delta_2)} \right]^{-1}. \quad (5.33)$$

In principle, we should now solve the two coupled equations for Δ_1 and Δ_2 in Eq. (5.30) for each temperature T , and any such solution then automatically satisfies the condition in Eq. (5.32). However, in the weak coupling regime where $\beta\omega_D \ll 1$, the hyperbolic tangent in the integrand of $f_2(\Delta_2)$ can be considered constant, so that that

$$f_2(\Delta_2) \approx \int_1^{W/\omega_D} \frac{dx}{\sqrt{x^2 + (\Delta_2/\omega_D)^2}} \approx \log\left(\frac{W}{\omega_D}\right), \quad (5.34)$$

where we have assumed that $W/\omega_D \gg 1$ in the last step.

Notably, this makes $f_2(\Delta_2)$ independent of Δ_2 , so that we may simply solve the equation in Eq. (5.33) by using the constant value $\log W/\omega_D$ for f_2 . The equation is then simply the well known gap equation which results BCS theory letting $v = 0$, but where $D_Fu \equiv \lambda$ has been replaced by $\lambda - \mu^*$, and we have introduced the Coulomb pseudo-potential

$$\mu^* = \frac{D_Fv}{1 + D_Fv \log W/\omega_D}. \quad (5.35)$$

Once the gap $\Delta_1(T)$ is known, one may obtain $\Delta_2(T)$ using

$$\Delta_2(T) = -\frac{\mu^*}{\lambda - \mu^*} \Delta_1(T), \quad (5.36)$$

which follows from either of the equations in Eq. (5.30) together with Eq. (5.33).

The gap equation in Eq. (5.33) has solutions with a finite gap $\Delta_1(T)$ for temperatures below a critical temperature T_c . Following the standard calculation [112, 117], one may show that the critical temperature in the weak coupling limit $\beta\omega_D \ll 1$ is given by

$$T_c \approx 1.14\omega_D \exp\left(-\frac{1}{\lambda - \mu^*}\right), \quad (5.37)$$

and the gap $\Delta_1(0)$ at zero temperature is given by

$$\Delta_1(0) = 2\omega_D \exp\left(-\frac{1}{\lambda - \mu^*}\right). \quad (5.38)$$

Although the characteristic phonon energy ω_D sets the energy scale for the critical temperature, the dimensionless electron-phonon coupling strength λ has to be significantly larger than the Coulomb pseudo-potential to avoid complete exponential suppression of the critical temperature. If λ is smaller than μ^* , there are no non-zero solutions of the gap equations, neither at finite nor zero temperature.

Remarkably, the Coulomb pseudo potential μ^* is limited to values of $1/\log(W/\omega_D)$ even in the limit $v \rightarrow \infty$. Thus, even an infinitely large repulsion v is not able to prevent the superconducting instability.

This can be understood in terms of the processes contributing to the pairing. While processes from a point \mathbf{k} on the Fermi surface to a point \mathbf{k}' close to the Fermi surface contribute repulsively in the gap equation due to the positive potential $v - u$, the repulsive part v of the interaction is counteracted by the processes between \mathbf{k} and points \mathbf{k}' far away from the surface acting attractively due to the sign change in the gap amplitude. The dip in the total pair scattering potential due to the phonon-mediated potential is then able to produce superconductivity because the gap adapts to the effective potential to cancel out most of the effect of the repulsion. This effect is only possible due to the large energy scale separation between the characteristic phonon frequency ω_D and the electron bandwidth W . Thus, the Morel-Anderson model provides a concrete justification for the often paraphrased saying that superconductivity can occur in spite of strong electronic repulsion because electrons are able to avoid each other in time.

The Morel-Anderson pseudo-potential is shown as function of the repulsion strength $D_F v$ in Fig. 5.2 (a). At intermediate temperatures, the gap equation has to be solved numerically, and the solutions are shown in Fig. 5.2 (b) for various values of v , where the gap component Δ_1 is shown with solid lines and the gap component Δ_2 with dashed lines. As v increases, the pseudopotential μ^* also increases, before eventually saturating at a finite value. As shown in (b), the critical temperature shows similar behaviour. With the increasing μ^* , the gap component $\Delta_2(T = 0)$ increases to compensate for the repulsive interaction, as discussed above.

5.1.6 Experimental consequences

By inspecting the expressions for the critical temperature and the gap at zero temperature from the calculation in the previous section, we notice that their functional forms are in fact identical. Using this, one finds the so-called universal amplitude ratio

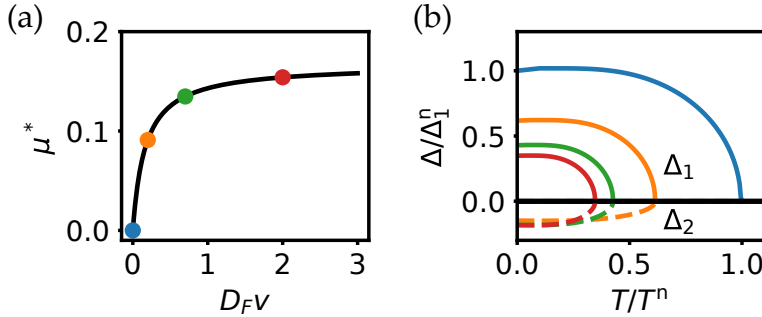


Figure 5.2: (a) Coulomb pseudopotential μ^* as function of v . (b) Gap temperature dependence for various v , with solid lines for Δ_1 and dashed lines for Δ_2 . The gap amplitudes and temperatures are normalized against the critical temperature T^n and gap Δ_1^n obtained by setting $v = 0$.

$$\frac{2\Delta_1(T=0)}{T_c} \approx 3.52. \quad (5.39)$$

This very famous result matches experiments in weak coupling superconductors well, and provided compelling evidence for the BCS theory. As shown here, the prediction holds also within the Morel-Anderson model.

The BCS theory is also able to explain the so-called isotope effect, which was historically one of clues which promoted electron-phonon coupling to prime suspect as underlying mechanism for superconductivity. In elemental superconductors, it was noticed that the critical temperature in samples constructed of different isotopes with different masses M scaled according to $T_c \sim M^{-1/2}$. As seen from Eq. (4.12), the typical phonon frequencies are proportional to $M^{-1/2}$, while the electron-phonon coupling strength λ is typically independent of the isotope mass. For the electron-phonon coupling, this can be seen from Eqs. (4.41) and (4.24), as both the coupling matrix element and phonon frequencies scale with $M^{-1/2}$. Thus the BCS theory is able to explain the isotope effect in elemental weak coupling superconductors.

Upon inclusion of a Coulomb pseudo-potential, we expect corrections to the exponent $-1/2$, as the Coulomb pseudopotential depends on the isotope mass through the phonon frequency. A simple calculation gives that a small change dM in the isotope should produce a small change dT in the critical temperature given by

$$\frac{dT}{T} = \frac{dM}{M} \left(-\frac{1}{2} \right) \left[1 - \left(\frac{\mu^*}{\lambda - \mu^*} \right)^2 \right]. \quad (5.40)$$

A comparison between experimental results and the isotope effect coefficient calculated with similar methods shows good agreement [139, 147].

The two primary properties of the superconductor, namely zero resistivity and the Meißner effect, can both be understood from BCS theory if we couple the system to electromagnetic fields. These properties can conveniently be understood within linear response theory and a Green's function formulation of BCS theory [45, 118]. In the research in this thesis, we are primarily concerned with whether various mechanism can give rise to superconductivity, and not the properties of the superconducting state itself. We will therefore not review this in further detail.

5.1.7 Numerical solution of the gap equation

Above, we have solved the gap equation with a simple assumption for the effective pair scattering potential $V_{\mathbf{k}\mathbf{k}'}$. If we instead use a detailed potential $V_{\mathbf{k}\mathbf{k}'}$, the equations can no longer be solved analytically. Thus, numerical methods are required.

In this thesis, we will primarily be interested in locating the superconducting transition and the gap profiles close to the superconducting instability. In this regime, we expect the gap to be small. The gap equation can then be linearized in the gap to obtain the equation

$$\Delta_{\mathbf{k}} = - \sum_{\mathbf{k}'} V_{\mathbf{k}\mathbf{k}'} \frac{\tanh \beta \xi_{\mathbf{k}'}/2}{2\xi_{\mathbf{k}'}} \Delta_{\mathbf{k}'}, \quad (5.41)$$

where the gap dependent excitation spectrum $E_{\mathbf{k}}$ has been replaced with the single particle energy $\xi_{\mathbf{k}}$.

In the following, we discuss two methods which can be used to solve such a gap equation, and which are applied to phonon-mediated superconductivity in graphene in Chapter 7.

Fermi surface averaged equation

In the simplest possible BCS theory, one assumes that the effective potential is constant close to the Fermi surface, and zero otherwise. An alternate approach keeping more details of the effective potential is to derive Fermi surface averaged equations.

In the linearized gap equation (5.41), the dominant contributions come from regions close to the Fermi surface. In the spirit of BCS theory, we then assume that the effective potential $V_{\mathbf{k}\mathbf{k}'}$ for pair scattering of a pair at momenta $\pm\mathbf{k}$ on the Fermi surface is attractive for scatterings to momenta $\pm\mathbf{k}'$ within a region corresponding to electron energy $|\xi_{\mathbf{k}'}| < \omega_D$, but zero otherwise. Assuming that the gap and the effective potential vary slowly along the direction perpendicular to the Fermi surface, we may then separate the integration into integrations along and perpendicular to the Fermi surface. Neglecting the perpendicular momentum dependence of the effective potential and the gap, we then obtain

$$\Delta_{\mathbf{k}_{\parallel}} = -\frac{1}{A_{\text{BZ}}} \int d^{d-1}k_{\parallel} \left| \frac{d\xi}{dk_{\perp}} \right|^{-1} V_{\mathbf{k}_{\parallel}\mathbf{k}'_{\parallel}} \Delta_{\mathbf{k}'_{\parallel}} \int_0^{\omega_D} d\xi \frac{\tanh \beta\xi/2}{\xi}, \quad (5.42)$$

where A_{BZ} is the Brillouin zone volume. This equation now represents an eigenvalue problem for the gap $\Delta_{\mathbf{k}_{\parallel}}$ on the Fermi surface, where the critical temperature T_c is determined as the largest value of T which is consistent with a solution of the equation. While the eigenvalue problem

$$-\frac{1}{A_{\text{BZ}}} \int d^{d-1}k_{\parallel} \left| \frac{d\xi}{dk_{\perp}} \right|^{-1} V_{\mathbf{k}_{\parallel}\mathbf{k}'_{\parallel}} \Delta_{\mathbf{k}'_{\parallel}} = \lambda \Delta_{\mathbf{k}_{\parallel}} \quad (5.43)$$

in general has many eigenvalues λ , we thus have to pick out the largest λ_{eff} , and the inverse critical temperature $\beta_c = 1/T_c$ is then obtained through

$$1 = \lambda_{\text{eff}} \int_0^{\omega_D} d\xi \frac{\tanh \beta\xi/2}{\xi} \approx \lambda_{\text{eff}} \log \left(\frac{2e^{\gamma}}{\pi} \beta\omega_D \right), \quad (5.44)$$

which has the well known BCS solution

$$T_c \approx 1.13\omega_D e^{-1/\lambda_{\text{eff}}}. \quad (5.45)$$

The gap profile on the Fermi surface close to the critical temperature is simply the eigenvector $\Delta_{\mathbf{k}_{\parallel}}$ corresponding to the largest eigenvalue λ_{eff} .

Although the above approach contains many of the same simplifications as BCS theory, it does allow a calculation of the gap profile on the Fermi surface based on detailed information about the pairing potential and the shape of the Fermi surface.

Full momentum dependent solution

In Paper [2], we solve the gap equation in two dimensions on a momentum grid with a finite number of momentum points. To ensure an appropriate resolution in the most important regions around the Fermi surface, we introduce points on a coarse grid in the entire Brillouin zone and add additional denser points close to the Fermi surface to pick up the sharply peaked features in the effective potential and in the susceptibility. Through a triangulation technique, we may then partition the Brillouin zone into triangles with these points as vertices. Since a point \mathbf{k} may be a vertex of several triangles t , we associate the point \mathbf{k} with the weight $w_{\mathbf{k}}$ given by

$$w_{\mathbf{k}} = \sum_t A_t \delta_{\mathbf{k}\in t} / 3, \quad (5.46)$$

with $\delta_{\mathbf{k}\in t} = 1$ if \mathbf{k} is a vertex in the triangle t , and 0 otherwise. The gap equation can then be written on the form

$$\Delta_{\mathbf{k}} = -\frac{1}{A_{\text{BZ}}} \sum_{\mathbf{k}'} V_{\mathbf{k}\mathbf{k}'} \chi_{\mathbf{k}'} w_{\mathbf{k}'} \Delta_{\mathbf{k}'} \quad (5.47)$$

where A_{BZ} is the Brillouin zone area. Linearizing this equation in the gap and setting the largest eigenvalue of the linear eigenvalue problem to 1, we obtain an equation for critical temperature T_c . Furthermore, the gap structure $\Delta_{\mathbf{k}}$ just below the critical point is given by the eigenvector corresponding to the largest eigenvalue of the linear eigenvalue problem.

5.2 Eliashberg theory

In the discussion of the Morel-Anderson model in the previous section, we saw that even a strong Coulombic repulsion only results in a surprisingly small renormalization of the dimensionless electron-phonon coupling strength. Thus, the qualitative properties of the superconductivity are hardly changed. From the argument, it was clear that this occurs due to the time scale separation of the electron and the ion dynamics through the large ratio W/ω_D , and we gave a rough interpretation of this in terms of electrons avoiding each other in time⁴.

Yet, when we consider the BCS theory and the Morel-Anderson model, time does not appear anywhere. The BCS interaction potential is in fact

⁴The argument can even be extended in terms of a discussion of the screening of the interaction from an oscillating ion on the lattice [123].

both instantaneous and non-local, as it depends, not only the scattering momentum $\mathbf{k}-\mathbf{k}'$, but also on \mathbf{k} and \mathbf{k}' individually. An alternate description of BCS theory was formulated by Gorkov based on Green's functions [83, 118, 148], which give electron correlations at different times. While the original formulation of the BCS theory was based on mean field theory, this particular formulation of BCS theory allowed the problem to be studied within the recently developed methods of quantum field theory [118]. The natural generalization of this BCS theory formulation lead G. Eliashberg to develop what we now know as Eliashberg theory [106, 107].

Although the BCS theory described the properties of many superconductors well, there were some exceptions. In the simplest BCS theory, the ratio $2\Delta(0)/k_B T_c$ takes on a “universal” value of approximately 3.53⁵. Although this matched well with observed values in most superconductors at the time, it deviates significantly from the values in lead and mercury, which have ratios of roughly 4.3 and 4.6 [149]. These were superconductors with a relatively small phonon Debye frequency and large values for the electron-phonon coupling strength, as witnessed for instance by the ratio T_c/ω_D or the effective mass enhancement factor extracted from specific heat measurements. At the same time, the dependence of the upper critical magnetic field in these materials deviated from the BCS expectation [149]. These deviations therefore called for a theory of “strong coupling superconductors”. When the amplitude ratio was calculated within Eliashberg theory [150, 151], there was excellent agreement, and Eliashberg theory seemed to fill this need.

Whereas BCS theory is only able to describe weak coupling superconductors with small $\lambda \lesssim 0.3$, Eliashberg theory can describe superconductors with larger λ . An interesting difference between BCS theory and Eliashberg theory is in fact that whereas the critical temperature within BCS theory would saturate at the phonon Debye frequency as $\lambda \rightarrow \infty$, the critical temperature in Eliashberg theory for large λ in principle approaches infinity as $\sqrt{\lambda}$. Yet, even Eliashberg theory is expected to break down at large λ [152], and for this reason, it is some times referred to as intermediate coupling theory today [153].

In the following, we discuss how one may formulate a Green's function approach for phonon-mediated superconductivity. Using a framework which can easily be generalized to treat also magnon-mediated superconductivity, we thus derive the Eliashberg equations. This is a multi-step processes,

⁵In fact, the “universal” amplitude ratio is not universal anymore even within BCS theory for larger electron-phonon coupling strength λ . Yet, the value seemed to saturate at 4 within BCS theory, so that BCS theory did not seem able to explain the values observed in mercury and lead, as discussed below [149].

which we discuss in some detail in the following subsections.

5.2.1 Model Hamiltonian

The starting point of BCS theory is the reduced BCS Hamiltonian in Eq. (5.1), which describes electrons interacting with each other through some potential $V_{\mathbf{k}\mathbf{k}'}$. In contrast, the starting point of Eliashberg theory is a more fundamental Hamiltonian $H = H_{\text{el}} + H_{\text{b}} + H_{\text{el-b}}$ describing both electrons, bosons, and their interaction explicitly.

To keep our discussion sufficiently general, we consider a model on the form

$$H = \sum_{\mathbf{k}\sigma} \xi_{\mathbf{k}} c_{\mathbf{k}\sigma}^\dagger c_{\mathbf{k}\sigma} + \sum_{\mathbf{q}\nu} \omega_{\mathbf{q}\nu} b_{\mathbf{q}\nu}^\dagger b_{\mathbf{q}\nu} + \sum_{\mathbf{k}\mathbf{q}} \sum_{\sigma\sigma'\mu} g_{\mathbf{k},\mathbf{k}+\mathbf{q}}^{\sigma\sigma';\mu} B_{\mathbf{q}\mu} c_{\mathbf{k}+\mathbf{q}\sigma'}^\dagger c_{\mathbf{k}\sigma}, \quad (5.48)$$

where $c_{\mathbf{k}\sigma}$ and $c_{\mathbf{k}\sigma}^\dagger$ are annihilation and creation operators for electrons with spin σ and quasimomentum \mathbf{k} , while $\xi_{\mathbf{k}}$ is the electron single particle spectrum. Similarly, $b_{\mathbf{q}\nu}$ and $b_{\mathbf{q}\nu}^\dagger$ are annihilation and creation operators for a boson in mode ν with quasimomentum \mathbf{q} . Furthermore, $B_{\mathbf{q}\mu}$ represents a bosonic excitation which can in general be constructed as a linear combination of the boson creation or annihilation operators carrying momentum \mathbf{q} , while $g_{\mathbf{k}\mathbf{k}'}^{\sigma\sigma';\mu}$ is the associated matrix element. In this thesis, we will encounter both phonon-mediated and magnon-mediated superconductivity, which can both be described within such a model.

To be concrete, the boson operator $B_{\mathbf{q}\nu}$ for phonon-mediated superconductivity is given by

$$B_{\mathbf{q}\nu} = a_{\mathbf{q}\nu} + a_{-\mathbf{q}\nu}^\dagger, \quad (5.49)$$

as seen in the general electron-phonon coupling Hamiltonian of Eq. (4.16), and where ν labels the phonon modes in the system. For magnon-mediated superconductivity as considered in Paper [4], we instead let $B_{\mathbf{q}\mu}$ correspond to four different magnon operators $M_{\mathbf{q}}^{R,U}$, $(M_{-\mathbf{q}}^{R,U})^\dagger$ constructed as linear combinations of the eigenmagnon operators in the system, as discussed in more detail in Chapter 8.

5.2.2 Building blocks: Green's functions

As already mentioned, Eliashberg theory is based on Green's function techniques and many-body perturbation theory. Thus, the basic building blocks

for the theory are electron and boson Green's functions. In the following, we will be working within a Matsubara Green's function formalism, and for an introduction to this, we refer to Refs. [6, 118]. In the following, we define the Green's functions we will be interested in. First, the electron Green's function $G_{\sigma\sigma'}(\mathbf{k}, \tau)$ is defined as

$$G_{\sigma\sigma'}(\mathbf{k}, \tau) = -\langle T_\tau c_{\mathbf{k}\sigma}(\tau) c_{\mathbf{k}\sigma'}^\dagger(0) \rangle, \quad (5.50)$$

where \mathbf{k} is the electron quasimomentum, σ and σ' are the spins of the electrons in the Green's function, τ the imaginary time, and T_τ the time ordering operator in imaginary time. As it will turn out to be useful later, we also introduce the Green's function

$$\bar{G}_{\sigma\sigma'}(\mathbf{k}, \tau) = -\langle T_\tau c_{-\mathbf{k},\sigma}^\dagger(\tau) c_{-\mathbf{k},\sigma'}(0) \rangle. \quad (5.51)$$

As we saw in the section on BCS theory, the BCS ground state is not a state with a fixed number of particles. Instead, the BCS ground consists of a linear combination of states where the single particle states \mathbf{k} with opposite spins are occupied and empty, as given in Eq. (5.16). Thus, cross terms from the two contributions give rise to a finite BCS ground state expectation value for the operators $c_{-\mathbf{k}\downarrow} c_{\mathbf{k}\uparrow}$ and $c_{\mathbf{k}\uparrow}^\dagger c_{-\mathbf{k}\downarrow}^\dagger$. A Green's function formalism which can successfully describe superconductivity must therefore also include the so-called anomalous correlations $F_{\sigma\sigma'}$ and $\bar{F}_{\sigma\sigma'}$ defined by

$$F_{\sigma\sigma'}(\mathbf{k}, \tau) = -\langle T_\tau c_{\mathbf{k},\sigma}(\tau) c_{-\mathbf{k},\sigma'}(0) \rangle \quad (5.52)$$

$$\bar{F}_{\sigma\sigma'}(\mathbf{k}, \tau) = -\langle T_\tau c_{-\mathbf{k},\sigma}^\dagger(\tau) c_{\mathbf{k},\sigma'}^\dagger(0) \rangle. \quad (5.53)$$

Our theory consists of both an electronic and a bosonic part. When studying superconductivity, however, we are primarily interested in pairing of the electrons, which interact with the bosons operators $B_{\mathbf{q}\nu}$ through the electron-boson coupling. Since it is always the operators $B_{\mathbf{q}\nu}$ that couple to the electrons, the relevant boson propagator is therefore

$$D_{\mu\nu}(\mathbf{q}, \tau) = -\langle B_{\mathbf{q}\mu}(\tau) B_{-\mathbf{q}\nu}(0) \rangle, \quad (5.54)$$

which in general has a matrix structure in the presence of several bosonic operators.

The above Green's functions are formulated in terms of quasimomentum and imaginary time. In the following, we will instead be working with their Fourier representations, which are given through the Fourier series expansion [118]

$$H(\mathbf{k}, \tau) = \frac{1}{\beta} \sum_{i\omega_n} e^{-i\omega_n \tau} H(\mathbf{k}, i\omega_n) \quad (5.55)$$

$$H(\mathbf{k}, i\omega_n) = \int_0^\beta d\tau e^{i\omega_n \tau} H(\mathbf{k}, \tau), \quad (5.56)$$

where the function H represents either electronic or bosonic Green's functions. Furthermore, $\omega_n = (2n+1)\pi/\beta$ in the fermionic case, and $\omega_n = 2n\pi/\beta$ in the bosonic case. In the following, we will typically be using the notation ω_n for a fermionic Matsubara frequency and ν_m for a bosonic Matsubara frequency.

5.2.3 Spinor representation

To structure the forthcoming calculations, it is useful to collect the interacting electron and boson operators in spinors, and the corresponding Green's functions in matrices.

Since we are interested in both normal and anomalous Green's functions, we introduce a Nambu spinor $\psi_{\mathbf{k}}$ given by

$$\psi_{\mathbf{k}} = \left(c_{\mathbf{k}\uparrow} \quad c_{\mathbf{k}\downarrow} \quad c_{-\mathbf{k}\uparrow}^\dagger \quad c_{-\mathbf{k}\downarrow}^\dagger \right)^T. \quad (5.57)$$

The electronic Green's functions we have introduced this far may therefore be combined into the electron Green's function matrix

$$\mathcal{G}(\mathbf{k}, \tau) = -\langle T_\tau \psi_{\mathbf{k}}(\tau) \psi_{\mathbf{k}}^\dagger(0) \rangle = \begin{pmatrix} G_{\sigma\sigma'}(\mathbf{k}, \tau) & F_{\sigma\sigma'}(\mathbf{k}, \tau) \\ \bar{F}_{\sigma\sigma'}(\mathbf{k}, \tau) & \bar{G}_{\sigma\sigma'}(\mathbf{k}, \tau) \end{pmatrix}, \quad (5.58)$$

which in the Fourier representation takes the form

$$\mathcal{G}(\mathbf{k}, i\omega_n) = \begin{pmatrix} G_{\sigma\sigma'}(\mathbf{k}, i\omega_n) & F_{\sigma\sigma'}(\mathbf{k}, i\omega_n) \\ \bar{F}_{\sigma\sigma'}(\mathbf{k}, i\omega_n) & \bar{G}_{\sigma\sigma'}(\mathbf{k}, i\omega_n) \end{pmatrix}. \quad (5.59)$$

With a single band and two spin species, this matrix consists of 16 elements. However, due to various relations between the operators in the spinors, the Green's function matrix satisfies several symmetry relations, so that not all matrix elements are independent. In particular, the Fourier representations of the 2×2 submatrices of the full electron Green's function matrix \mathcal{G} satisfy

$$G(\mathbf{k}, i\omega_n)^\dagger = G(\mathbf{k}, -i\omega_n) \quad \bar{G}(\mathbf{k}, i\omega_n) = -G(-\mathbf{k}, -i\omega_n)^T \quad (5.60a)$$

$$\bar{F}(\mathbf{k}, i\omega_n) = F(\mathbf{k}, -i\omega_n)^\dagger \quad F(\mathbf{k}, i\omega_n) = -F(-\mathbf{k}, -i\omega_n)^T. \quad (5.60b)$$

Similarly, we may collect the relevant boson operators in the system in a spinor. For the case of phonon-mediated superconductivity, this is trivial, as the spinor has only one element per phonon mode. In general, however, the spinor may have several elements. In Paper [4], the boson spinor takes the form

$$B_{\mathbf{q}} = \left(M_{\mathbf{q}}^R \quad (M_{-\mathbf{q}}^R)^\dagger \quad M_{\mathbf{q}}^U \quad (M_{-\mathbf{q}}^U)^\dagger \right)^T, \quad (5.61)$$

with magnon operators $M_{\mathbf{q}}^R$ and $M_{\mathbf{q}}^U$ as discussed in further detail there.

The interaction Hamiltonian in Eq. (5.48) can furthermore be symmetrized in particle and hole operators by letting

$$c_{\mathbf{k}'\sigma'}^\dagger c_{\mathbf{k}\sigma} \rightarrow \frac{1}{2} \left(c_{\mathbf{k}'\sigma'}^\dagger c_{\mathbf{k}\sigma} - c_{\mathbf{k}\sigma} c_{\mathbf{k}'\sigma'}^\dagger \right). \quad (5.62)$$

The interaction Hamiltonian itself can then be written on the symmetrized form⁶

$$H_{\text{el-b}} \rightarrow H_{\text{el-b}}^s = \frac{1}{2} \sum_{\mathbf{k}\mathbf{q}} \sum_{\alpha\beta\gamma} g_{\mathbf{k},\mathbf{k}+\mathbf{q}}^{\alpha\beta,\nu} B_{\mathbf{q}\nu} \psi_{\mathbf{k}+\mathbf{q},\alpha}^\dagger \psi_{\mathbf{k}\beta}, \quad (5.63)$$

where the indices α, β denote elements in the electron spinor, and the index ν elements in the boson spinor.

5.2.4 S -matrix expansion

Having introduced the model and spinor and matrix representations for operators and Green's functions, we are now ready to develop an S -matrix expansion for the electron Green's function using many-body perturbation theory. Useful references on the topic are provided by Refs. [6, 118, 119].

Within many-body perturbation theory, the electron Green's function can be written

⁶At this point, it may not be entirely clear why we choose to symmetrize the Hamiltonian and write it on this form. Furthermore, it may look like fermion anticommutation relations should give an additional term. In reality, however, we are simply preparing for an S -matrix expansion. Using Wicks theorem in the S -matrix expansion, fermion operators can be switched without introducing additional anticommutators.

$$\mathcal{G}(\mathbf{k}, \tau) = -\frac{\langle T_\tau \psi_{\mathbf{k}}(\tau) \psi_{\mathbf{k}}^\dagger(0) S(\beta, 0) \rangle_0}{\langle S(\beta, 0) \rangle_0}, \quad (5.64)$$

where $\psi_{\mathbf{k}}$ is the Nambu spinor defined above, and S is the so-called S -matrix. With interaction Hamiltonian $H_{\text{int}}(\tau)$ in the interaction picture, it can be written

$$S(\tau, 0) = \sum_n \frac{(-1)^n}{n!} \int_0^\tau d\tau_1 \cdots d\tau_n T_\tau [H_{\text{int}}(\tau_1) \cdots H_{\text{int}}(\tau_n)], \quad (5.65)$$

and corresponds to the time evolution operator in the interaction picture. The thermal average should be evaluated with respect to the non-interacting Hamiltonian, which is quadratic. Thus, we may use Wick's theorem to contract operators in the expansion for the Green's function. This allows us to represent the Green's function as a diagrammatic expansion.

As usual in many-body perturbation theory, the disconnected diagrams in the numerator of Eq. (5.64) cancel against the denominator, and we may write

$$\mathcal{G}(\mathbf{k}, \tau) = -\langle T_\tau \psi_{\mathbf{k}}(\tau) \psi_{\mathbf{k}}^\dagger(0) S(\beta, 0) \rangle_0^{\text{con}}, \quad (5.66)$$

where the superscript “con” indicates that only connected contributions are allowed into the propagator expansion.

As shown in Fig. 5.3 (a), we may represent electron Green's functions by solid lines and boson Green's functions by dashed lines, where single lines denote non-interacting Green's functions and double lines the corresponding interacting Green's functions. Furthermore, an electron-boson interaction is indicated by a dot.

By combining the incoming and outgoing electron operators in a propagator with electron operators from the interactions, and combining the boson operators in the interactions with each other, we may obtain Feynman diagram contributions to the interacting Green's function. The complete expansion for the electron and boson propagators can then be collapsed into the compact forms shown in Fig. 5.3 (b) and (c). From this, we obtain

$$\mathcal{G}(k) = \mathcal{G}_0(k) + \mathcal{G}_0(k) \Sigma(k) \mathcal{G}(k) \quad (5.67a)$$

$$D(q) = D_0(q) + D_0(q) \Pi(q) D(q), \quad (5.67b)$$

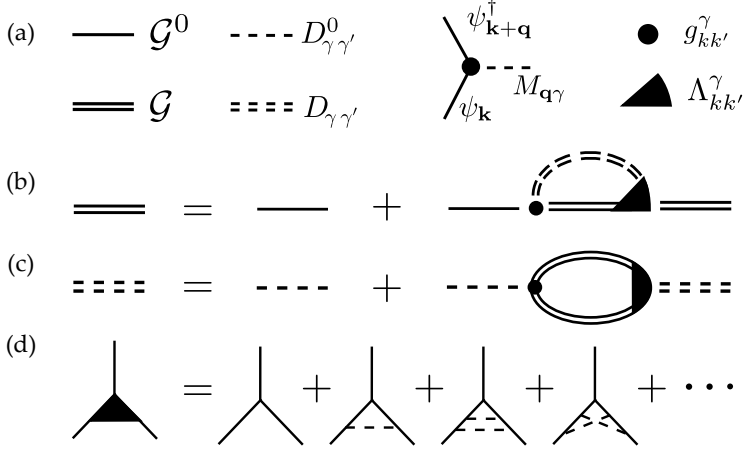


Figure 5.3: Feynman diagram expansion in terms of matrix Green's functions and vertices. (a) Electron and phonon Green's functions, interaction, and interaction vertices. (b) Electron Green's function expansion. (c) Boson Green's function expansion. (d) Diagram expansion for the renormalized vertex.

where $k = (\mathbf{k}, i\omega_n)$ and $q = (\mathbf{q}, i\nu_m)$, \mathcal{G}_0 and D_0 denote the unperturbed electron and boson Green's functions, and we have introduced electron self-energy $\Sigma(k)$ and polarization $\Pi(q)$ given by

$$\Sigma(k) = -\frac{1}{\beta} \sum_q \sum_{\gamma\gamma'} D_{\gamma\gamma'}(q) g_{\mathbf{k}, \mathbf{k}+\mathbf{q}}^\gamma \mathcal{G}(k+q) \Lambda_{\mathbf{k}+\mathbf{q}, \mathbf{k}}^{\gamma'} \quad (5.68)$$

$$\Pi_{\gamma\gamma'}(q) = \frac{1}{4\beta} \sum_k \text{Tr} \left[g_{\mathbf{k}, \mathbf{k}+\mathbf{q}}^\gamma \mathcal{G}(k+q) \Lambda_{\mathbf{k}+\mathbf{q}, \mathbf{k}}^{\gamma'} \mathcal{G}(k) \right]. \quad (5.69)$$

Here, we have introduced a renormalized vertex $\Lambda_{kk'}^\gamma$, which has a diagram expansion as shown in Fig. 5.3 (d). Both the self-energy, the electron Green's functions, and the coupling g are matrices in the electron indices, which we have suppressed in the notation, while we keep the boson indices explicit to avoid confusion between electron and boson matrix operations. The trace in the definition of the polarization runs over electronic indices.

The latter two equations are referred to as the self-consistent equations, and together with the Dyson equations in Eq. (5.67) and the diagram expansion

sion for the renormalized vertex⁷, they can be used to determine the electron and boson Green's functions.

So far, we have assumed that we only have normal and anomalous correlations, and that other correlations which may in principle occur from spontaneous symmetry breaking are zero. Apart from this, however, our equations are still exact. They do, however, represent very complicated integral equations.

In Sec. 5.2.8, we argue that the renormalized vertex can be replaced by the bare vertex $g_{\mathbf{k}\mathbf{k}'}^{\gamma'}$ within phonon-mediated superconductivity. This is known as Migdal's theorem, although it is by no means exact. In the following, we also assume that boson propagator renormalization is insignificant, so that we may use the unperturbed Green's function $D_{\gamma\gamma'}^0$ in the self-consistent equation for the electron self-energy. Then, the self-consistent equation

$$\Sigma(k) = -\frac{1}{\beta} \sum_q \sum_{\gamma\gamma'} D_{\gamma\gamma'}^0(q) g_{\mathbf{k},\mathbf{k}-\mathbf{q}}^{\gamma} \mathcal{G}(k-q) g_{\mathbf{k}-\mathbf{q},\mathbf{k}}^{\gamma'}, \quad (5.70)$$

determines the electron Green's function together with the Dyson equation

$$\mathcal{G}^{-1}(k) = \mathcal{G}_0^{-1}(k) - \Sigma(k) \quad (5.71)$$

relating Σ and \mathcal{G} .

5.2.5 Phonon-mediated superconductivity

So far, our discussion has been general and applies to superconductivity mediated by any boson with electron-boson coupling on the form in Eq. (5.48). While in Paper [4], we discuss magnon-mediated superconductivity, we here specialize to phonon-mediated superconductivity. The procedure to derive the Eliashberg equations is perfectly analogous for the two cases, but the details are somewhat different, and we comment on some of these differences in Chapter 8.

For electron-phonon coupling, the interaction Hamiltonian is given by

$$H_{\text{int}} = \sum_{\mathbf{k}\mathbf{q}\sigma} g_{\mathbf{k},\mathbf{k}+\mathbf{q}} A_{\mathbf{q}} c_{\mathbf{k}+\mathbf{q},\sigma}^{\dagger} c_{\mathbf{k}\sigma}, \quad (5.72)$$

where we have introduced the operator $A_{\mathbf{q}} = a_{\mathbf{q}} + a_{-\mathbf{q}}^{\dagger}$. Explicit calculation of the corresponding phonon propagator then gives [6]

⁷The diagram expansion for the renormalized vertex can also be expressed as an integral equation [83], but we do not discuss this in further detail here.

$$D_0(\mathbf{q}, i\nu_m) = -\frac{2\omega_{\mathbf{q}}}{\nu_m^2 + \omega_{\mathbf{q}}^2}. \quad (5.73)$$

Introducing again the Nambu spinor $\psi_{\mathbf{k}}$, the symmetrized Hamiltonian takes the form

$$H_{\text{int}}^s = \sum_{\mathbf{k}\mathbf{q}} \sum_{\alpha\beta} f_{\mathbf{k},\mathbf{k}+\mathbf{q}}^{\alpha\beta} A_{\mathbf{q}} \psi_{\mathbf{k}+\mathbf{q},\alpha}^\dagger \psi_{\mathbf{k},\beta} \quad (5.74)$$

with electron-phonon coupling matrix

$$f_{\mathbf{k},\mathbf{k}+\mathbf{q}}^{\alpha\beta} = \frac{1}{2} \begin{pmatrix} g_{\mathbf{k},\mathbf{k}+\mathbf{q}} & 0 & 0 & 0 \\ 0 & g_{\mathbf{k},\mathbf{k}+\mathbf{q}} & 0 & 0 \\ 0 & 0 & -g_{-\mathbf{k}-\mathbf{q},-\mathbf{k}} & 0 \\ 0 & 0 & 0 & -g_{-\mathbf{k}-\mathbf{q},-\mathbf{k}} \end{pmatrix}. \quad (5.75)$$

Assuming the system to be time reversal symmetric, the electron-phonon coupling matrix element satisfies the symmetry relations $g_{-\mathbf{k}',-\mathbf{k}} = (g_{\mathbf{k}',\mathbf{k}})^*$ and $g_{\mathbf{k}\mathbf{k}'} = g_{\mathbf{k}'\mathbf{k}}^*$. Thus, the electron-phonon coupling matrix can be written

$$f_{\mathbf{k},\mathbf{k}+\mathbf{q}} = g_{\mathbf{k},\mathbf{k}+\mathbf{q}} \tau_3 \sigma_0. \quad (5.76)$$

Inserting into the self-consistent equation, the self-consistent equation takes the form

$$\Sigma(k) = -\frac{1}{\beta} \sum_{\mathbf{q}} |g_{\mathbf{k},\mathbf{k}-\mathbf{q}}|^2 D_0(q) \tau_3 \mathcal{G}(k-q) \tau_3, \quad (5.77)$$

which is the usual self-consistent equation in Eliashberg theory [154].

5.2.6 Eliashberg equations

As a final step to derive the Eliashberg equations, we decompose the Green's function matrix into various terms with associated fields, and derive equations for these fields based on the self-consistent equation together with the Dyson equation.

To represent the Green's function, one may in general express it in terms of 4×4 basis matrices which span the Hermitian matrices⁸. A set of such basis matrices are the Pauli matrix outer products

⁸Although the Green's function itself is not Hermitian, we can still represent it in terms of Hermitian basis matrices by multiplying the Hermitian matrices with complex numbers. Subsequently, by using the symmetry relations for \mathcal{G} , it turns out that with our choice of basis, these complex numbers are either purely real or purely imaginary.

$$\tau_\alpha \otimes \sigma_\beta \quad \alpha, \beta \in \{0, 1, 2, 3\}, \quad (5.78)$$

with Pauli matrices τ_α acting on the particle/hole and σ_β acting on the spin degree of freedom. In general, we can construct 16 different such basis matrices, but for simplicity, we assume that the self-energy takes the form

$$\Sigma(k) = [1 - Z(k)]i\omega_n\tau_0\sigma_0 + \chi(k)\tau_3\sigma_0 + \phi_s(k)\tau_2\sigma_2. \quad (5.79)$$

Here, Z corresponds to a spin-independent quasiparticle renormalization, while χ represents a quasiparticle energy shift. Furthermore, since σ_2 is antisymmetric in interchange of spin, ϕ_s represents a spin singlet anomalous pairing. From the symmetry relations in Eq. (5.60), these fields satisfy

$$Z(-k) = Z(k), \quad Z(\mathbf{k}, i\omega_n) = Z(\mathbf{k}, -i\omega_n)^*, \quad (5.80a)$$

$$\chi(-k) = \chi(k), \quad \chi(\mathbf{k}, i\omega_n) = \chi(\mathbf{k}, -i\omega_n)^*, \quad (5.80b)$$

$$\phi_s(-k) = \phi_s(k), \quad \phi_s(\mathbf{k}, i\omega_n) = \phi_s(\mathbf{k}, -i\omega_n)^*. \quad (5.80c)$$

From the electron self-energy, the Green's function can be obtained by utilizing the Dyson equation. While the non-interacting Green's function is given by

$$\mathcal{G}_0^{-1} = i\omega_n\tau_0\sigma_0 - \xi_{\mathbf{k}}\tau_3\sigma_0, \quad (5.81)$$

the inverse of \mathcal{G} becomes

$$\mathcal{G}^{-1} = \mathcal{G}_0^{-1} - \Sigma = i\omega_n Z\tau_0\sigma_0 - \tilde{\xi}_{\mathbf{k}}\tau_3\sigma_0 - \phi_s\tau_2\sigma_2, \quad (5.82)$$

where we have introduced $\tilde{\xi}_{\mathbf{k}} = \xi_{\mathbf{k}} + \chi(k)$. This is a 4×4 matrix which decomposes into two blocks of size 2×2 , and is easily inverted to obtain

$$\mathcal{G}(k) = \frac{1}{\Theta(k)} [i\omega_n Z(k) + \tilde{\xi}_{\mathbf{k}}\tau_3\sigma_0 + \phi_s(k)\tau_2\sigma_2], \quad (5.83)$$

where

$$\Theta(\mathbf{k}, i\omega_n) = [i\omega_n Z(k)]^2 - \tilde{\xi}_{\mathbf{k}}^2 - |\phi_s(k)|^2 \quad (5.84)$$

is the submatrix determinant.

The Eliashberg equations are simply non-linear equations in the fields $Z(k)$, $\chi(k)$, and $\phi_s(k)$ which can be obtained by inserting the decomposition

of \mathcal{G} and Σ into the self-consistent equation for phonon-mediated superconductivity in Eq. (5.77). Comparing term by term, one obtains

$$i\omega_n[1 - Z(k)] = -\frac{1}{\beta} \sum_{k'} \sum_{\nu} |g_{\mathbf{k}\mathbf{k}'}^{\nu}|^2 D_{\nu}(k - k') \frac{i\omega_{n'} Z(k')}{\Theta(k')} \quad (5.85a)$$

$$\chi(k) = -\frac{1}{\beta} \sum_{k'} \sum_{\nu} |g_{\mathbf{k}\mathbf{k}'}^{\nu}|^2 D_{\nu}(k - k') \frac{\xi_{\mathbf{k}'} + \chi(k')}{\Theta(k')} \quad (5.85b)$$

$$\phi_s(k) = +\frac{1}{\beta} \sum_{k'} \sum_{\nu} |g_{\mathbf{k}\mathbf{k}'}^{\nu}|^2 D_{\nu}(k - k') \frac{\phi_s(k')}{\Theta(k')}. \quad (5.85c)$$

Considering the more general case of spin triplet pairing, the diagonalization procedure would be somewhat more involved, as the 4×4 matrix would not decouple into two blocks. This is analogous to the discussion of the spin triplet pairing in BCS theory in Ref. [122]. In Chapter 8, we will be considering unpolarized spin triplet pairing, which corresponds to a term $\phi_t \tau_3 \sigma_3$ in the self energy. When only this triplet contribution is present, the analysis is again perfectly analogous to the spin singlet case, except for the symmetry relation satisfied by $\phi_t(k)$.

Contrary to the BCS gap equation, the Eliashberg equations are eigenvalue equations for fields which have both momentum and frequency dependence. While the BCS equation with the Fröhlich effective potential $V_{\mathbf{k}\mathbf{k}'}$ have relatively strong dependence on momentum due to resonances in the potential, however, this is not the case here, as the effective potential has been replaced by the frequency dependent phonon propagator instead.

The full Eliashberg equations can be solved numerically with detailed electron-phonon coupling matrix elements and phonon propagators [155–157], but this constitutes a heavy numerical problem. In the following, we therefore discuss how the equations can instead be reduced to an eigenvalue problem in Matsubara frequency by introducing Fermi surface averaged quantities. The quasiparticle renormalization $\chi(k)$ is small in typical superconductors, and at half-filling, it vanishes [154]. We therefore consider the equations only for the fields $Z(k)$ and $\phi_s(k)$.

Considering an *s*-wave superconductor, we furthermore assume that both $Z(k)$ and $\phi_s(k)$ are momentum independent. As shown in Refs. [83, 154, 158], the Fermi surface averaging procedure then gives Eliashberg equations

$$Z(i\omega_n) = 1 + \frac{\pi}{\beta\omega_n} \sum_{i\omega_{n'}} \frac{\lambda(i\omega_n - i\omega_{n'})}{\sqrt{(\omega_{n'}Z')^2 + |\phi'_s|^2}} \omega_{n'} Z' \quad (5.86a)$$

$$\phi_s(i\omega_n) = \frac{\pi}{\beta} \sum_{i\omega_{n'}} \frac{\lambda(i\omega_n - i\omega_{n'})}{\sqrt{(\omega_{n'}Z')^2 + |\phi'_s|^2}} \phi_s(i\omega_{n'}), \quad (5.86b)$$

where we have introduced

$$\lambda(i\omega_n - i\omega_{n'}) = -\frac{1}{N_F} \sum_{\mathbf{k}\mathbf{k}'\nu} \delta(\xi_{\mathbf{k}})\delta(\xi_{\mathbf{k}'}) |g'_{\mathbf{k}\mathbf{k}'\nu}|^2 D_\nu(\mathbf{k} - \mathbf{k}', i\omega_n - i\omega_{n'}). \quad (5.87)$$

This quantity can be interpreted as a frequency dependent Fermi surface averaged electron-phonon coupling strength, and reduces to the dimensionless electron-phonon coupling strength introduced in Chapter 4 for zero frequency.

5.2.7 Solving the Eliashberg equations

To solve the Eliashberg equations in Eq. (5.86), one may assume that only a finite number of frequencies are significant, and use an iterative procedure to calculate the Matsubara frequency dependence of the quasiparticle renormalization and anomalous pairing. To determine the critical temperature, however, we may linearize the equations in the anomalous pairing. Then, $Z(i\omega_n)$ can be calculated independently of $\phi(i\omega_n)$, and be used as input in the equation for $\phi(i\omega_n)$. Thus, we again have to solve a linear eigenvalue problem where the temperature has to be adjusted so that the largest eigenvalue is 1. This determines the critical temperature.

To gain some understanding of the Fermi surface averaged Eliashberg equations, it is useful to solve them with a simple model for the frequency dependent electron-boson coupling strength $\lambda(i\nu_m)$. Starting from the definition in Eq. (5.87), we assume that the superconducting pairing is dominated by a single phonon frequency, and that the electron-phonon coupling matrix element can be considered constant for these contributions. Thus, we assume that $\lambda(i\nu_m)$ takes the form [83]

$$\lambda(i\nu_m) = \frac{\lambda_0}{1 + \nu_m^2/\omega_E^2}, \quad (5.88)$$

where ω_E is the characteristic boson frequency and λ_0 is the value at $\nu_m = 0$.

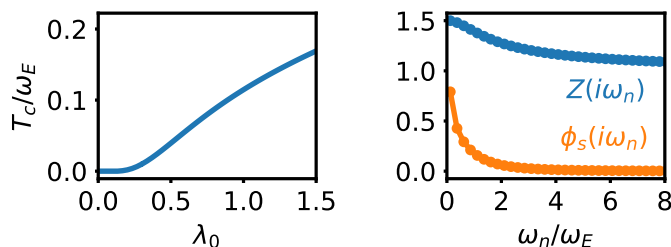


Figure 5.4: (a) Critical temperature as function of the electron-phonon coupling strength λ_0 in the Einstein model. (b) Matsubara frequency dependence of $Z(i\omega_n)$ and $\phi_s(i\omega_n)$ just below the critical temperature for $\lambda_0 = 0.5$.

Inserting this into the Eliashberg equations in Eq. (5.86), the critical temperature is shown in Fig. 5.4 (a), while the Matsubara frequency dependence of $Z(i\omega_n)$ and $\phi_s(i\omega_n)$ is shown in Fig 5.4 (b).

The procedure above is very convenient for determining the critical temperature, and in Paper [4], this is also what we are interested in. To extract further superconducting properties such as for instance the excitation gap, the heat capacity, and the isotope effect exponent, however, we also need the quasiparticle renormalization and the superconducting gap as function of real frequency. The usual way of obtaining real frequency Green's functions from Matsubara Green's functions is to perform analytic continuation of the Matsubara Green's function. This is simple when we know an analytic expression for the Matsubara Green's function. Here, however, we only know $Z(i\omega_n)$ and $\phi_s(i\omega_n)$ for a finite set of Matsubara frequencies. Thus, it is not immediately clear how the real frequency Green's functions can be obtained.

One option is to convert the Eliashberg equations into real frequency equations before we solve them. This procedure gives a set of integral equations for the gap and the quasiparticle renormalization [154, 159], which one may then go on to solve. However, it is also possible to deduce the real frequency dependence of the Green's function from the values at a finite set of Matsubara frequencies through the use of so-called Padé approximants [154].

When the real frequency gap function $\Delta(\omega)$ has been determined, one may determine the excitation gap Δ_e , by solving the equation

$$\Delta_e = \text{Re } \Delta(\omega = \Delta_e). \quad (5.89)$$

Experimentally, the excitation gap is accessible for instance through tunneling experiments [159, 160].

For a detailed review of superconducting properties such as the isotope effect, heat capacity and the “universal” amplitude ratio from an Eliashberg theory perspective, the reader should consult Refs. [92, 149, 159].

5.2.8 Migdal’s theorem

Eliashberg theory is based on many-body perturbation theory, and as always in many-body perturbation theory, we pick out our favourite self energy diagrams and throw away the rest. A natural question to ask is therefore how this is justified.

The question was first investigated Migdal [161], who formulated what we today know as Migdal’s theorem [6]. It is built on the observation that there are two different energy scales in the system; one relatively small characteristic boson energy ω_D , and one characteristic electron energy E_F , which is typically much larger. In the expansion for the renormalized vertex in Fig. 5.3 (d), we disregarded all diagrams beyond the first. Migdal argued that for electron-phonon coupled systems, the vertex corrections can be disregarded when the ratio ω_D/E_F is small. Thus, a time scale separation between the electron and phonon dynamics is an important precondition for Eliashberg theory to be valid, and also an important reason that BCS theory works so well.

Vertex correction estimate

In the following, we discuss Migdal’s argument in some more detail. To see whether the vertex corrections are important, one may try to evaluate the relative size of the zeroth and first order contributions to the renormalized vertex in Fig. 5.3 (d). Disregarding the momentum dependence of the electron-phonon coupling matrix element, this relative size can be estimated as

$$\Gamma_{k,k+q}^1 = \frac{1}{\beta} \sum_{q'} |g|^2 G(k+q') G(k+q+q') D(q'), \quad (5.90)$$

where the renormalized vertex is related to the lowest order relative contribution through $\Lambda_{kk'} = g_{kk'}(1 + \Gamma_{kk'})$, and the sum over q' runs over both momentum and frequency. To estimate this expression, we replace the interacting Green’s functions by their non-interacting counterparts, which are given by

$$G_0(\mathbf{k}, ik_n) = \frac{1}{ik_n - \xi_{\mathbf{k}}} \quad (5.91)$$

$$D_0(\mathbf{q}, iq_n) = -\frac{2\omega_{\mathbf{q}}}{q_n^2 + \omega_{\mathbf{q}}^2}, \quad (5.92)$$

where k_n and q_n denote fermionic and bosonic Matsubara frequencies. For Matsubara frequencies larger than typical phonon frequencies, the phonon propagator decays fast. Thus, we may assume that the dominant contributions to the above sum arise from Matsubara frequencies where $|q'_n| < \omega_D$, and this corresponds to roughly $\omega_D/2\pi T$ different frequencies. Since the typical energy scale for the electrons is E_F , we expect the vertex correction to be of order

$$\Gamma_{k,k+q}^1 \sim \frac{1}{\beta} |g|^2 \left(\frac{\omega_D}{2\pi T} \right) \left(\frac{1}{E_F^2} \right) \left(\frac{1}{\omega_D} \right) \sim \frac{|g|^2}{E_F^2}. \quad (5.93)$$

As one may realize by considering the definition of the dimensionless electron-phonon coupling strength in Eq. (4.41), the electron-phonon coupling matrix element $|g|^2$ is typically of order $|g|^2 \sim \lambda \omega_D E_F$. Thus, the relative importance of the lowest order vertex correction is of order

$$\Gamma_{k,k+q}^1 \sim \lambda \frac{\omega_D}{E_F}. \quad (5.94)$$

This quantity is typically small in superconductors with a phonon-based pairing mechanism. By a similar argument, we expect higher order vertex corrections to be of even higher order in this small quantity.

Above, we considered contributions to the renormalized vertex where the electron momenta for the Green's functions in Eq. (5.90) are in general far away from the Fermi surface. Thus, the Green's functions are typically of order $1/E_F$. Instead, we may consider processes with scattering momentum \mathbf{q}' such that the intermediate momenta $\mathbf{k} + \mathbf{q}'$ and $\mathbf{k} + \mathbf{q} + \mathbf{q}'$ are close to the Fermi surface, and the Green's functions are instead of order $1/\omega_D$. However, as illustrated in Fig. 5.5, this can only occur for a restricted set of momenta in the Brillouin zone. Letting $D_F = N_F/N$ be the intensive density of states and assuming \mathbf{k} and $\mathbf{k} + \mathbf{q}$ to lie on the Fermi surface, the momentum \mathbf{q}' can only be picked among a fraction $D_F \omega_D$ of the full Brillouin zone if we want one of the electron Green's functions in Eq. (5.90) to be on the Fermi surface, and within a fraction $(D_F \omega_D)^2$ to have both electron momenta close to the Fermi surface. Thus, nothing is gained by considering processes close to

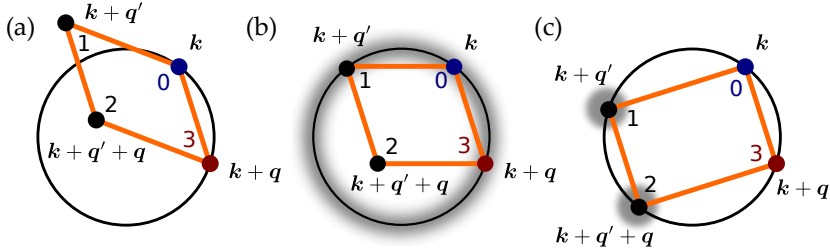


Figure 5.5: Hierarchy of processes contributing to lowest order vertex correction with momenta \mathbf{k} and $\mathbf{k} + \mathbf{q}$ on the Fermi surface (black circle). Points denote electron momenta, which vertices on a parallelogram due to conservation of momentum. (a) A general momentum \mathbf{q}' yields intermediate momenta far away from the Fermi surface. Restricting the momentum sum to the grey regions in (b) and (c) gives larger electron Green's functions, but contributions from fewer momenta.

the Fermi surface, and there is a hierarchy of processes which all contribute similarly to the vertex corrections.

Finally, we notice that the first order contribution to the renormalized vertex is small compared to the zeroth order contribution when the electron-boson coupling matrix element is small compared to the typical electron energy scale, as seen in Eq. (5.93). It is the relation $|g|^2 \sim \lambda\omega_D E_F$ which we expect with electron-phonon coupling which allows us to rewrite the estimate in terms of $\lambda\omega_D/E_F$, and which gives the most common formulation of Migdal's theorem.

Failure of Migdal's theorem

The argument above is not very rigorous, but it illustrates that vertex corrections will typically tend to be small. However, there are exceptions. In a qualitative picture, one may argue that vertex corrections are small because not all momenta are in general close to the Fermi surface when we choose \mathbf{q}' such that $\mathbf{k} + \mathbf{q}'$ is close to the Fermi surface, as shown in Fig. 5.5 (b). If this were actually the case, the argument would break down. In the following, we will be discussing two cases where this may be possible.

A simple example is the limit $\mathbf{q} \rightarrow 0$, when we let the outgoing momentum labelled by 3 in Fig. 5.6 (a) approach the incoming momentum labelled by 0. Estimating the vertex correction in Eq. (5.90), one may show that [162]

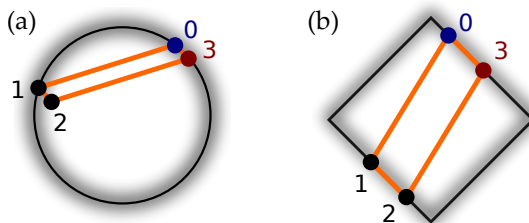


Figure 5.6: Situations where Migdal's theorem may break down. (a) Scattering with small momentum \mathbf{q} . (b) Strongly nested Fermi surface.

$$\Gamma(k, q \rightarrow 0) \sim \frac{N_F |g|^2}{\sqrt{(v_F q)^2 + q_m^2}}. \quad (5.95)$$

Qualitatively, this can be understood as follows: Compared with the estimate in Eq. (5.93), a factor $1/E_F$ has been replaced with $\sqrt{v_F^2 q^2 + q_m^2}$. By considering electrons at momenta \mathbf{k} and $\mathbf{k} + \mathbf{q}$ close to the Fermi surface, the dominant contributions come from the situation where $\mathbf{k} + \mathbf{q}'$ is also close to the Fermi surface. This is because the smallness of \mathbf{q} allows the electron at $\mathbf{k} + \mathbf{q}' + \mathbf{q}$ to be reasonably close to the Fermi surface without having to pay the cost of restricting the momentum sum any further. The typical energy scale of this last electron is therefore dominated either by its electronic energy of order $v_F q$ or the frequency $i q_m$ depending on their respective values. The square root interpolates between these two.

A second situation where Migdal's theorem may not hold, is when the Fermi surface is strongly nested, as shown in Fig. 5.6 (b). The nesting ensures the existence of a large set of momenta \mathbf{q} which allow us to pick \mathbf{q}' such that all electrons are close to the Fermi surface. Thus, the vertex correction is drastically enhanced. Nesting can often be a problem in low-dimensional systems, where nesting is more common.

5.3 Spin-fluctuation mechanism

With the development of Eliashberg theory, the properties of almost all known superconductors at the time could be understood⁹, and it was spec-

⁹An exception was the so-called A15 compounds [159, 163], which had, on the contemporary scale, rather large critical temperatures. However, superconductivity in these materials turned out to be due to strong electron-phonon coupling [93].

ulated that electron-phonon coupling is the cause of superconductivity in all superconductors [150]. Spin fluctuations, on the other hand, were only believed to suppress superconductivity [140, 164, 165].

In the 1980s, this view was drastically changed, primarily due the discovery superconductivity in two new classes of superconductors; heavy fermion compounds [108] and high- T_c cuprates [109].

Heavy fermion compounds have their name due to their very large effective mass, as observed through the rapid increase of specific heat with temperature [166, 167] at intermediate temperatures. This was believed to be caused by a Kondo effect [6, 168, 169], and can be described within the Kondo model [6]. There, coupling to spin fluctuations of local moments cause strong renormalization, and give rise to a minimum in the heat capacity and resistivity as function of temperature at the so-called Kondo temperature. This behaviour motivated detailed experimental studies of the low-temperature properties of heavy fermion systems [170]. An investigation of the resistivity, however, showed that in some materials, it instead dropped to zero below critical temperatures between 0.5 K and 2 K [108, 170, 171].

As the importance of spin fluctuations in heavy fermion systems was already well established through the behaviour of the specific heat, spin fluctuations were also a primary candidate as pairing glue for the observed superconductivity [170]. Heavy fermion superconductivity occurs in close proximity to antiferromagnetic order [172], and observations indicated that the gap amplitude had nodes on the Fermi surface [122, 173–175]. This behaviour was very similar to anisotropic pairing in Helium-3, where spin fluctuations had been identified as underlying mechanism [176]. Yet, it was clear that understanding superconductivity in heavy fermion materials was a huge challenge due to strong correlation effects. The large effective mass of the heavy electrons makes the characteristic electron energy scale small, and the time scale separation between the electrons and the bosons which allows BCS and Eliashberg theory to work so well is missing.

Although the discovery of heavy fermion superconductors was of significant theoretical interest, the technological implications were minute due to the small critical temperatures. In contrast, the discovery of high- T_c cuprates [109] not only reshaped known truths about superconductivity, but also represented a major technological advancement due to large critical temperatures quickly reaching beyond 100 K [109, 177–180]. It soon became clear that a phonon-mediated mechanism could not explain the enormous critical temperature within the standard theories of superconductivity [93, 181], and the spin fluctuation mechanism was a prime suspect [7]. Similar to heavy fermion compounds, superconductivity occurs in close prox-

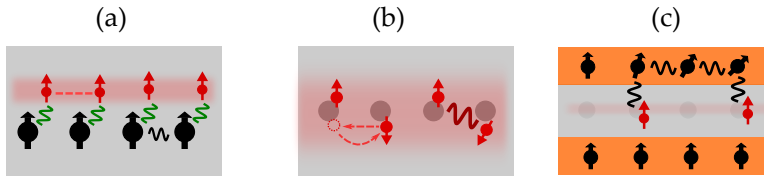


Figure 5.7: Spin-fluctuation mechanisms generating an effective electron-electron interaction. (a) Kondo lattice. s-d exchange generates RKKY interaction and magnetic order, around which localized spins may fluctuate. (b) Paramagnon mechanism in the Hubbard model. Electron repulsion generate short ranged antiferromagnetic spin correlations, around which electrons may fluctuate. (c) Heterostructure. Localized spins in a magnetic insulator may fluctuate around magnetic order.

imity to antiferromagnetically ordered phases. Furthermore, the pairing symmetry was shown to be d -wave [182], which again allowed parallels to Helium-3 to be drawn up [7, 181].

Although spin fluctuations are believed to play an important role in the superconductivity of both heavy fermion materials and high- T_c cuprates, the underlying nature of the spin fluctuations is presumably somewhat different, as illustrated in Fig. 5.7.

First as shown in Fig. 5.7 (a), heavy-fermion compounds can be described in terms of delocalized electrons interacting with localized spins through a so-called s-d exchange coupling [6, 172]. Through this interaction, the itinerant electrons can mediate an RKKY interaction between the localized spins [6, 183], which may give rise to antiferromagnetic order for a dense lattice [184, 185]. In turn, fluctuations of the localized spins around the antiferromagnetic order, typically entangled with spin fluctuations of the electrons themselves [172, 186], may then mediate an effective interaction between the electrons.

Second, a spin fluctuation mechanism which may possibly cause superconductivity in high- T_c materials is illustrated in Fig. 5.7 (b), and is due to spin fluctuations in the spins of the electrons themselves. Strong electronic repulsion may generate short range antiferromagnetic order, and spin fluctuations on top of this order can mediate an effective interaction between electrons, which may cause superconductivity. This is often referred to as the paramagnon mechanism, and the paradigmatic Hubbard model is believed to contain this behaviour [187].

There has been significant efforts in understanding superconductivity in

high- T_c cuprates through spin fluctuation mechanisms [7, 12, 13, 187], and a number of other mechanisms have also been proposed [93, 153]. However, there is still no consensus even on the fundamental mechanism causing superconductivity in the cuprates [7, 93]. Quite simply, a microscopic theory for superconductivity in heavy fermion superconductors and high- T_c cuprates is still missing [7, 188].

Regardless of the true nature of superconductivity in heavy fermion compounds and high- T_c cuprates, spin-fluctuation mediated superconductivity is of great fundamental interest. A somewhat different context where it may in principle occur, is in heterostructures of magnetically ordered insulators proximity coupled to a normal metal. There, as shown in Fig. 5.7 (c), localized spins within a magnetic insulator may fluctuate to give rise to an effective interaction between the electrons in an adjacent normal metal. We will be studying such a system in Paper [4], and discuss this in more detail in Chapter 8.

Chapter 6

Topological magnons

In Chapter 3, we primarily discussed topological classification of electronic band structures. However, as pointed out in Sec. 3.4, the topological classification of band structures can equally well be applied also to bosonic band structures. Thus, the concept of topology may also provide insight into the physics of collective excitations in magnetic systems, which can often be described in terms of bosons.

A magnetic insulator modelled by some spin model will have a ground state, and may host excitations on top of the ground state. As we have already discussed, there are several ways to describe these spin excitations, and the suitability of each of these descriptions may depend on the properties of the system. In Paper [1], we will be considering the fluctuations on top of a ferromagnetically ordered state, and we will therefore be working within linear spin wave theory in this chapter. However, the excitations of magnetic systems may also be classified according to their topology within alternate descriptions.

Today, several model systems exist which are known to host topological magnon band structures [36, 67]. Kagomé and pyrochlore lattices have received much attention [189–194] motivated by the experimental discovery of a thermal Hall effect in similar systems [70, 195, 196]. Furthermore, models with topological magnons have also been investigated on honeycomb [32, 197, 198], Lieb [199] and Shastry-Sutherland [200, 201] lattices. The typical mechanism for generating the topologically non-trivial band structure in these systems is the Dzyaloshinskii-Moriya interaction discussed in Sec. 2.4. Since the Dzyaloshinskii-Moriya interaction may also give rise to exotic spin textures such as skyrmion crystals, there has also been significant

interest in systems with such non-collinear magnetic order [202–204]. However, topological magnons may also occur due to other interactions, such as the Kitaev interaction [205, 206], dipolar interactions [207, 208], or exchange couplings in non-coplanar spin textures [209]. Topology can also be used to classify gapless magnetic systems hosting Dirac cones [210, 211], analogous to Weyl semimetals [212].

It should by now be clear that topology is a useful tool to study the properties of magnon band structures, and that a multitude of models displaying topologically non-trivial band structures are known. The challenge is therefore rather to identify fingerprints of topology in magnon band structures through observable quantities.

The topological nature of the bands is typically manifest in two main properties. First, topological magnon band structures may give rise to various Hall conductivities [213]. Yet, since the the Hall conductivity is not quantized, it cannot uniquely identify a topologically non-trivial band structures as underlying cause [214], as finite Hall conductivities can for instance arise in systems which are magnetically disordered and topologically trivial [215].

The second main property of topologically non-trivial systems is the presence of edge modes. However, the direct observation of these with usual techniques such as inelastic X-ray and neutron scattering is very challenging due to the surface nature of the modes [36]. Both experimental progress and new ideas therefore seem necessary to establish direct proof of the topological nature of magnon band structures.

In this chapter, we discuss topological magnons, and start with a discussion of magnon Hall conductivities in Sec. 6.1. We then proceed to construct a topologically non-trivial spin model in Sec. 6.2. Finally, we couple topological magnons to phonons in Sec. 6.3, and discuss the main results of Paper [1].

6.1 Hall conductivities

In electronic systems, it was the observation of Hall conductivities that motivated the classification of electronic band structures according to their topology. It is therefore also natural to investigate if Hall conductivities in magnetic systems may also contain information about the topology of excitation bands. In electronic systems, the Hall conductivity we refer to is the transverse transport of charge due to an electric field. For magnetic systems, the first question we have to ask is what kind of driving we should subject

the system to, and which response we are looking for.

Charge in an electronic system is measured by the number operator $n_i = c_i^\dagger c_i$. In a spin system, it is therefore natural to think of the \hat{z} -component of the spin, $S_i^z = S - a_i^\dagger a_i$ in the Holstein-Primakoff representation, as the analog of charge in the spin system. Furthermore, an electric field can be generated by a potential energy term on the form $V = \sum_i V_i c_i^\dagger c_i$, where V_i describes a potential gradient across the sample. Similarly, the analog of an electric field in the magnetic system is therefore a magnetic field gradient. In the following, we therefore consider transverse spin currents generated by magnetic field gradients. The associated Hall effect is some times referred to as the magnon spin Hall effect [213].

Applying a magnetic field gradient $\partial_y B$, we expect a spin current j_x related to the applied magnetic field gradient through the linear relation

$$j_x = \sigma_{xy}(\partial_y B), \quad (6.1)$$

where σ_{xy} is the transverse Hall conductivity for the magnon spin Hall effect.

It should however be pointed out that other Hall effects have received equally much or more attention within topological magnetic systems. In addition to subjecting the system to a magnetic field gradient, we may subject it to a temperature gradient and study the transport of both spin and heat. Generally, the response in spin currents j_μ and heat currents j_μ^E due to magnetic field gradients $\partial_\nu B$ or a thermal gradient $\partial_\nu T$ can then be written as the linear relation

$$\begin{pmatrix} j_x \\ j_x^E \end{pmatrix} = \begin{pmatrix} L_{11}^{xy} & L_{12}^{xy} \\ L_{21}^{xy} & L_{22}^{xy} \end{pmatrix} \begin{pmatrix} \partial_y B \\ \partial_y (1/T) \end{pmatrix}. \quad (6.2)$$

Hence, we may generate both spin currents and heat currents by applying either a magnetic field gradient or a temperature gradient through various Hall effects. In addition to the magnon spin Hall effect discussed above, spin currents can be generated by a temperature gradient through the magnon Nernst effect, while generating a heat current through a temperature gradient is referred to as the thermal magnon Hall effect. Both the thermal Hall effect [70, 195, 196, 216–218] and the magnon Nernst effect [219] have been measured experimentally.

To compute the response of a weak perturbation in a quantum system, the standard method is to use linear response theory [220]. In the following, we use it to derive an expression for the matrix element L_{11}^{xy} , which we also denote by σ_{xy} . We remark, however, that when considering the response

due to a temperature gradient, a complication arises because the temperature gradient cannot strictly speaking be described by adding a term in the Hamiltonian. Instead, as pointed out in Refs. [221, 222], it is a statistical force. To account for this, the remaining matrix elements in the transverse conductivity matrix can for instance be calculated using Luttinger's pseudo-gravitational field method [83, 223, 224].

Within the context of electronic systems, we used linear response theory to derive the Kubo formula for the Hall conductivity, and by manipulating this formula, it was possible to show that the conductivity was related to the Berry curvature and the Chern number. Here, we establish a similar link through an analogous procedure. We first discuss the identification of the spin current in Sec. 6.1.1, before discussing the Kubo formula and the relation to Berry curvatures and Chern numbers in Sec. 6.1.2.

6.1.1 Spin currents

We consider a ferromagnetically ordered magnetic system described by a spin Hamiltonian H consisting of single spin terms and two-spin interactions. Furthermore, we assume that spin along the \hat{z} -direction is conserved. This is not always the case, but does hold for the spin Hamiltonian in Paper [1].

In the Heisenberg picture, the spin component S_i^z on lattice site i satisfies the Heisenberg equation of motion¹

$$\frac{dS_i^z}{dt} - \frac{i}{\hbar}[H, S_i^z] = 0. \quad (6.3)$$

Since we have assumed the Hamiltonian to conserve the quantity $S^z = \sum_i S_i^z$, this equation of motion can be interpreted as a continuity equation²

$$\dot{S}_i^z + \sum_{\delta} j_{i, i+\delta} = 0, \quad (6.4)$$

where $j_{i \rightarrow i+\delta}$ is the spin current flowing from lattice site i to lattice site $i + \delta$. This allows us to identify expressions for the spin currents $j_{i \rightarrow i+\delta}$ in terms of the spin operators, and to obtain an expression for the local spin current density vector

$$\mathbf{j}_i = \frac{1}{V_{\text{uc}}} \sum_{\delta} j_{i \rightarrow i+\delta} \delta, \quad (6.5)$$

¹Assuming the spin Hamiltonian does not contain any explicit time dependence.

²If H does not conserve S^z , we would in addition get source and drain terms in the equation below.

where V_{uc} is the unit cell volume.

Within linear spin wave theory, the magnon Hamiltonian takes the form

$$H = \sum_{\mathbf{q}} \sum_{\alpha\beta} h_{\alpha\beta}(\mathbf{q}) a_{\mathbf{q}\alpha}^\dagger a_{\mathbf{q}\beta}, \quad (6.6)$$

where α and β describe the sublattice degree of freedom. Yet again, we also introduce the velocity matrix

$$v_{\mu}^{\alpha\beta}(\mathbf{q}) = \frac{1}{\hbar} \left(\frac{\partial h_{\alpha\beta}}{\partial q_{\mu}} \right). \quad (6.7)$$

Expressing also the spin currents in terms of magnon operators to quadratic order in linear spin wave theory, we show in Appendix A that the total spin current $\mathbf{j}(\mathbf{q} = 0) = (1/\sqrt{N}) \sum_i \mathbf{j}_i$ can be expressed as

$$j_{\mu}(\mathbf{q} = 0) = \frac{1}{V_{\text{uc}}\sqrt{N}} \sum_{\mathbf{q}} \sum_{\alpha\beta} \left(\frac{\partial h_{\alpha\beta}}{\partial q_{\mu}} \right) a_{\mathbf{q}\alpha}^\dagger a_{\mathbf{q}\beta}. \quad (6.8)$$

Apart from the prefactor, this expression matches the expression for the electronic current. Eventually, it will allow us to express the Hall conductivity in terms of the Berry curvature of the magnon bands.

6.1.2 Transverse conductivities

In the electronic case, we calculated the Hall conductivity by subjecting the system to an oscillating electric field through an electromagnetic vector potential. Since the vector potential couples directly to the electric current in the Hamiltonian, this immediately allowed us to express conductivity as a current-current response function.

In the present case, the link between the Kubo formula and the current-current correlation function is less clear, as there is no obvious ways to represent a magnetic field gradient in terms of some effective vector potential. To show that the conductivity can still be represented as a correlation between two spin currents, we therefore choose an alternate approach invented by Luttinger in the context of electronic systems [83, 224].

To calculate the Hall conductivity, we subject the system to a perturbation

$$H' = - \sum_i h_i^z(t) S_i^z \quad (6.9)$$

with temporally and spatially dependent magnetic field $h_i^z(t)$. Eventually, we consider the magnetic field to be time independent, but keep the time dependence for now.

Using linear response theory for the local spin current

$$j_\gamma(l, t) = \frac{1}{V_{\text{uc}}} \sum_{\delta} \dot{j}_{l \rightarrow l+\delta}(\delta \cdot \hat{\gamma}) \quad (6.10)$$

on lattice site l at time t and in direction $\hat{\gamma}$, we obtain

$$\langle j_\gamma(l, t) \rangle = - \sum_j \frac{1}{\hbar} \int_{-\infty}^{\infty} dt' \chi(l, j; t-t') h_j^z(t') \quad (6.11)$$

with response function [220]

$$\chi_\gamma(l, m, t-t') = i\Theta(t-t') \langle [j_\gamma(l, t), S_m^z(t')] \rangle. \quad (6.12)$$

Performing the temporal Fourier transform, cleverly writing

$$e^{i\omega t} = (1/i\omega)(d/dt)e^{i\omega t} \quad (6.13)$$

and using partial integration, one may rewrite the correlation function in terms of a time derivative of S_m^z . Furthermore, this time derivative can be replaced by spin currents through the continuity equation. By carefully carrying out these steps and taking the limit $\mathbf{q} \rightarrow 0$, the transverse conductivity can be extracted from the response function, and this gives

$$\sigma_{xy} = \frac{V_{\text{uc}}}{\hbar\omega} \int_0^{\infty} dt e^{i\omega t} \langle [j_x(\mathbf{q}=0, t), j_y(-\mathbf{q}=0, 0)] \rangle. \quad (6.14)$$

This is the Kubo formula for the magnon spin Hall effect, which is on exactly the same form as in the electronic case.

In Appendix A, we show that this Kubo formula for bosonic modes can be expressed as

$$\sigma_{xy} = \frac{\hbar}{V_{\text{uc}}} \sum_{\mathbf{q}} \sum_{\alpha\beta} n_B(E_{\mathbf{q}\alpha}) [1 + n_B(E_{\mathbf{q}\beta})] \mathcal{F}^{\alpha\beta}(\mathbf{q}) \quad (6.15)$$

in terms of an antisymmetric curvature tensor

$$\mathcal{F}^{\alpha\beta}(\mathbf{q}) = i\hbar^2 \frac{\tilde{v}_x^{\alpha\beta} \tilde{v}_y^{\beta\alpha} - \tilde{v}_y^{\alpha\beta} \tilde{v}_x^{\beta\alpha}}{(E_{\mathbf{q}\alpha} - E_{\mathbf{q}\beta})^2}, \quad (6.16)$$

where $\tilde{v}_\mu^{\alpha\beta}(\mathbf{q})$ are the velocity matrix elements in the eigenmagnon basis. These are related to the velocity matrix elements $v_\mu^{\rho\sigma}(\mathbf{q})$ in the sublattice basis through

$$\tilde{v}_\mu^{\alpha\beta}(\mathbf{q}) = U_{\alpha\rho}^\dagger(\mathbf{q})v_\mu^{\rho\sigma}(\mathbf{q})U_{\sigma\beta}(\mathbf{q}), \quad (6.17)$$

where $U_{\alpha\beta}(\mathbf{q})$ is the unitary matrix which diagonalizes $h(\mathbf{k})$.

Compared with the electronic result in Eq. (3.15), we see that the Fermi distribution factors in the Hall conductivity expression have been replaced with Bose distribution factors according to the replacement

$$n_F(E_{\mathbf{q}\alpha})[1 - n_F(E_{\mathbf{q}\beta})] \rightarrow n_B(E_{\mathbf{q}\alpha})[1 + n_B(E_{\mathbf{q}\beta})]. \quad (6.18)$$

In the following, we assume that the temperature is small. Then, the occupation numbers of the states contributing to the Hall conductivity are small, and we may neglect the term proportional to two Bose distributions. As also shown in Appendix A, this allows us to identify the quantity $\sum_{\beta \neq \alpha} \mathcal{F}^{\alpha\beta}(\mathbf{q})$ with the Berry curvature $\Omega^\alpha(\mathbf{q})$ introduced in Eq. (3.20). The transverse conductivity then becomes

$$\sigma_{xy} = \frac{\hbar}{V_{\text{uc}}} \sum_{\mathbf{q}} \sum_{\alpha} n_B(E_{\mathbf{q}\alpha}) \Omega^\alpha(\mathbf{q}), \quad (6.19)$$

and is calculated as an average of the Berry curvature over the Brillouin zone weighted with the bosonic thermal occupation numbers. Contrary to a Fermi distribution with chemical potential inside a band gap, the Bose distribution weights the states in a band differently. Therefore, we cannot in general relate the Hall conductivity to the Chern number, and there is no quantization of conductance. However, the Hall conductivity still does provide information about the Berry curvature of the band structure, which is again intimately connected with its topology.

6.2 A magnon Haldane model

In this section, we argue our way to a spin Hamiltonian with a topologically non-trivial magnon band structure.

A band structure can be thought of as a mapping from the Brillouin zone to the Hilbert space corresponding to a quasimomentum \mathbf{q} . Since we need this mapping to be topologically non-trivial, we need a two-band system. In one dimension, a natural place to start would therefore be a dimerized spin chain. In two-dimensions, a natural starting point is the honeycomb

lattice, which has a triangular Bravais lattice and two atoms in the basis. Considering this in the following, we may next ask whether it is possible to construct a spin model giving rise to a magnon analog of the Haldane model [51]. In the following, we reverse-engineer such a spin model [197, 225].

The Haldane model consists of three terms. First, it has a hopping term between nearest neighbours on the lattice. Second, we have a staggered potential term. Third, we have a next-to-nearest neighbour hopping term associated with a phase on the links. Finally, we can also think of the Haldane model as having a chemical potential which has been set to zero, so that the term does not appear explicitly in the Hamiltonian. We now have to come up spin interactions giving rise to these terms.

In Chapter 2, we have already seen that for the excitations on top of a ferromagnet, an exchange interaction gives rise to hopping terms similar to the electron nearest-neighbour hoppings in the Haldane model. Furthermore, a potential energy term in the Hamiltonian can be obtained by coupling the Hamiltonian to a magnetic field oriented along the \hat{z} -direction.

As a starting point, we may therefore write down a ferromagnetic Heisenberg Hamiltonian on the honeycomb lattice, which takes the form

$$H_m^0 = -J \sum_{\langle i,j \rangle} \mathbf{S}_i \cdot \mathbf{S}_j - \mathcal{B} \sum_i S_i^z. \quad (6.20)$$

Assuming magnetic order in the \hat{z} -direction and introducing the linearized Holstein-Primakoff representation, we obtain the bosonic hopping Hamiltonian

$$H_m^0 = (3JS + \mathcal{B}) \sum_i d_i^\dagger d_i - JS \sum_{\langle ij \rangle} (d_i^\dagger d_j + \text{h.c.}). \quad (6.21)$$

Thus, we already have almost all the terms we need, and the only remaining term is the Haldane hopping. What does a spin interaction corresponding to that term look like?

We know that the magnon creation and annihilation operators in linear spin wave theory correspond to spin raising and lower operators, so a spin interaction which gives rise to the Haldane hopping term can be written on the form

$$H_m^T = -\frac{\mathcal{D}}{2} \sum_{\langle\langle ij \rangle\rangle} (e^{i\nu_{ij}\phi} S_i^- S_j^+ + e^{-i\nu_{ij}\phi} S_j^- S_i^+), \quad (6.22)$$

where $-\mathcal{D}$ is some constant and ν_{ij} is the Haldane sign introduced in Chapter 3. Rewritten in terms of Cartesian spin components, this gives

$$H_m^T = -\mathcal{D} \cos \phi \sum_{\langle\langle ij \rangle\rangle} \mathbf{S}_i \cdot \mathbf{S}_j + \mathcal{D} \sin \phi \sum_{\langle\langle ij \rangle\rangle} \nu_{ij} \hat{z} \cdot \mathbf{S}_i \times \mathbf{S}_j. \quad (6.23)$$

Thus, the spin interaction which produces the Haldane hopping with phase ϕ is a combination of an exchange interaction and a Dzyaloshinskii-Moriya interaction on the next-to-nearest neighbour lattice sites.

For simplicity, we disregard the next-to-nearest neighbour exchange coupling in the following, corresponding to $\phi = \pi/2$. The full spin model analog of the Haldane model is then

$$H_m = -J \sum_{\langle i,j \rangle} \mathbf{S}_i \cdot \mathbf{S}_j + \mathcal{D} \sum_{\langle\langle i,j \rangle\rangle} \nu_{ij} \hat{z} \cdot \mathbf{S}_i \times \mathbf{S}_j - \mathcal{B} \sum_i S_i^z. \quad (6.24)$$

After introducing the Holstein-Primakoff transformation to linear order in magnon operators, the real space magnon Hamiltonian therefore takes the form

$$H_0 = (3JS + \mathcal{B}) \sum_i d_i^\dagger d_i - JS \sum_{\langle ij \rangle} (d_i^\dagger d_j + \text{h.c.}) - \mathcal{D} S \sum_{\langle\langle ij \rangle\rangle} (i\nu_{ij} d_i^\dagger d_j + \text{h.c.}). \quad (6.25)$$

This is nothing else to the Haldane model in Eq. (3.31) for $\phi = \pi/2$, where the nearest neighbour exchange coupling J plays the role of the nearest neighbour hopping, and the Dzyaloshinskii-Moriya interaction strength is associated with the next-to-nearest neighbour Haldane hopping. The onsite potential term proportional to $(3JS + \mathcal{B})$ shifts the energy, but does not affect the eigenstates of the system, and is therefore entirely insignificant in the topological classification of the band structure.

In momentum space, the Hamiltonian can be written

$$H = \sum_{\mathbf{q}} \begin{pmatrix} a_{\mathbf{q}}^\dagger & b_{\mathbf{q}}^\dagger \end{pmatrix} \begin{pmatrix} A + h^z(\mathbf{q}) & h^-(\mathbf{q}) \\ h^+(\mathbf{q}) & A - h^z(\mathbf{q}) \end{pmatrix} \begin{pmatrix} a_{\mathbf{q}} \\ b_{\mathbf{q}} \end{pmatrix}, \quad (6.26)$$

where $a_{\mathbf{q}}$ and $b_{\mathbf{q}}$ are the sublattice magnon operators, and we have introduced quantities $A = 3JS + \mathcal{B}$, $h^z(\mathbf{q}) = 2\mathcal{D}S \sum_{\beta} \sin(\mathbf{q} \cdot \beta)$, $h^-(\mathbf{q}) = -JS \sum_{\alpha} \exp(-i\mathbf{q} \cdot \alpha)$, and $h^+ = (h^-)^*$. Here, the sums over α and β are sums over the nearest and next-to-nearest neighbour vectors of Fig. 3.2. The bulk spectrum is shifted with respect to the Haldane model spectrum in Fig. 3.3, but is otherwise exactly the same.

Since the above spin model is in the topological regime, the spin model also has topological edge modes which are exactly the same as in Chapter 3, except, of course, for the fact that the edge states now represent spin excitations consisting of spin flips on the edges instead of electrons.

Above, we have shown that the spin Hamiltonian in Eq. (6.24) is topologically non-trivial within the magnon description in linear spin wave theory. By instead using a Schwinger boson description [19], the spin excitation band structure is still topological [32]. There, the spins are represented by two boson species, and the spin model instead turns into a bosonic version of the Kane-Mele model [226, 227].

6.3 Topological magnons coupled to phonons

The topological classification of band structures is simple when the system is non-interacting. Turning on interactions, however, the system can in general no longer be diagonalized in terms of well defined bands. Instead, we typically calculate Green's functions and spectral functions, and the quasi-particles which can be identified within this description in general have finite lifetimes. It is therefore not obvious how the concept of band structure topology can be applied.

Of course, however, real life systems typically do have interactions, and interacting topological systems is an active research topic within electronic systems. The most natural question to ask may be whether topological insulators are still topological when turning on interaction [228, 229]. However, interactions may also be the cause of topologically non-trivial phases, such as for instance in topological Mott insulators [64] and topological Kondo insulators [6].

Recently, there has also been significant interest in magnetic systems with interacting magnons. In the standard method to obtain magnon band structures, one performs a Taylor expansion in magnon operators to obtain a quadratic Hamiltonian. Thus, third and higher order terms are neglected. These represent magnon interactions, which may affect topological stability or induce topologically non-trivial phases [230–232].

Magnons may however also interact with other degrees of freedom such as phonons [233–237], and in Paper [1], we study this for the magnon Haldane model above. In the following, we discuss the approach and the main results in that paper.

6.3.1 Model and diagonalization

We consider a system of ferromagnetically ordered localized spins on a honeycomb lattice described by the magnon Haldane model. Furthermore, the lattice sites on which the spins reside are allowed to vibrate out-of-plane. We therefore consider a model Hamiltonian on the form

$$H = H_m + H_{\text{ph}} + H_{\text{me}}, \quad (6.27)$$

consisting of three terms. First, H_m is given by Eq. (6.24). Second, we assume the out-of-plane vibrations to be described by the nearest neighbour force constant model

$$H = \sum_i \frac{(P_i^z)^2}{2m} + \frac{1}{2} \sum_{\langle i,j \rangle} C (u_i^z - u_j^z)^2, \quad (6.28)$$

which can be rewritten on the same form as the models considered in Chapter 4. Since we consider only nearest neighbour interaction, we only have a single force constant C .

Finally, we assume the topological magnons to be coupled to phonons through the magnetoelastic coupling term [1, 236, 237]

$$H_{\text{me}} = \kappa \sum_D \sum_{i \in D} \sum_{\alpha_D} \mathbf{S}_i \cdot \alpha_D (u_i^z - u_{i+\alpha_D}^z), \quad (6.29)$$

as also discussed in Sec. 4.3. Here, $D \in \{A, B\}$ labels the sublattices, α_A are the nearest neighbour vectors from the A to the B sublattices shown in Fig. 3.2, while α_B are the nearest neighbour vectors from the B to the A sublattice.

We now introduce linear spin-wave theory and the phonon representation for the lattice site deviations u_i^z . Since the spin components S_i^x and S_i^y are constructed from spin raising and lowering operators, both magnon creation and annihilation operators are coupled to the lattice site deviations. Furthermore, since lattice site deviations can be expressed in terms of phonon creation and annihilation operators, the magnetoelastic coupling Hamiltonian in general takes the form

$$H_{\text{me}} = \sum_{\mathbf{q}} \mu_{\mathbf{q}}^\dagger N_{\mathbf{q}} \pi_{\mathbf{q}}, \quad (6.30)$$

where we have introduced magnon and phonon spinors

$$\mu_{\mathbf{q}} = (a_{\mathbf{q}} \quad b_{\mathbf{q}} \quad a_{-\mathbf{q}}^\dagger \quad b_{-\mathbf{q}}^\dagger)^T \quad (6.31)$$

$$\pi_{\mathbf{q}} = (c_{\mathbf{q},-} \quad c_{\mathbf{q},+} \quad c_{-\mathbf{q},-}^\dagger \quad c_{-\mathbf{q},+}^\dagger)^T, \quad (6.32)$$

where $c_{\mathbf{q}\pm}$ are the phonon annihilation operators for the upper and lower phonon branches labelled by \pm . The matrix $N_{\mathbf{q}}$ can be written

$$N_{\mathbf{q}} = \begin{pmatrix} g_{A-} & g_{A+} & f_{A-} & f_{A+} \\ g_{B-} & g_{B+} & f_{B-} & f_{B+} \\ f_{A-}^* & f_{A+}^* & g_{A-}^* & g_{A+}^* \\ f_{B-}^* & f_{B+}^* & g_{B-}^* & g_{B+}^* \end{pmatrix} \quad (6.33)$$

with coupling matrix elements $g_{D\pm}$ describing boson conserving interactions between the sublattice D magnons and the phonon mode \pm , while the corresponding $f_{D\pm}$ describe a magnon-phonon coupling which does not conserve the boson number.

In the following, we employ the so-called rotating wave approximation, and neglect the terms in the Hamiltonian which do not conserve boson numbers. We expect this to be a good approximation when the coupling strength is small compared to the typical phonon and magnon energies. The Hamiltonian then becomes

$$H = \sum_{\mathbf{q}} \psi_{\mathbf{q}}^\dagger M_{\mathbf{q}} \psi_{\mathbf{q}}, \quad (6.34)$$

where we now have introduced the spinor

$$\psi_{\mathbf{q}} = (a_{\mathbf{q}} \quad b_{\mathbf{q}} \quad c_{\mathbf{q}-} \quad c_{\mathbf{q}+})^T, \quad (6.35)$$

and the matrix $M_{\mathbf{q}}$ is given by

$$M_{\mathbf{q}} = \begin{pmatrix} A + h^z & h^- & g_{A-} & g_{A+} \\ h^+ & A - h^z & g_{B-} & g_{B+} \\ g_{A-}^* & g_{B-}^* & \omega_{\mathbf{q}-}^{\text{ph}} & 0 \\ g_{A+}^* & g_{B+}^* & 0 & \omega_{\mathbf{q}+}^{\text{ph}} \end{pmatrix}. \quad (6.36)$$

The Hamiltonian can be diagonalized by introducing a new spinor of bosonic excitations through $\psi_{\mathbf{q}} = U_{\mathbf{q}} \phi_{\mathbf{q}}$, where $\phi_{\mathbf{q}} = (d_{\mathbf{q}1} \quad d_{\mathbf{q}2} \quad d_{\mathbf{q}3} \quad d_{\mathbf{q}4})^T$.

The resulting bulk spectrum is shown in Fig. 6.1. As we assume the magnetoelastic coupling to be small, the magnon-phonon coupling has a significant effect only close to the avoided mode crossings. Consistent with what we expect from the simple analysis for the two-level system in Sec. 4.3, the character of the modes becomes of hybrid nature close to the avoided crossings, whose direct gaps are determined by the coupling strength.

6.3.2 Hall conductivity

To compute the Hall conductivity in the model, we use the spin current defined according to the prescription in Sec. 6.1.1, and write

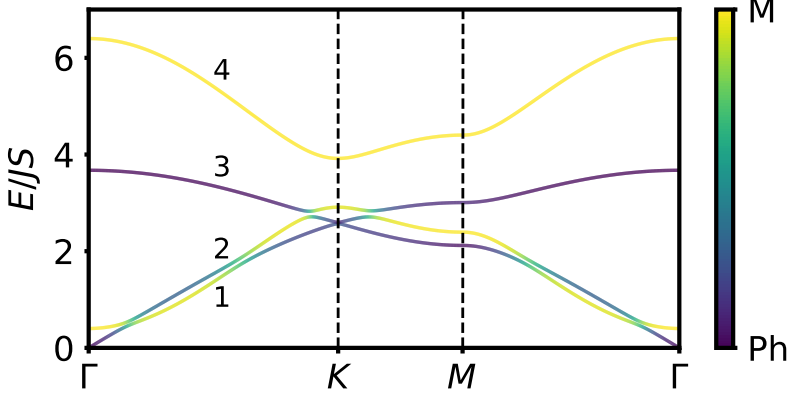


Figure 6.1: Energy spectrum for the system of phonons and topological magnons with magnetoelastic coupling. The mode character is indicated with color, where modes with dominant magnon (phonon) content is shown in yellow (purple).

$$j_\gamma = \sum_{\mathbf{q}} \begin{pmatrix} a_{\mathbf{q}}^\dagger & b_{\mathbf{q}}^\dagger \end{pmatrix} \left(\frac{\partial h_m(\mathbf{q})}{\partial q_\gamma} \right) \begin{pmatrix} a_{\mathbf{q}} \\ b_{\mathbf{q}} \end{pmatrix}, \quad (6.37)$$

where $h_m(\mathbf{q})$ is the pure magnon Hamiltonian. Through the diagonalization procedure, we get eigenoperators $d_{\mathbf{q}i}$ with $i \in \{1, 2, 3, 4\}$, which are in general superpositions of both phonons and magnons. In terms of these eigenbosons, we may therefore write the current operator as

$$\hat{j}_\mu = \sum_{\mathbf{q}} \sum_{\alpha\beta} \hat{j}_\mu^{\alpha\beta}(\mathbf{q}) d_{\mathbf{q}\alpha}^\dagger d_{\mathbf{q}\beta}, \quad (6.38)$$

where the labels α and β are now ranging over all the four bands in the spectrum. The matrix elements can be extracted based on the matrix $U_{\mathbf{q}}$ used to diagonalize the Hamiltonian, which can be used to replace the original operators $a_{\mathbf{q}}$ and $b_{\mathbf{q}}$ in the definition of the current with the eigenbosons.

As discussed in Sec. 6.1.2, this representation for the spin current allows us to write the magnon spin Hall conductivity as

$$\sigma_{xy} = \frac{\hbar}{V_{\text{uc}}} \sum_{\alpha} n_B(E_{\mathbf{q}\alpha}) \mathcal{F}^\alpha(\mathbf{q}) \quad (6.39)$$

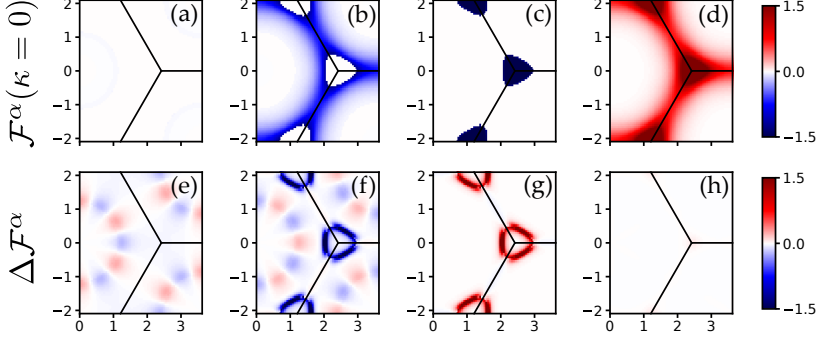


Figure 6.2: (a-d) Band curvature \mathcal{F}^α for the four bands in the absence of magnon-phonon coupling. The bands are labelled according to energy. (e-h) Curvature transfer $\Delta\mathcal{F}^\alpha(\mathbf{q}; \kappa) = \mathcal{F}^\alpha(\mathbf{q}; \kappa) - \mathcal{F}^\alpha(\mathbf{q}; 0)$ in the presence of magnetoelastic coupling. Close to the avoided crossings, curvature is transferred between the bands.

with a band curvature $\mathcal{F}^\alpha(\mathbf{q}) = \sum_{\beta \neq \alpha} \mathcal{F}^{\alpha\beta}(\mathbf{q})$ and curvature tensor

$$\mathcal{F}^{\alpha\beta}(\mathbf{q}) = i \frac{j_x^{\alpha\beta}(\mathbf{q})j_y^{\beta\alpha}(\mathbf{q}) - j_y^{\alpha\beta}(\mathbf{q})j_x^{\beta\alpha}(\mathbf{q})}{(E_{\mathbf{q}\alpha} - E_{\mathbf{q}\beta})^2}. \quad (6.40)$$

We remark that while the band curvature $\mathcal{F}^\alpha(\mathbf{q})$ could be related to the Berry curvature of the bands in the absence of magnon-phonon coupling, this is not the case here, as the spin current is defined as a derivative of the magnon Hamiltonian and not the full Hamiltonian. The situation would be different if we instead considered heat transport, where both phonons and magnons may contribute.

The band curvature $\mathcal{F}^\alpha(\mathbf{q})$ is plotted in Figs. 6.2 (a-d) in the absence of electron-magnon coupling. In that case, only magnon bands carry a non-zero Berry curvature, and since we label the energy bands according to their energy at any given point \mathbf{q} in the Brillouin zone, there are abrupt changes in the Berry curvature where the phonon and magnon frequencies cross. Turning on magnetoelastic coupling, we instead get band curvature $\mathcal{F}^\alpha(\mathbf{q}; \kappa)$, and in Figs. 6.2(e-g), we plot the quantity $\Delta\mathcal{F}^\alpha(\mathbf{q}; \kappa) = \mathcal{F}^\alpha(\mathbf{q}; \kappa) - \mathcal{F}^\alpha(\mathbf{q}; 0)$. Comparing with the location of the avoided band crossings shown in Fig. 6.1, we see that curvature is transferred between the bands by the magnon-phonon coupling.

Since the magnon spin Hall conductivity is determined as a weighted average of the band curvature over the Brillouin zone, this curvature transfer

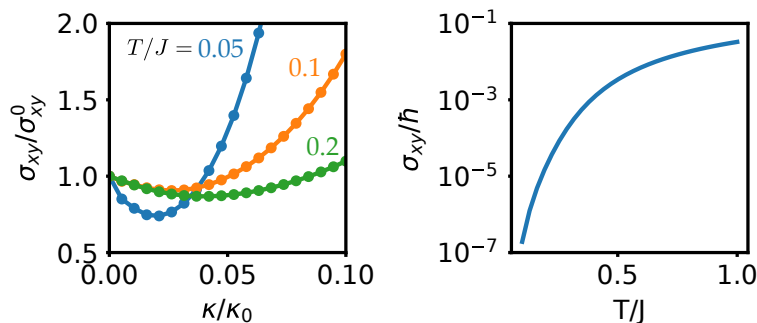


Figure 6.3: (a) Magnon spin Hall conductivity as function of magnon-phonon coupling strength normalized to the value at zero coupling. (b) Hall conductivity as function of temperature.

also affects the magnon spin Hall conductivity. This is shown in Fig. 6.3 (a), which shows the transverse conductivity as function of coupling strength κ normalized to the value at zero magnon-phonon coupling. The curvature transfer can make significant contributions to the transverse Hall conductivity, especially at small temperatures. The transverse conductivity as function of temperature is shown in Fig. 6.3 (b).

6.3.3 Edge modes and transport

The second key property of topologically non-trivial systems is the presence of topologically protected edge modes. As the model for the topological magnons is simply the Haldane model, we know that it hosts chiral edge modes. One may now ask how these are affected by magnetoelastic coupling.

As we have seen, the topological edge magnon modes are conveniently studied on a ribbon geometry. This time, we do so on a ribbon geometry with a so-called armchair edge, as shown in the upper left of Fig. 6.5. The resulting magnon spectrum is shown in Fig. 6.4 (a). As expected, the magnon spectrum contains localized chiral magnon modes within the bulk gap. In contrast, the phonon spectrum is not gapped. However, the armchair edge ribbon still has localized edge modes outside the bulk spectrum. As discussed in Paper [1], these modes have a localization length inversely proportional to the momentum q_x along the edge of the sample.

When the momenta and energies of these edge modes match, we expect the chiral edge magnon modes to hybridize with the edge phonons to produce

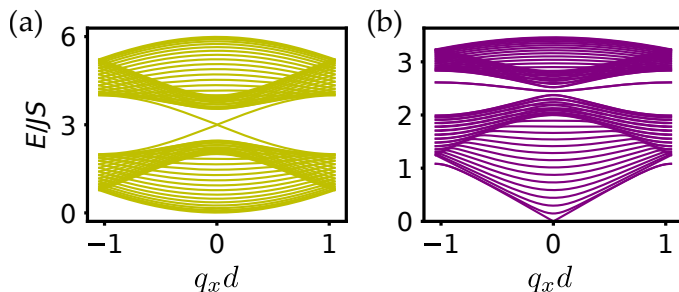


Figure 6.4: Energy spectra for magnon (a) and phonon (b) models on an armchair edge ribbon geometry with 30 layers.

new magnon-polaron excitations. To demonstrate this, we show the energy spectra for the coupled magnon and phonon modes on a ribbon geometry in Fig. 6.5. The edge magnons and phonons hybridize within the region indicated with a red circle. A schematic spectrum for the modes on one edge of the ribbon is shown in Fig. 6.6 (a).

In Paper [1], we propose that this hybridization imprints on the elastic properties of the system, and that the chiral nature of the magnon mode may therefore cause chirality also in the elastic edge transport, as illustrated in Fig. 6.6 (b). This may provide evidence for the presence of topological edge magnon modes in the system.

6.4 Further developments

As we have seen, Berry curvatures can be transferred between bands at avoided crossings [1, 233]. Furthermore, this curvature transfer is not dependent on the existence of a large Berry curvature to begin with³. Thus, magnetoelastic coupling induces Berry curvature. Building on these ideas, it has been shown that the magnetoelastic coupling itself may induce topologically non-trivial hybridized magnon and phonon bands [234–236, 238]. Furthermore, these studies show that the magnetoelastically induced contributions to the thermal Hall conductivity may dominate. Similar considerations apply also to the magnon Nernst effect [238]. These findings suggest that thermal, Nernst and spin Hall conductivity measurements may provide a somewhat surprising signature of magnetoelastic coupling.

³This can be seen by comparing Fig. 6.2 (e) with Fig. 6.2 (a).

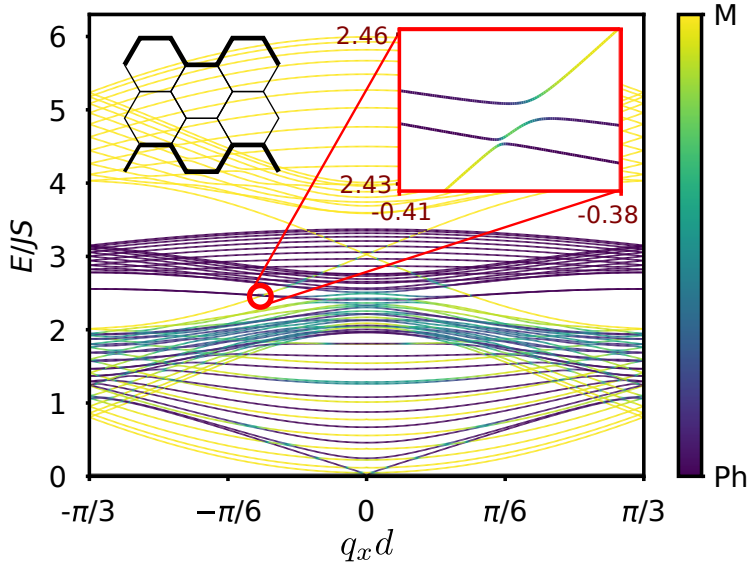


Figure 6.5: Excitations spectrum for coupled magnon and phonon modes on an armchair ribbon. The inset shows that topological edge magnon modes may hybridize with edge phonons.

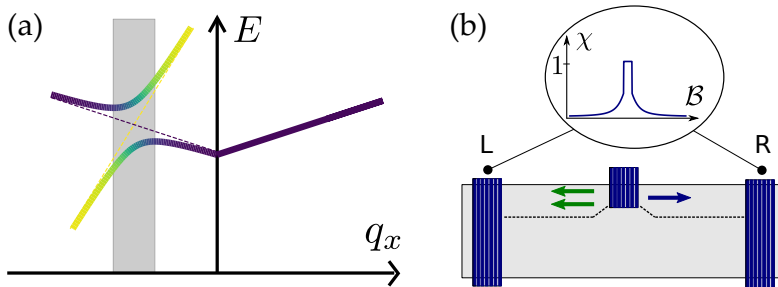


Figure 6.6: (a) Schematic spectrum on one armchair edge of the sample. (b) Elastic excitation of modes is suggested to produce chiral phonon transport since the mode at $-k_x$ may hybridize with the chiral magnon mode, in contrast with the phonon mode at $+k_x$. The chirality at a given excitation frequency can be tuned through a peak with the magnetic field, as the chiral transport requires hybridization and the magnetic field controls magnon energies.

Magnon-phonon coupling in magnetic systems can be detected experimentally in magnetic systems through measurement of the emergent direct gap at an avoided crossing [239, 240]. Furthermore, magnon-phonon coupling also has signatures through magnon energy renormalization, spontaneous magnon decay, and thermal conductivities [241]. Very recently, evidence for magnon-phonon coupling has been obtained in an antiferromagnet believed to host topological magnons [241]. This gives hope that magnon-phonon coupling effects can be studied experimentally also in topological magnetic systems.

Chapter 7

Graphene superconductivity

The most impressive property of graphene is arguably its stability in monolayer form. A multitude of materials with weakly coupled two-dimensional layers stacked on top of each other exist, and typical examples are the already mentioned high- T_c cuprates, graphite, and various other van der Waals materials. Yet, isolated sheets of single atom thickness are hard to synthesize, as they tend to reorganize in other configurations. In fact, due to a famous theorem by Peierls and Landau [242–244], strictly two-dimensional materials were believed to be thermodynamically unstable.

The discovery of graphene in 2004 therefore came as a surprise [245, 246], and the new material was quickly propelled to the forefront of condensed matter research. In particular, graphene has been celebrated for its ability to mimic relativistic physics in a condensed matter setting, and astonishingly even in a material theoretical physicists are able to produce routinely with their pencils [247].

By now, graphene has established itself as the most prominent two-dimensional material, and provides an excellent platform to study the physics in two spatial dimensions. Discussions of a varied number effects are given in numerous treatises on the subject, for instance Refs. [247–250].

One phenomenon, however, is notably absent in monolayer graphene, namely superconductivity. The reason is simple: The electron spectrum of graphene close to half filling consists of two Dirac cones. Exactly at half-filling, the Fermi surface therefore consists of two single points. As we have seen, superconductivity occurs due to a Fermi surface instability, and

without a Fermi surface, there cannot be superconductivity. Upon doping graphene, however, a finite Fermi surface appears. Yet, for small dopings, the density of states is still small, and this limits the dimensionless electron-phonon coupling strength. Recent experimental progress has, however, showed that large doping even beyond the van Hove singularity in graphene is possible [251], and approaching this regime, the density of states is significant. Thus, one may hypothesize that superconductivity in monolayer graphene may be possible after all.

In Paper [2], we discuss the possibility of phonon-mediated superconductivity in graphene using detailed tight binding and force constant models to describe the electronic and phononic properties of graphene. In this chapter, we discuss the various physics and models underlying these calculations, and briefly describe the main results. We start by a brief review of the electronic properties of graphene in Sec. 7.1, and move on to discuss the phonon spectrum and electron-phonon coupling in Sec. 7.2. Finally, we introduce superconductivity in graphene in Sec. 7.3, and move on to describe some of our main results.

7.1 Electronic properties of graphene

Graphene is a two-dimensional material constructed out of carbon atoms forming a honeycomb lattice. Carbon has atomic number 6, so that 6 electrons per atom have to be distributed into the bands. Since the honeycomb lattice can be thought of as a triangular Bravais lattice with two atoms in the basis, we will be counting the number of states per unit cell in the Bravais lattice. First, a total of 4 electrons can be placed in the $1s$ state of the two atoms, corresponding to the two possible spin orientations. The remaining 8 electrons have to be distributed into the orbitals $2s$, $2p_x$, $2p_y$, and $2p_z$. Since these have similar single atom energies, they may hybridize into 8 bands, out of which 4 should be populated by electrons with spin up and spin down. As it happens, the three orbitals $2s$, $2p_x$ and $2p_y$ may hybridize to form covalent bonds with its neighbours in the plane in the so-called σ -bands. Since there are three electrons contributing to this bonding, graphene forms its characteristic honeycomb lattice. The $2p_z$ orbital, however, does not hybridize with these orbitals, as it is anti-symmetric with respect to the symmetry operation $z \rightarrow -z$. We therefore get two bands constructed exclusively out of the $2p_z$ orbital, and we refer to these as the π -bands. Since the $2p_z$ -orbital cannot hybridize with the remaining bands, the energy of the lowest π -band is typically larger than the energy of the lowest σ -bands.

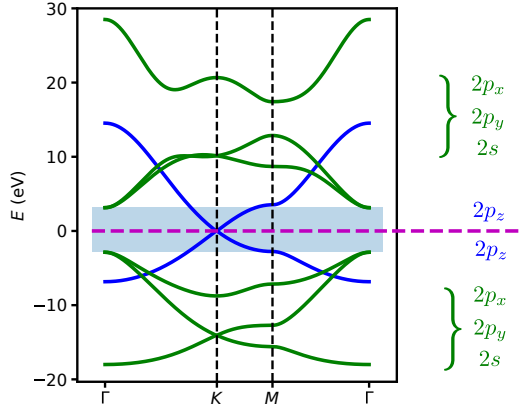


Figure 7.1: Graphene band structure along high symmetry path calculated using a tight binding model, where σ -bands are shown in green and π -bands in blue, and the Fermi surface is indicated in magenta. Close to the Fermi surface (shaded blue), only the π -band is present.

To calculate the band structure of the π - and σ -bands we may use a tight binding model as described in Ref. [252], and the result is shown in Fig. 7.1. As indicated by the shaded blue region in the figure, only the π -band is present close to half filling. Since the electronic properties of graphene are dominated by the physics close to the Fermi surface, we may therefore disregard the σ -bands for typical dopings.

To describe the electronic properties of the π -band in graphene, we may write down the single band hopping model

$$H = -t \sum_{\langle ij \rangle, \sigma} c_{i\sigma}^\dagger c_{j\sigma} - \mu \sum_{i, \sigma} c_{i\sigma}^\dagger c_{i\sigma} + u \sum_i n_{i\uparrow} n_{i\downarrow}, \quad (7.1)$$

where $c_{i\sigma}^\dagger$ and $c_{i\sigma}$ are creation and annihilation operators for an electron with spin σ on lattice site i on the honeycomb lattice, and $n_{i\sigma} = c_{i\sigma}^\dagger c_{i\sigma}$ the corresponding density operator. Here, t is the nearest neighbour hopping amplitude, and μ is the chemical potential, while u is the onsite repulsion strength.

In Paper [2], we set the onsite repulsion to a finite value and consider the competition between an attractive phonon-mediated electron-electron interaction and this repulsive contribution. In the following discussion, however, we set $u = 0$. Then, the graphene tight binding model for the π -band

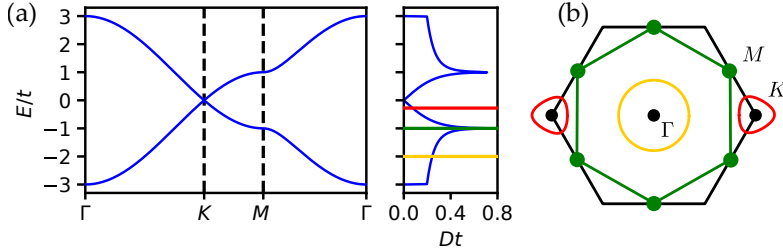


Figure 7.2: (a) Electronic band structure and density of states D for the π -band of graphene. (b) Fermi surface in the first Brillouin zone for values of the chemical potential indicated with horizontal colored lines in (a).

coincides with the Haldane model in the absence of sublattice asymmetry and the next-to-nearest neighbour hopping associated with a phase, and in Sec. 3.2, we discussed how it can be diagonalized.

The resulting electron band structure for graphene is shown in Fig. 7.2 (a) along the usual high-symmetry path. Close to half-filling, the bands have the shape of two touching Dirac cones, so that at half filling, the Fermi surface consists of two points at $\pm K$. The Fermi surface is shown for three different values of the chemical potential in Fig. 7.2 (b). For small dopings, the Fermi surface consists of two surfaces growing out from the points $\pm K$, while at $\mu = \pm t$, the Fermi surface topology changes, and the Fermi surface is instead centered around the Γ -point. The density of states is shown in the right subfigure of (a), and is linear around half-filling, as expected for a band on the form $\epsilon_{\mathbf{k}} = v|\mathbf{k}|$ in two dimensions. When the Fermi surface topology changes, the density of states has a van Hove singularity, which is a logarithmic divergence in the density of states occurring from the saddle point structure of the spectrum for $\mu = \pm t$ at the points in Fig. 7.2 (b) marked in green¹.

7.2 Phonons and electron-phonon coupling

As mentioned in the introduction, graphene was, before its discovery, thought to be thermodynamically unstable in its monolayer form [242–244, 250, 253]. Since phonons are fluctuations of lattice ions around their equilibrium lattice site positions, the excitations responsible for this instability have to be

¹That a saddle point in the energy spectrum gives rise to a logarithmic divergence in the density of states can be shown by calculating the integral $\int dk_x dk_y \delta(E - k_x^2 + k_y^2)$.

phonons. An analysis based on theory of elasticity reveals that even without quantum fluctuations, 2D materials are unstable with respect to out-of-plane fluctuations within the harmonic approximation. An analysis beyond second order is therefore necessary to study its thermodynamic stability, and reveals that at higher order, coupling between the in-plane and out-of-plane modes in fact renders graphene stable [250].

The above considerations are concerned with the long-wavelength properties of graphene. Phonon-mediated superconductivity, however, is not especially sensitive to the long-wavelength phonons due to the suppression of the electron-phonon coupling matrix element in the long-wavelength limit. An analysis based on the harmonic approximation is therefore sufficient for our purposes. In this section, we will therefore be discussing the phonon spectra in graphene in Sec. 7.2.1, before turning to electron-phonon coupling in Sec. 7.2.2.

7.2.1 Phonon spectrum

Already prior to the discovery of graphene, the phonon spectrum of graphite, which we may think of as weakly coupled layers of graphene, had been mapped out in great detail. The primary techniques which allows the detailed study of the full momentum dependence of these spectra are inelastic neutron scattering [254–257] and electron energy loss spectroscopy (EELS) [258, 259].

Measuring the phonon spectra of graphene is a far more challenging task, since a single atomic layer of graphene cannot usually scatter neutrons sufficiently strong to make inelastic neutron scattering an efficient technique [250]. To extract information about the phonon spectra of graphene, the primary technique has therefore been Raman spectroscopy [260]. This technique, however, only allows access to the phonon energies at a few special points in the Brillouin zone, and not a complete mapping of the momentum dependence. However, recent experimental developments give hopes that the full momentum characterization of the phonon spectra in graphene are also within reach [261].

Theoretically, the calculation of phonon spectra is typically based on force constant model descriptions of the lattice vibrations, as described in Sec. 4.1. While the diagonalization itself is straightforward, the challenge is to obtain reasonable values for the force constants. One strategy is to adopt a model with a finite number of force constants corresponding to the interactions between some set of the nearest neighbour atoms on the lattice, and fit these force constants to experimental values for the phonon

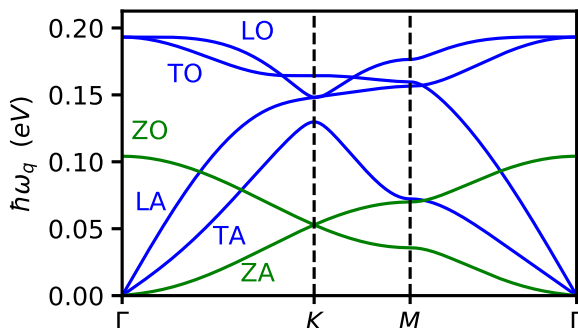


Figure 7.3: Graphene phonon spectrum along high-symmetry path in the Brillouin zone. Out-of-plane modes in green and out-of-plane modes in blue. The modes are labelled as acoustic (A) or optical (O), and transverse (T), longitudinal (L), or out-of-plane (Z) according to their small- \mathbf{q} behaviour.

frequencies on special points in the Brillouin zone, as obtained for instance through Raman spectroscopy methods [77, 262]. Alternately, one may try to estimate the force constants from some more fundamental model. This can for instance be done either through ab-initio calculations [263–265], or through the empirical interatomic potential (EIP) method [266–268].

In Paper [2], we use the former approach. First, however, a somewhat extensive symmetry analysis is necessary to arrive at the set of independent force constants describing the model. This symmetry analysis is based on Refs. [77, 262], and outlined in Paper [2]. Here, we simply point out that the in-plane and out-of-plane modes are decoupled to quadratic order in lattice site deviations due to mirror symmetry with respect to the transformation $z \rightarrow -z$. Since we have two atoms in the basis for graphene, we therefore have two out-of-plane modes. Furthermore, since there are two Cartesian in-plane directions and two atoms in the basis, we have four in-plane modes. The graphene phonon spectrum is shown in Fig. 7.3, as calculated in Paper [2] using appropriate force constants [77].

7.2.2 Electron-phonon coupling

To study phonon-mediated superconductivity in graphene, we also need a model describing the coupling between electrons and phonons.

Experimentally, the electron-phonon coupling in graphene can be mea-

sured from kinks and linewidths in angular resolved photo-emission spectra [269–271]. Electron-phonon coupling in graphene can be understood and analyzed within a tight binding approach [269, 272–277], and has also been analyzed from a symmetry point of view [278], and calculated using ab-initio techniques based on density functional theory and the *GW*-approximation [269, 279, 280].

To model the electron-phonon coupling in graphene, we use a tight binding model approach as discussed in Chapter 4, with the proper generalization to systems with two atoms in the basis. Including the contributions from nearest-neighbour hoppings, we obtain real space electron-phonon coupling Hamiltonian

$$H_{\text{el-ph}} = \sum_{i \in A, \delta_A} \frac{t_{\text{nn}}^0 \gamma_{\text{nn}}}{d} (\boldsymbol{\delta}_A/d) \cdot (\mathbf{u}_{i+\delta_A}^B - \mathbf{u}_i^A) (c_{i+\delta_A, B}^\dagger c_{iA} + c_{iA}^\dagger c_{i+\delta_A, B}). \quad (7.2)$$

This gives rise to the standard electron-phonon coupling

$$H_{\text{el-ph}} = \sum_{\mathbf{k}, \mathbf{q}} \sum_{\eta \eta'} \sum_{\nu, \sigma} g_{\mathbf{k}, \mathbf{k}+\mathbf{q}}^{\eta \eta', \nu} (a_{\mathbf{q}\nu} + a_{-\mathbf{q}, \nu}^\dagger) c_{\eta' \sigma}^\dagger(\mathbf{k} + \mathbf{q}) c_{\eta \sigma}(\mathbf{k}), \quad (7.3)$$

where an explicit expression for the coupling matrix element is given in Paper [2]. The matrix element is expressed in terms of the phonon energies, as well as the unitary matrices required to diagonalize the electron Hamiltonian on the form in Eq. (3.33) and the phonon Hamiltonian on the form in Eq. (4.8). Since the system is symmetric with respect to $z \rightarrow -z$, the electron-phonon coupling matrix element for scattering within the π -band due to out-of-plane modes is zero². Thus, we may consider only on the in-plane modes.

The state-dependent dimensionless electron-phonon coupling strength is given by

$$\lambda_{\mathbf{k}\eta} = \sum_{\mathbf{q}\nu} \sum_{\eta'} \frac{2}{\hbar \omega_{\mathbf{q}\nu}} |g_{\mathbf{k}, \mathbf{k}+\mathbf{q}}^{\eta \eta', \nu}|^2 \delta(\epsilon_{\mathbf{k}+\mathbf{q}, \eta'} - \epsilon_{\mathbf{k}\eta}). \quad (7.4)$$

Averaging over the Fermi surface as discussed in Chapter 4, one obtains the energy dependent electron-phonon coupling strength

²Within the tight binding model for the electron-phonon coupling model, this is easily seen from Eq. (7.2), as the vectors $\boldsymbol{\delta}_A$ are always in-plane, and therefore only couple to the in-plane deviations. More generally, the in-plane phonons couple to intraband transitions $\pi \rightarrow \pi$ and $\sigma \rightarrow \sigma$, while the out-of-plane phonons couple to the interband transitions $\pi \rightarrow \sigma$ and $\sigma \rightarrow \pi$, but not the intraband transitions.

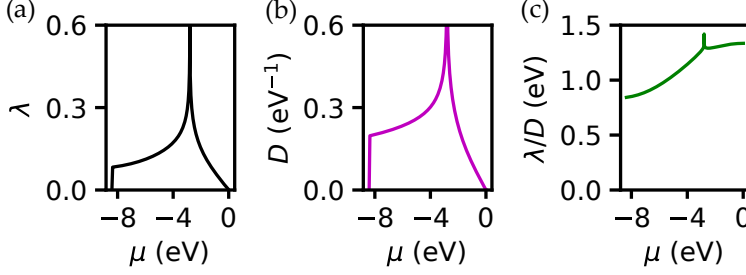


Figure 7.4: (a) Fermi surface averaged electron phonon coupling strength λ as function of doping μ . (b) Density of states D . (c) Effective Fermi surface averaged potential λ/D .

$$\lambda(\epsilon) = \frac{1}{N(\epsilon)} \sum_{\mathbf{k}\mathbf{q}\nu} \sum_{\eta\eta'} \frac{2}{\hbar\omega_{\mathbf{q}\nu}} |g_{\mathbf{k},\mathbf{k}+\mathbf{q}}^{\eta\eta',\nu}|^2 \delta(\epsilon_{\mathbf{k}+\mathbf{q},\eta'} - \epsilon) \delta(\epsilon_{\mathbf{k}\eta} - \epsilon), \quad (7.5)$$

where $N(\epsilon)$ is the electronic density of states at single particle energy ϵ .

As we expect the states close to the Fermi surface to dominate the physics, we may neglect the bands which are far away from the Fermi surface in doped graphene. Thus, we may focus on a single band in the above electron-phonon coupling Hamiltonian, and only consider the contribution from $\eta = \eta'$.

In Fig. 7.4, we show the dimensionless electron-phonon coupling $\lambda(\epsilon)$ as function of single particle energy ϵ together with the intensive electronic density of states $D(\epsilon) = N(\epsilon)/N_{\text{uc}}$, where N_{uc} is the number of unit cells. The two profiles are qualitatively similar, and this emphasizes the important role played by the electronic density of states.

7.3 Superconductivity in graphene

Superconductivity is well known in a few graphene-like materials. Most notably, superconductivity was discovered in the C_{60} molecule buckminsterfullerene intercalated with potassium in 1991 with a critical temperature of 18 K [281]. Superconductivity has also been discovered in intercalated graphite compounds. Whereas the first examples of superconductivity in these systems were obtained at critical temperatures between 0.15 K and 1.8 K [282–284], graphite intercalation compounds were discovered in 2005 with

critical temperatures of 6.5 and 11.5 K [285]. Furthermore, superconductivity has also recently been observed in intercalated bilayer graphene [286, 287], and it is believed that interlayer states are important for the superconductivity in many of these systems [288, 289]. Superconductivity in monolayer graphene has, however, remained elusive, although some evidence for superconductivity in monolayer graphene was reported in Ref. [290].

Close to the van-Hove singularity, it has been suggested that repulsive electron-electron interactions may give rise to d -wave superconductivity. On the other hand, phonon-mediated superconductivity in intercalated monolayer graphene was studied in Ref. [291] using Eliashberg theory and assuming an isotropic gap, while Ref. [292] uses an ab-initio approach. In Paper [2], we use BCS theory based on an electron tight binding and phonon force constant models to study phonon-mediated superconductivity in doped monolayer graphene. We discuss this in the following.

Following the Fröhlich procedure as discussed in Sec. 5.1.4, we obtain effective pair scattering potential

$$V_{\mathbf{k}\mathbf{k}'}^{\text{ph}} = \sum_{\nu} \frac{|g_{\mathbf{k}\mathbf{k}'}^{\eta\nu}|^2}{(\xi_{\mathbf{k}} - \xi_{\mathbf{k}'})^2 - (\omega_{\mathbf{k}-\mathbf{k}'}^{\nu})^2} \quad (7.6)$$

for singlet pairing. Retaining only pair scattering terms also in the Coulomb repulsion, we obtain the reduced BCS Hamiltonian

$$H = \sum_{\mathbf{k}\eta} \xi_{\mathbf{k}\eta} c_{\eta\sigma}^{\dagger}(\mathbf{k}) c_{\eta\sigma}(\mathbf{k}) + \sum_{\mathbf{k}\mathbf{k}'} V_{\mathbf{k}\mathbf{k}'} c_{\eta\uparrow}^{\dagger}(\mathbf{k}') c_{\eta\downarrow}^{\dagger}(-\mathbf{k}') c_{\eta\downarrow}(-\mathbf{k}) c_{\eta\uparrow}(\mathbf{k}), \quad (7.7)$$

where the effective potential can be written $V_{\mathbf{k}\mathbf{k}'} = V_{\mathbf{k}\mathbf{k}'}^{\text{el-ph}} + V_{\mathbf{k}\mathbf{k}'}^{\text{C}}$. Here, interband scattering processes have been neglected since only one of the bands is close to the Fermi surface in the doping regime down to the van Hove singularity. Assuming singlet pairing, we may use mean field theory as described in Chapter 5 to derive the BCS gap equation

$$\Delta_{\mathbf{k}} = - \sum_{\mathbf{k}'} V_{\mathbf{k}\mathbf{k}'} \left(\frac{\tanh \beta E_{\mathbf{k}'}/2}{2E_{\mathbf{k}'}} \right) \Delta_{\mathbf{k}'}, \quad (7.8)$$

with excitation energy $E_{\mathbf{k}} = \sqrt{\xi_{\mathbf{k}}^2 + |\Delta_{\mathbf{k}}|^2}$.

As discussed in Sec. 5.1.7, solving this gap equation with the general potential $V_{\mathbf{k}\mathbf{k}'}$ is a challenging task. However, the numerical complexity can be simplified massively by instead solving the Fermi surface averaged equations, as this effectively reduces the dimensionality of the problem. In Fig. 7.5 (a), we show the results for the largest gap equation eigenvalue λ_{eff}

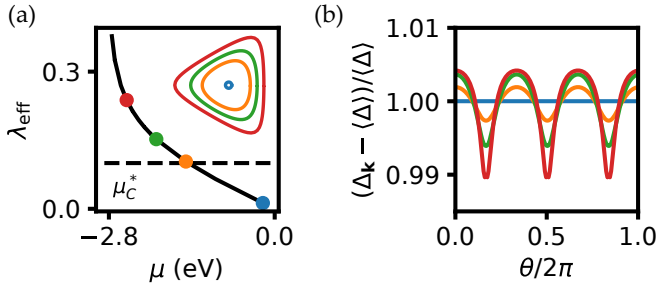


Figure 7.5: Solutions to the Fermi surface averaged gap equation. (a) The largest eigenvalue λ_{eff} , serving as effective electron-phonon coupling strength. The inset shows the shape of the Fermi surface at a given doping. (b) Gap structure on the Fermi surface for dopings as indicated in (a).

within this approach. The corresponding critical temperature can be calculated through the BCS formula $T_c \approx 1.14\omega_D \exp[-1/(\lambda - \mu_C^*)]$, where the Coulomb pseudopotential μ_C^* has to be chosen appropriately. Furthermore, the gap structures on the Fermi surface are shown in Fig. 7.5 (b) for dopings as indicated in (a). As the doping increases, an anisotropy in the gap develops.

In Paper [2], we instead solve the gap equation while keeping the full momentum dependence of the potential, obtaining solutions as shown in Fig. 7.6. There, (a) shows the critical temperature as function of doping, while (b) shows the critical temperature as function of onsite repulsion u_0 in pristine graphene³. Dots indicate critical temperatures obtained by solving the gap equation, and these solutions have been fitted to a Morel-Anderson functional form agreeing excellently with the obtained results. A sample gap structure just below the critical temperature is shown in (c), where the gap structure perpendicular to (orange) and along (green) the Fermi surface is shown in the insets. The results were obtained with a finite value for the onsite repulsion, and consistent with what we expect from the Morel-Anderson model, the gap changes sign a distance away from the Fermi surface corresponding to the phonon Debye energy. Then, the gap decays to a finite value. The calculation also confirms the existence of the Fermi surface gap anisotropy obtained by solving the Fermi surface averaged equations. Although the anisotropy is small, it can in principle be measured using for instance angular resolved photo-emission spectroscopy (ARPES).

³We refer to Paper [2] for the precise definition of the quantity u_0 .

From the above results, it is clear that phonon-mediated superconductivity in doped graphene is a viable option. However, since the critical temperature is very sensitive to an already relatively small effective dimensionless electron-phonon coupling, the critical temperature is on the verge of becoming so small that we cannot expect to observe the superconductivity. It is also clear that Coulomb interaction plays an important role in suppressing critical temperatures due to the relatively modest electron-phonon coupling strength. Furthermore, intercalation is required to reach the necessary doping regime. The intercalant atoms may change the properties of the system, and incorporating this in the analysis could be important.

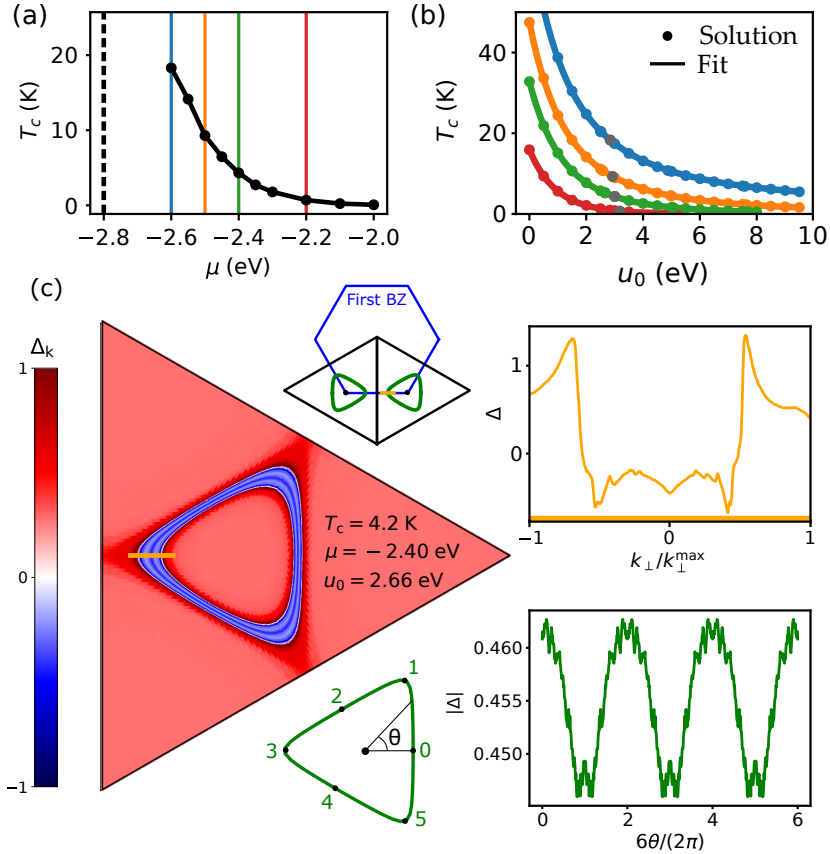


Figure 7.6: Solution to gap equation with full momentum dependence. (a) Critical temperature as function of doping. (b) Critical temperature (dots) as function of onsite repulsion, where lines are fits to the Morel-Anderson model. (c) Gap equation structure within triangular part of the Brillouin zone as shown in inset. Gap structure perpendicular to (orange) and along (green) the Fermi surface.

Chapter 8

Magnon-mediated superconductivity

For phonon-mediated superconductivity, electrons interact with a lattice, which can mediate an effective electron-electron interaction. Similarly, the spin fluctuations in a magnetic insulator coupled to a normal metal can mediate an effective interaction between two electrons in the normal metal. In principle, this may give rise to superconductivity.

Previously, magnon mediated superconductivity in heterostructures of metallic systems coupled to magnetic insulators has been studied within a few different settings. A normal metal coupled to ferromagnets with oppositely aligned magnetic moments was studied in Ref. [293], finding p -wave superconductivity. By instead coupling to an antiferromagnet, d -wave superconductivity was obtained for small doping in Ref. [294], using a somewhat artificial model for the electron band structure. In contrast, the large doping regime of a similar model was studied in Ref. [141]. There, p -wave superconductivity was obtained for large doping by coupling asymmetrically to the two sublattices of an antiferromagnet. Spin fluctuation mediated superconductivity in similar systems has also been studied within a Schwinger boson approach [295], and on the surface of topological insulators [296–298].

In Paper [4], we bring together several of these ideas. Utilizing insights from Paper [3], we study the possible superconducting phases that may occur in a normal metal coupled to antiferromagnetic insulators. We study both the small and large doping regimes, and allow for asymmetry in the coupling to the two sublattices. This allows a comprehensive qualitative understanding of the various processes, mechanisms, and superconducting phases in

the system. While the previously mentioned studies rely on BCS theory, we analyze the system with Eliashberg theory, thus properly accounting for the retarded nature of the effective interaction. As we will discuss, this turns out to be crucial.

In Sec. 8.1, we discuss Paper [3] and the interpretation of antiferromagnetic magnons as squeezed bosonic states. In the remainder of the chapter, we consider magnon-mediated superconductivity as discussed in Paper [4]. In Sec. 8.1, we introduce the model used in the paper, and in Sec. 8.3, we construct an Eliashberg theory for magnon-mediated superconductivity. In Sec. 8.4, we discuss some of the main results. Finally, in Sec. 8.3, we comment on some of the underlying assumptions, and some further aspects of the results.

8.1 Squeezed antiferromagnetic magnons

In Sec. 2.3, we discussed the eigenexcitations of the quantum antiferromagnet in a Heisenberg model with an easy axis anisotropy using linear spin wave theory. There, we showed that the ground state was in general not the Néel state, but rather a superposition of states with multiple pairs of spin flips on top of the Néel state. In fact, as we discuss in further detail below, this allows the ground state of the antiferromagnet to be interpreted as a squeezed state.

8.1.1 Squeezed states

One of the most fundamental properties of quantum mechanics is the uncertain nature of quantum observables. If we consider two non-commuting observables X and Y with commutation relation

$$[X, Y] = iC, \quad (8.1)$$

the two observables satisfy the Heisenberg uncertainty relation [299]

$$\langle (\delta X)^2 \rangle \langle (\delta Y)^2 \rangle \geq \frac{1}{4} |\langle C \rangle|^2, \quad (8.2)$$

where $\delta X = X - \langle X \rangle$ and $\delta Y = Y - \langle Y \rangle$. Depending on the operator C , this places a fundamental lower bound on the the product of the variances of the quantum variables X and Y in a given quantum state. If we now change the quantum state so that the fluctuations in one of the operators are reduced

at the expense of enhancing the fluctuations in the other, we may think of this as squeezing the state.

Considering two bosonic modes with annihilation operators a and b , one may construct a so-called two-mode squeezed state [300, 301]

$$|\psi_{\text{sq}}\rangle = \exp(\xi ab - \xi^* a^\dagger b^\dagger) |0, 0\rangle \equiv S|0, 0\rangle, \quad (8.3)$$

where $\xi = re^{i\theta}$ is some complex number, $|0, 0\rangle$ is the vacuum state for the two bosonic modes, and we refer to S as the squeezing operator. To show that this can indeed be thought of as a squeezed state, we introduce the quantities X and Y given by

$$X = \frac{1}{2} (a + a^\dagger + b + b^\dagger) \quad (8.4a)$$

$$Y = \frac{1}{2} (a - a^\dagger + b - b^\dagger), \quad (8.4b)$$

which satisfy the commutation relation $[X, Y] = i$. Thus, the product of their fluctuations is fundamentally limited by the Heisenberg uncertainty relation. By explicit calculation, one may show that for $\theta = 0$, the operator variances are given by

$$\langle \psi_{\text{sq}} | (\delta X)^2 | \psi_{\text{sq}} \rangle = \frac{1}{2} e^{-2r} \quad (8.5)$$

$$\langle \psi_{\text{sq}} | (\delta Y)^2 | \psi_{\text{sq}} \rangle = \frac{1}{2} e^{+2r} \quad (8.6)$$

The two-mode squeezed state is therefore a state where the product of the two uncertainties is at its fundamental limit, and $r = |\xi|$ determines their relative size.

Let us now see how this relates to the quantum antiferromagnet. In Sec. 2.3, we introduced the Bogoliubov transformation by introducing new operators

$$\alpha_{\mathbf{k}} = u_{\mathbf{k}} a_{\mathbf{k}} - v_{\mathbf{k}} b_{-\mathbf{k}}^\dagger \quad (8.7)$$

$$\beta_{-\mathbf{k}}^\dagger = u_{\mathbf{k}} b_{-\mathbf{k}}^\dagger - v_{\mathbf{k}} a_{\mathbf{k}}, \quad (8.8)$$

where $u_{\mathbf{k}}$ and $v_{\mathbf{k}}$ can be expressed as $u_{\mathbf{k}} = \cosh \theta_{\mathbf{k}}$ and $v_{\mathbf{k}} = \sinh \theta_{\mathbf{k}}$. Alternately, we may think of the Bogoliubov transformation as being generated by the unitary operator $S_{\mathbf{k}}$ through

$$\begin{pmatrix} \alpha_{\mathbf{k}} \\ \beta_{-\mathbf{k}}^\dagger \end{pmatrix} = S_{\mathbf{k}} \begin{pmatrix} a_{\mathbf{k}} \\ b_{-\mathbf{k}}^\dagger \end{pmatrix} S_{\mathbf{k}}^\dagger, \quad (8.9)$$

where $S_{\mathbf{k}}$ is given by

$$S_{\mathbf{k}} = \exp[-\theta_{\mathbf{k}}(a_{\mathbf{k}}b_{-\mathbf{k}} - a_{\mathbf{k}}^\dagger b_{-\mathbf{k}}^\dagger)]. \quad (8.10)$$

The equivalence with the usual form of the Bogoliubov transformation in Eq. (8.8) can be shown using the Baker-Hausdorff-Campbell lemma¹. We now immediately recognize the operator $S_{\mathbf{k}}$ as the two-mode squeezing operator with squeezing parameter $|\theta_{\mathbf{k}}|$.

This way of expressing the Bogoliubov transformation also implies that the vacuum state $|\{0_{\mathbf{k}}, 0_{\mathbf{k}}\}\}_{\text{sq}}$ for the eigenmagnons and the vacuum state $|\{0_{\mathbf{k}}, 0_{\mathbf{k}}\}\}_{\text{subl}}$ for the sublattice magnons are related through

$$|\{0_{\mathbf{k}}, 0_{\mathbf{k}}\}\}_{\text{sq}} = S_{\mathbf{k}}|\{0_{\mathbf{k}}, 0_{\mathbf{k}}\}\}_{\text{subl}}. \quad (8.11)$$

The ground state of the antiferromagnet is therefore generated from the sublattice vacuum state by applying the squeezing operator. Thus, the quantities $X_{\mathbf{k}}$ and $Y_{\mathbf{k}}$ defined analogous to Eq. (8.4) do not commute, and instead satisfy an uncertainty relation. The operators $X_{\mathbf{k}}$ and $Y_{\mathbf{k}}$ can be interpreted in terms of the spin operators in the original model by using the linear spin wave theory representations. For simplicity, we consider the limit $\mathbf{k} \rightarrow 0$, for which we have,

$$X_{\mathbf{k} \rightarrow 0} = \frac{1}{\sqrt{2NS}} \sum_n (S_{nA}^x + S_{nB}^x) \quad (8.12a)$$

$$Y_{\mathbf{k} \rightarrow 0} = \frac{1}{\sqrt{2NS}} \sum_n (S_{nA}^y - S_{nB}^y). \quad (8.12b)$$

Thus, fluctuations in the net spin of one in-plane spin component are suppressed and enhanced conjugate to the fluctuations in the orthogonal in-plane component of the Néel order parameter.

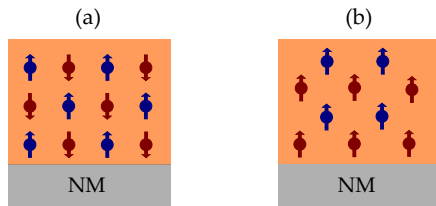


Figure 8.1: (a) Compensated antiferromagnetic interface. The normal metal couples equally to both sublattices. (b) Uncompensated interface. The normal metal couples asymmetrically to the two sublattices.

8.1.2 Sublattice interferences and enhanced interaction

In Sec. 2.3, we pointed out that when $\theta_{\mathbf{k}}$ is large, the quantum ground is a superposition consisting of terms with many spin-flips on top of the Néel state. Under these circumstances, the magnitude of the coherence factors $u_{\mathbf{k}}$ and $v_{\mathbf{k}}$ may also be large.

Consider now a situation where the spins in an antiferromagnet are coupled to some other degrees of freedom. Within linear spin-wave theory these spins can be represented in terms of sublattice magnons $a_{\mathbf{k}}$ and $b_{-\mathbf{k}}^\dagger$. When expressing the coupling in terms of the eigenexcitations, we therefore get an effective coupling proportional to coherence factors $u_{\mathbf{k}}$ and $v_{\mathbf{k}}$. Since these can become large, the effective interaction strength may be drastically enhanced.

However, these coherence factors may also interfere destructively to suppress the effective coupling strengths. These interferences are sensitive to how we couple to the two sublattices of the antiferromagnet. In Fig. 8.1, we show a normal metal coupled to a compensated interface in (a), and to an uncompensated interface in (b) [302]. Sublattice interferences may then produce drastically different effective coupling strengths in the two cases.

In Paper [3] we discuss this briefly in the context of electron-magnon and magnon-magnon coupling. In the remainder of this chapter, we will see how the mechanism can unfold by studying superconductivity in a normal metal mediated by magnons in an adjacent antiferromagnet.

¹In short, the Baker-Hausdorff-Campbell lemma states that [33]

$$e^B A e^{-B} = A + [B, A] + \frac{1}{2!} [B, [B, A]] + \frac{1}{3!} [B, [B, [B, A]]] + \dots,$$

where A and B are operators.

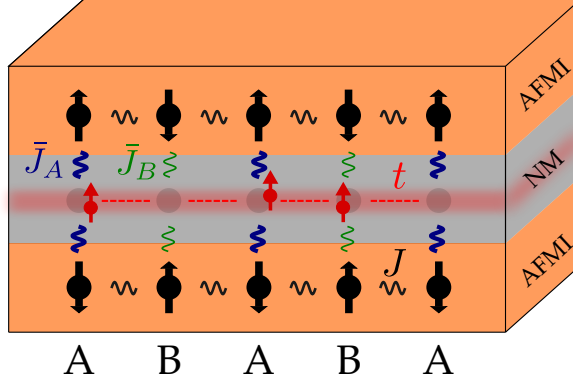


Figure 8.2: Model system. A normal metal is sandwiched between two antiferromagnetic insulators. The spins in the AFMIs interact with the electrons in the normal metal through their spin, and we allow this coupling to be sublattice dependent, with coupling $\bar{J}_A = \bar{J}\Omega_A$ to the A -sublattice and $\bar{J}_B = \bar{J}\Omega_B$ to the B -sublattice.

8.2 Heterostructure model system

We study superconductivity in a heterostructure consisting of a normal metal sandwiched between two antiferromagnetic insulators, as sketched in Fig. 8.2. We therefore consider a model Hamiltonian on the form $H = H_{NM} + H_{AFMI} + H_{\text{int}}$, where the respective terms describe electrons in the normal metal, spins in the antiferromagnetic insulators, and the interaction between the layers. We assume that both the normal metal and the antiferromagnetic insulators can be modelled by matching square lattices.

To describe the normal metal, we use a hopping model

$$H_{NM} = -t \sum_{(ij),\sigma} c_{i\sigma}^\dagger c_{j\sigma} - \mu \sum_{i\sigma} c_{i\sigma}^\dagger c_{i\sigma}, \quad (8.13)$$

where t is the nearest neighbour hopping amplitude, and μ the chemical potential controlling the doping.

Furthermore, we assume the antiferromagnetic insulators to be described by an antiferromagnetic Heisenberg model

$$H_{AFMI} = \sum_{ij,\eta} J_{ij} \mathbf{S}_{i\eta} \cdot \mathbf{S}_{j\eta} - K \sum_{i,\eta} (S_{i\eta}^z)^2, \quad (8.14)$$

where $\mathbf{S}_{i\eta}$ is a spin on the lattice site i , $\eta \in \{H, L\}$ specifies whether the spin resides in the upper (H) or lower (L) antiferromagnet. We also assume that the antiferromagnetic order in the two antiferromagnets is such that the spins of corresponding lattices sites are oriented oppositely, as shown in Fig. 8.2. The exchange coupling J_{ij} between lattices sites i and j is assumed to take the value $J_1 > 0$ for nearest neighbour sites and $J_2 > 0$ for the next-to-nearest neighbour sites. Furthermore, K is an easy axis anisotropy. The excitation spectrum, eigenexcitations, and ground state of this model have been discussed within linear spin wave theory in Chapter 2.

Finally, we assume the electrons in the normal metal to interact with the antiferromagnet through their spin through the interaction Hamiltonian

$$H_{\text{int}} = -2\bar{J} \sum_{\eta, \Upsilon} \sum_{i \in \Upsilon} \Omega_{\Upsilon} c_i^{\dagger} \boldsymbol{\sigma} c_i \cdot \mathbf{S}_{i\eta}, \quad (8.15)$$

where $\boldsymbol{\sigma}$ is the Pauli matrix vector in electron spin space, and we have introduced an electron spinor $c_i = (c_{i\uparrow}, c_{i\downarrow})^T$. While the sum over Υ runs over the sublattices of an antiferromagnet, the sum over i runs over the lattice sites i on sublattice Υ , while i is also used to denote the corresponding lattice sites in the normal metal and the other antiferromagnet. The interfacial exchange coupling strength is denoted by \bar{J} , while the dimensionless parameter Ω_{Υ}^{η} allows the introduction of a sublattice coupling asymmetry.

8.3 Processes and Eliashberg theory

Although the square lattices of the normal metal and the antiferromagnets match, the subsystems have different periodicity due to the antiferromagnetic order in the magnetic insulators, as illustrated in Fig. 8.3 (a). Therefore, as shown in Fig. 8.3 (b), the magnon Brillouin zone is reduced compared to the electron Brillouin zone. This incompatibility gives rise to two different kinds of scattering processes in the electron-magnon interaction Hamiltonian, which takes the form

$$H_{\text{int}} = V \sum_{\substack{\mathbf{k} \in \square \\ \mathbf{q} \in \diamond}} \left[M_{\mathbf{q}}^R c_{\mathbf{k}+\mathbf{q},\downarrow}^{\dagger} c_{\mathbf{k},\uparrow} + M_{\mathbf{q}}^U c_{\mathbf{k}+\mathbf{q}+\mathbf{Q},\downarrow}^{\dagger} c_{\mathbf{k},\uparrow} + \text{h.c.} \right]. \quad (8.16)$$

Here, the sum over \mathbf{k} runs over the electron Brillouin zone, and the sum over \mathbf{q} over the magnon Brillouin zone. Furthermore, $c_{\mathbf{k}\sigma}$ are electron annihilation operators in momentum space, and as discussed further down, $M_{\mathbf{q}}^R$ and

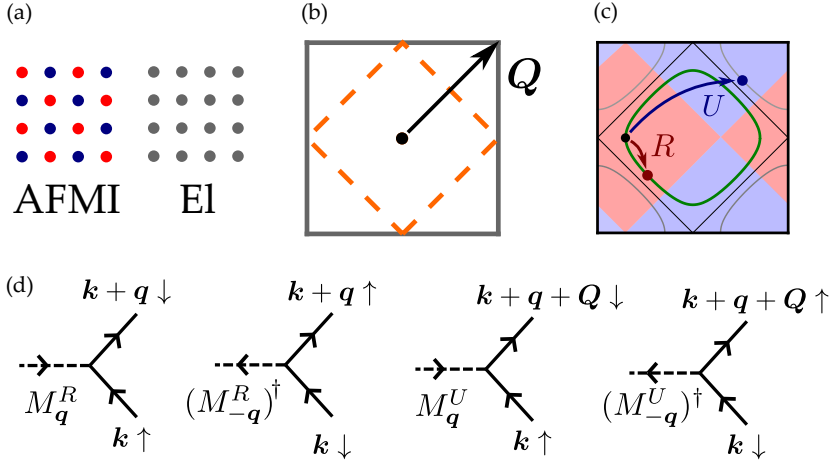


Figure 8.3: (a) The periodicity of the AFMI system is enlarged compared to the electrons. (b) The magnon Brillouin zone (orange) is reduced compared to the electron Brillouin zone (grey). (c) Regular (red) and Umklapp processes (blue) from a point on the Fermi surface (green). (d) The four different magnon scattering processes in the system.

M_q^U are linear combinations of the eigenmagnon operators in the antiferromagnets. Thus, there are two kinds of electron scattering processes. In the regular processes (R), electrons scatter from a momentum \mathbf{k} to a momentum \mathbf{k}' such that $\mathbf{k}' - \mathbf{k}$ is within the first magnon Brillouin zone². In the Umklapp processes (U), the electron gains an additional momentum kick \mathbf{Q} corresponding to a magnon reciprocal lattice vector. This is also shown in Fig. 8.3 (c). Since the electron spin can either flip from \downarrow to \uparrow or \uparrow to \downarrow , this gives a total of four different scattering processes in the system, which are shown in Fig. 8.3 (d). We also notice that since the magnon operators carry finite spin ± 1 , spin is conserved in the scattering processes.

The explicit expression for the magnon operator M_q^κ is $M_q^\kappa = M_{qH}^\kappa + M_{qL}^\kappa$, where the contributions from the upper (H) and the lower (L) antiferromagnets can be written

²Or, to be precise, a momentum which can be obtained by adding an electron reciprocal lattice vector to a momentum within the first magnon Brillouin zone.

$$\begin{aligned}
M_{\mathbf{q}H}^\kappa &= (\Omega_A u_{\mathbf{q}} + \kappa \Omega_B v_{\mathbf{q}}) \alpha_{\mathbf{q}H} + (\Omega_A v_{\mathbf{q}} + \kappa \Omega_B u_{\mathbf{q}}) \beta_{-\mathbf{q}H}^\dagger \\
M_{\mathbf{q}L}^\kappa &= (\Omega_A u_{\mathbf{q}} + \kappa \Omega_B v_{\mathbf{q}}) \alpha_{-\mathbf{q}L}^\dagger + (\Omega_A v_{\mathbf{q}} + \kappa \Omega_B u_{\mathbf{q}}) \beta_{\mathbf{q}L},
\end{aligned} \tag{8.17}$$

and $\kappa \in \{R, U\}$, where we have associated the indices with the values $R \rightarrow +1$ and $U \rightarrow -1$. Here, $\alpha_{\mathbf{q}\eta}$ and $\beta_{\mathbf{q}\eta}$ are eigenmagnon annihilation operators for antiferromagnet η , as discussed in Chapter 2.

Eventually, we aim at constructing Eliashberg theory for the system. The key building blocks are therefore the magnon operator propagators, which are defined by

$$\mathcal{D}^{\kappa\kappa'}(\mathbf{q}, \tau) = -\langle T_\tau M_{\mathbf{q}}^\kappa(\tau) (M_{\mathbf{q}}^{\kappa'})^\dagger(0) \rangle \tag{8.18}$$

in Matsubara space. By explicit calculation utilizing the eigenmagnon propagators in the non-interacting theory, we obtain frequency dependent magnon propagators

$$\mathcal{D}_0^{\kappa\kappa'}(\mathbf{q}, i\nu_m) = -2A_e^{\kappa\kappa'}(\mathbf{q}) \frac{2\omega_{\mathbf{q}}}{\nu_m^2 + \omega_{\mathbf{q}}^2}, \tag{8.19}$$

where we have introduced quantities

$$A_e^{RR}(\mathbf{q}) = \frac{1}{2} [(\Omega_A u_{\mathbf{q}} + \Omega_B v_{\mathbf{q}})^2 + (\Omega_A v_{\mathbf{q}} + \Omega_B u_{\mathbf{q}})^2], \tag{8.20a}$$

$$A_e^{UU}(\mathbf{q}) = \frac{1}{2} [(\Omega_A u_{\mathbf{q}} - \Omega_B v_{\mathbf{q}})^2 + (\Omega_A v_{\mathbf{q}} - \Omega_B u_{\mathbf{q}})^2], \tag{8.20b}$$

$$A_e^{RU}(\mathbf{q}) = A_e^{UR}(\mathbf{q}) = \frac{1}{2} (\Omega_A^2 - \Omega_B^2) (u_{\mathbf{q}}^2 + v_{\mathbf{q}}^2). \tag{8.20c}$$

We refer to these as boosting factors.

In addition to terms originating from the A -sublattice proportional to Ω_A^2 and terms from the B -sublattice proportional to Ω_B^2 , the boosting factors have interference terms proportional to $\Omega_A \Omega_B$. Thus, there are sublattice interferences when coupling equally to the sublattices ($\Omega \equiv \Omega_B / \Omega_A = 1$), while the interferences are completely suppressed when coupling only to one sublattice ($\Omega = 0$).

The coherence factors and boosting factors are shown in Fig. 8.4 for momenta \mathbf{q} corresponding to scattering processes between points on the Fermi surface. Since $u_{\mathbf{q}}$ is positive and $v_{\mathbf{q}}$ is negative for small scattering processes,

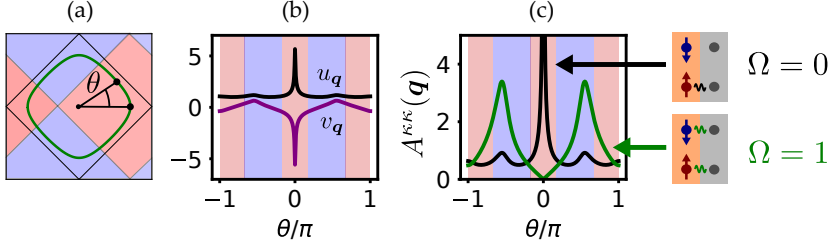


Figure 8.4: (a) Scattering of electrons between points on the Fermi surfaces is described by angle θ . (b) Magnon coherence factors for scattering processes between points on the Fermi surface. (c) Boosting factor for magnon scattering processes between points on the Fermi surface coupling asymmetrically ($\Omega = 0$) and symmetrically ($\Omega = 1$) to the sublattices of the antiferromagnet. Parameter values for the AFM have been set to $K/J_1 = 10^{-4}J_1$ and $J_2/J_1 = 0.2$.

as shown in (b), the sublattice interference effects suppress the regular process boosting factors for small scattering momenta. The Umklapp scattering processes, however, are enhanced. Thus, the sublattice coupling asymmetry acts as gatekeeper controlling the relative importance of the regular processes and the Umklapp processes in the system.

Using electron and magnon Green's functions, we may now derive the Eliashberg equations for magnon-mediated superconductivity using the approach discussed in Chapter 5. The details are given in Paper [4], and the result is

$$[1 - Z(k)]i\omega_n = -V^2 \frac{1}{\beta} \sum_{k'} \mathcal{D}(k - k') \frac{i\omega_{n'} Z(k')}{\Theta(k')} \quad (8.21a)$$

$$\chi(k) = -V^2 \frac{1}{\beta} \sum_{k'} \mathcal{D}(k - k') \frac{\xi_{k'} + \chi(k')}{\Theta(k')} \quad (8.21b)$$

$$\phi_s(k) = -V^2 \frac{1}{\beta} \sum_{k'} \mathcal{D}(k - k') \frac{\phi_s(k')}{\Theta(k')} \quad (8.21c)$$

$$\phi_t(k) = +V^2 \frac{1}{\beta} \sum_{k'} \mathcal{D}(k - k') \frac{\phi_t(k')}{\Theta(k')}, \quad (8.21d)$$

where we assume that one symmetry channel dominates and consider only spin singlet pairing or only spin triplet pairing. Here, we have also introduced

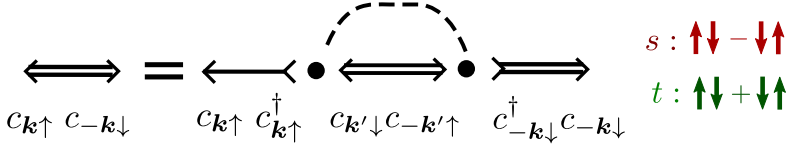


Figure 8.5: Feynman diagram for the Eliashberg gap equation. Electron propagators are represented with arrows with arrowheads corresponding to creation or annihilation operators pointing in or out from the line. Spin is flipped at vertices.

the magnon propagator

$$\mathcal{D}(\mathbf{q}, i\nu_m) = \theta_{\mathbf{q}} \mathcal{D}^{RR}(\mathbf{q}, i\nu_m) + \theta_{\mathbf{q}+\mathbf{Q}} \mathcal{D}^{UU}(\mathbf{q} + \mathbf{Q}, i\nu_m), \quad (8.22)$$

where $\theta_{\mathbf{q}} = 1$ when \mathbf{q} is equivalent to a point in the first magnon Brillouin zone, and zero otherwise. The propagator therefore represents both regular processes and Umklapp processes depending on electron scattering momentum $\mathbf{k}' - \mathbf{k}$, as indicated with the shaded blue and red regions in Fig. 8.4(a). The factor Θ is given by

$$\Theta(\mathbf{k}, i\omega_n) = [i\omega_n Z(\mathbf{k}, i\omega_n)]^2 - \tilde{\xi}_k^2 - |\phi_{s,t}(\mathbf{k}, i\omega_n)|^2, \quad (8.23)$$

with gap $\phi_{s,t}$ depending on whether we consider spin triplet or spin singlet pairing.

Crucially, we notice that the sign in front of the spin singlet and spin triplet pairing equations are different. Comparing with the Eliashberg equations for phonon-mediated superconductivity, in Eq. (5.85), the sign in front of the spin singlet equation has been changed. This can quite easily be understood by drawing the Feynman diagram corresponding to the equations, as shown in Fig. 8.5. The vertices of the electron-magnon interaction are associated with a spin flip since the magnons carry a spin. Therefore, and in contrast with phonon-mediated superconductivity, the spin singlet amplitude acquires an additional sign change.

In the Eliashberg equations, both Θ and $\mathcal{D}(q)$ above are negative. Therefore, electron scattering processes are attractive with respect to spin singlet pairing when $\phi_s(k)$ and $\phi_s(k')$ have opposite signs, while the processes are attractive with respect to spin triplet pairing when $\phi_t(k)$ and $\phi_t(k')$ have the same sign.

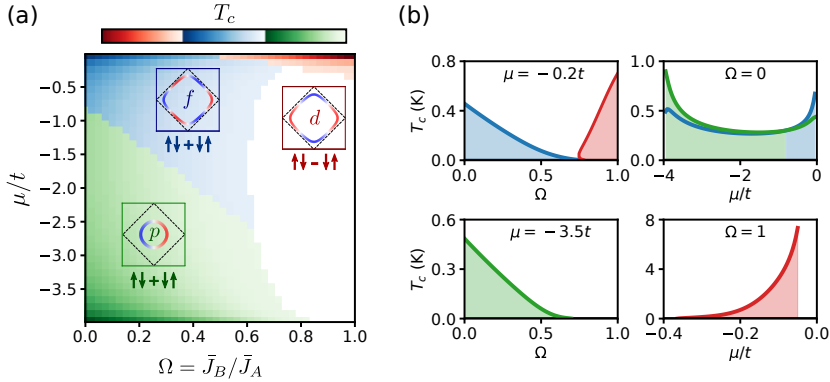


Figure 8.6: (a) Phase diagram for superconducting phases in the μ - Ω plane. (b) Critical temperature along various lines in the phase diagram.

8.4 Phase diagram and results

Integrating out the momentum perpendicular to the Fermi surface, one may obtain Fermi surface averaged equations from the fully momentum dependent equations in Eq. (8.21). By introducing various Ansätze for the anomalous correlation momentum structure on the Fermi surface, one may furthermore simplify the equations to an eigenvalue problem in the Matsubara frequency dependent fields. Solving the linearized eigenvalue problem, we then obtain the critical temperature of the superconducting instability for various phases.

In Paper [4], we consider Ansätze for even frequency spin triplet p -wave and f -wave pairing, as well as even frequency spin singlet d -wave pairing. For each of these pairing symmetries, we calculate a critical temperature, and assume the phase with the largest critical temperature to dominate. One may then calculate a phase diagram in the μ - Ω plane as shown in Fig. 8.6 (a), while the critical temperature along different lines in the phase diagram is shown in (b). In the following, we discuss these results in further detail.

8.4.1 Understanding the phase diagram

Depending on sublattice coupling asymmetry Ω and doping μ , we find three different phases in the phase diagram. For small Ω to the left in the phase diagram, we find spin triplet phases, with a p -wave phase for large dopings and small Fermi surfaces, and an f -wave phase for small dopings and large

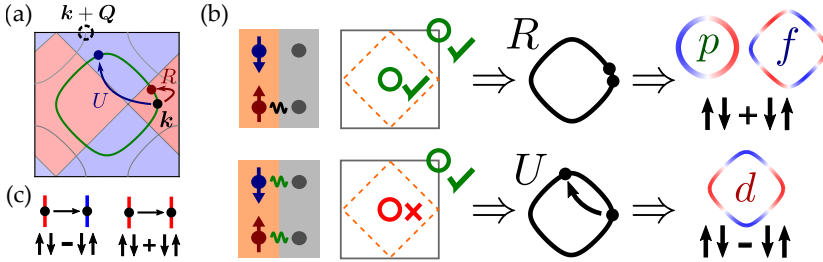


Figure 8.7: (a) The dominant scattering processes are regular processes on the Fermi surface with outgoing momentum \mathbf{k}' close to \mathbf{k} and $\mathbf{k} + \mathbf{Q}$, corresponding to regular and Umklapp processes. (b) Qualitative explanation for the general structure of the phase diagram in Fig. 8.6, as discussed in the main text. (c) The spin singlet (triplet) channel is attractive for processes where $\phi(\mathbf{k})$ and $\phi(\mathbf{k}')$ have opposite (the same) signs.

Fermi surfaces. For $\Omega \approx 1$, however, we find a d -wave phase for small dopings corresponding to small $|\mu|$.

This can be understood qualitatively based on the various processes that contribute to the pairing, and the argument is illustrated in Fig. 8.7. The magnon propagator acts as effective pairing potential in the Eliashberg equations, and the zero frequency contribution is $D(\mathbf{q}, i\nu_m = 0) \propto A^{\kappa\kappa}(\mathbf{q})/\omega_{\mathbf{q}}$. Thus, we expect the processes with small magnon frequency to dominate the pairing. As illustrated in Fig. 8.7 (a), magnon frequencies may be small both when the outgoing momentum \mathbf{k}' is close to the incoming momentum \mathbf{k} , and when it is close $\mathbf{k} + \mathbf{Q}$. This corresponds to regular processes and Umklapp processes.

When we couple to only one sublattice, there are no sublattice interferences magnon propagator. Thus, as shown in (b), we may in principle have significant contributions both from regular and Umklapp processes. Yet, the regular processes tend to dominate because they are associated with lower magnon frequencies and larger boosting factors, as a momentum \mathbf{k}' on the Fermi surface can come arbitrarily close to the momentum \mathbf{k} but not to $\mathbf{k} + \mathbf{Q}$. Small momentum scattering processes must necessarily be between parts of the Fermi surface where the gap has the same sign. Furthermore, the spin triplet channel is attractive for scattering processes between momenta \mathbf{k} and \mathbf{k}' where the anomalous pairing has the same sign, as indicated in (c). In contrast, the spin singlet channel is repulsive. Since the electron pair wave function has to be antisymmetric in total, we therefore expect pairing which

is even in frequency, spin triplet, and odd in momentum when coupling only to one sublattice. As seen on the left side of the phase diagram, this is exactly what we find.

When we instead couple equally to both sublattices, sublattice interferences suppress the regular processes with small momentum \mathbf{q} and enhance the Umklapp processes, as also discussed in Sec. 8.3. Thus, Umklapp processes dominate the pairing. In principle, both spin triplet and spin singlet pairing may result from these processes. For the triplet pairing channel, however, the gap would typically have to be small in one out of two adjacent corners of the Fermi surface (see the p -wave and f -wave profiles), as the gap would have to be antisymmetric in momentum. This would suppress pairing. In contrast, spin singlet d -wave pairing matches the Umklapp processes perfectly, as the Umklapp process connects momenta on the Fermi surface where the gap has different signs, and the processes are therefore attractive in the spin singlet channel. In the phase diagram, we therefore find a d -wave phase for $\Omega \approx 1$ and small doping. As we increase the doping, the minimum distance between the a point \mathbf{k}' on the Fermi surface and $\mathbf{k} + \mathbf{Q}$ increases, and the critical temperature of the d -wave phase becomes suppressed. Notably, sublattice interferences is the very reason that the d -wave phase can occur, since otherwise, the critical temperature for spin singlet pairing would be completely suppressed due to the repulsive regular processes with small momentum scattering.

The above argument explains the general structure of the phase diagram. However, it does not immediately explain why we find a p -wave solution to the gap equation for large dopings and an f -wave solution for small dopings for $\Omega = 0$. This is discussed in somewhat more detail in Paper [4], but in short, it can be explained as follows: Regular processes dominate the pairing, but subleading Umklapp processes become attractive instead of repulsive when there is an additional node in the gap on the Fermi surface. Moving from large doping towards the small doping regime, the importance of the Umklapp processes increases, and eventually, the f -wave phase is preferred over the p -wave phase.

8.4.2 Characteristic magnon frequency

Comparing our results for the critical temperature with previous results for the p -wave phase using BCS theory [141], we find that it has been significantly reduced. This occurs because Eliashberg theory, unlike BCS theory, handles the retarded nature of the effective interaction properly through the frequency dependence of the fields. This is one of the central points in Pa-

per [4]. We discuss it in detail there, also including an explicit calculation of the characteristic magnon frequency and the Eliashberg function $\alpha^2F(\omega)$.

Qualitatively, the effect can be understood based on the knowledge of which processes that dominate in the pairing interaction. For the p -wave phase, these are regular processes with a small momentum transfer \mathbf{q} , corresponding to small magnon frequencies. Thus, the characteristic magnon frequency in the pairing is significantly reduced, and this also reduces the critical temperature. For the d -wave phase, we have a similar effect, but the reduction is less dramatic there, since the typical processes contributing to the pairing have a larger magnon frequency.

8.4.3 Comparison with phonon-mediated superconductivity

Our previous discussion allows an instructive and rather general comparison of magnon-mediated and phonon-mediated superconductivity. This serves to highlight some special features of magnon-mediated superconductivity, but also allows us to appreciate some of the properties of the phonon mechanism of superconductivity which could easily be taken for granted.

The first, and maybe most obvious difference, is that in magnon-mediated superconductivity, the bosons responsible for the superconducting pairing carry a spin. This is important because it causes the spin singlet pairing amplitude to be repulsive for scattering processes where the pairing amplitudes have the same sign. Therefore, the magnon-mediated superconductivity does not have s -wave pairing symmetry, in contrast with almost all superconductors with a phonon-mediated pairing mechanism.

Second, the coupling between the electrons and the spin excitations is via the spin, and the coupling across the interface is therefore effectively local in space. Thus, the coupling matrix element does not go to zero for scattering processes $\mathbf{q} \rightarrow 0$. Since the magnon frequencies are small close to $\mathbf{q} = 0$ and $\mathbf{q} = \mathbf{Q}$, this allows scattering processes with magnon momenta close to these values to dominate the superconducting pairing. As we have already discussed, this is also the reason that a detailed investigation of the characteristic magnon frequency is necessary. In contrast, the electron-phonon coupling matrix element goes to zero as $\mathbf{q} \rightarrow 0$ for acoustic modes because electron-phonon coupling is a coupling between the electrons and modulations of ion densities. Since the effective pairing potential on the Fermi surface is then on the form $V_{\mathbf{k},\mathbf{k}+\mathbf{q}} \sim |g_{\mathbf{k},\mathbf{k}+\mathbf{q}}|^2/\omega_{\mathbf{q}}$ for scattering processes on the Fermi surface, where $|g_{\mathbf{k},\mathbf{k}+\mathbf{q}}|^2 \propto q$, the effective pairing potential approaches a constant for acoustic modes. Thus, scattering processes on the

Fermi surface are roughly equally important. This simplifies the theoretical treatment of phonon-mediated superconductivity, and also tends to favour s -wave superconductivity.

8.5 Discussion

Whereas Eliashberg theory is based on several assumptions regardless of whether we consider superconductivity due to phonons or magnons, some points should be addressed specifically in light of our model and the magnon-mediated mechanism. Broadly speaking, a number of these points are related to two underlying properties of the system.

The first set of points is related to the peaked nature of the effective interaction. As discussed in the previous section, phonon-mediated superconductivity is rather democratic in the sense that almost all processes between points on the Fermi surface are allowed to contribute similarly to the pairing. Thus, the magnon propagator typically depends weakly on momentum, and this allows the Fermi surface averaging procedure to work well. The situation is less clear within magnon-mediated superconductivity, where the effective potential is peaked. The electron-magnon interaction also renormalizes the effective magnon frequency, and the relative change is larger for small magnon frequencies. Finally, we know that Migdals theorem for phonon-mediated superconductivity becomes questionable for small momentum processes with a small scattering momentum \mathbf{q} . Since the small momentum scattering processes are dominant in the spin triplet pairing phases in our results, the importance of vertex corrections should also be discussed.

The second set of points is related to the shape of the Fermi surface close to half filling. At half filling, there is a van Hove singularity in the density of states, and the Fermi surface becomes perfectly nested. Close to half-filling, we therefore expect on-set of spin density wave correlations [22, 23, 303], which have been neglected. Furthermore, nesting also enhances vertex corrections. Evaluating the behaviour of the system very close to half-filling therefore becomes very challenging.

We discuss all these points in significantly more detail in Paper [4], but a full quantitative investigation is outside the scope of the paper. Although we expect that some of the effects can be important for properties such as the critical temperature, it seems likely that the main features of superconductivity induced by interfacial coupling to antiferromagnets are captured within the approach in the paper.

We have developed Eliashberg theory for magnon-mediated superconduc-

tivity in a heterostructure of a normal metal coupled to antiferromagnetic insulators. We find various superconducting phases such as even frequency spin triplet p - and f -wave phases, and an even frequency spin singlet d -wave phase. These phases occur in various regimes depending on doping and sublattice coupling asymmetry, and this emphasizes the important role played by sublattice interferences in superconductivity mediated by antiferromagnetic magnons. Furthermore, Eliashberg theory captures the retarded nature of the interaction, and compared with BCS theory estimates, this impacts critical temperature estimates significantly.

Chapter 9

Conclusion

The three fundamental degrees of freedom in the solid state are the motion of the electrons, the vibrations of the lattice, and the spins of electrons and ions. In this thesis, and in Papers [1–4] which form the core of this thesis, we have been studying collective effects which occur when these degrees of freedom interact.

In Paper [1], we considered topological magnons interacting with phonons. The two main characteristic properties of topologically non-trivial systems are finite Hall conductivities and the presence of edge modes. We discussed how these properties are affected by magnon-phonon coupling.

In Paper [2], we considered phonons interacting with electrons in doped graphene. Specifically, we discussed the possibility of a phonon-induced superconducting instability within a tight binding approach.

In Paper [3], we interpreted the eigenexcitations of quantum antiferromagnets as squeezed magnons, and discussed some implications of this.

In Paper [4], we considered electrons in a normal metal coupled to the magnons of adjacent antiferromagnets, and discussed the possibility of magnon-mediated superconductivity in the system. Developing an Eliashberg theory for the system, we found various superconducting phases, and demonstrated the importance of handling the retarded nature of the effective electron-electron interaction properly.

Understanding interacting quantum systems is in general a highly non-trivial task, as we have seen numerous examples of throughout this thesis. To understand a particular effect, a common tactic is to isolate the interaction believed to be responsible for the effect, and hope that the resulting problem is sufficiently simple to be analytically or numerically tractable. This

approach has generally been very successful in condensed matter physics, but there is always a risk of oversimplifying the system or missing out on fascinating physics which occur due to the interplay of interaction effects. With this in mind, we may identify a few possible avenues for further investigations.

Since the concept of topological classification of band structures is designed specifically to describe quadratic Hamiltonians, the presence of interactions introduces significant complications. While typical interactions in an electronic system such as electron-phonon coupling or Coulomb interaction conserve electron numbers, in topological bosonic systems, however, we are often working with systems where the boson number is not conserved. There are several unresolved matters concerning how the concept of topology should be applied to these systems, and how it can be connected to observables.

Although simple models exist to incorporate the effect of Coulomb interactions in superconductors, a detailed understanding of their effect is a notoriously difficult task. Also in graphene, attempts to understand possible superconductivity have typically been based on very simple approaches to include Coulomb interaction, and going beyond these approaches is of high interest. Furthermore, a study of possible phonon-mediated superconductivity in graphene at the van Hove singularity would require the incorporation also of the strong correlation effects occurring in that doping regime.

Within Eliashberg theory for magnon-mediated superconductivity, we already discussed correlation effects such as vertex corrections and magnon renormalization. More detailed studies of these effects are desirable, but also very challenging. Close to half-filling, we expect the onset of spin density wave correlations, and these have previously been studied within Eliashberg theory due to a phonon-induced mechanism. An interesting avenue for further research is therefore to see whether the expected magnon induced instability is similar, and potentially how spin density wave correlations interplay with superconductivity.

Appendix A

Currents and Hall conductivities

In this Appendix, we discuss the derivation of the linear response expressions for the Hall conductivity in somewhat more detail. We first discuss electron and spin currents in Sec. A.1. In Sec. A.2, we then discuss how the Hall conductivity can be expressed in terms of band structure Berry curvatures in bosonic and fermionic systems.

A.1 Current operators

A.1.1 Electron current

To discuss the calculation of operator expressions for electron currents, we consider a system of electrons described by a tight binding hopping model on a lattice. In the absence of an electromagnetic field, this system can be described by a Hamiltonian on the form

$$H = - \sum_{ij} t_{ij} c_i^\dagger c_j, \quad (\text{A.1})$$

where $t_{ij} = t_{ji}^*$ is in general complex. We aim at deriving an expression for the current operator in second quantization. The Fourier representation of the Hamiltonian is

$$H = \sum_{\mathbf{k}} \sum_{\alpha\beta} h_{\alpha\beta}(\mathbf{k}) c_{\mathbf{k}\alpha}^\dagger c_{\mathbf{k}\beta}, \quad (\text{A.2})$$

where the matrix $h_{\alpha\beta}(\mathbf{k})$ is given by

$$h_{\alpha\beta}(\mathbf{k}) = - \sum_{\boldsymbol{\delta}^{\alpha\beta}} t(\boldsymbol{\delta}^{\alpha\beta}) e^{i\mathbf{k}\cdot\boldsymbol{\delta}^{\alpha\beta}}. \quad (\text{A.3})$$

Here, the sum over $\boldsymbol{\delta}^{\alpha\beta}$ denotes a sum over neighbour vectors from sublattice α to sublattice β , where $t(\boldsymbol{\delta}^{\alpha\beta}) = t_{i_\alpha, i_\alpha + \boldsymbol{\delta}^{\alpha\beta}}$ for any lattice point i_α on sublattice α .

In general, the current operator j_μ along direction μ for a system in an electromagnetic field consists of a paramagnetic and a diamagnetic part, since the canonical and kinematic momenta are in general different [45]. However, since the diamagnetic part does not contribute to Hall conductivities [46], we focus on the paramagnetic part in the following.

Electron charge is a conserved quantity, and it must therefore satisfy the continuity equation

$$e\dot{n}_i + \sum_{\delta} j_{i, i+\delta} = 0, \quad (\text{A.4})$$

where $j_{i, i+\delta}$ is the current flowing from lattice site i to lattice site $i+\delta$. Within the Heisenberg picture [33], the continuity equation is an operator equation, describing the relation between the time evolution of the density operator n_i and the current operators. Furthermore, we know that the time evolution of this density operator is given by the Heisenberg equation of motion¹

$$e\dot{n}_i = -\frac{ie}{\hbar} [n_i, H], \quad (\text{A.5})$$

where H is the Hamiltonian describing the system in the absence of the electromagnetic field. Using the explicit form of the Hamiltonian in Eq. (3.4), the bond currents can be written

$$j_{ij} = -\frac{ie}{\hbar} (t_{ij}c_i^\dagger c_j - t_{ji}c_j^\dagger c_i) \quad (\text{A.6})$$

From this, we may define the paramagnetic current density associated with lattice site i as

$$\mathbf{j}_i = \frac{1}{V_{\text{uc}}} \sum_j j_{ij} \boldsymbol{\delta}_{ij}, \quad (\text{A.7})$$

where $\boldsymbol{\delta}_{ij}$ is the displacement vector between lattice sites i and j , and V_{uc} is the real space unit cell volume. We may now also introduce the Fourier transform of the current through

¹ Assuming that the Hamiltonian is not explicitly time dependent.

$$\mathbf{j}(\mathbf{q}) = \frac{1}{2\sqrt{N}} \sum_i e^{i\mathbf{q}\cdot\mathbf{x}_i} \mathbf{j}_i, \quad (\text{A.8})$$

where N is the number of unit cells in the system and \mathbf{x}_i the position of lattice site i . Expressing this Fourier transformed current in terms of the Fourier transformed creation and annihilation operators, we obtain current

$$\mathbf{j}(\mathbf{q}) = -\frac{e}{2\hbar} \sum_{\alpha\beta} \sum_{\mathbf{k}} \sum_{\delta^{\alpha\beta}} \left(t(\delta^{\alpha\beta}) e^{i\mathbf{k}\cdot\delta^{\alpha\beta}} i\delta^{\alpha\beta} c_{\mathbf{k}+\mathbf{q},\alpha}^\dagger c_{\mathbf{k},\beta} + \text{h.c.} \right). \quad (\text{A.9})$$

When calculating Hall conductivities, we are interested in the homogeneous zero frequency response. We therefore let $\mathbf{q} \rightarrow 0$, and obtain

$$j_\mu(\mathbf{q}=0) = \frac{e}{\hbar} \left(\frac{1}{V_{\text{uc}}\sqrt{N}} \right) \sum_{\mathbf{k}} \left(\frac{\partial h_{\alpha\beta}(\mathbf{k})}{\partial k_\mu} \right) c_{\mathbf{k}\alpha}^\dagger c_{\mathbf{k}\beta}. \quad (\text{A.10})$$

When the matrix is diagonal, the result has a very simple interpretation, as it is simply the number of electrons in a given state multiplied by the group velocity.

This important result eventually allows us to express Hall conductivities in terms of Berry curvatures and Chern numbers.

A.1.2 Calculation of spin current

To illustrate how one may derive an expression for the spin current of the component along the \hat{z} -direction, we use the Hamiltonian of Paper [1] as an example. As we will see, the derivation is very similar to the electronic case above.

We consider the spin model

$$H = -J \sum_{\langle ij \rangle} \mathbf{S}_i \cdot \mathbf{S}_j + \mathcal{D} \sum_{\langle\langle ij \rangle\rangle} \nu_{ij} \hat{z} (\mathbf{S}_i \times \mathbf{S}_j) - B \sum_i S_i^z, \quad (\text{A.11})$$

as discussed in more detail in Sec. 6.2. The model can be rewritten

$$H = -J \sum_{\langle ij \rangle} \left[S_i^z S_j^z + \frac{1}{2} (S_i^+ S_j^- + S_i^- S_j^+) \right] + \frac{\mathcal{D}}{2} \sum_{\langle\langle ij \rangle\rangle} (e^{i\phi\nu_{ij}} S_i^+ S_j^- + \text{h.c.}) - B \sum_i S_i^z, \quad (\text{A.12})$$

where we let $\phi = \pi/2$ and have utilized that $\nu_{ij} = \pm 1$. Introducing the linearized Holstein-Primakoff transformation and the Fourier representation of

the sublattice magnon creation and annihilation operators, the Hamiltonian takes the form

$$H = \sum_{\mathbf{k}} \sum_{\alpha\beta} h_{\alpha\beta}(\mathbf{k}) a_{\mathbf{k}\alpha}^\dagger a_{\mathbf{k}\beta}, \quad (\text{A.13})$$

where α and β label the sublattice degree of freedom.

From the Heisenberg equation of motion, we may again extract the spin current j_{ij} from lattice site i to lattice site j . Introducing the Fourier component $\mathbf{j}(\mathbf{q})$ of the spin current density vector similar to Eqs. (A.7) and (A.8), we obtain zero momentum component on the form $\mathbf{j}(\mathbf{q} = 0) = \mathbf{j}^{\text{H}} + \mathbf{j}^{\text{DM}}$, with Heisenberg and Dzyaloshinskii-Moriya contributions on the form

$$\mathbf{j}^{\text{H}}(\mathbf{q} = 0) = \frac{1}{V_{\text{uc}}\sqrt{N}} \left(-\frac{J}{2} \right) \sum_{\langle ij \rangle} [(S_i^+ S_j^- - S_i^- S_j^+)] i\boldsymbol{\delta}_{ij} \quad (\text{A.14})$$

$$\mathbf{j}^{\text{DM}}(\mathbf{q} = 0) = \frac{1}{V_{\text{uc}}\sqrt{N}} \left(\frac{\mathcal{D}}{2} \right) \sum_{\langle\langle ij \rangle\rangle} (e^{i\phi\nu_{ij}} S_i^+ S_j^- - e^{-i\phi\nu_{ij}} S_i^- S_j^+) i\boldsymbol{\delta}_{ij}. \quad (\text{A.15})$$

We notice that the only different between the representations here and the kinetic terms in the Hamiltonian on the form in Eq. (A.12) is the sign between the two contributions and the factor $i\boldsymbol{\delta}_{ij}$. Furthermore, we remark that the terms in the Hamiltonian in Eq. (A.12) constructed from S_i^z do not contribute to the spin current since they necessarily commute with S_i^z .

By replacing the spin raising and lowering operators with annihilation and creation operators through the linearized Holstein-Primakoff representation, we then obtain

$$\mathbf{j}_\mu(\mathbf{q} = 0) = \frac{1}{V_{\text{uc}}\sqrt{N}} \sum_{\mathbf{k}} \sum_{\alpha\beta} \left(\frac{\partial h_{\alpha\beta}(\mathbf{k})}{\partial k_\mu} \right) a_{\mathbf{k}\alpha}^\dagger a_{\mathbf{k}\beta}. \quad (\text{A.16})$$

Thus, we have perfectly analogous results for the charge current density in the electronic system and the spin current density in the magnetic system, where electrons carry charge and the magnons spin.

A.2 Kubo formula manipulations

In this appendix, we show that the Hall conductivity in electronic and bosonic systems can be written in terms of the Berry curvature of the underlying bands in fermionic and bosonic systems.

In both cases, we start from the Kubo formula for the Hall conductivity σ_{xy} in the limit $\mathbf{q} \rightarrow 0$, which takes the form

$$\sigma_{xy} = -\frac{V_{\text{uc}}}{\hbar\omega} \int_0^\infty dt e^{i\omega t} \langle [j_x(t), j_y(0)] \rangle, \quad (\text{A.17})$$

where the brackets $\langle \dots \rangle$ denote a thermal average. Here, j_μ are current operators for the current along the Cartesian direction μ , which we assume can be written on the form

$$j_\mu = \frac{K}{V_{\text{uc}}\sqrt{N}} \sum_{\mathbf{k}} \left(\frac{\partial h_{\alpha\beta}(\mathbf{k})}{\partial k_\mu} \right) c_{\mathbf{k}\alpha}^\dagger c_{\mathbf{k}\beta}, \quad (\text{A.18})$$

where $c_{\mathbf{k}\alpha}$ is an annihilation operator for the underlying electronic or bosonic particles, and K is a constant depending on whether we consider the electronic or magnetic system. Furthermore, we introduce the velocity matrix

$$v_\mu^{\alpha\beta} = \frac{1}{\hbar} \left(\frac{\partial h_{\alpha\beta}}{\partial k_\mu} \right), \quad (\text{A.19})$$

so that the current can be written on the form

$$j_\mu = \frac{K\hbar}{V_{\text{uc}}\sqrt{N}} \sum_{\mathbf{k}} v_\mu^{\alpha\beta}(\mathbf{k}) c_{\mathbf{k}\alpha}^\dagger c_{\mathbf{k}\beta}. \quad (\text{A.20})$$

We now let $U(\mathbf{k})$ be a unitary matrix diagonalizing the Hamiltonian in Eq. (A.3), so that $U^\dagger h U = D$ with some diagonal matrix D . The current operators in Eq. (A.18) can then be written

$$j_\mu = \sum_{\mathbf{k}} j_\mu^{\rho\sigma}(\mathbf{k}) d_{\mathbf{k}\rho}^\dagger d_{\mathbf{k}\sigma}, \quad (\text{A.21})$$

where $d_{\mathbf{k}\alpha}$ are annihilation operators for electrons in the energy band α , and with the transformed current matrix elements $j^{\rho\sigma}(\mathbf{k})$ given by

$$j^{\rho\sigma}(\mathbf{k}) = \frac{\hbar K}{V_{\text{uc}}\sqrt{N}} U_{\rho\alpha}^\dagger(\mathbf{k}) v_\mu^{\alpha\beta}(\mathbf{k}) U_{\beta\sigma}(\mathbf{k}) \equiv \frac{\hbar K}{V_{\text{uc}}\sqrt{N}} \tilde{v}_\mu^{\rho\sigma}. \quad (\text{A.22})$$

A.2.1 Summing out particle statistics

Knowing the expression for the Hall conductivity in linear response theory, it is now somewhat tedious, but fairly straightforward to derive an expression for the Hall conductivity in terms of the eigenstates and -energies of the system.

Making use of the equilibrium density matrix $\rho_{\text{eq}} = e^{-\beta H}/Z$ and inserting a resolution of the identity into the Kubo formula, we have

$$\sigma_{xy} = -\frac{V_{\text{uc}}}{\hbar\omega Z} \int_0^\infty dt e^{i\omega t} \sum_{mn} e^{-\beta E_n} [\langle n|j_x|m\rangle\langle m|j_y|n\rangle e^{i(E_n-E_m)t/\hbar} - \langle n|j_y|m\rangle\langle m|j_x|n\rangle e^{-i(E_n-E_m)t/\hbar}]. \quad (\text{A.23})$$

When $n = m$, the two contributions cancel, so we may restrict the sum over m to $m \neq n$ in the following. Integrating out the time, we get [47]

$$\sigma_{xy} = -\frac{V_{\text{uc}}}{\omega Z} \sum_{n,m \neq n} \left[\frac{\langle n|j_x|m\rangle\langle m|j_y|n\rangle}{\hbar\omega + E_n - E_m} - \frac{\langle n|j_y|m\rangle\langle m|j_x|n\rangle}{\omega - E_n + E_m} \right]. \quad (\text{A.24})$$

Since we are interested in the static limit $\omega \rightarrow 0$, we may now Taylor expand the denominators in each term using [47, 304]

$$\frac{1}{\hbar\omega - E_n + E_m} \simeq \frac{1}{E_m - E_n} - \frac{\hbar\omega}{(E_m - E_n)^2} + \mathcal{O}(\omega^2). \quad (\text{A.25})$$

The zeroth order contribution in the above expansion vanishes when we insert it in Eq. (A.24) due to gauge invariance [47]. We are then left with the linear term. There, the factor ω cancels the prefactor $1/\omega$, and the transverse conductivity can be written

$$\sigma_{xy} = -\frac{i\hbar V_{\text{uc}}}{Z} \sum_{m,n \neq m} \frac{\langle n|j_x|m\rangle\langle m|j_y|n\rangle - \langle n|j_y|m\rangle\langle m|j_x|n\rangle}{(E_n - E_m)^2} e^{-\beta E_n}. \quad (\text{A.26})$$

Inserting expressions for the current operators, we then get

$$\sigma_{xy} = -\frac{\hbar K^2}{V_{\text{uc}} N} \sum_{n,m \neq n} \sum_{\mathbf{k}\mathbf{k}'} \sum_{\alpha\beta\gamma\delta} \frac{e^{-\beta E_n}}{Z} i\hbar^2 \frac{(\tilde{v}_x^{\alpha\beta} \tilde{v}_y^{\gamma\delta} - \tilde{v}_y^{\alpha\beta} \tilde{v}_x^{\gamma\delta})}{(E_n - E_m)^2} \cdot \langle n|d_{\mathbf{k}\alpha}^\dagger d_{\mathbf{k}\beta}|m\rangle \langle m|d_{\mathbf{k}'\gamma}^\dagger d_{\mathbf{k}'\delta}|n\rangle \quad (\text{A.27})$$

Here, the states labelled by indices n and m are general many particle states. Thus, we may think of them as states specified by the occupation numbers for all single particle states. Furthermore, we notice that since we only have terms with $n \neq m$ in our sum, we need $\mathbf{k} = \mathbf{k}'$, $\alpha = \delta$, and $\gamma = \beta$ to have non-zero contributions. Furthermore, since n and m have to be different, we need $\alpha \neq \beta$.

Since $|n\rangle$ can be obtained from $|m\rangle$ by moving a particle from state β to α , we have

$$E_n - E_m = E_{\mathbf{k}\alpha} - E_{\mathbf{k}\beta}. \quad (\text{A.28})$$

Thus, we may write

$$\sigma_{xy} = -\frac{\hbar K^2}{V_{\text{uc}}N} \sum_{n, m \neq n} \sum_{\mathbf{k}} \sum_{\alpha\beta} \frac{e^{-\beta E_n}}{Z} i\hbar^2 \frac{(\tilde{v}_x^{\alpha\beta} \tilde{v}_y^{\beta\alpha} - \tilde{v}_y^{\alpha\beta} \tilde{v}_x^{\gamma\delta})}{(E_{\mathbf{k}\alpha} - E_{\mathbf{k}\beta})^2} |\langle m | c_{\mathbf{k}\beta}^\dagger c_{\mathbf{k}\alpha} | n \rangle|^2. \quad (\text{A.29})$$

Her, the sums over n and m represents sums over the the many particle states in the system. To proceed, we now want to sum over the states n . To to this, we have to calculate the matrix element $\langle m | d_{\mathbf{k}\beta}^\dagger d_{\mathbf{k}\alpha} | n \rangle$. In the following, we let the many-particle state $|n\rangle$ have occupation number $n_{\mathbf{k}\alpha}$ for the single particle state specified by \mathbf{k} and α . With bosonic particles, we then get²

$$\sum_m |\langle m | d_{\mathbf{k}\beta}^\dagger d_{\mathbf{k}\alpha} | n \rangle|^2 = n_{\mathbf{k}\alpha} (n_{\mathbf{k}\beta} + 1), \quad (\text{A.30})$$

while for fermions, we have³

$$\sum_m |\langle m | d_{\mathbf{k}\beta}^\dagger d_{\mathbf{k}\alpha} | n \rangle|^2 = n_{\mathbf{k}\alpha}^2 (1 - n_{\mathbf{k}\beta})^2 = n_{\mathbf{k}\alpha} (1 - n_{\mathbf{k}\beta}). \quad (\text{A.31})$$

Thus, the conductivity $\sigma_{xy}^{B,F}$ for bosonic and fermionic particles can be written

$$\sigma_{xy}^{B,F} = -\frac{\hbar K^2}{V_{\text{uc}}N} \sum_{\mathbf{k}} \sum_n \sum_{\alpha, \beta \neq \alpha} n_{\mathbf{k}\alpha} (1 + \zeta_{B,F} n_{\mathbf{k}\beta}) \frac{e^{-\beta E_n}}{Z} i\hbar^2 \frac{(\tilde{v}_x^{\alpha\beta} \tilde{v}_y^{\alpha\beta} - \tilde{v}_x^{\alpha\beta} \tilde{v}_y^{\alpha\beta})}{(E_{\mathbf{k}\alpha} - E_{\mathbf{k}\beta})^2}, \quad (\text{A.32})$$

where $\zeta_B = +1$ and $\zeta_F = -1$. Summing over the occupation numbers $n_{\mathbf{k}\alpha}$ and $n_{\mathbf{k}\beta}$, they are replaced by either Bose or Fermi distributions n_B or n_F . Introducing

$$W_{\mathbf{k}, \alpha\beta}^{B,F} = n_{B,F}(E_{\mathbf{k}\alpha}) [1 + \zeta_{B,F} n_{B,F}(E_{\mathbf{k}\beta})], \quad (\text{A.33})$$

²Recall the identities $a|n\rangle = \sqrt{n}|n-1\rangle$ and $a^\dagger|n\rangle = \sqrt{n+1}|n+1\rangle$.

³Recall $n_{\mathbf{k}\alpha}^2 = n_{\mathbf{k}\alpha}$.

we then have

$$\sigma_{xy}^{B,F} = -\frac{\hbar K^2}{V_{\text{uc}} N} \sum_{\mathbf{k}} \sum_{\alpha, \beta \neq \alpha} W_{\mathbf{k}, \alpha \beta}^{B,F} \frac{(\tilde{v}_x^{\alpha\beta} \tilde{v}_y^{\alpha\beta} - \tilde{v}_x^{\alpha\beta} \tilde{v}_y^{\alpha\beta})}{(E_{\mathbf{k}\alpha} - E_{\mathbf{k}\beta})^2} (i\hbar^2), \quad (\text{A.34})$$

Introducing also the curvature tensor

$$\mathcal{F}^{\alpha\beta}(\mathbf{k}) = i\hbar^2 \frac{\tilde{v}_x^{\alpha\beta} \tilde{v}_y^{\beta\alpha} - \tilde{v}_y^{\alpha\beta} \tilde{v}_x^{\beta\alpha}}{(E_{\mathbf{k}\alpha} - E_{\mathbf{k}\beta})^2}, \quad (\text{A.35})$$

we may then rewrite the Hall conductivity as

$$\sigma_{xy}^{B,F} = -\frac{\hbar K}{2\pi} \sum_{\alpha, \beta \neq \alpha} \int_{\text{BZ}} \frac{d^2 k}{2\pi} W_{\mathbf{k}, \alpha \beta}^{B,F} \mathcal{F}^{\alpha\beta}(\mathbf{k}), \quad (\text{A.36})$$

where we have utilized that $V_{\text{uc}} V_{\text{BZ}} = (2\pi)^2$, and V_{BZ} is the Brillouin zone area.

As discussed in the main text of Sec. 3.1, the Fermi distributions can be replaced by step functions when the temperature is small compared to the gap, and this allows the Hall conductivity to be related to the Brillouin zone integral of the quantity

$$\mathcal{F}^\alpha(\mathbf{k}) = \sum_{\beta \neq \alpha} \mathcal{F}^{\alpha\beta}(\mathbf{k}). \quad (\text{A.37})$$

In the bosonic case, the Hall conductivity is given as an average of this quantity weighted with a Bose distribution when the occupation number $n_B(E_{\mathbf{k}\beta})$ is small compared to 1. As we show next, the quantity $\mathcal{F}^\alpha(\mathbf{k})$ is simply the Berry curvature of band α .

A.2.2 Berry curvature

The curvature tensor $\mathcal{F}^{\alpha\beta}(\mathbf{k})$ is given in terms of the velocity matrix elements $\tilde{v}^{\rho\sigma}$. Denoting the column vector α of $U_{\beta\alpha}(\mathbf{k})$ by $|u_{\mathbf{k}\alpha}\rangle$, we the have

$$\tilde{v}_\mu^{\alpha\beta} = \langle u_{\mathbf{k}\alpha} | v_\mu | u_{\mathbf{k}\beta} \rangle. \quad (\text{A.38})$$

Since we may furthermore write

$$\hbar \tilde{v}_\mu^{\alpha\beta} = \langle u_{\mathbf{k}\alpha} | \frac{\partial h}{\partial k_\mu} | u_{\mathbf{k}\beta} \rangle = \langle u_{\mathbf{k}\alpha} | \partial_\mu [h | u_{\mathbf{k}\beta} \rangle] - \langle u_{\mathbf{k}\alpha} | h | \partial_\mu u_{\mathbf{k}\beta} \rangle, \quad (\text{A.39})$$

and $|u_{\mathbf{k}\alpha}\rangle$ is an eigenvector of h with eigenvalue $E_{\mathbf{k}\alpha}$, we then get

$$\langle u_{\mathbf{k}\alpha} | \frac{\partial h}{\partial k_\mu} | u_{\mathbf{k}\beta} \rangle = (E_{\mathbf{k}\beta} - E_{\mathbf{k}\alpha}) \langle u_{\mathbf{k}\alpha} | \partial_\mu u_{\mathbf{k}\beta} \rangle \quad (\text{A.40})$$

where we have used that $\langle u_{\mathbf{k}\alpha} | u_{\mathbf{k}\beta} \rangle = 0$ when $\alpha \neq \beta$. Similarly, by letting the derivative act on the bra vector instead of the ket, we have

$$\langle u_{\mathbf{k}\alpha} | \frac{\partial h}{\partial k_\mu} | u_{\mathbf{k}\beta} \rangle = (E_{\mathbf{k}\alpha} - E_{\mathbf{k}\beta}) \langle \partial_\mu u_{\mathbf{k}\alpha} | u_{\mathbf{k}\beta} \rangle. \quad (\text{A.41})$$

Inserting these two in the definition of $\mathcal{F}^\alpha(\mathbf{k})$, we then have

$$\mathcal{F}^\alpha(\mathbf{k}) = i \sum_{\beta \neq \alpha} [\langle \partial_x u_{\mathbf{k}\alpha} | u_{\mathbf{k}\beta} \rangle \langle u_{\mathbf{k}\beta} | \partial_y u_{\mathbf{k}\alpha} \rangle - \langle \partial_y u_{\mathbf{k}\alpha} | u_{\mathbf{k}\beta} \rangle \langle u_{\mathbf{k}\beta} | \partial_x u_{\mathbf{k}\alpha} \rangle]. \quad (\text{A.42})$$

For each \mathbf{k} , the eigenfunctions $|u_{\mathbf{k}\alpha}\rangle$ form an orthonormal basis. Thus, we have a completeness relation

$$1 - |u_{\mathbf{k}\alpha}\rangle \langle u_{\mathbf{k}\alpha}| = \sum_{\beta \neq \alpha} |u_{\mathbf{k}\beta}\rangle \langle u_{\mathbf{k}\beta}| \quad (\text{A.43})$$

Exploiting this, we then obtain

$$\mathcal{F}^\alpha(\mathbf{k}) = i [\langle \partial_x u_{\mathbf{k}\alpha} | \partial_y u_{\mathbf{k}\alpha} \rangle - \langle \partial_y u_{\mathbf{k}\alpha} | \partial_x u_{\mathbf{k}\alpha} \rangle] = \Omega^\alpha(\mathbf{k}). \quad (\text{A.44})$$

This is precisely the Berry curvature as introduced in the main text. Thus, both fermionic and bosonic Hall conductivities can, subject to some assumptions regarding the thermal occupation factors, be expressed in terms of the Berry curvature of the band structure.

Appendix B

Dimensionless electron-phonon coupling

In this Appendix, we discuss the electron-phonon coupling, and aim at showing that the mass enhancement parameter $\tilde{\lambda}_{\mathbf{k}}$ can in fact be approximated by the dimensionless electron-phonon coupling $\lambda_{\mathbf{k}}$ when we use the assumption that the electron energy scale is much larger than the phonon energy scale.

As discussed in the main text, the self-energy of the system is given by

$$\Sigma_1(\mathbf{k}, z) = \sum_{q\nu} |g_{\mathbf{k}, \mathbf{k}+\mathbf{q}}^\nu|^2 \left[\frac{1 + n_B(\omega_{\mathbf{q}}) - n_F(\xi_{\mathbf{k}+\mathbf{q}})}{z - (\xi_{\mathbf{k}+\mathbf{q}} + \omega_{\mathbf{q}})} + \frac{n_B(\omega_{\mathbf{q}}) + n_F(\xi_{\mathbf{k}+\mathbf{q}})}{z - (\xi_{\mathbf{k}+\mathbf{q}} - \omega_{\mathbf{q}})} \right]. \quad (\text{B.1})$$

By introducing δ -functions $\delta(\Omega - \omega_{\mathbf{q}\lambda})$ and $\delta(\xi' - \xi_{\mathbf{k}+\mathbf{q}})$ and integrating over the energies Ω and ξ' , we may then rewrite the self energy as

$$\Sigma(\mathbf{k}, z) = \int d\xi' \int d\Omega \left[\frac{1 + n_B(\Omega) - n_F(\xi')}{z - \xi' - \Omega} + \frac{n_B(\Omega) + n_F(\xi')}{z - \xi' + \Omega} \right] \alpha_{\mathbf{k}}^2 F(\xi', \Omega), \quad (\text{B.2})$$

where we have introduced the function

$$\alpha^2 F_{\mathbf{k}}(\epsilon, \omega) = \sum_{q\nu} |g_{\mathbf{k}+\mathbf{q}, \mathbf{k}}^\nu|^2 \delta(\Omega - \omega_{q\nu}) \delta(\epsilon - \epsilon_{\mathbf{k}+\mathbf{q}}) \quad (\text{B.3})$$

containing the two delta functions in energy which we used to rewrite the above expression.

At zero temperature, one may now calculate the real part of the self energy under the assumption that the function $\alpha^2 F_{\mathbf{k}}(\xi, \omega)$ depends slowly on ξ compared to the square brackets. The result is

$$\Sigma(\mathbf{k}, z) = \int_0^\infty d\Omega \alpha^2 F_{\mathbf{k}}(\Omega) \log\left(\frac{\Omega - z}{\Omega + z}\right). \quad (\text{B.4})$$

By inserting $z = \omega + i\eta$ with an infinitesimal η , differentiating with respect to ω , and evaluating at $\omega = \epsilon_{\mathbf{k}}$, we then get

$$\tilde{\lambda}_{\mathbf{k}} = \int d\Omega \frac{2}{\Omega} \alpha_{\mathbf{k}}^2 F(\epsilon_{\mathbf{k}}, \Omega). \quad (\text{B.5})$$

We recognize this as $\lambda_{\mathbf{k}}$, and have thus shown that $\tilde{\lambda}_{\mathbf{k}} \approx \lambda_{\mathbf{k}}$ for momenta \mathbf{k} close to the Fermi surface.

Bibliography

- [1] E. Thingstad, A. Kamra, A. Brataas, and A. Sudbø, Phys. Rev. Lett. **122**, 107201 (2019).
- [2] E. Thingstad, A. Kamra, J. W. Wells, and A. Sudbø, Phys. Rev. B **101**, 214513 (2020).
- [3] A. Kamra, E. Thingstad, G. Rastelli, R. A. Duine, A. Brataas, W. Belzig, and A. Sudbø, Phys. Rev. B **100**, 174407 (2019).
- [4] E. Thingstad, E. Erlandsen, and A. Sudbø, arXiv:2105.02235 (2021).
- [5] J. F. Cochran and D. E. Mapother, Phys. Rev. **111**, 132 (1958).
- [6] P. Coleman, *Introduction to Many-Body Physics* (Cambridge University Press, 2015).
- [7] M. R. Norman, *Unconventional superconductivity* (2014).
- [8] P. A. Grünberg, Rev. Mod. Phys. **80**, 1531 (2008).
- [9] I. Herbut, *A modern approach to critical phenomena* (Cambridge University Press, 2007).
- [10] A. Hirohata, K. Yamada, Y. Nakatani, I.-L. Prejbeanu, B. Diény, P. Pirro, and B. Hillebrands, Journal of Magnetism and Magnetic Materials **509**, 166711 (2020).
- [11] A. Abanov, A. V. Chubukov, and J. Schmalian, Advances in Physics **52**, 119 (2003).
- [12] T. Moriya and K. Ueda, Reports on Progress in Physics **66**, 1299 (2003).

- [13] D. Scalapino, *Journal of Low Temperature Physics* **117**, 179 (1999).
- [14] L. Balents, *Nature* **464**, 199 (2010).
- [15] L. Savary and L. Balents, *Reports on Progress in Physics* **80**, 016502 (2016).
- [16] T. Senthil, L. Balents, S. Sachdev, A. Vishwanath, and M. P. A. Fisher, *Phys. Rev. B* **70**, 144407 (2004).
- [17] T. Senthil, A. Vishwanath, L. Balents, S. Sachdev, and M. P. A. Fisher, *Science* **303**, 1490 (2004).
- [18] A. W. Sandvik, *Phys. Rev. Lett.* **98**, 227202 (2007).
- [19] A. Auerbach, *Interacting electrons and quantum magnetism* (Springer Science & Business Media, 2012).
- [20] S. Sachdev, *Quantum phase transitions*, 2nd ed. (Cambridge University Press, Cambridge, 2011).
- [21] A. Kitaev, *Annals of Physics* **321**, 2 (2006).
- [22] E. Fradkin, *Field theories of condensed matter physics* (Cambridge University Press, 2013).
- [23] N. Nagaosa, *Quantum field theory in strongly correlated electronic systems*, Texts and monographs in physics (Springer, Berlin, 1999).
- [24] A. Altland and B. D. Simons, *Condensed matter field theory* (Cambridge university press, 2010).
- [25] C. Kittel, *Quantum Theory of Solids* (John Wiley & Sons, 1987).
- [26] J. L. van Hemmen, *Zeitschrift für Physik B Condensed Matter* **38**, 271 (1980).
- [27] C. Tsallis, *Journal of Mathematical Physics* **19**, 277 (1978).
- [28] M.-w. Xiao, arXiv:0908.0787 (2009).
- [29] K. Mæland, arXiv:2011.10999 (2020).
- [30] E. Thingstad, *Two-Component Spin-Orbit Coupled Ultracold Atoms in the Weak and Strong Coupling Regimes*, Master's thesis, NTNU, Trondheim (2017).

- [31] J. M. Losada, A. Brataas, and A. Qaiumzadeh, *Phys. Rev. B* **100**, 060410 (2019).
- [32] S. K. Kim, H. Ochoa, R. Zarzuela, and Y. Tserkovnyak, *Phys. Rev. Lett.* **117**, 227201 (2016).
- [33] J. J. Sakurai, *Advanced quantum mechanics* (Pearson Education India, 2006).
- [34] M. Hälg, W. E. A. Lorenz, K. Y. Povarov, M. Månsson, Y. Skourski, and A. Zheludev, *Phys. Rev. B* **90**, 174413 (2014).
- [35] S. Mühlbauer, B. Binz, F. Jonietz, C. Pfleiderer, A. Rosch, A. Neubauer, R. Georgii, and P. Böni, *Science* **323**, 915 (2009).
- [36] P. McClarty, arXiv:2106.01430 (2021).
- [37] G. E. Volovik, *Journal of Experimental and Theoretical Physics* **129**, 618 (2019).
- [38] M. Sato and Y. Ando, *Reports on Progress in Physics* **80**, 076501 (2017).
- [39] Y. Liu, X. Chen, and Y. Xu, *Topological Phononics: From Fundamental Models to Real Materials* (2020).
- [40] Inside the Quantum Race: Microsoft — Computerworld, <https://www.computerworld.com/article/3527218/inside-the-quantum-race-microsoft.html>, Accessed: 2021-06-23.
- [41] M. Nakahara, *Geometry, topology and physics*, 2nd ed., Graduate student series in physics (Taylor & Francis, Bristol, 2003).
- [42] S. M. Girvin and K. Yang, *Modern Condensed Matter Physics* (Cambridge University Press, 2019).
- [43] K. v. Klitzing, G. Dorda, and M. Pepper, *Phys. Rev. Lett.* **45**, 494 (1980).
- [44] K. R. Sopka, in *The Hall Effect and Its Applications* (Springer, 1980) pp. 523–545.
- [45] H. Bruus, *Many-body quantum theory in condensed matter physics : an introduction*, Oxford graduate texts (Oxford University Press, Oxford, 2004).

- [46] B. A. Bernevig and T. L. Hughes, *Topological insulators and topological superconductors* (Princeton University Press, 2013).
- [47] D. Tong, Lectures on the Quantum Hall Effect (2016), arXiv:1606.06687 .
- [48] D. Xiao, M.-C. Chang, and Q. Niu, Rev. Mod. Phys. **82**, 1959 (2010).
- [49] B. A. Bernevig, T. L. Hughes, and S.-C. Zhang, Solid State Communications **143**, 20 (2007).
- [50] M. Z. Hasan and C. L. Kane, Rev. Mod. Phys. **82**, 3045 (2010).
- [51] F. D. M. Haldane, Phys. Rev. Lett. **61**, 2015 (1988).
- [52] J. Cayssol, Comptes Rendus Physique **14**, 760 (2013).
- [53] G. Jotzu, M. Messer, R. Desbuquois, M. Lebrat, T. Uehlinger, D. Greif, and T. Esslinger, Nature **515**, 237 (2014).
- [54] B.-H. Chen and D.-W. Chiou, Physics Letters A **384**, 126168 (2020).
- [55] M. Aidelsburger, M. Atala, M. Lohse, J. T. Barreiro, B. Paredes, and I. Bloch, Phys. Rev. Lett. **111**, 185301 (2013).
- [56] N. Goldman, J. C. Budich, and P. Zoller, Nature Physics **12**, 639 (2016).
- [57] M. Lohse, C. Schweizer, O. Zilberberg, M. Aidelsburger, and I. Bloch, Nature Physics **12**, 350 (2016).
- [58] C. L. Kane and T. C. Lubensky, Nature Physics **10**, 39 (2013).
- [59] S. D. Huber, Nature Physics **12**, 621 (2016).
- [60] B. Peng, Y. Hu, S. Murakami, T. Zhang, and B. Monserrat, Science Advances **6** (2020), 2011.06269 .
- [61] Y. Liu, Y. Xu, S. C. Zhang, and W. Duan, Physical Review B **96**, 064106 (2017), 1606.08013 .
- [62] Y. Liu, Y. Xu, and W. Duan, National Science Review **5**, 314 (2017).
- [63] F. D. Haldane and S. Raghu, Physical Review Letters **100**, 013904 (2008).

- [64] S. Raghu and F. D. Haldane, *Physical Review A - Atomic, Molecular, and Optical Physics* **78**, 033834 (2008).
- [65] Z. Wang, Y. Chong, J. D. Joannopoulos, and M. Soljačić, *Nature* **461**, 772 (2009).
- [66] L. Lu, J. D. Joannopoulos, and M. Soljačić, *Topological photonics* (2014), 1408.6730 .
- [67] M. Malki and G. S. Uhrig, *EPL (Europhysics Letters)* **132**, 20003 (2020).
- [68] R. Fleury, D. L. Sounas, C. F. Sieck, M. R. Haberman, and A. Alù, *Science* **343**, 516 (2014).
- [69] L. Zhang, J. Ren, J.-S. Wang, and B. Li, *Phys. Rev. Lett.* **105**, 225901 (2010).
- [70] M. Hirschberger, R. Chisnell, Y. S. Lee, and N. P. Ong, *Phys. Rev. Lett.* **115**, 106603 (2015).
- [71] C. T. Walker and G. A. Slack, *American Journal of Physics* **38**, 1380 (1970).
- [72] G. Grimvall, *The electron-phonon interaction in metals* (North-Holland Pub. Co., 1981).
- [73] G. Rickayzen, *Theory of superconductivity*, Interscience monographs and texts in physics and astronomy, Vol. 14 (Interscience, New York, 1965).
- [74] C. Kittel, *Rev. Mod. Phys.* **21**, 541 (1949).
- [75] P. Hemmer, *Faste stoffers fysikk* (Tapir, Trondheim, 1987).
- [76] S. Baroni, S. de Gironcoli, A. Dal Corso, and P. Giannozzi, *Rev. Mod. Phys.* **73**, 515 (2001).
- [77] L. A. Falkovsky, *Journal of Experimental and Theoretical Physics* **105**, 397 (2007).
- [78] P. Hofmann, I. Y. Sklyadneva, E. D. L. Rienks, and E. V. Chulkov, *New Journal of Physics* **11**, 125005 (2009).

- [79] J. P. Carbotte and F. Marsiglio, Electron-phonon superconductivity, in *The Physics of Superconductors: Vol. I. Conventional and High-Tc Superconductors*, edited by K. H. Bennemann and J. B. Ketterson (Springer Berlin Heidelberg, Berlin, Heidelberg, 2003) pp. 233–345.
- [80] F. Giustino, *Rev. Mod. Phys.* **89**, 015003 (2017).
- [81] F. Bloch, *Z. Phys* **52**, 555 (1928).
- [82] L. Sham and J. Ziman (Academic Press, 1963) pp. 221–298.
- [83] G. D. Mahan, *Many-Particle Physics* (Kluwer Academic/Plenum, New York, 2000).
- [84] H. Fröhlich, *Proceedings of the Royal Society of London. Series A. Mathematical and Physical Sciences* **215**, 291 (1952).
- [85] T. K. Mitra, *Journal of Physics C: Solid State Physics* **2**, 52 (1969).
- [86] S. Barišić, J. Labbé, and J. Friedel, *Phys. Rev. Lett.* **25**, 919 (1970).
- [87] S. Barišić, *Phys. Rev. B* **5**, 932 (1972).
- [88] S. Barišić, *Phys. Rev. B* **5**, 941 (1972).
- [89] A. Birnboim and H. Gutfreund, *Phys. Rev. B* **9**, 139 (1974).
- [90] A. Birnboim and H. Gutfreund, *Phys. Rev. B* **12**, 2682 (1975).
- [91] J. Ashkenazi, M. Dacorogna, and M. Peter, *Solid State Communications* **29**, 181 (1979).
- [92] F. Marsiglio and J. P. Carbotte, Electron-phonon superconductivity, in *Superconductivity: Conventional and Unconventional Superconductors*, edited by K. H. Bennemann and J. B. Ketterson (Springer Berlin Heidelberg, Berlin, Heidelberg, 2008) pp. 73–162.
- [93] V. Z. Kresin, *Superconducting state : mechanisms and properties*, International series of monographs on physics, Vol. 161 (Oxford University Press, Oxford, 2014).
- [94] B. Hellsing, A. Eiguren, and E. V. Chulkov, *Journal of Physics: Condensed Matter* **14**, 5959 (2002).
- [95] F. Mazzola, T. Frederiksen, T. Balasubramanian, P. Hofmann, B. Hellsing, and J. W. Wells, *Phys. Rev. B* **95**, 075430 (2017).

- [96] A. Olabi and A. Grunwald, *Materials & Design* **29**, 469 (2008).
- [97] C.-H. Hsu, Y.-M. Huang, M.-F. Hsieh, C.-M. Fu, S. Adireddy, and D. B. Chrisey, *AIP Advances* **7**, 056681 (2017).
- [98] C. Kittel, *Phys. Rev.* **110**, 836 (1958).
- [99] C. Kittel, *J. Phys. Radium* **20**, 145 (1959).
- [100] S. Guerreiro and S. Rezende, *Revista Brasileira de fisica* **1**, 207 (1971).
- [101] H. T. Simensen, R. E. Troncoso, A. Kamra, and A. Brataas, *Phys. Rev. B* **99**, 064421 (2019).
- [102] H. K. Onnes, Further experiments with liquid helium, in *Proceedings of the KNAW*, Vol. 13 (1911) pp. 1910–1911.
- [103] W. Meissner and R. Ochsenfeld, *Naturwissenschaften* **21**, 787 (1933).
- [104] J. Bardeen, L. N. Cooper, and J. R. Schrieffer, *Phys. Rev.* **108**, 1175 (1957).
- [105] A. B. Migdal, *JETP* **34**, 1438 (1958).
- [106] G. Eliashberg, *Sov. Phys. JETP* **11**, 696 (1960).
- [107] G. Eliashberg, *Sov. Phys. JETP* **12**, 1000 (1961).
- [108] F. Steglich, J. Aarts, C. D. Bredl, W. Lieke, D. Meschede, W. Franz, and H. Schäfer, *Phys. Rev. Lett.* **43**, 1892 (1979).
- [109] J. G. Bednorz and K. A. Müller, *Zeitschrift für Physik B Condensed Matter* **64**, 189 (1986).
- [110] F. London, *Superfluids: Macroscopic theory of superconductivity*, Structure of matter series (Wiley, 1950).
- [111] V. L. Ginzburg and L. D. Landau, *Zh. Eksp. Teor. Fiz.* **20**, 1064 (1950).
- [112] K. Fossheim and A. Sudbø, *Superconductivity : physics and applications* (Wiley, Chichester, 2004).
- [113] E. Maxwell, *Phys. Rev.* **78**, 477 (1950).
- [114] C. A. Reynolds, B. Serin, W. H. Wright, and L. B. Nesbitt, *Phys. Rev.* **78**, 487 (1950).

- [115] H. Fröhlich, Phys. Rev. **79**, 845 (1950).
- [116] L. N. Cooper, Phys. Rev. **104**, 1189 (1956).
- [117] C. Timm, Theory of superconductivity (2021).
- [118] A. Abrikosov, *Methods of quantum field theory in statistical physics* (Prentice-Hall, Englewood Cliffs, 1963).
- [119] A. L. Fetter and J. D. Walecka, *Quantum theory of many-particle systems* (Dover Publications, Mineola, N.Y., 2003).
- [120] H. G. Hugdal, *A study of proximity-induced and magnon-mediated superconductivity on the surface of topological insulators*, Ph.D. thesis, NTNU, Trondheim (2021).
- [121] R. Richardson, Physics Letters **3**, 277 (1963).
- [122] M. Sigrist and K. Ueda, Rev. Mod. Phys. **63**, 239 (1991).
- [123] M. Sigrist, Introduction to unconventional superconductivity, in *AIP Conference Proceedings*, Vol. 789 (2005) pp. 165–243.
- [124] P. Coleman, *Introduction to Many-Body Physics* (Cambridge University Press, 2015).
- [125] M. T. Béal-Monod, C. Bourbonnais, and V. J. Emery, Phys. Rev. B **34**, 7716 (1986).
- [126] D. J. Scalapino, E. Loh, and J. E. Hirsch, Phys. Rev. B **34**, 8190 (1986).
- [127] K. Miyake, S. Schmitt-Rink, and C. M. Varma, Phys. Rev. B **34**, 6554 (1986).
- [128] Y. Takada, Journal of the Physical Society of Japan **45**, 786 (1978).
- [129] F. P. Laussy, A. V. Kavokin, and I. A. Shelykh, Phys. Rev. Lett. **104**, 106402 (2010).
- [130] A. Kavokin and P. Lagoudakis, Nature Materials **15**, 599 (2016).
- [131] F. Schlawin, A. Cavalleri, and D. Jaksch, Phys. Rev. Lett. **122**, 133602 (2019).
- [132] W. Kohn and J. M. Luttinger, Phys. Rev. Lett. **15**, 524 (1965).

- [133] S. Maiti and A. V. Chubukov, AIP Conference Proceedings **1550**, 3 (2013).
- [134] S. Raghu, S. A. Kivelson, and D. J. Scalapino, Phys. Rev. B **81**, 224505 (2010).
- [135] S. Bravyi, D. P. DiVincenzo, and D. Loss, Annals of Physics **326**, 2793 (2011).
- [136] J. M. Luttinger and W. Kohn, Phys. Rev. **97**, 869 (1955).
- [137] J. R. Schrieffer and P. A. Wolff, Phys. Rev. **149**, 491 (1966).
- [138] R. Heid, Electron-phonon coupling, in *The Physics of Correlated Insulators, Metals and Superconductors*, Modeling and Simulation, Vol. 7, edited by E. Pavarini, E. Koch, R. Scalettar, and R. M. Martin (Verlag des Forschungszentrum Jülich, Jülich, 2017) Chap. 15, pp. 399–427.
- [139] G. Rickayzen, The theory of Bardeen, Cooper, and Schrieffer, in *Superconductivity*, Vol. 1, edited by R. D. Parks (Marcel Decker Inc., New York, 1969) Chap. 1, pp. 51–115.
- [140] S. V. Vonsovskii and Y. A. Izyumov, Soviet Physics Uspekhi **5**, 723 (1963).
- [141] E. Erlandsen, A. Kamra, A. Brataas, and A. Sudbø, Phys. Rev. B **100**, 100503 (2019).
- [142] S. Kehrein, *The flow equation approach to many-particle systems*, Springer tracts in modern physics, Vol. 217 (Springer, Berlin, 2006).
- [143] P. Lenz and F. Wegner, Nuclear Physics B **482**, 693 (1996).
- [144] A. Mielke, Annalen der Physik **509**, 215 (1997).
- [145] A. Hübsch and K. W. Becker, The European Physical Journal B - Condensed Matter and Complex Systems **33**, 391 (2003).
- [146] P. Morel and P. W. Anderson, Phys. Rev. **125**, 1263 (1962).
- [147] J. W. Garland, Phys. Rev. Lett. **11**, 114 (1963).
- [148] L. Gor'Kov, Sov. Phys. JETP **7**, 158 (1958).
- [149] D. J. Scalapino, in *Superconductivity* (CRC Press, 2018) pp. 449–560.

- [150] D. J. Scalapino, Y. Wada, and J. C. Swihart, Phys. Rev. Lett. **14**, 102 (1965).
- [151] J. C. Swihart, D. J. Scalapino, and Y. Wada, Phys. Rev. Lett. **14**, 106 (1965).
- [152] A. V. Chubukov, A. Abanov, I. Esterlis, and S. A. Kivelson, Annals of Physics **417**, 168190 (2020), eliashberg theory at 60: Strong-coupling superconductivity and beyond.
- [153] A. Alexandrov, *Theory of superconductivity : From weak to strong coupling* (Institute of Physics Publishing, Bristol, 2003).
- [154] G. Umharrino, Eliashberg theory, in *Emergent Phenomena in Correlated Matter*, Schriften des Forschungszentrums Jülich. Reihe modeling and simulation, Vol. 3, edited by E. Pavarini, E. Koch, and U. Schollwöck (Verlag des Forschungszentrum Jülich, Jülich, 2013) p. 520 S.
- [155] E. R. Margine and F. Giustino, Phys. Rev. B **87**, 024505 (2013).
- [156] A. Aperis, P. Maldonado, and P. M. Oppeneer, Phys. Rev. B **92**, 054516 (2015).
- [157] A. Aperis and P. M. Oppeneer, Phys. Rev. B **97**, 060501 (2018).
- [158] F. Marsiglio, Annals of Physics **417**, 168102 (2020).
- [159] P. B. Allen and B. Mitrović, *Theory of Superconducting Tc*, edited by H. Ehrenreich, F. Seitz, and D. Turnbull, Solid State Physics, Vol. 37 (Academic Press, 1983) pp. 1–92.
- [160] I. Giaever, H. R. Hart, and K. Megerle, Phys. Rev. **126**, 941 (1962).
- [161] A. B. Migdal, JETP **34**, 1438 (1958).
- [162] B. Roy, J. D. Sau, and S. Das Sarma, Phys. Rev. B **89**, 165119 (2014).
- [163] J. Hirsch, M. Maple, and F. Marsiglio, Physica C: Superconductivity and its Applications **514**, 1 (2015).
- [164] N. F. Berk and J. R. Schrieffer, Phys. Rev. Lett. **17**, 433 (1966).
- [165] S. Doniach and S. Engelsberg, Phys. Rev. Lett. **17**, 750 (1966).

- [166] K. Andres, J. E. Graebner, and H. R. Ott, *Phys. Rev. Lett.* **35**, 1779 (1975).
- [167] G. R. Stewart, *Rev. Mod. Phys.* **56**, 755 (1984).
- [168] N. Mott, *Philosophical Magazine* **30**, 403 (1974).
- [169] S. Doniach, *Physica B+C* **91**, 231 (1977).
- [170] G. R. Stewart, Z. Fisk, J. O. Willis, and J. L. Smith, *Phys. Rev. Lett.* **52**, 679 (1984).
- [171] H. R. Ott, H. Rudigier, Z. Fisk, and J. L. Smith, *Phys. Rev. Lett.* **50**, 1595 (1983).
- [172] P. Coleman, Heavy fermions and the Kondo lattice: A 21st century perspective, in *Many-Body Physics: From Kondo to Hubbard*, Modeling and Simulation, Vol. 5, edited by E. Pavarini, E. Koch, and P. Coleman (Verlag des Forschungszentrum Jülich, Jülich, 2015) Chap. 1, pp. 9–42.
- [173] H. R. Ott, H. Rudigier, T. M. Rice, K. Ueda, Z. Fisk, and J. L. Smith, *Phys. Rev. Lett.* **52**, 1915 (1984).
- [174] H. R. Ott, H. Rudigier, Z. Fisk, and J. L. Smith, *Phys. Rev. B* **31**, 1651 (1985).
- [175] R. Fisher, S. Kim, B. Woodfield, N. Phillips, L. Taillefer, K. Hasselbach, J. Flouquet, A. Giorgi, and J. Smith, in *Ten Years of Superconductivity: 1980–1990* (Springer, 1989) pp. 189–192.
- [176] A. J. Leggett, *Rev. Mod. Phys.* **47**, 331 (1975).
- [177] R. J. Cava, R. B. van Dover, B. Batlogg, and E. A. Rietman, *Phys. Rev. Lett.* **58**, 408 (1987).
- [178] C. W. Chu, P. H. Hor, R. L. Meng, L. Gao, Z. J. Huang, and W. Y. Q., *Phys. Rev. Lett.* **58**, 405 (1987).
- [179] M. K. Wu, J. R. Ashburn, C. J. Torng, P. H. Hor, R. L. Meng, L. Gao, Z. J. Huang, Y. Q. Wang, and C. W. Chu, *Phys. Rev. Lett.* **58**, 908 (1987).

- [180] R. M. Hazen, C. T. Prewitt, R. J. Angel, N. L. Ross, L. W. Finger, C. G. Hadidiacos, D. R. Veblen, P. J. Heaney, P. H. Hor, R. L. Meng, Y. Y. Sun, Y. Q. Wang, Y. Y. Xue, Z. J. Huang, L. Gao, J. Bechtold, and C. W. Chu, *Phys. Rev. Lett.* **60**, 1174 (1988).
- [181] M. R. Norman, *Science* **332**, 196 (2011).
- [182] D. A. Wollman, D. J. Van Harlingen, W. C. Lee, D. M. Ginsberg, and A. J. Leggett, *Phys. Rev. Lett.* **71**, 2134 (1993).
- [183] M. A. Ruderman and C. Kittel, *Phys. Rev.* **96**, 99 (1954).
- [184] C. Geibel, C. Schank, S. Thies, H. Kitazawa, C. D. Bredl, A. Böhm, M. Rau, A. Grauel, R. Caspary, R. Helfrich, U. Ahlheim, G. Weber, and F. Steglich, *Zeitschrift für Physik B Condensed Matter* **84**, 1 (1991).
- [185] C. Geibel, S. Thies, D. Kaczorowski, A. Mehner, A. Grauel, B. Seidel, U. Ahlheim, R. Helfrich, K. Petersen, C. D. Bredl, and F. Steglich, *Zeitschrift für Physik B Condensed Matter* **83**, 305 (1991).
- [186] R. Flint, M. Dzero, and P. Coleman, *Nature Physics* **4**, 643 (2008).
- [187] P. A. Lee, N. Nagaosa, and X.-G. Wen, *Rev. Mod. Phys.* **78**, 17 (2006).
- [188] A. J. Leggett, *Nature Physics* **2**, 134 (2006).
- [189] L. Zhang, J. Ren, J.-S. Wang, and B. Li, *Phys. Rev. B* **87**, 144101 (2013).
- [190] A. Mook, J. Henk, and I. Mertig, *Phys. Rev. B* **90**, 024412 (2014).
- [191] P. Laurell and G. A. Fiete, *Phys. Rev. Lett.* **118**, 177201 (2017).
- [192] R. Seshadri and D. Sen, *Phys. Rev. B* **97**, 134411 (2018).
- [193] P. Laurell and G. A. Fiete, *Phys. Rev. B* **98**, 094419 (2018).
- [194] K. H. Lee, S. B. Chung, K. Park, and J.-G. Park, *Phys. Rev. B* **97**, 180401 (2018).
- [195] Y. Onose, T. Ideue, H. Katsura, Y. Shiomi, N. Nagaosa, and Y. Tokura, *Science* **329**, 297 (2010).
- [196] M. Hirschberger, J. W. Krizan, R. J. Cava, and N. P. Ong, *Science* **348**, 106 (2015).

- [197] S. A. Owerre, *Journal of Physics: Condensed Matter* **28**, 386001 (2016).
- [198] S. A. Owerre, *Journal of Applied Physics* **120**, 043903 (2016).
- [199] X. Cao, K. Chen, and D. He, *Journal of Physics: Condensed Matter* **27**, 166003 (2015).
- [200] M. Malki and G. S. Uhrig, *Phys. Rev. B* **99**, 174412 (2019).
- [201] D. Bhowmick and P. Sengupta, *Phys. Rev. B* **101**, 214403 (2020).
- [202] A. Roldán-Molina, A. S. Nunez, and J. Fernández-Rossier, *New Journal of Physics* **18**, 045015 (2016).
- [203] S. A. Díaz, J. Klinovaja, and D. Loss, *Phys. Rev. Lett.* **122**, 187203 (2019).
- [204] S. A. Díaz, T. Hirose, J. Klinovaja, and D. Loss, *Phys. Rev. Research* **2**, 013231 (2020).
- [205] P. A. McClarty, X.-Y. Dong, M. Gohlke, J. G. Rau, F. Pollmann, R. Moessner, and K. Penc, *Phys. Rev. B* **98**, 060404 (2018).
- [206] D. G. Joshi, *Phys. Rev. B* **98**, 060405 (2018).
- [207] R. Shindou, R. Matsumoto, S. Murakami, and J.-i. Ohe, *Phys. Rev. B* **87**, 174427 (2013).
- [208] X. S. Wang, Y. Su, and X. R. Wang, *Phys. Rev. B* **95**, 014435 (2017).
- [209] K.-S. Kim, K. H. Lee, S. B. Chung, and J.-G. Park, *Phys. Rev. B* **100**, 064412 (2019).
- [210] J. Fransson, A. M. Black-Schaffer, and A. V. Balatsky, *Phys. Rev. B* **94**, 075401 (2016).
- [211] K. Li, C. Li, J. Hu, Y. Li, and C. Fang, *Phys. Rev. Lett.* **119**, 247202 (2017).
- [212] N. P. Armitage, E. J. Mele, and A. Vishwanath, *Rev. Mod. Phys.* **90**, 015001 (2018).
- [213] A. Mook, J. Henk, and I. Mertig, *Phys. Rev. B* **94**, 174444 (2016).
- [214] J. Liu, L. J. Cornelissen, J. Shan, T. Kuschel, and B. J. van Wees, *Phys. Rev. B* **95**, 140402 (2017).

- [215] C. Carnahan, Y. Zhang, and D. Xiao, Thermal hall effect of chiral spin fluctuations (2021), arXiv:2104.02168 [cond-mat.mes-hall] .
- [216] T. Ideue, Y. Onose, H. Katsura, Y. Shiomi, S. Ishiwata, N. Nagaosa, and Y. Tokura, *Phys. Rev. B* **85**, 134411 (2012).
- [217] Y. Kasahara, T. Ohnishi, Y. Mizukami, O. Tanaka, S. Ma, K. Sugii, N. Kurita, H. Tanaka, J. Nasu, Y. Motome, T. Shibauchi, and Y. Matsuda, *Nature* **559**, 227 (2018).
- [218] R. Hentrich, M. Roslova, A. Isaeva, T. Doert, W. Brenig, B. Büchner, and C. Hess, *Phys. Rev. B* **99**, 085136 (2019).
- [219] Y. Shiomi, R. Takashima, and E. Saitoh, *Phys. Rev. B* **96**, 134425 (2017).
- [220] F. Schwabl, *Quantenmechanik für Fortgeschrittene* (Springer-Verlag, 2008).
- [221] R. Matsumoto and S. Murakami, *Phys. Rev. B* **84**, 184406 (2011).
- [222] R. Matsumoto and S. Murakami, *Phys. Rev. Lett.* **106**, 197202 (2011).
- [223] H. Lee, J. H. Han, and P. A. Lee, *Phys. Rev. B* **91**, 125413 (2015).
- [224] J. M. Luttinger, *Phys. Rev.* **135**, A1505 (1964).
- [225] H.-S. Kim and H.-Y. Kee, *npj Quantum Materials* **2**, 20 (2017).
- [226] C. L. Kane and E. J. Mele, *Phys. Rev. Lett.* **95**, 226801 (2005).
- [227] C. L. Kane and E. J. Mele, *Phys. Rev. Lett.* **95**, 146802 (2005).
- [228] S. Rachel, *Reports on Progress in Physics* **81**, 116501 (2018).
- [229] L. M. Cangemi, A. S. Mishchenko, N. Nagaosa, V. Cataudella, and G. De Filippis, *Phys. Rev. Lett.* **123**, 046401 (2019).
- [230] A. L. Chernyshev and P. A. Maksimov, *Phys. Rev. Lett.* **117**, 187203 (2016).
- [231] A. Mook, K. Plekhanov, J. Klinovaja, and D. Loss, *Phys. Rev. X* **11**, 021061 (2021).
- [232] P. A. McClarty and J. G. Rau, *Phys. Rev. B* **100**, 100405 (2019).
- [233] R. Takahashi and N. Nagaosa, *Phys. Rev. Lett.* **117**, 217205 (2016).

- [234] X. Zhang, Y. Zhang, S. Okamoto, and D. Xiao, *Phys. Rev. Lett.* **123**, 167202 (2019).
- [235] S. Park and B.-J. Yang, *Phys. Rev. B* **99**, 174435 (2019).
- [236] G. Go, S. K. Kim, and K.-J. Lee, *Phys. Rev. Lett.* **123**, 237207 (2019).
- [237] S. Zhang, G. Go, K.-J. Lee, and S. K. Kim, *Phys. Rev. Lett.* **124**, 147204 (2020).
- [238] S. Park, N. Nagaosa, and B.-J. Yang, *Nano Letters* **20**, 2741 (2020).
- [239] S. Petit, F. Moussa, M. Hennion, S. Pailhès, L. Pinsard-Gaudart, and A. Ivanov, *Phys. Rev. Lett.* **99**, 266604 (2007).
- [240] S. L. Holm, A. Kreisel, T. K. Schäffer, A. Bakke, M. Bertelsen, U. B. Hansen, M. Retuerto, J. Larsen, D. Prabhakaran, P. P. Deen, Z. Yamani, J. O. Birk, U. Stuhr, C. Niedermayer, A. L. Fennell, B. M. Andersen, and K. Lefmann, *Phys. Rev. B* **97**, 134304 (2018).
- [241] S. Bao, Z. Cai, W. Si, W. Wang, X. Wang, Y. Shangguan, Z. Ma, Z.-Y. Dong, R. Kajimoto, K. Ikeuchi, S.-L. Yu, J. Sun, J.-X. Li, and J. Wen, *Phys. Rev. B* **101**, 214419 (2020).
- [242] R. Peierls, *Helv. Phys. Acta* **7**, 81 (1934).
- [243] R. Peierls, *Annales de l'institut Henri Poincaré* **5**, 177 (1935).
- [244] L. Landau, *Z. Sowjetunion* **11**, 26 (1937).
- [245] K. S. Novoselov, A. K. Geim, S. V. Morozov, D. Jiang, Y. Zhang, S. V. Dubonos, I. V. Grigorieva, and A. A. Firsov, *Science* **306**, 666 (2004).
- [246] K. S. Novoselov, D. Jiang, F. Schedin, T. J. Booth, V. V. Khotkevich, S. V. Morozov, and A. K. Geim, *Proceedings of the National Academy of Sciences* **102**, 10451 (2005).
- [247] A. H. Castro Neto, F. Guinea, N. M. R. Peres, K. S. Novoselov, and A. K. Geim, *Rev. Mod. Phys.* **81**, 109 (2009).
- [248] D. Abergel, V. Apalkov, J. Berashevich, K. Ziegler, and T. Chakraborty, *Advances in Physics* **59**, 261 (2010).
- [249] V. N. Kotov, B. Uchoa, V. M. Pereira, F. Guinea, and A. H. Castro Neto, *Rev. Mod. Phys.* **84**, 1067 (2012).

- [250] M. I. Katsnelson, *Graphene* (Cambridge University Press, Cambridge, 2012).
- [251] P. Rosenzweig, H. Karakachian, D. Marchenko, K. Küster, and U. Starke, *Phys. Rev. Lett.* **125**, 176403 (2020).
- [252] B. Gharekhanlou and S. Khorasani, An overview of tight-binding method for two-dimensional carbon structures, in *Graphene: Properties, synthesis and applications*, edited by Z. Xu (Nova Science Publishers Inc., 2012) Chap. 1, pp. 1–36.
- [253] L. Landau, *Statistical physics*, Course of theoretical physics, Vol. 5 (Pergamon, Oxford, 1969).
- [254] R. Nicklow, N. Wakabayashi, and H. G. Smith, *Phys. Rev. B* **5**, 4951 (1972).
- [255] F. Tuinstra and J. L. Koenig, *The Journal of chemical physics* **53**, 1126 (1970).
- [256] S. Siebentritt, R. Pues, K.-H. Rieder, and A. M. Shikin, *Physical Review B* **55**, 7927 (1997).
- [257] J. Maultzsch, S. Reich, C. Thomsen, H. Requardt, and P. Ordejón, *Physical Review Letters* **92**, 075501 (2004).
- [258] C. Oshima, T. Aizawa, R. Souda, Y. Ishizawa, and Y. Sumiyoshi, *Solid State Communications* **65**, 1601 (1988).
- [259] S. Vig, A. Kogar, M. Mitran, A. A. Husain, V. Mishra, M. S. Rak, L. Venema, P. D. Johnson, G. D. Gu, E. Fradkin, *et al.*, *SciPost Phys* **3**, 026 (2017).
- [260] H. Yanagisawa, T. Tanaka, Y. Ishida, M. Matsue, E. Rokuta, S. Otani, and C. Oshima, *Surface and Interface Analysis* **37**, 133 (2005).
- [261] R. Senga, K. Suenaga, P. Barone, S. Morishita, F. Mauri, and T. Pichler, *Nature* **573**, 247 (2019).
- [262] L. A. Falkovsky, *The Journal of the Acoustical Society of America* **123**, 3453 (2008).
- [263] N. Mounet and N. Marzari, *Phys. Rev. B* **71**, 205214 (2005).
- [264] L. Wirtz and A. Rubio, *Solid State Communications* **131**, 141 (2004).

- [265] O. Dubay and G. Kresse, Phys. Rev. B **67**, 035401 (2003).
- [266] V. K. Tewary and B. Yang, Phys. Rev. B **79**, 075442 (2009).
- [267] L. Lindsay and D. A. Broido, Phys. Rev. B **81**, 205441 (2010).
- [268] L. Karssemeijer and A. Fasolino, Surface Science **605**, 1611 (2011).
- [269] S. Piscanec, M. Lazzeri, F. Mauri, A. C. Ferrari, and J. Robertson, Phys. Rev. Lett. **93**, 185503 (2004).
- [270] F. Mazzola, J. W. Wells, R. Yakimova, S. Ulstrup, J. A. Miwa, R. Balog, M. Bianchi, M. Leandersson, J. Adell, P. Hofmann, and T. Balasubramanian, Phys. Rev. Lett. **111**, 216806 (2013).
- [271] F. Mazzola, T. Frederiksen, T. Balasubramanian, P. Hofmann, B. Hellsing, and J. W. Wells, Phys. Rev. B **95**, 075430 (2017).
- [272] L. Pietronero, S. Strässler, H. R. Zeller, and M. J. Rice, Physical Review B **22**, 904 (1980).
- [273] L. M. Woods and G. D. Mahan, Physical Review B **61**, 10651 (2000).
- [274] H. Suzuura and T. Ando, Physical Review B **65**, 235412 (2002).
- [275] P. Venezuela, M. Lazzeri, and F. Mauri, Phys. Rev. B **84**, 035433 (2011).
- [276] C. H. Park, N. Bonini, T. Sohler, G. Samsonidze, B. Kozinsky, M. Calandra, F. Mauri, and N. Marzari, Nano Letters **14**, 1113 (2014).
- [277] T. Sohler, *Electrons and phonons in graphene: electron-phonon coupling, screening and transport in the field effect setup*, Ph.D. thesis, Université Pierre et Marie Curie-Paris VI (2015).
- [278] J. L. Mañes, Physical Review B - Condensed Matter and Materials Physics **76**, 045430 (2007).
- [279] M. Lazzeri, C. Attaccalite, L. Wirtz, and F. Mauri, Phys. Rev. B **78**, 081406 (2008).
- [280] C. Attaccalite, L. Wirtz, M. Lazzeri, F. Mauri, and A. Rubio, Nano Letters **10**, 1172 (2010).
- [281] A. Hebard, M. Rosseinsky, R. Haddon, D. Murphy, S. Glarum, T. Palstra, A. Ramirez, and A. Karton, Nature **350**, 600 (1991).

- [282] N. B. Hannay, T. H. Geballe, B. T. Matthias, K. Andres, P. Schmidt, and D. MacNair, *Phys. Rev. Lett.* **14**, 225 (1965).
- [283] Y. Koike, H. Suematsu, K. Higuchi, and S. Tanuma, *Physica B+C* **99**, 503 (1980).
- [284] I. Belash, A. Bronnikov, O. Zharikov, and A. Pal'nichenko, *Solid State Communications* **69**, 921 (1989).
- [285] T. E. Weller, M. Ellerby, S. S. Saxena, R. P. Smith, and N. T. Skipper, *Nature Physics* **1**, 39 (2005).
- [286] S. Ichinokura, K. Sugawara, A. Takayama, T. Takahashi, and S. Hasegawa, *ACS Nano* **10**, 2761 (2016).
- [287] J. Chapman, Y. Su, C. A. Howard, D. Kundys, A. N. Grigorenko, F. Guinea, A. K. Geim, I. V. Grigorieva, and R. R. Nair, *Scientific Reports* **6**, 23254 (2016).
- [288] I. I. Mazin, *Phys. Rev. Lett.* **95**, 227001 (2005).
- [289] M. Calandra and F. Mauri, *Phys. Rev. Lett.* **95**, 237002 (2005).
- [290] B. M. Ludbrook, G. Levy, P. Nigge, M. Zonno, M. Schneider, D. J. Dvorak, C. N. Veenstra, S. Zhdanovich, D. Wong, P. Dosanjh, C. Straßer, A. Stöhr, S. Forti, C. R. Ast, U. Starke, and A. Damascelli, *Proceedings of the National Academy of Sciences* **112**, 11795 (2015).
- [291] M. Einenkel and K. B. Efetov, *Phys. Rev. B* **84**, 214508 (2011).
- [292] E. R. Margine and F. Giustino, *Phys. Rev. B* **90**, 014518 (2014).
- [293] N. Rohling, E. L. Fjærbu, and A. Brataas, *Phys. Rev. B* **97**, 115401 (2018).
- [294] E. L. Fjærbu, N. Rohling, and A. Brataas, *Phys. Rev. B* **100**, 125432 (2019).
- [295] E. Erlandsen and A. Sudbø, *Phys. Rev. B* **102**, 214502 (2020).
- [296] M. Kargarian, D. K. Efimkin, and V. Galitski, *Phys. Rev. Lett.* **117**, 076806 (2016).
- [297] H. G. Hugdal, S. Rex, F. S. Nogueira, and A. Sudbø, *Phys. Rev. B* **97**, 195438 (2018).

- [298] E. Erlandsen, A. Brataas, and A. Sudbø, *Phys. Rev. B* **101**, 094503 (2020).
- [299] P. C. Hemmer, *Kvantemekanikk* (Tapir akademisk, 2005).
- [300] D. F. Walls, *Nature* **306**, 141 (1983).
- [301] C. Gerry and P. Knight, *Introductory Quantum Optics* (Cambridge University Press, Cambridge, 2004).
- [302] W. Zhang and K. M. Krishnan, *Materials Science and Engineering: R: Reports* **105**, 1 (2016).
- [303] R. Szczyński, *Physics Letters A* **336**, 402 (2005).
- [304] S. Rex, *Electric and magnetic signatures of boundary states in topological insulators and superconductors*, Ph.D. thesis, NTNU, Trondheim (2017).

Paper 1

E. Thingstad, A. Kamra, A. Brataas, and A. Sudbø,

Chiral phonon transport induced by topological magnons,

Phys. Rev. Lett. **122**, 107201 (2019).

Chiral Phonon Transport Induced by Topological Magnons

Even Thingstad, Akashdeep Kamra, Arne Brataas, and Asle Sudbø*

Center for Quantum Spintronics, Department of Physics, Norwegian University of Science and Technology, NO-7491 Trondheim, Norway

(Received 9 August 2018; revised manuscript received 19 December 2018; published 11 March 2019)

The plethora of recent discoveries in the field of topological electronic insulators has inspired a search for boson systems with similar properties. There are predictions that ferromagnets on a two-dimensional honeycomb lattice may host chiral edge magnons. In such systems, we theoretically study how magnons and phonons couple. We find topological magnon polarons around the avoided crossings between phonons and topological magnons. Exploiting this feature along with our finding of Rayleigh-like edge phonons in armchair ribbons, we demonstrate the existence of chiral edge modes with a phononic character. We predict that these modes mediate a chirality in the coherent phonon response and suggest measuring this effect via elastic transducers. These findings reveal a possible approach towards heat management in future devices.

DOI: 10.1103/PhysRevLett.122.107201

Introduction.—Topological electronic insulators [1–5] are characterized by an insulating bulk with conducting “chiral” edge states. The unidirectional propagation of these chiral modes is “topologically protected” against defects at low temperatures when we can disregard inelastic scattering from phonons [5]. This has led to the development of a wide range of essential concepts, including Majorana modes [6–9], topological quantum computation [10,11], and chiral transport. Inspired by these findings, there has been an upsurge of efforts towards finding similar states in other systems [12] with an emphasis on bosonic excitations [13–19]. There are predictions of topological magnons [15–17] in honeycomb ferromagnets with an engineered Dzyaloshinskii-Moriya interaction [20,21] that induces the necessary band gap. In contrast to fermionic systems with Fermi energy within this band gap, the bulk is not necessarily insulating in bosonic systems [22].

The field of magnonics [23–26] focuses on pure spin transport mediated by magnons [27]. It is possible to exploit the low-dissipation and wavelike nature of these excitations in information processing [28,29]. The coherent pumping of chiral surface spin wave (Damon-Eshbach) modes induces cooling via incoherent magnon-phonon scattering [30]. Besides application oriented properties, the bosonic nature of magnons, combined with spintronic manipulation techniques [24,31], allows for intriguing physics [32–35]. The coupling [36] between magnons and phonons fundamentally differs from the electron-phonon interaction and results in a coherent hybridization of the modes [37], in addition to the temperature dependent incoherent effects [30,38] discussed above. The direct influence of the hybridization between magnons and phonons, known as magnon polarons [39,40], has been observed in spin and energy transport in magnetic systems [41–46].

In this Letter, we address the robustness of the topological magnons in a honeycomb ferromagnet [15–17] against their coupling with the lattice vibrations. In contrast to the case of electron-phonon coupling, where phonons can be disregarded at low temperatures, the magnon dispersion may undergo significant changes with new states emerging in the band gap [45,46]. We find that in the honeycomb ferromagnet with spins oriented orthogonal to the lattice plane, only transverse phonon modes with out-of-plane displacement couple to spin. To understand the eigenmodes, we evaluate and analyze the coupled spin and out-of-plane phonon modes for an infinitely large plane as well as for a finite ribbon geometry. We quantify the effect of the magnetoelastic coupling on the magnon Hall conductivity and find a nonmonotonic dependence on the coupling strength. Our analysis of the finite ribbons shows that topological magnons hybridize with bulk phonons around the avoided crossings in their coupled dispersion, forming magnon polarons with topological chiral properties. Hence, while their edge localization is weakened, the magnetoelastic coupling does not completely remove the topological magnons. Furthermore, we find that armchair edges support Rayleigh-like edge phonon modes in sharp contrast to the zigzag edges. When topological magnons hybridize with these edge phonons, edge magnon polarons with almost undiminished chirality are formed. We suggest a setup that utilizes this induced chirality in coherent phonon transport. Such systems enable the observation of the topological physics and serve as a prototype for a unidirectional heat pump. This offers a highly feasible alternative to producing topological phonon diodes [47–49].

Model.—We consider a ferromagnetic material with localized spins on a two-dimensional honeycomb lattice, allow for out-of-plane vibrations of the lattice sites, and

assume there is magnetoelastic coupling. This system can be modelled by a Hamiltonian of the form $H = H_m + H_{\text{ph}} + H_{\text{me}}$, where H_m is the magnetic Hamiltonian, H_{ph} describes the phonons, and H_{me} represents the magnetoelastic coupling.

The Hamiltonian we consider is inspired by the Haldane model [1], and given by [15–17]

$$H_m = -J \sum_{\langle i,j \rangle} \mathbf{S}_i \cdot \mathbf{S}_j + \mathcal{D} \sum_{\langle\langle i,j \rangle\rangle} \nu_{ij} \hat{z} \cdot \mathbf{S}_i \times \mathbf{S}_j - \mathcal{B} \sum_i S_i^z. \quad (1)$$

The first term describes the ferromagnetic exchange coupling between nearest neighbor sites, while the second accounts for the Dzyaloshinskii-Moriya interaction [20,21] between next-to-nearest neighbors [50]. The Haldane sign $\nu_{ij} = \pm 1$ depends on the relative orientation of the next-to-nearest neighbors as shown in Fig. 1(a), and is the root of nontrivial topological properties. We let the nearest neighbor distance be d and the next-to-nearest neighbor distance be a . References [16,17] discuss the dispersion relation and Berry curvature of this spin model in linear spin wave theory.

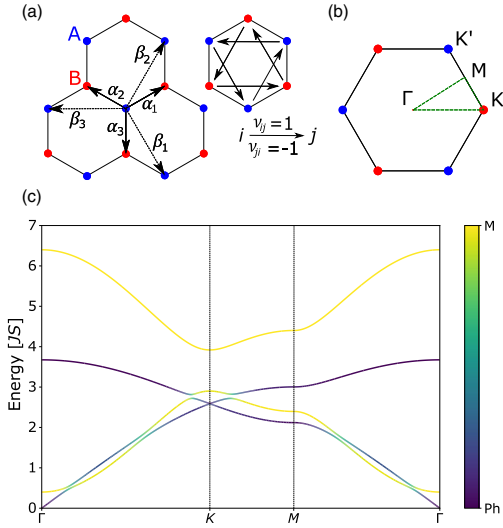


FIG. 1. (a) Lattice geometry showing the nearest neighbor vectors α , next-to-nearest neighbor vectors β , and the Haldane sign $\nu_{ij} = \pm 1$. (b) The first Brillouin zone in reciprocal space, including the paths along which we plot the dispersion relation in (c). The parameter values used are $\mathcal{D} = 0.1J$, $\mathcal{B} = 0.4JS$, $\sqrt{C/m} = 1.5JS$, and rescaled coupling strength $\tilde{\kappa} = 0.03$ (see main text). The magnon (yellow) and phonon (purple) character of the modes is indicated with colors. The modes are significantly affected by the magnetoelastic coupling only close to avoided crossings.

For the phonon Hamiltonian, we consider only the out-of-plane degrees of freedom since only these modes couple to the spin to lowest order in the linear spin wave expansion. We assume nearest-neighbor interactions with elastic constant C , let the mass associated with the spins on the lattice sites be m , and disregard substrate coupling. Introducing $S_k = \sum_{\beta} \cos(\mathbf{k} \cdot \boldsymbol{\beta})$, where the sum is over the three next-to-nearest neighbor vectors $\boldsymbol{\beta}$ of Fig. 1(a), we obtain the dispersion relation

$$\omega_{\pm}^{\text{ph}}(\mathbf{k}) = \sqrt{\frac{C}{m}} \sqrt{3 \pm \sqrt{3 + 2S_k}} \quad (2)$$

for the free phonon modes.

Motivated by the continuum limit description [36,37], we write down the lattice magnetoelastic coupling to linear order in the magnon amplitude, obtaining

$$H_{\text{me}} = \kappa \sum_D \sum_{i \in D} \sum_{\alpha_D} \mathbf{S}_i \cdot \boldsymbol{\alpha}_D (u_i^z - u_{i+\alpha_D}^z), \quad (3)$$

where κ parametrizes the strength of the magnon-phonon coupling, \sum_D denotes the sum over sublattices, $\sum_{i \in D}$ is the sum over the lattice sites on the D sublattice, and α_D are the corresponding nearest neighbor vectors. The out-of-plane deviation for lattice site i is denoted by u_i^z .

Bulk spectrum.—We introduce the Holstein-Primakoff representation of spins and use linear spin wave theory in the spin- and magnetoelastic terms [27]. Within the rotating wave approximation [51], the resulting Hamiltonian describing the phonon and magnon modes of the system is obtained as $H = \sum_k \psi_k^\dagger M_k \psi_k$, where $\psi_k^\dagger = (a_k^\dagger, b_k^\dagger, c_{k-}^\dagger, c_{k+}^\dagger)$. Here, a_k and b_k are annihilation operators for the sublattice magnon modes on the A and B sublattices, while $c_{k\pm}$ are the annihilation operators for the phonon modes. The matrix M_k takes the form

$$M_k = \begin{pmatrix} A + h^z & h^- & g_{A-} & g_{A+} \\ h^+ & A - h^z & g_{B-} & g_{B+} \\ g_{A-}^* & g_{B-}^* & \omega_{k-}^{\text{ph}} & 0 \\ g_{A+}^* & g_{B+}^* & 0 & \omega_{k+}^{\text{ph}} \end{pmatrix}, \quad (4)$$

where $A = 3JS + \mathcal{B}$, $h^z(\mathbf{k}) = 2\mathcal{D}S \sum_{\beta} \sin(\mathbf{k} \cdot \boldsymbol{\beta})$, $h^-(\mathbf{k}) = -JS \sum_a \exp(-i\mathbf{k} \cdot \boldsymbol{\alpha})$, and $h^+ = (h^-)^*$. The coupling between the D -sublattice magnons and the phonon branch \pm is captured by $g_{D\pm}$, which is proportional to the dimensionless coupling strength $\tilde{\kappa} = (\kappa d / JS) \times \sqrt{\hbar^2 S^2 / 16m^2 (C/m)}$. The spectrum obtained by diagonalizing this matrix is plotted in Fig. 1(c) along the paths displayed in Fig. 1(b).

Hall conductivity.—The topological nature of the spin model is manifested in the magnon Hall conductivity that

arises because of the time-reversal symmetry breaking caused by the Dzyaloshinskii-Moriya interaction.

The spin current operator J_γ may be found from a continuity equation or magnon group velocity approach [52], both yielding

$$J_\gamma = \sum_k \begin{pmatrix} a_k^\dagger & b_k^\dagger \end{pmatrix} \left(\frac{\partial H_m(\mathbf{k})}{\partial k_\gamma} \right) \begin{pmatrix} a_k \\ b_k \end{pmatrix} \quad (5)$$

along the Cartesian direction γ . Here, $H_m(\mathbf{k})$ is the matrix representation of the magnon Hamiltonian. Assuming we apply a weak in-plane magnetic field gradient $\nabla\mathcal{B}$, we are interested in the current $\mathbf{j} = \sigma\nabla\mathcal{B}$, which is determined by the conductivity tensor σ [52]. The Hall conductivity can be calculated using the Kubo formula, giving

$$\sigma_{xy} = \sum_k \sum_{\alpha, \beta \neq \alpha} n_B(E_{k\alpha}) C_{\alpha\beta}(\mathbf{k}), \quad (6)$$

where $E_{k\alpha}$ is the energy eigenvalue of band α and $n_B(E_{k\alpha})$ is the corresponding Bose factor. The curvature tensor $C_{\alpha\beta}$ is given by

$$C_{\alpha\beta}(\mathbf{k}) = i \frac{J_y^{\alpha\beta}(\mathbf{k})J_x^{\beta\alpha}(\mathbf{k}) - J_x^{\alpha\beta}(\mathbf{k})J_y^{\beta\alpha}(\mathbf{k})}{(E_{k\alpha} - E_{k\beta})^2}, \quad (7)$$

where (α, β) are band indices, and $J_\gamma^{\alpha\beta}(\mathbf{k})$ are the energy eigenstate matrix elements of the current operator at quasimomentum \mathbf{k} . Disregarding the magnetoelastic coupling, the band curvature $C_\alpha = \sum_{\beta \neq \alpha} C_{\alpha\beta}$ can be identified as the Berry curvature.

Expressing the sublattice magnon operators in terms of the eigenmode operators, one may identify the current matrix elements $J_\gamma^{\alpha\beta}$ and integrate the curvature over the Brillouin zone to obtain the Hall conductivity. We are particularly interested in the effect of the magnetoelastic coupling, and therefore present the dependence of the Hall conductivity on the dimensionless coupling $\tilde{\kappa}$ in Fig 2.

To understand this dependence, we consider the curvature tensor $C_{\alpha\beta}$. When the bands α and β both have a predominant magnon content, the topological nature of the underlying magnons gives a finite curvature. This magnon curvature is largest close to the Dirac points [16,17]. Close to an avoided crossing, the magnetoelastic coupling changes the spectrum and causes transfer of band curvature between the relevant bands α and β . The latter can be seen by plotting the curvature tensor element $C_{\alpha\beta}$ for the band pairs with avoided crossings, as shown in the insets of Fig 2. The resulting change in Hall conductivity is given by these curvature tensor elements weighted with the difference between the Bose factors of the relevant bands. This follows from the antisymmetry property of the curvature tensor. The two band pairs in the insets contribute oppositely to the Hall conductivity, and the competition between

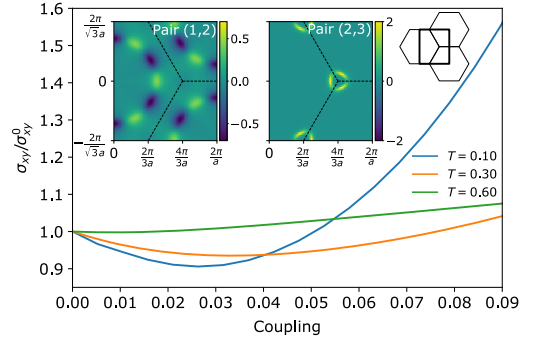


FIG. 2. Dependence of the Hall conductivity on the magnetoelastic coupling strength $\tilde{\kappa}$ for parameter values $\mathcal{D} = 0.1J$, $\mathcal{B} = 0.4JS$, and $\sqrt{C/m} = 1.5JS$ for different temperatures T in units of JS . The insets show the quasimomentum dependence of the curvature tensor at $\tilde{\kappa} = 0.03$ for band pairs (1,2) and (2,3), where the bands are labeled according to their energy, and band 1 is the lowest band. The dominant contribution in these band pairs comes from the regions with avoided crossings of the respective bands.

their curvature transfer explains the nonmonotonic behavior of the Hall conductivity.

Ribbon geometry and coherent transport.—Due to the topological nature of the magnon model under consideration and the bulk-boundary correspondence, there are gapless magnon edge states in a finite sample [5,15–17]. Considering an armchair ribbon with finite width, the one-dimensional projection of the energy spectrum is plotted in Fig. 3. The corresponding spectrum for the zigzag edge ribbon is given in the Supplemental Material [53], where also Refs. [54–58] appear. Magnon and phonon modes hybridize in regions with an avoided crossing. When the upper phonon band lies within the band gap of the pure magnon spectrum, there are modes with a mixed content of chiral magnon edge states and phonons. Although the spectra look qualitatively similar, there is a crucial distinction between the two cases. For the zigzag edge configuration, all the phonon modes are delocalized throughout the sample, while the armchair edges host “Rayleigh-like” edge phonon modes. In direct analogy with Rayleigh modes on the surface of a three-dimensional material, the localization length of these modes is directly proportional to their wavelength, as shown in the Supplemental Material [53]. These edge phonon modes are supported by the half-hexagon protrusions of the armchair edge that can pivot around the bonds parallel to the edges connecting these protrusions, see Fig. 3. No such parallel bonds exist for the zigzag edge.

The Hall conductivity is a hallmark of topological electronic properties and motivates a similar role for the Hall conductivity mediated by topological magnons. However,

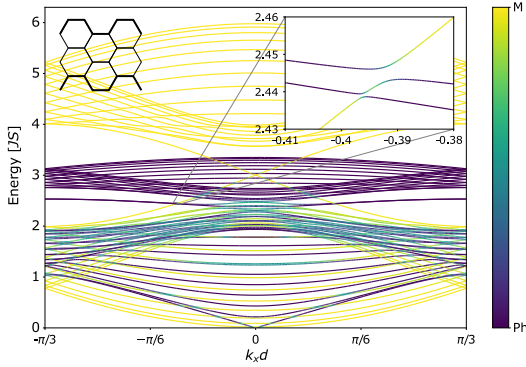


FIG. 3. One-dimensional projection of the dispersion relation for the magnetoelastic modes on a honeycomb ribbon with armchair edges. In addition to the bulk bands, there are two topological edge magnon states crossing the magnon band gap, as well as Rayleigh-like edge phonons. The inset shows the avoided crossing of a topological magnon edge mode with the two quasidegenerate edge phonon modes. The parameter values are $B = 0$, $\sqrt{C/m} = 1.37JS$, $D = 0.1J$, and $\tilde{\kappa} = 0.03$.

in contrast to electrons, the bosonic nature of the magnons results in the lack of a general proportionality between the magnon Hall conductivity and the Chern number [52]. Furthermore, the observation of a magnon planar Hall effect [59] in a cubic, nontopological magnet suggests that this Hall conductivity may not be regarded as a smoking-gun signature for topological properties. Thus, we suggest a complementary approach to observe the topological nature of the underlying magnons by elastically probing the chirality of the magnetoelastic hybrid modes.

We propose to observe coherent chiral phonon propagation in the experimental setup of Fig. 4(b) by utilizing the edge modes, as depicted schematically in Fig. 4(a) [60], on the upper armchair edge of the sample. Taking inspiration from previous related experiments [41,61], we suggest injecting elastic energy into the sample middle at the upper edge using a nanoscale variant of the interdigital transducer design [62,63], elaborated further in the Supplemental Material [53]. For a given transducer design, modes are excited with fixed wave vectors $\pm k_x$ and a tunable frequency. Similar transducers can be used to detect the elastic response $p_{L/R}$ on the left (L) and right (R) edges of the sample. Here, $p_{L/R}$ is the elastic power detected at the transducers.

Figure 4(a) schematically depicts the dispersion for the magnetoelastic modes localized on an armchair edge. Disregarding magnetoelastic coupling, the edge hosts two counterpropagating Rayleigh-like edge phonons and a single chiral edge magnon. There is thus no chirality in the phononic response. Due to magnetoelastic coupling, the Rayleigh-like phonon with wave vector $-k_x$ hybridizes

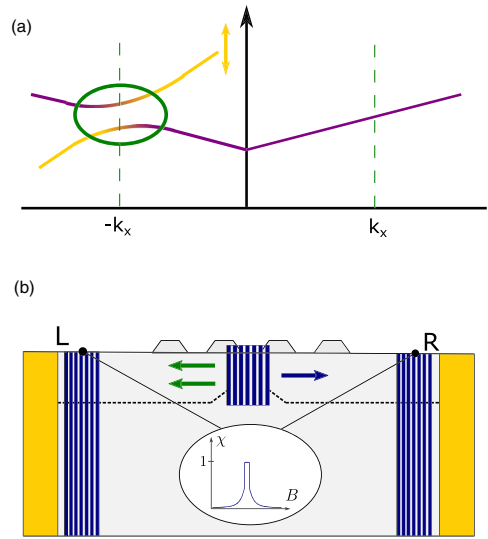


FIG. 4. (a) Schematic spectrum for the coupled Rayleigh-like edge phonons and the topological edge magnon on the upper armchair sample edge. The phonon at quasimomentum $-k_x$ hybridizes with the chiral magnon, while the phonon at quasimomentum $+k_x$ is unaffected due to the lack of a magnon with a matching wave vector at this edge. At the avoided crossing, there is propagation direction reversal for the modes with a phononic content. The color of the dispersion represents its nature with purple representing phononic and yellow magnonic character. (b) Proposed experimental setup for detecting coherent chiral transport through excitation of phononic modes. Elastic energy is injected in the sample middle on the upper armchair edge and detected at the left (L) and right (R) edges using wave vector and frequency resolved elastic transducers (purple). By exciting modes at the avoided crossing in (a), only the elastic excitations at one of the two quasimomenta $\pm k_x$ are converted into hybridized modes (green arrows). This gives a chiral response, and the chirality is peaked when the wave vector of the avoided crossing coincides with the fixed wave vector of the transducer.

with the chiral magnon to form a magnon polaron while the other phonon remains unchanged. This breaks the symmetry between the counterpropagating phononic modes and the result is nonzero chirality $\chi = (p_R - p_L)/(p_R + p_L)$. Furthermore, as shown in Fig. 4(a), the hybridization with the magnon mode reverses the group velocity direction of the participating phonon mode. In principle, this gives perfectly chiral phonon transport.

The wave vector location of the avoided crossing can be tuned via the Zeeman shift in the magnon dispersion. Performing a frequency integrated measurement over an energy range of the same order as the magnetoelastic coupling, one obtains a peaked chirality when the magnetic field is such that the wave vector of the avoided crossing coincides with the wave vector of the transducer, obtaining

a chirality as shown in Fig. 4(b). Performing a similar transport experiment on the zigzag edge does not give chiral phonon transport since the delocalized phonons hybridize with counterpropagating magnons on both the edges, thereby destroying the overall chirality. In addition, the size of the avoided crossing is smaller due to the smaller overlap with the localized chiral magnon. The armchair edge is therefore crucial for obtaining the chirality.

Summary.—We have examined the robustness of topological magnons in a honeycomb ferromagnet against their interaction with phonons. Their topological properties, albeit weakened, survive the magnetoelastic coupling. The magnon Hall conductivity of the system is found to depend on the magnetoelastic coupling strength in a nonmonotonic, temperature-sensitive manner. Exploiting the Rayleigh-like edge phonons in armchair ribbons, we predict the existence of topological magnon polarons confined to the boundary. We have suggested an experimental setup capable of probing the chiral nature of the topological magnon polarons by elastic means, which thus serves as a platform for chiral coherent phononic transport.

We acknowledge support from the Research Council of Norway Grant No. 262633 “Center of Excellence on Quantum Spintronics,” and No. 250985, “Fundamentals of Low-dissipative Topological Matter.”

*asle.sudbo@ntnu.no

- [1] F. D. M. Haldane, Model for a Quantum Hall Effect without Landau Levels: Condensed-Matter Realization of the “Parity Anomaly”, *Phys. Rev. Lett.* **61**, 2015 (1988).
- [2] C. L. Kane and E. J. Mele, Z_2 Topological Order and the Quantum Spin Hall Effect, *Phys. Rev. Lett.* **95**, 146802 (2005).
- [3] C. L. Kane and E. J. Mele, Quantum Spin Hall Effect in Graphene, *Phys. Rev. Lett.* **95**, 226801 (2005).
- [4] B. Bernevig, T. L. Hughes, and S.-C. Zhang, Quantum spin hall insulator state in hgte quantum wells, *Science* **314**, 1757 (2006).
- [5] V. Z. Hasan and C. L. Kane, Colloquium: Topological Insulators, *Rev. Mod. Phys.* **82**, 3045 (2010).
- [6] C. W. J. Beenakker, Search for majorana fermions in superconductors, *Annu. Rev. Condens. Matter Phys.* **4**, 113 (2013).
- [7] J. Alicea, New directions in the pursuit of majorana fermions in solid state systems, *Rep. Prog. Phys.* **75**, 076501 (2012).
- [8] V. Mourik, K. Zuo, S. M. Frolov, S. R. Plissard, E. P. A. M. Bakkers, and L. P. Kouwenhoven, Signatures of majorana fermions in hybrid superconductor-semiconductor nanowire devices, *Science* **336**, 1003 (2012).
- [9] L. Fu and C. L. Kane, Superconducting Proximity Effect and Majorana Fermions at the Surface of a Topological Insulator, *Phys. Rev. Lett.* **100**, 096407 (2008).
- [10] C. Nayak, S. H. Simon, A. Stern, M. Freedman, and S. Das Sarma, Non-abelian anyons and topological quantum computation, *Rev. Mod. Phys.* **80**, 1083 (2008).
- [11] S. Das Sarma, M. Freedman, and C. Nayak, Topologically Protected Qubits from a Possible Non-Abelian Fractional Quantum Hall State, *Phys. Rev. Lett.* **94**, 166802 (2005).
- [12] G. Jotzu, M. Messer, R. Desbuquois, M. Lebrat, T. Uehlinger, D. Greif, and T. Esslinger, Experimental realization of the topological haldane model with ultracold fermions, *Nature (London)* **515**, 237 (2014).
- [13] S. Lannebère and M. G. Silveirinha, Link between the photonic and electronic topological phases in artificial graphene, *Phys. Rev. B* **97**, 165128 (2018).
- [14] Y. Liu, Y. Xu, S.-C. Zhang, and W. Duan, Model for topological phononics and phonon diode, *Phys. Rev. B* **96**, 064106 (2017).
- [15] S. A. Owerre, A first theoretical realization of honeycomb topological magnon insulator, *J. Phys. Condens. Matter* **28**, 386001 (2016).
- [16] S. A. Owerre, Topological honeycomb magnon hall effect: A calculation of thermal hall conductivity of magnetic spin excitations, *J. Appl. Phys.* **120**, 043903 (2016).
- [17] S. K. Kim, H. Ochoa, R. Zarzuela, and Y. Tserkovnyak, Realization of the Haldane-Kane-Mele Model in a System of Localized Spins, *Phys. Rev. Lett.* **117**, 227201 (2016).
- [18] S. A. Owerre and J. Nsofini, Squeezed dirac and topological magnons in a bosonic honeycomb optical lattice, *J. Phys. Condens. Matter* **29**, 455802 (2017).
- [19] H.-S. Kim and H.-Y. Kee, Realizing haldane model in fe-based honeycomb ferromagnetic insulators, *npj Quantum Mater.* **2**, 20 (2017).
- [20] I. Dzyaloshinsky, A thermodynamic theory of weak ferromagnetism of antiferromagnetics, *J. Phys. Chem. Solids* **4**, 241 (1958).
- [21] T. Moriya, Anisotropic superexchange interaction and weak ferromagnetism, *Phys. Rev.* **120**, 91 (1960).
- [22] A. Rückriegel, A. Brataas, and R. A. Duine, Bulk and edge spin transport in topological magnon insulators, *Phys. Rev. B* **97**, 081106 (2018).
- [23] V. V. Kruglyak, S. O. Demokritov, and D. Grundler, Magnonics, *J. Phys. D* **43**, 264001 (2010).
- [24] A. V. Chumak, V. I. Vasyuchka, A. A. Serga, and B. Hillebrands, Magnon spintronics, *Nat. Phys.* **11**, 453 (2015).
- [25] G. E. W. Bauer, E. Saitoh, and B. J. van Wees, Spin caloritronics, *Nat. Mater.* **11**, 391 (2012).
- [26] K. Uchida, J. Xiao, H. Adachi, J. Ohe, S. Takahashi, J. Ieda, T. Ota, Y. Kajiwara, H. Umezawa, H. Kawai, G. E. W. Bauer, S. Maekawa, and E. Saitoh, Spin seebeck insulator, *Nat. Mater.* **9**, 894 (2010).
- [27] A. I. Akhiezer, V. G. Bar’iakhtar, and S. V. Peletminski, *Spin Waves* (North-Holland Publishing Company, Amsterdam, 1968).
- [28] A. V. Chumak, A. A. Serga, and B. Hillebrands, Magnon transistor for all-magnon data processing, *Nat. Commun.* **5**, 4700 (2014).
- [29] K. Ganzhorn, S. Klingler, T. Wimmer, S. Geprgs, R. Gross, H. Huebl, and S. T. B. Goennenwein, Magnon-based logic in a multi-terminal yig/pt nanostructure, *Appl. Phys. Lett.* **109**, 022405 (2016).
- [30] T. An, V. I. Vasyuchka, K. Uchida, A. V. Chumak, Y. Yamaguchi, K. Harii, J. Ohe, M. B. Jungfleisch, Y. Kajiwara, H. Adachi, B. Hillebrands, S. Maekawa,

- and E. Saitoh, Unidirectional spin-wave heat conveyer, *Nat. Mater.* **12**, 549 (2013).
- [31] E. Saitoh, M. Ueda, H. Miyajima, and G. Tatara, Conversion of spin current into charge current at room temperature: Inverse spin-hall effect, *Appl. Phys. Lett.* **88**, 182509 (2006).
- [32] E. B. Sonin, Spin currents and spin superfluidity, *Adv. Phys.* **59**, 181 (2010).
- [33] S. Takei, B. I. Halperin, A. Yacoby, and Y. Tserkovnyak, Superfluid spin transport through antiferromagnetic insulators, *Phys. Rev. B* **90**, 094408 (2014).
- [34] A. Kamra and W. Belzig, Super-Poissonian Shot Noise of Squeezed-Magnon Mediated Spin Transport, *Phys. Rev. Lett.* **116**, 146601 (2016).
- [35] A. Kamra, U. Agrawal, and W. Belzig, Noninteger-spin magnonic excitations in untextured magnets, *Phys. Rev. B* **96**, 020411 (2017).
- [36] C. Kittel, Physical theory of ferromagnetic domains, *Rev. Mod. Phys.* **21**, 541 (1949).
- [37] C. Kittel, Interaction of spin waves and ultrasonic waves in ferromagnetic crystals, *Phys. Rev.* **110**, 836 (1958).
- [38] K. Uchida, H. Adachi, T. An, T. Ota, M. Toda, B. Hillebrands, S. Maekawa, and E. Saitoh, Long-range spin seebeck effect and acoustic spinpumping, *Nat. Mater.* **10**, 737 (2011).
- [39] A. Kamra, H. Keshtgar, P. Yan, and G. E. W. Bauer, Coherent elastic excitation of spin waves, *Phys. Rev. B* **91**, 104409 (2015).
- [40] A. Kamra and G. E. W. Bauer, Actuation, propagation, and detection of transverse magnetoelastic waves in ferromagnets, *Solid State Commun.* **198**, 35 (2014).
- [41] M. Weiler, H. Huebl, F. S. Goerg, F. D. Czeschka, R. Gross, and S. T. B. Goennenwein, Spin Pumping with Coherent Elastic Waves, *Phys. Rev. Lett.* **108**, 176601 (2012).
- [42] L. Dreher, M. Weiler, M. Pernpeintner, H. Huebl, R. Gross, M. S. Brandt, and S. T. B. Goennenwein, Surface acoustic wave driven ferromagnetic resonance in nickel thin films: Theory and experiment, *Phys. Rev. B* **86**, 134415 (2012).
- [43] B. Flebus, K. Shen, T. Kikkawa, K.-i. Uchida, Z. Qiu, E. Saitoh, R. A. Duine, and G. E. W. Bauer, Magnon-polaron transport in magnetic insulators, *Phys. Rev. B* **95**, 144420 (2017).
- [44] T. Kikkawa, K. Shen, B. Flebus, R. A. Duine, K.-i. Uchida, Z. Qiu, G. E. W. Bauer, and E. Saitoh, Magnon Polarons in the Spin Seebeck Effect, *Phys. Rev. Lett.* **117**, 207203 (2016).
- [45] D. A. Bozhko, P. Clausen, G. A. Melkov, V. S. L'vov, A. Pomyalov, V. I. Vasyuchka, A. V. Chumak, B. Hillebrands, and A. A. Serga, Bottleneck Accumulation of Hybrid Magnetoelastic Bosons, *Phys. Rev. Lett.* **118**, 237201 (2017).
- [46] A. Rückriegel, P. Kopietz, D. A. Bozhko, A. A. Serga, and B. Hillebrands, Magnetoelastic modes and lifetime of magnons in thin yttrium iron garnet films, *Phys. Rev. B* **89**, 184413 (2014).
- [47] N. Li, J. Ren, L. Wang, G. Zhang, P. Hänggi, and B. Li, Colloquium: Phononics: Manipulating heat flow with electronic analogs and beyond, *Rev. Mod. Phys.* **84**, 1045 (2012).
- [48] M. Maldovan, Sound and heat revolutions in phononics, *Nature (London)* **503**, 209 (2013).
- [49] Y. Liu, Y. Xu, S.-C. Zhang, and W. Duan, Model for topological phononics and phonon diode, *Phys. Rev. B* **96**, 064106 (2017).
- [50] The demagnetization energy is disregarded since it only causes minor shifts in the dispersion [35].
- [51] M. O. Scully and M. S. Zubairy, *Quantum Optics* (Cambridge University Press, Cambridge, 1997).
- [52] K. Nakata, J. Klinovaja, and D. Loss, Magnonic quantum hall effect and wiedemann-franz law, *Phys. Rev. B* **95**, 125429 (2017).
- [53] See Supplemental Material at <http://link.aps.org/supplemental/10.1103/PhysRevLett.122.107201> for details of the derivation of the main results of the paper.
- [54] C. Kittel, *Quantum Theory of Solids* (John Wiley & Sons, New York, 1987).
- [55] G. S. Kino, *Acoustic Waves: Devices, Imaging, and Analog Signal Processing*, Prentice-Hall Contemporary Topics in Accounting Series (Prentice-Hall, Englewood Cliffs, New Jersey, 1987).
- [56] A. A. Maradudin and G. I. Stegeman, Surface Acoustic Waves, in *Surface Phonons*, edited by F. W. de Wette and W. Kress (Springer-Verlag, Berlin-Heidelberg, 1991), Chap. 2, pp. 5–36.
- [57] B. Andrei Bernevig and T. L. Hughes, *Topological Insulators and Topological Superconductors* (Princeton University Press, Princeton, New Jersey, 2013).
- [58] P. Ruello and V. E. Gusev, Physical mechanisms of coherent acoustic phonons generation by ultrafast laser action, *Ultrasonics* **56**, 21 (2015).
- [59] J. Liu, L. J. Cornelissen, J. Shan, T. Kuschel, and B. J. van Wees, Magnon planar hall effect and anisotropic magnetoresistance in a magnetic insulator, *Phys. Rev. B* **95**, 140402 (2017).
- [60] The inset of Fig. 3(b) shows two phonon modes. One is irrelevant since it is localized on the opposite edge.
- [61] P. G. Gowtham, T. Moriyama, D. C. Ralph, and R. A. Buhrman, Traveling surface spin-wave resonance spectroscopy using surface acoustic waves, *J. Appl. Phys.* **118**, 233910 (2015).
- [62] S. Datta, *Surface Acoustic Wave Devices* (Prentice-Hall, Englewood Cliffs, New Jersey, 1986).
- [63] A. V. Mamišev, K. Sundara-Rajan, Fumin Yang, Yanqing Du, and M. Zahn, Interdigital sensors and transducers, *Proc. IEEE* **92**, 808 (2004).

**Supplemental Material to the manuscript “Chiral Phonon Transport Induced
by Topological Magnons” by**

Even Thingstad, Akashdeep Kamra, Arne Brataas, and Asle Sudbø

RAYLEIGH-LIKE PHONON EDGE MODES

To describe the phonons, as discussed in the main paper, we consider a force constant model for out-of-plane phonon modes on the honeycomb lattice with only nearest neighbour interaction. This is described by the Hamiltonian

$$H = \sum_i \frac{p_i^2}{2m} + \frac{1}{2} \sum_{\langle i,j \rangle} C(u_i - u_j)^2, \quad (1)$$

where i and j are lattice site indices running over both the A and B sublattices of the honeycomb lattice.

To investigate edge modes in the system, we consider a finite ribbon geometry with periodic boundary conditions in one direction, and with a finite number of unit cells in the other direction. The edges of such ribbons can mainly be of two types: zigzag and armchair. The lattice geometries of these cases are shown in Fig. 1.

To find the phonon energy spectrum for these lattice geometries, we introduce the partial Fourier transform of the lattice site deviations and momenta, which for the lattice site deviation takes the form

$$u_{x,y}^D = \frac{1}{\sqrt{N_x}} \sum_k u_{ky} \exp(ik\hat{x} \cdot \mathbf{r}_n^D), \quad (2)$$

where $u_{x,y}^D$ is the lattice site deviation on sublattice D in unit cell (x,y) , $\mathbf{r}_{x,y}^D$ is the corresponding equilibrium position, and N_x is the number of unit cells in the horizontal direction. The periodicity requirement $u_{x,y}^D = u_{x+N_x,y}^D$ then gives $k = 2\pi n/N_x\lambda$, where λ is the periodicity of the lattice in the horizontal direction and n is an integer. For the zigzag edge ribbon, $\lambda = \sqrt{3}d$, while $\lambda = 3d$ for the armchair edge ribbon. This determines the size of the Brillouin zone.

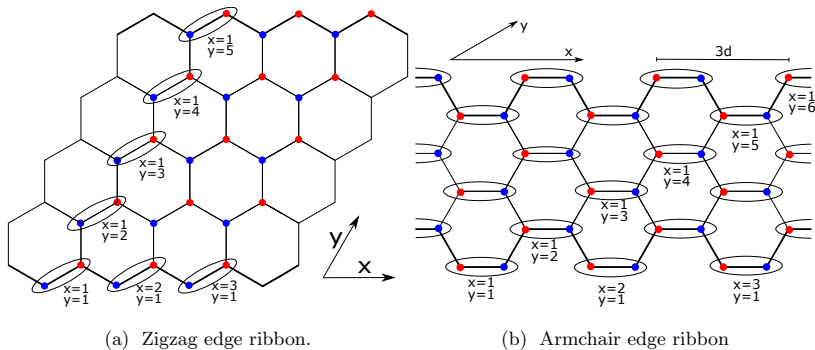


FIG. 1. Lattice geometries for the zigzag- and armchair edge ribbons, including unit cell labelling. We assume periodic boundary conditions in the horizontal direction and a finite number of hexagon layers in the vertical direction.

Introducing

$$u_k^\dagger = (u_{-k1}^A, u_{-k1}^B, u_{-k2}^A, u_{-k2}^B, \dots, u_{-kN_y}^A, u_{-kN_y}^B) \quad (3)$$

with similar notation for the momentum, the phonon Hamiltonian can be written on the form

$$H = \frac{1}{2m} \sum_k p_k^\dagger p_k + \frac{C}{2} \sum_k u_k^\dagger M_k u_k, \quad (4)$$

with a matrix M_k coupling the deviations on the various sublattices and neighbouring unit cell layers. This Hamiltonian is diagonalized through a unitary transform of the deviations and momenta followed by introducing phonon creation and annihilation operators c_k^\dagger and c_k [1]. The excitation spectrum is then given by the phonon frequencies ω_{kn} , where $\omega_{kn}^2 = (C/m)\lambda_{kn}$ and $\{\lambda_{kn}\}$ are the eigenvalues of M_k .

Following this procedure for the ribbon geometry with zigzag edges, we obtain the spectrum in Fig. 2(a). The upper and lower branches of the phonon spectrum meet at $k_x d = 2\pi/3\sqrt{3}$ and $k_x d = 4\pi/3\sqrt{3}$, consistent with the result obtained by taking the 1-dimensional projection of the bulk bands. In Fig. 3, we plot the spatial profile of some selected eigenstates at quasimomentum $k_x d = 2\pi/3\sqrt{3}$. All the modes are delocalized.

Examining the armchair ribbon spectrum in Fig. 2(b), one may notice that the modes marked with green arrows stand out from the rest. If we were to compute the bulk spectrum and then perform

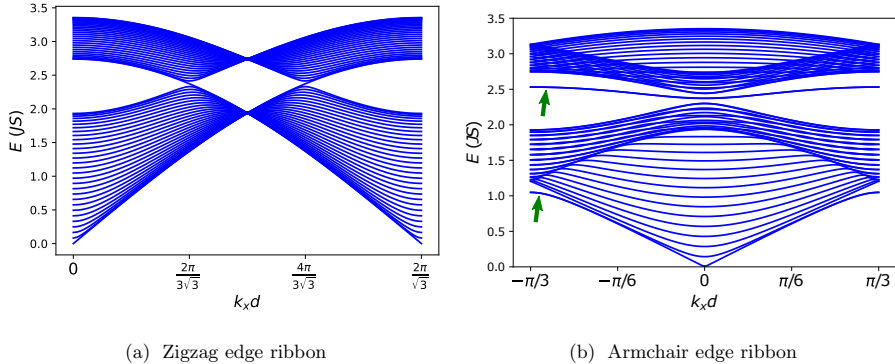


FIG. 2. One-dimensional projection of the energy spectrum for phonon modes on the honeycomb ribbon geometry with zigzag and armchair edges for $N_y = 30$ unit cells in the vertical direction (see Fig. 1). For the armchair ribbon, in addition to the bulk modes, there are edge modes marked with green arrows.

a 1D projection, the two modes marked in green would not be found. We therefore conclude that they must originate from an edge effect.

This is confirmed by examining the spatial profile of the modes, as shown in Fig. 4 for the modes between the upper and lower bulk phonon branches. The deviation amplitudes are finite on the outer armchair edges of the sample, and exponentially decaying into the interior of the sample. The inset shows the decay length as function of the inverse quasimomentum, and demonstrates that $\xi \propto 1/k_x$. This is perfectly analogous to the behaviour of so-called Rayleigh modes on the surface of a three-dimensional material [2]. Our modes can therefore be characterized as one-dimensional analogs of Rayleigh modes.

From the above discussion, it follows that that while the armchair edges support edge modes, the zigzag edge does not. This is rooted in the fact that on the edge unit cells of the armchair ribbon, both atoms have 2 nearest neighbours. For the zigzag ribbon, one atom has 2 nearest neighbours, but the other has 3. Vibrations are therefore easier to excite on the edges of the armchair ribbon.

COUPLED MAGNETOELASTIC MODES IN ZIGZAG RIBBON

To compute the excitation spectrum for the model with coupled magnon and phonon modes, we first calculate the phonon and magnon edge modes for the uncoupled model. The phonon modes

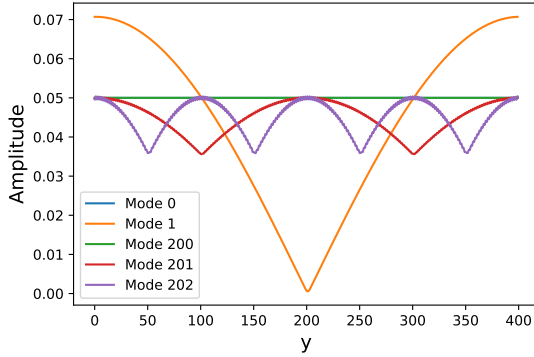


FIG. 3. Deviation amplitudes for selected zigzag ribbon phonon modes at $k_x d = 2\pi/3\sqrt{3}$ for $N_y = 200$ unit cells in the vertical direction. Fast oscillations have been averaged out. All modes are delocalized.

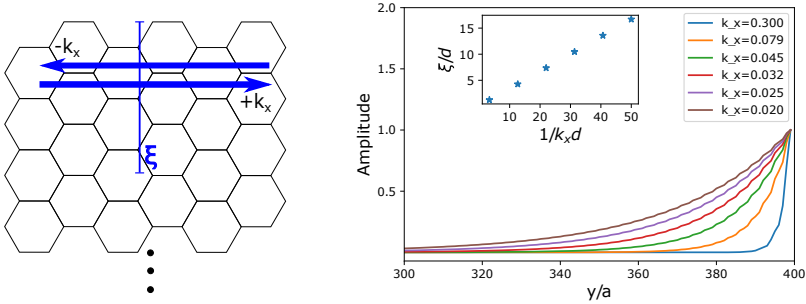


FIG. 4. (a) Rayleigh mode schematic. At a given armchair edge, two Rayleigh-like modes propagate along the edge with quasimomenta $\pm k_x$. The modes are localized within a distance $\xi(k_x)$ from the edge. (b) Deviation amplitudes for the Rayleigh-like edge modes as function of the vertical position y in units of the Bravais lattice constant a for different momenta k_x . The amplitudes are normalized to the value on the edge for easier comparison. The inset shows the localization length $\xi(k_x)$ as function of the inverse quasimomentum, demonstrating that $\xi \propto 1/k_x$, consistent with the behaviour expected from ordinary Rayleigh modes.

were discussed in the previous section, and we refer to the literature for the magnon spectrum [3]. Expressing the magneto-elastic coupling in terms of these eigenmodes and diagonalizing the resulting matrix, we obtain the excitation spectra.

For the zigzag edge ribbon, the spectrum is shown in Fig. 5. All phonon modes are delocalized. In the inset, we show the hybridization of the chiral edge magnon mode with some of these delocalized

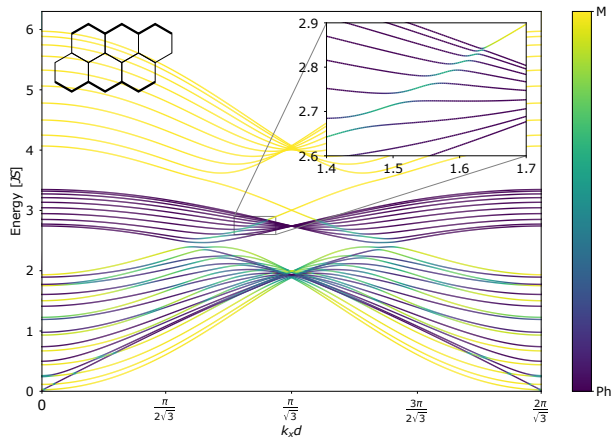


FIG. 5. Energy spectrum for the coupled magnon and phonon modes of the ribbon geometry with zigzag edge as function of quasimomentum k_x . The magnon (yellow) and phonon (purple) content of each mode is indicated with color.

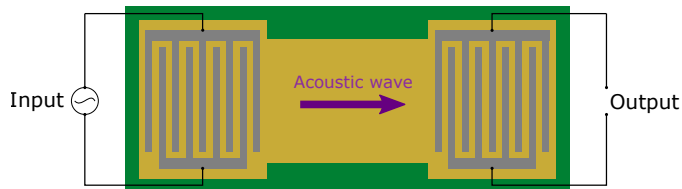


FIG. 6. Schematic depiction of an interdigital transducer employed to excite Rayleigh waves via an ac voltage on the left hand side. The same structure converts the acoustic waves back to ac voltage on the right and enables their detection. The metallic electrodes are lithographically patterned on top of a piezoelectric material, such as Lithium Niobate, into the depicted comb structure.

modes. The armchair ribbon spectrum has already been discussed in the main text.

INTERDIGITAL ELASTIC TRANSDUCERS

General principles and qualitative description

The interdigital transducer [4, 5] (IDT) consists of two metallic electrodes with a series of sections, called fingers, which are patterned into a comb-like structure on top of a piezoelectric material (Fig. 6). When a voltage is applied across the two electrodes, it creates a pattern of alternating charges on adjacent fingers via the capacitive effect. Via the constitutive properties of the piezo-

electric material, this results in a pattern of alternating strains. An applied ac voltage with angular frequency ω thus excites acoustic waves at the same frequency in the piezoelectric material. The wavelength is determined by the corresponding dispersion relation $\omega = ck$ [6], where c is the speed of sound in the material and k is the wavenumber. If the ensuing wavelength $\lambda = 2\pi/k$ is equal to the spacing between the adjacent fingers belonging to the same electrode, the acoustic signal interferes constructively and the excitation efficiency is high. If there is a mismatch between the finger spacing and the wavelength excited at the applied ac voltage frequency, the acoustic waves tend to cancel each other and excitation efficiency is low. With an increasing number N of fingers, the reinforcement or cancellation effect is stronger and the excitation resonances become sharper. Thus, the operation principle of an IDT is similar to that of a Bragg grating. Then, it is easy to understand that peaks in excitation are observed at multiple frequencies (and wavelengths) corresponding to the finger spacing being multiples of the acoustic wavelength. The fundamental peak is the strongest and subsequent overtones are progressively weaker as demonstrated by the frequency transfer characteristics discussed below.

Conventionally, IDTs have been employed in applications such as analog filters, and their desired operation frequency range has been from MHz to several tens of GHz [4]. A typical piezoelectric material employed is Lithium Niobate with a Rayleigh wave speed of 3.3 km/s. Thus, the fundamental peak corresponding to a center frequency of 1 GHz requires finger spacing of around 1 μm , which could easily be achieved via photolithography techniques. With contemporary electron-beam lithography techniques, a finger spacing of several tens of nanometers is readily possible, thus allowing a fundamental frequency of tens of GHz. Employing higher overtones allows pushing the operation frequency to several tens of GHz, and is predominantly limited by the driving electronics [5]. Due to the purview of their conventional applications, attempts to achieve higher frequencies have been limited. With recent advances in ultrafast lasers, several conventional methods have been adapted to achieve coherent phonon generation in the THz regime [7]. Thus, the operation range of the proposed method is estimated to be rather wide with up to hundreds of GHz in frequency and tens of nanometers in wavelength. The wavenumber selectivity can also be increased, in principle to arbitrary values, by using a large number of fingers. Combined with the tunability of the exact magnon-phonon anticrossing point (via an applied field, for example) across a broad range of frequencies and wavevectors, the proposed experimental method is well within the range of the contemporary state-of-the-art technology.

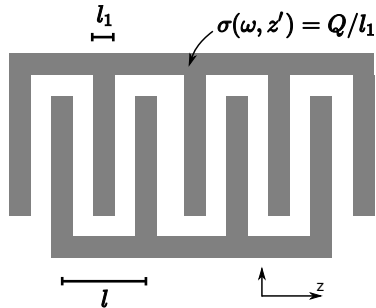


FIG. 7. Modeling the acoustic output of an interdigital transducer within the delta function model. An applied voltage generates charges on the metallic electrodes via the capacitive effect. The accumulated charge (or equivalently electric field) is converted into strain via the piezoelectric effect.

Frequency resolved acoustic output

To supplement the above qualitative discussion of the operating principles of an IDT, we now discuss its frequency resolved excitation efficiency within the so-called delta function model (Fig. 7). This model assumes that the charge accumulated on each finger is distributed uniformly and that the acoustic output is a linear superposition of the strain produced by the full charge distribution. In evaluating the strain (and thus the acoustic output) at a given point due to different fingers, the phase difference due to wave propagation from the fingers needs to be accounted adequately. The amplitude of the excited acoustic wave $A(z, \omega)$ at a position z is thus given by

$$A(z, \omega) = \alpha \int \sigma(\omega, z') e^{-ik(z-z')} dz', \quad (5)$$

where α is the charge-strain coupling factor of the piezoelectric material and $\sigma(\omega, z')$ is the charge density accumulated at position z' . The acoustic output of the IDT is thus simply the Fourier transform of the accumulated charge density. The square-wave like pattern of the accumulated charge on the comb-like structure thus suggests a sinc function response.

Referring the readers to detailed derivations and discussion in Ref. 4, we simply present the key result here. For an N -finger comb, the overall acoustic amplitude outside the IDT region becomes

$$A(\omega, z) = i\alpha Q \frac{\sin(kNl/2)}{\cos(kl/4)} \text{sinc}\left(\frac{l_1}{\lambda}\right) e^{ik(N-1)l/2} e^{i(\omega t - kz)}, \quad (6)$$

where Q is the charge on a single finger, l and l_1 are defined in Fig. 7, and $\text{sinc}(x) = \sin(\pi x)/(\pi x)$. The equation above fully describes all the design characteristics of the device. Its further analysis

shows that the center or fundamental frequency ω_0 is determined by the condition $k_0 l = 2\pi$ (Note that $\omega_0 = ck_0$), while the bandwidth between the zeros in the response is given by $\Delta\omega/\omega_0 = 2/N$, in consistence with the qualitative discussion above.


-
- [1] Kittel, *Quantum Theory of Solids* (1987).
- [2] A. A. Maradudin and G. I. Stegeman, in *Surface phonons*, edited by F. W. d. W. W. Kress (Springer-Verlag, Berlin-Heidelberg, 1991) Chap. 2, pp. 5–36.
- [3] B. A. Bernevig and T. L. Hughes, *Topological insulators and topological superconductors* (Princeton University Press).
- [4] G. Kino, *Acoustic Waves: Devices, Imaging, and Analog Signal Processing*, Prentice-Hall Contemporary Topics in Accounting Series (Prentice-Hall, 1987).
- [5] A. V. Mamishev, K. Sundara-Rajan, F. Yang, Y. Du, and M. Zahn, *Proceedings of the IEEE* **92**, 808 (2004).
- [6] For simplicity, and as a concrete example, we consider the linear dispersion of the Rayleigh waves typical of a conventional IDT system. The technique however works for an arbitrary dispersion $\omega(k)$.
- [7] P. Ruello and V. E. Gusev, *Ultrasonics* **56**, 21 (2015).

Paper 2

E. Thingstad, A. Kamra, J.W. Wells, and A. Sudbø,

Phonon-mediated superconductivity in doped monolayer materials,

Phys. Rev. B **101**, 214513 (2020).

Phonon-mediated superconductivity in doped monolayer materialsEven Thingstad, Akashdeep Kamra, Justin W. Wells, and Asle Sudbø *Center for Quantum Spintronics, Department of Physics, Norwegian University of Science and Technology, NO-7491 Trondheim, Norway*

(Received 12 November 2019; revised manuscript received 5 May 2020; accepted 19 May 2020; published 9 June 2020)

Insight into why superconductivity in pristine and doped monolayer graphene seems strongly suppressed has been central for the recent years' various creative approaches to realize superconductivity in graphene and graphene-like systems. We provide further insight by studying electron-phonon coupling and superconductivity in doped monolayer graphene and hexagonal boron nitride based on intrinsic phonon modes. Solving the graphene gap equation using a detailed model for the effective attraction based on electron tight binding and phonon force constant models, the various system parameters can be tuned at will. Consistent with results in the literature, we find slight gap modulations along the Fermi surface, and the high-energy phonon modes are shown to be the most significant for the superconductivity instability. The Coulomb interaction plays a major role in suppressing superconductivity at realistic dopings. Motivated by the direct onset of a large density of states at the Fermi surface for small charge dopings in hexagonal boron nitride, we also calculate the dimensionless electron-phonon coupling strength there, but the comparatively large density of states cannot immediately be capitalized on, and the charge doping necessary to obtain significant electron-phonon coupling is similar to the value in graphene.

DOI: [10.1103/PhysRevB.101.214513](https://doi.org/10.1103/PhysRevB.101.214513)**I. INTRODUCTION**

The discovery of graphene has attracted massive attention in condensed matter physics, stimulating an enormous number of theoretical and experimental investigations into a class of novel materials broadly denoted as Dirac materials [1–5]. Among their interesting properties is the Dirac-cone-shaped electron band structure at half filling, enabling the study of relativistic physics in a condensed matter setting [3,6–8]. However, the cone structure with a vanishing density of states and Fermi surface at the Dirac point suppresses phenomena such as superconductivity, which precisely rely on the existence of a Fermi surface.

In spite of this obstacle, there is a plethora of graphene-like systems where superconductivity has been predicted or observed. In carbon nanotubes and the carbon based fullerene crystals also known as “buckyballs,” superconductivity was observed already decades ago in crystals intercalated with potassium [9,10]. Superconductivity is also well known in graphite intercalation compounds [11–15], where the interlayer interactions and the additional dopant phonon modes enhance superconductivity [12]. A similar picture arises also for intercalated bilayer graphene, where interlayer interactions are crucial for the resulting superconductivity [16,17]. In bilayer graphene, a different route to superconductivity is the magic angle twist approach [18–21], where strong correlations are believed to play a key role. Superconductivity has also been demonstrated in effectively one-dimensional carbon nanotubes [22,23], which have strong screening of the repulsive Coulomb interaction. In addition to these intrinsic mechanisms, superconductivity may also be induced by proximity [24–27]. There, the resulting superconductivity in graphene will necessarily inherit extrinsic key properties from the superconductor it is placed in proximity to [27].

Although superconductivity is already well established in a multitude of these graphene-like systems, its observation in monolayer graphene has proven very challenging. For phonon-mediated superconductivity, the key quantity is the dimensionless electron-phonon coupling (EPC) strength λ , which is determined by both the density of states at the Fermi level and the strength of the effective phonon-mediated potential. The first challenge that has to be overcome is therefore doping the system away from the Dirac point. The primary ways of doing this are chemical doping [28–32] and deposition of elements onto (or under) the graphene sheet [33–43]. Using these methods, doping levels approaching the van Hove singularity have been achieved [35]. Second, one must make sure that λ has a sufficiently large value at the achievable doping. Additional dopant phonon modes and modifications of the electron band structure in decorated monolayer graphene may enhance the electron-phonon coupling strength [36,41–44], and in these systems, one has even observed some evidence [43,45] for the desired monolayer graphene superconductivity.

The EPC strength λ can be measured by examining kinks and broadening in the electronic band structure using angular-resolved photoemission spectroscopy (ARPES) [46–48]. At realistic doping energies in the vicinity of the van Hove singularity in the π band, λ values of the same order as in many known conventional superconductors [49] have been predicted and measured experimentally [48,50,51]. In light of this, superconductivity in single-layer graphene with reasonable critical temperatures does not seem inconceivable even without dopant phonon modes and special electron band structure modifications. Why superconductivity in monolayer graphene remains so hard to achieve is therefore not entirely clear.

In conventional superconducting materials, the Coulomb interaction does not play a significant role in reducing T_c , since the effective phonon-mediated potential is attractive only in a small region around the Fermi surface, whereas the repulsive Coulomb interaction has much longer Brillouin zone variations. The mechanism at work, retardation, can be seen by solving the gap equation with a simplified model [52] for the combined potential. In graphene, however, we do expect the Coulomb interaction [53] to reduce the critical temperature significantly [41,44,54,55] due to the modest electron-phonon coupling strength. A crude estimate of the Morel-Anderson renormalization of the dimensionless EPC strength λ shows that the renormalization is of the same order as λ itself. A detailed study of phonon-mediated superconductivity in graphene is therefore necessary.

Eliashberg theory for doped monolayer graphene was developed in Ref. [55], where the pair scattering processes within and between the Fermi surface segments centered around the inequivalent Brillouin zone points K and K' were accounted for explicitly. The authors estimate the critical temperature based on the assumption of an isotropic gap, Fermi surface averaged Coulomb interaction [41,53] in the linear spectrum regime, and various estimates for the electron-phonon coupling strength based on other works. The resulting critical temperature is of order 10 K with the optimistic estimates.

In Ref. [44], the electron-phonon coupling strength and superconducting gap were calculated with anisotropic Eliashberg theory based on *ab initio* calculation of the quasimomentum and energy dependent electron-phonon coupling strength. Coulomb interaction effects are incorporated through a Morel-Anderson pseudopotential, which is treated as a semiempirical parameter. For n -type doping, they find that superconductivity may be possible due to the presence of a free-electron-like (FEL) band. For p -type doping, this band is not present, and the Coulomb interaction seems likely to suppress superconductivity.

In this paper, we perform detailed calculations of the electron-phonon coupling based on an electron tight binding model and a phonon force constant model in the presence of a Hubbard-type Coulomb interaction. We then solve an anisotropic BCS-type gap equation, which should give reasonable estimates for the superconducting properties due to the relatively modest electron-phonon coupling strength. The various system parameters in our model can easily be tuned to investigate how various physical mechanisms affect the superconducting properties. Understanding this is essential in the pursuit of realizing superconductivity in monolayer graphene based on the intrinsic in-plane phonon modes.

Our results show that superconductivity with an experimentally measurable gap may be possible for large dopings approaching the van Hove singularity. We find an electron-phonon coupling strength and gap anisotropy qualitatively similar and of the same order as in Ref. [44], and the Coulomb interaction is shown to be crucial in reducing the critical temperature of the system. We also look into the contributions to the electron-phonon coupling from the various phonon modes in the system [41], and identify the high-energy phonons as the most significant for the superconducting instability in the realistically achievable doping regime.

The two-dimensional material hexagonal boron nitride (h -BN) was discovered shortly [2] after graphene [1] using

the same micromechanical cleavage technique to exfoliate monolayers from the stacks of weakly interacting layers also known as van der Waals materials. In many respects, the two are very similar [56]. They have the same lattice structure and a similar lattice constant, which makes h -BN a good substrate for graphene [57,58] and suitable for graphene heterostructure engineering [59]. Like graphene, it also has strong chemical bonding, and a comparable phonon Debye frequency [60]. Unlike graphene, however, boron nitride has two different ions, boron and nitrogen, on the two honeycomb sublattices. This has dramatic consequences for the electronic band structure, since the Dirac cone in graphene is protected by time-reversal and inversion symmetry. Breaking of the latter symmetry therefore renders hexagonal boron nitride a large-gap insulator [61].

The possibility of superconductivity in doped hexagonal boron nitride is a lot less studied than in doped graphene, but a recent density functional theory study [62] suggests that decorated h -BN may become superconducting with a transition temperature of up to 25 K. Although the dopant phonon modes are again responsible for this relatively large transition temperature, this also hints at possibilities for superconductivity mediated by intrinsic in-plane phonon modes. Furthermore, and very different from graphene, the parabolic nature of the electron band close to the valence band maximum gives a direct onset of a large density of states even at small charge doping. Motivated by this, we use the same methodology as in the graphene case to calculate the dimensionless electron-phonon coupling strength λ for hexagonal boron nitride. Due to suppression of the electron-phonon coupling matrix element due to the small Fermi surface, however, this effect cannot be capitalized on, and we find that h -BN has an electron-phonon coupling strength similar to graphene.

In Sec. II of this paper, we first present the free electron and the free phonon models for graphene briefly, followed by a more thorough derivation of the tight binding electron-phonon coupling. In Sec. III, we introduce and discuss the Hubbard-type Coulomb interaction used in this paper. In Sec. IV, we introduce the assumed pairing, resulting gap equation, and effective phonon-mediated potential, before presenting the numerical results for graphene in Sec. V. In Sec. VI, we discuss some qualitative aspects of these results. Switching to boron nitride in Sec. VII, we discuss how the opening of a gap changes the band structure and electron-phonon coupling. Finally, the paper is summarized in Sec. VIII.

II. ELECTRONS, PHONONS, AND ELECTRON-PHONON COUPLING

We consider a model for electrons on the graphene lattice, and allow for lattice site vibrations. For the electrons, we use a nearest neighbor tight binding model [4] describing the π bands, as explained in further detail in Appendix A. Other bands are disregarded, since only the π bands are close to the Fermi surface for realistically achievable doping levels in graphene. For the phonons, we use a force constant model with nearest and next-to-nearest neighbor couplings as introduced in Refs. [63,64] and elaborated in Appendices B and C. These models give a realistic band structure and realistic phonon spectra.

The electron-phonon coupling model is derived by assuming the electrons to follow the lattice site ions adiabatically, and by Taylor-expanding the overlap integral t_{ij} in the hopping Hamiltonian

$$H = - \sum_{(i,j),\sigma} (t_{ij} c_{i\sigma}^\dagger c_{j\sigma} + \text{H.c.}) \quad (1)$$

to linear order in the deviations. Here, $c_{i\sigma}^\dagger$ and $c_{i\sigma}$ are creation and annihilation operators for an electron at site i with spin $\sigma \in \{\uparrow, \downarrow\}$. Considering only the nearest neighbor hoppings, we obtain

$$t_{i+\delta_A,i} = t_1 + (\mathbf{u}_{i+\delta_A} - \mathbf{u}_i) \cdot \nabla t_1(\boldsymbol{\delta}), \quad (2)$$

where t_1 is the nearest neighbor hopping amplitude, \mathbf{u}_i is the ionic displacement of lattice site i from its equilibrium position, and the overlap integral $t_1(\boldsymbol{\delta})$ is regarded as a function of the relative position $\boldsymbol{\delta}$ of the two lattice sites i and $i + \delta_A$, where δ_A is the equilibrium nearest neighbor vector from the A to the B sublattice. Due to the mirror symmetry about the line connecting the lattice sites i and $i + \delta_A$, the electron-phonon coupling can be written as

$$H_{\text{el-ph}} = \frac{\gamma t_1}{d^2} \sum_{i \in A, \delta_A, \sigma} \boldsymbol{\delta}_A \cdot (\mathbf{u}_{i+\delta_A} - \mathbf{u}_i) (c_{i+\delta_A, \sigma}^\dagger c_{i, \sigma} + \text{H.c.}), \quad (3)$$

where $\gamma = -d \ln t_1/d \ln d$ is a dimensionless number of order 1, and d is the equilibrium nearest neighbor distance, which we use as our unit of length. In quasimomentum space, this gives the electron-phonon coupling

$$H_{\text{el-ph}} = \sum_{\mathbf{k}, \mathbf{q}} \sum_{\eta \eta'} \sum_{\nu, \sigma} g_{\mathbf{k}, \mathbf{k}+\mathbf{q}}^{\eta \eta', \nu} (a_{\mathbf{q}\nu} + a_{-\mathbf{q}, \nu}^\dagger) c_{i, \sigma}^\dagger(\mathbf{k} + \mathbf{q}) c_{i, \sigma}(\mathbf{k}), \quad (4)$$

where $a_{\mathbf{q}\nu}$ and $a_{-\mathbf{q}, \nu}^\dagger$ are creation and annihilation operators for in-plane phonons labeled by $\nu \in \{0, 1, 2, 3\}$, and $\eta, \eta' = \pm$ denote electron bands. To linear order in the lattice site deviations, the out-of-plane phonon modes do not couple to the electrons due to the assumed $z \rightarrow -z$ mirror symmetry of the system [65]. The coupling matrix element $g_{\mathbf{k}, \mathbf{k}+\mathbf{q}}^{\eta \eta', \nu}$ is given by

$$\begin{aligned} g_{\mathbf{k}, \mathbf{k}+\mathbf{q}}^{\eta \eta', \nu} &= \frac{g_0}{\sqrt{N_A}} \sqrt{\frac{\omega_\Gamma}{\omega_{\mathbf{q}\nu}}} \sum_{\delta_A} \left(\frac{\delta_A}{d} \right) [e^{i\mathbf{q} \cdot \delta_A} \mathbf{e}_\nu^B(\mathbf{q}) - \mathbf{e}_\nu^A(\mathbf{q})] \\ &\times [e^{i\mathbf{k} \cdot \delta_A} F_{A\eta}^*(\mathbf{k} + \mathbf{q}) F_{B\eta}(\mathbf{k}) \\ &+ e^{-i(\mathbf{k}+\mathbf{q}) \cdot \delta_A} F_{B\eta}^*(\mathbf{k} + \mathbf{q}) F_{A\eta}(\mathbf{k})], \end{aligned} \quad (5)$$

where $F_{D\eta}(\mathbf{k})$ is the sublattice amplitude of electron band η at quasimomentum \mathbf{k} and follows from the diagonalization of the free electron model, as elaborated in Appendix A. Similarly, $\mathbf{e}_\nu^D(\mathbf{q})$ is the phonon polarization vector at sublattice $D \in \{A, B\}$ for the phonon mode (\mathbf{q}, ν) , and follows from diagonalization of the in-plane phonon Hamiltonian (see Appendix B for details). The phonon mode frequencies are denoted by $\omega_{\mathbf{q}\nu}$, N_A is the number of lattice sites on the A sublattice, and the energy scale g_0 is given by

$$g_0 = \sqrt{\left(\frac{\hbar^2}{2Md^2} \right) \frac{1}{\hbar\omega_\Gamma} \gamma t_1}, \quad (6)$$

where M is the carbon atom mass, and ω_Γ is a phonon energy scale given by the optical phonon frequency at the Γ point $\mathbf{q} = (0, 0)$.

To quantify the strength of the electron-phonon coupling, one may introduce the dimensionless electron-phonon coupling strength parameter [47,66]

$$\lambda_{\mathbf{k}\eta} = \sum_{\mathbf{q}\nu} \frac{2}{\hbar\omega_{\mathbf{q}\nu}} |\rho_{\mathbf{k}, \mathbf{k}+\mathbf{q}}^{\eta \eta', \nu}|^2 \delta(\epsilon_{\mathbf{k}+\mathbf{q}, \eta} - \epsilon_{\mathbf{k}\eta}), \quad (7)$$

where $\epsilon_{\mathbf{k}\eta}$ is the electron single-particle energy. We have neglected interband scattering processes since the π band only overlaps with the lower lying σ bands at unrealistic doping levels [48,67].

Averaging $\lambda_{\mathbf{k}\eta}$ over the Fermi surface corresponding to the energy of the incoming momentum often provides a simple and useful tool for understanding the dependence of the critical temperature of a superconductor on other system parameters through the BCS formula $k_B T_c \approx \hbar\omega_D \exp(-1/\lambda)$, where λ is the Fermi surface average of $\lambda_{\mathbf{k}\eta}$.

III. COULOMB INTERACTION

To include the effect of the Coulomb interaction, we use the repulsive Hubbard interaction

$$V^C = u_0 \sum_i n_{i\uparrow} n_{i\downarrow}, \quad (8)$$

where $n_{i\sigma}$ is the electron number operator. The on-site repulsion u_0 has been calculated from *ab initio* in undoped graphene [54]. At significant doping of order 2 eV, as discussed in Appendix D, the screening length is a small fraction of the nearest neighbor bond length, and we therefore disregard longer ranged interactions.

For doped graphene, we expect the onset of π -band screening to reduce the on-site repulsion. A simple model for $u_0(\mu)$ is obtained by calculating the polarization bubble in the linear spectrum approximation for intravalley scattering processes [53]. The resulting polarization bubble is momentum independent, and this gives

$$u_0(\mu) = \frac{u_0(0)}{1 + \alpha u_0(0) \rho(\mu) A_{\text{cell}}}, \quad (9)$$

where $\rho(\mu)$ is the density of states per area in the linear spectrum approximation, and A_{cell} is the real-space area associated with the unit cell. We have introduced a factor α to be able to study polarization strength dependence. The doping dependence can also be interpreted as an interpolation between the known on-site Coulomb repulsion $u_0(0)$ for pristine graphene, and the known result of doping-independent Coulomb pseudopotential μ_C at the Fermi surface [41,44], requiring $u_0 \propto 1/\rho(\mu)$.

In momentum space, the Coulomb interaction takes the form

$$V^C = \frac{u_0}{2N_A} \sum_{\mathbf{k}\mathbf{q}} \sum_{\eta_1 \dots \eta_4} c_{\eta_1 \uparrow}^\dagger(\mathbf{k} + \mathbf{q}) c_{\eta_2 \downarrow}^\dagger(\tilde{\mathbf{k}} - \mathbf{q}) c_{\eta_3 \downarrow}(\tilde{\mathbf{k}}) c_{\eta_4 \uparrow}(\mathbf{k}) \quad (10)$$

in terms of the momentum band basis annihilation operators $c_{\eta\sigma}(\mathbf{k})$.

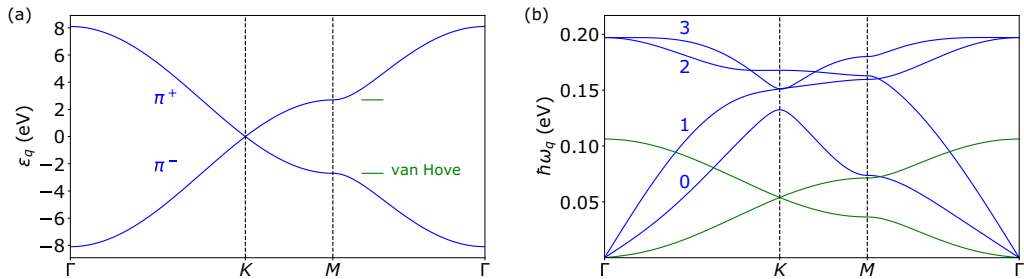


FIG. 1. (a) Electron spectrum for the π bands of graphene in a tight binding hopping model. (b) Phonon spectrum for freestanding graphene in the force constant model. In-plane modes are shown in blue, with out-of-plane modes in green. At any point in the Brillouin zone, the in-plane phonon modes are labeled according to energy.

IV. PAIRING AND GAP EQUATION

The in-plane phonons yield an effective interaction between the electrons in the system that may cause pairing and superconductivity. Assuming spin-singlet pairing at $\pm\mathbf{k}$ and considering only the electron band π^- , the relevant interaction can be written in the form

$$V = \sum_{\mathbf{k}\mathbf{k}'} V_{\mathbf{k}\mathbf{k}'} c_{-\uparrow}^\dagger(\mathbf{k}') c_{-\downarrow}^\dagger(-\mathbf{k}') c_{-\downarrow}(-\mathbf{k}) c_{-\uparrow}(\mathbf{k}) \quad (11)$$

with a potential $V_{\mathbf{k}\mathbf{k}'}$ that contains contributions both from the Coulomb potential and an effective phonon-mediated potential $V_{\mathbf{k}\mathbf{k}'}^{\text{ph-m}}$, so that

$$V_{\mathbf{k}\mathbf{k}'} = V_{\mathbf{k}\mathbf{k}'}^C + V_{\mathbf{k}\mathbf{k}'}^{\text{ph-m}}. \quad (12)$$

The Coulomb contribution is given by Eq. (10). The effective phonon-mediated potential follows from a canonical transformation [68], and is given by

$$V_{\mathbf{k}\mathbf{k}'}^{\text{ph-m}} = \sum_{\mathbf{q}} |g_{\mathbf{k},\mathbf{k}+\mathbf{q}}^{-,v}|^2 \frac{2\hbar\omega_{\mathbf{q}v}}{(\epsilon_{\mathbf{k}+\mathbf{q}} - \epsilon_{\mathbf{k}})^2 - (\hbar\omega_{\mathbf{q}v})^2}, \quad (13)$$

where the quasimomentum \mathbf{q} is defined by $\mathbf{k}' = \mathbf{k} + \mathbf{q}$.

Due to the singlet pairing assumption, the gap has to be symmetric under $\mathbf{k} \rightarrow -\mathbf{k}$, and therefore, the potential $V_{\mathbf{k}\mathbf{k}'}$ can be replaced with the symmetrized potential

$$V_{\mathbf{k},\mathbf{k}'}^{\text{symm}} = \frac{1}{2}(V_{\mathbf{k},\mathbf{k}'} + V_{\mathbf{k}',-\mathbf{k}}), \quad (14)$$

which is symmetric under $\mathbf{k} \rightarrow -\mathbf{k}$ and $\mathbf{k}' \rightarrow -\mathbf{k}'$, as well as interchange of the incoming and outgoing momenta \mathbf{k} and \mathbf{k}' .

To proceed, we have to solve the gap equation

$$\Delta_{\mathbf{k}} = - \sum_{\mathbf{k}'} V_{\mathbf{k}\mathbf{k}'}^{\text{symm}} \chi_{\mathbf{k}'} \Delta_{\mathbf{k}'}, \quad (15)$$

with susceptibility

$$\chi_{\mathbf{k}} = \frac{\tanh \beta E_{\mathbf{k}}/2}{2E_{\mathbf{k}}}, \quad E_{\mathbf{k}} = \sqrt{\xi_{\mathbf{k}}^2 + |\Delta_{\mathbf{k}}|^2}, \quad (16)$$

where $E_{\mathbf{k}}$ is the quasiparticle excitation energy, and $\xi_{\mathbf{k}} = \epsilon_{\mathbf{k}} - \mu$ is the single-particle energy $\epsilon_{\mathbf{k}}$ measured relative to the Fermi surface at chemical potential μ .

To find the critical temperature and the gap structure $\Delta_{\mathbf{k}}$ just below the critical temperature, it suffices to neglect the gap in the excitation spectrum $E_{\mathbf{k}}$ in the gap equation. This gives an eigenvalue problem linear in the eigenvectors and

nonlinear in the eigenvalue, which is solved as discussed in Appendix E to obtain the critical temperature and gap momentum dependence.

V. GRAPHENE NUMERICAL RESULTS

A. Parameter values and free spectra

We set the equilibrium electron hopping amplitude t_1 to 2.8 eV [53]. The resulting electron band structure for the π bands of graphene is shown in Fig. 1(a). For the phonon force constant model used to derive the phonon spectrum, we use the same parameter values as Ref. [63], and the resulting excitation spectrum is shown in Fig. 1(b).

The dimensionless parameter γ can be estimated from *ab initio*, and is roughly 2.5 [69]. This gives reasonable values [50] for the dimensionless electron-phonon coupling strength λ . With phonon energy scale $\hbar\omega_{\Gamma} = 0.20$ eV and nearest neighbor distance $d = 1.42$ Å [70], this gives $g_0 = 0.15$ eV. All system parameters involved in the calculation of the energy scale are tabulated in Appendix F.

B. Electron-phonon coupling strength and effective potential

Using the parameter values in the preceding subsection, one may calculate the electron-phonon coupling strength λ as function of the chemical potential μ . This is shown in Fig. 2(a), with contributions from the four in-plane phonon modes shown in color. The parameter λ incorporates both the strength of the effective potential at the Fermi surface and the density of states. Since the latter has a very systematic variation with the chemical potential, λ and the electronic density of states have similar profiles. In the low-doping regime, the optical phonon modes, and the highest-energy mode in particular, dominate the electron-phonon coupling strength completely. Figure 2(b) shows the angular dependence of $\lambda_{\mathbf{k}}$ on the Fermi surface for various dopings. As shown also in the inset, the Fermi surface anisotropy is increasing with doping, reaching values of order 2% close to the van Hove singularity.

The effective potential $V_{\mathbf{k}\mathbf{k}'}^{\text{ph-m}}$ is shown in Fig. 3(a) for incoming momentum \mathbf{k} at various outgoing momenta \mathbf{k}' . The potential is attractive in a finite region around the Fermi surface corresponding to the energy of the incoming momentum, and becomes repulsive when the kinetic energy transfer exceeds the phonon energy scale.

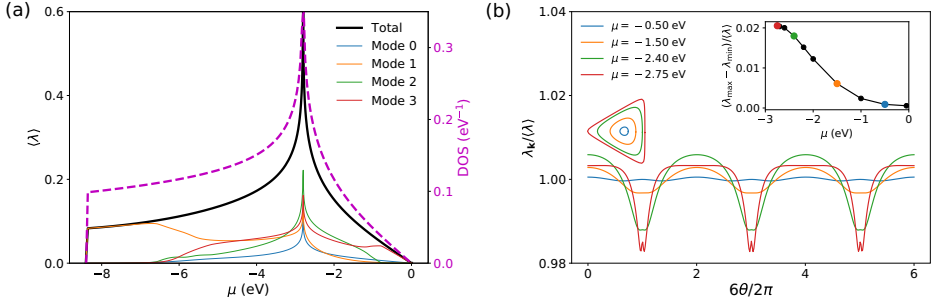


FIG. 2. (a) Calculated electron-phonon coupling strength λ averaged over the Fermi surface (black) and electronic density of states (magenta) as function of chemical potential. Since λ is highly dependent on the density of states but also dependent on the electron-phonon coupling element $|g_{\mathbf{k}\mathbf{k}'}^{\nu}|$, the two have similar but not identical shapes. The contributions to λ from the various in-plane phonon modes are shown in colors. (b) Electron-phonon coupling strength along the Fermi surface normalized to the mean value for various doping levels. As shown in the inset, the electron-phonon coupling strength modulations are increasing with doping toward the van Hove singularity.

The potential has contributions from the four in-plane phonon modes, and these contributions are shown in Fig. 3(b) for the incoming momentum as indicated in Fig. 3(a). The size of the region with attractive interaction is determined by the energy of the relevant phonon mode. The optical high-energy phonon modes therefore give the largest attractive Brillouin zone area. The effective potential for intra- and intervalley scattering processes on the Fermi surface is shown in Fig. 3(c). Comparing the effective potential contribution from the various in-plane phonon modes on the Fermi surface reveals that the high-energy phonon modes corresponding to high mode index or large quasimomentum scattering also give rise to a stronger attractive potential at the important Fermi surface than their low-energetic counterparts.

C. Solutions of the gap equation

To contain the divergences of the effective electronic potential, we introduce an energy cutoff $\Lambda = 6$ eV in the potential. Solving the linearized self-consistent equation (15) in the full Brillouin zone as discussed in Appendix E, we obtain the gap structure at the critical temperature T_c for which the superconducting instability occurs. This is shown in Fig. 4, where the superconducting gap at a given point is given by color. The gap equation solution shows that the gap has a given sign within the attractive region of the Brillouin zone for incoming momenta at or close to the Fermi surface. Outside this region, the gap changes sign, and subsequently decays to a roughly constant value far away from the Fermi surface. Furthermore, the gap has modulations of the same order as $\lambda_{\mathbf{k}}$ along the Fermi surface.

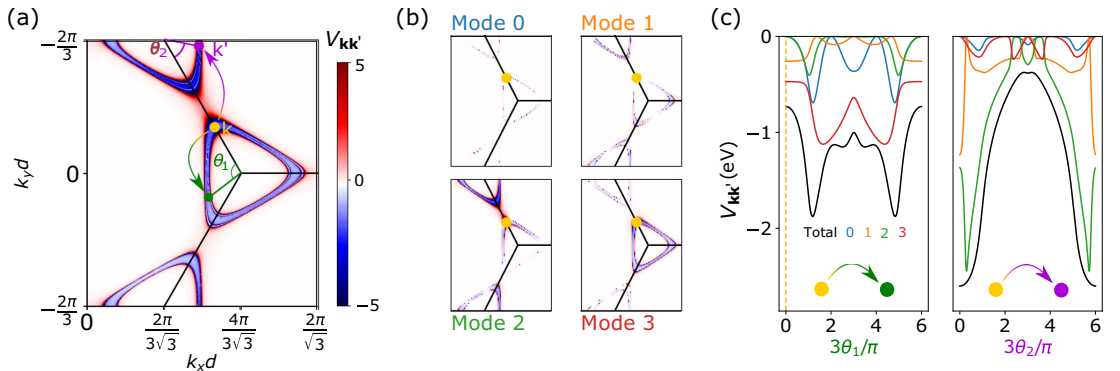


FIG. 3. (a) Graphene effective interaction $V_{\mathbf{k}\mathbf{k}'}^{\text{ph-m}}$ in eV for incoming electron momentum \mathbf{k} (yellow dot) at outgoing momentum \mathbf{k}' indicated by position in the plot. There can be both intra- (green) and intervalley (magenta) scattering processes to the Fermi surface. The potential is attractive close to the Fermi surface, before it turns repulsive at a characteristic phonon frequency, and then decays to zero. (b) Decomposition of effective potential in phonon mode contributions. The size of the attractive region clearly depends on the phonon energy. (c) Effective potential $V_{\mathbf{k}\mathbf{k}'}$ (black) for incoming momentum \mathbf{k} given by the yellow dot in (a) to outgoing momentum given by angle θ_1 for intravalley and θ_2 for intervalley scattering processes. Phonon mode contributions are shown in colors. Although the electron-phonon coupling strength $\lambda_{\mathbf{k}}$ has only slight modulations, the effective potential is strongly dependent on the scattering momentum for a given incoming momentum.

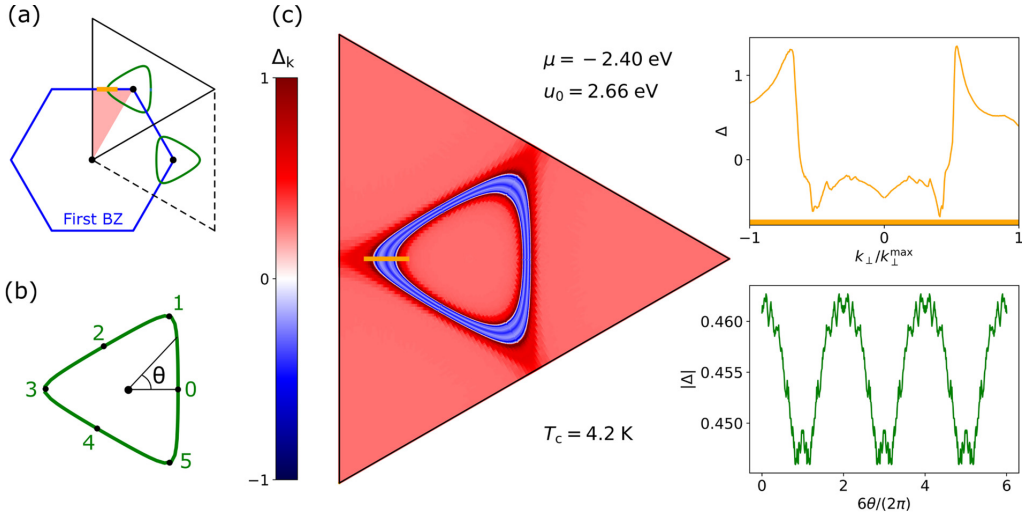


FIG. 4. Typical superconducting gap structure at the indicated chemical potential μ just below the superconducting transition at critical temperature T_c . (a) Hexagonal Brillouin zone of the triangular Bravais lattice in blue. The rhombus (black) contains an equivalent set of quasimomenta. The green contours indicate the Fermi surface, and the short orange line is perpendicular to the Fermi surface. (b) Position on the Fermi surface is specified with the angle θ . (c) Gap structure around the point K' in color for the given doping and on-site repulsion. The insets show the gap structure perpendicular to (orange) and along (green) the Fermi surface.

The critical temperature is shown as a function of doping in Fig. 5(a). As expected, the critical temperature increases rapidly with increasing doping due to the increasing electron-phonon coupling strength.

The presence of the Coulomb interaction decreases the critical temperature significantly. This is shown in Fig. 5(b), which shows the dependence of the critical temperature on the on-site Coulomb repulsion strength u_0 . The data points from the solution of the gap equation have been fitted to the simple functional form that is expected from the Morel-Anderson model [52], as discussed in Appendix G.

VI. DISCUSSION OF GRAPHENE RESULTS

In conventional superconductors, the effect of a Coulomb interaction is small, and the quantitative effect on the critical temperature can be incorporated through renormalization [52,71] of the electron-phonon coupling strength λ in the simple BCS result $k_B T_c \approx \hbar \omega_D \exp(-1/\lambda)$ according to $\lambda \rightarrow \lambda - \mu^*$, where

$$\mu^* = \frac{N_0 u}{1 + N_0 u \ln(W/\hbar \omega_D)}. \quad (17)$$

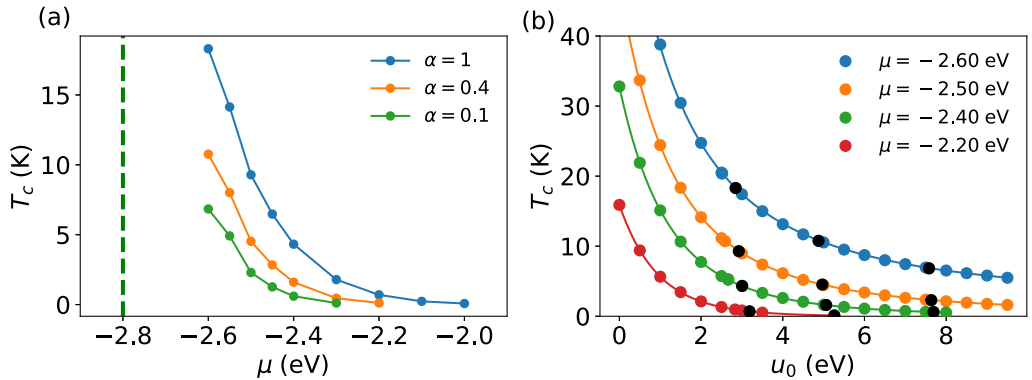


FIG. 5. Critical temperature for the superconducting transition. (a) Critical temperature as function of doping with Hubbard repulsion given by Eq. (9) for various polarization strengths parametrized by α . The green dashed line indicates the van Hove singularity. (b) Critical temperature as function of on-site interaction u_0 . The calculated data points are fitted to the simple functional form (line) that follows from the Morel-Anderson model. The black points correspond to points in (a).

Here, u is the constant repulsive interaction strength that is added on top of the attractive interaction close to the Fermi surface, N_0 is the density of states at the Fermi surface, W is the electron bandwidth, and ω_D the Debye frequency. For strong Coulomb repulsion, the renormalization is suppressed down to values of $1/\ln(W/\hbar\omega_D)$, so that Cooper pair formation is possible despite the Coulomb repulsion being much stronger than the attraction at the Fermi surface.

In the graphene case, simple estimates for the renormalization μ^* give a value of 0.2 in the presence of a strong Coulomb interaction. This is larger than, but not very far away from, estimates [41,44] based on the long-wavelength limit, arriving at 0.10–0.15. Since the simple Morel-Anderson model predicts the absence of superconductivity for $\mu^* \geq \lambda$ and we expect to be quite close to this situation, we would expect the Coulomb interactions to have a dramatic effect on the critical temperature of the superconducting transition. Our detailed solution of the gap equation in the presence of the Coulomb interaction confirms this picture. Although boosting the electron-phonon coupling λ would be essential for realizing superconductivity in graphene or graphene-like materials, within the realistic regime for λ , the repulsive Coulomb interaction also has to be taken into account explicitly.

Calculations of the critical temperature are notoriously unreliable. On the other hand, the Fermi surface structure of the gap calculated in this paper should give reasonable estimates for the \mathbf{k} -space modulation of the gap on the Fermi surface. The modulations we find within our methodology are similar and of the same order as in Ref. [44]. The modulations are small, but could in principle be measured by ARPES.

In our calculations, we have considered the electron and phonon band structures of pristine graphene. The presence of intercalant atoms may affect the electron band structure and phonon modes significantly, and this would be dependent on the method chosen to dope graphene [42,44]. To understand why realizing superconductivity in graphene is so challenging, it is nevertheless useful to study superconductivity based on the intrinsic phonon modes and electronic properties.

In practice, graphene is often mounted on a substrate. A small substrate coupling can be included in our phonon spectrum analysis by adding an on-site potential quadratic in the displacement. This modifies the phonon spectrum by lifting the low-energy modes to finite values. Our analysis clearly indicates that it is primarily the high-energy phonons that are responsible for the superconducting instability. Thus, we do not expect a slight alteration of the low-energy phonon modes to significantly impact our results. Since the introduction of a substrate may break the $z \rightarrow -z$ mirror symmetry of the system, the out-of-plane modes could in principle also give some contribution to the effective potential, but we expect this to be a higher-order effect in the lattice site deviations.

VII. BORON NITRIDE

So far, we have only considered graphene, but our methodology can easily be carried over to other graphene-like materials. In particular, we consider hexagonal boron nitride (*h*-BN), which is a two-dimensional material very similar to graphene, but where the atoms on the two different sublattices are boron and nitrogen. The associated sublattice symmetry breaking

opens a gap in the electronic spectrum, and in this section, we discuss how this affects the electron-phonon coupling.

Due to the sublattice symmetry breaking of boron nitride, the electron tight binding model in Eq. (1) has to be modified by the addition of a sublattice asymmetric potential term

$$H_{\text{imb}} = \frac{\Delta_{\text{BN}}}{2} \left(\sum_{i \in A} c_i^\dagger c_i - \sum_{j \in B} c_j^\dagger c_j \right). \quad (18)$$

The resulting electron band structure is shown in Fig. 6(a), where $t_1 = 2.92$ eV and $\Delta_{\text{BN}} = 4.3$ eV [61,72].

For the phonon excitation spectrum, we again use a force constant model as outlined in Appendix B. Values for the boron nitride force constants are obtained by fitting the excitation energies at the high-symmetry points to values from density functional theory values in Ref. [60], as discussed in Appendix C. The resulting excitation spectrum is shown in Fig. 6(b).

As in the graphene calculation, the electron-phonon coupling is obtained by Taylor-expanding the hopping element integral in Eq. (1), and the resulting electron-phonon coupling matrix element is similar [73] to Eq. (5). To compare the boron nitride results with graphene, we set the value of the dimensionless quantity γ to the same value that was used for graphene. All quantities involved in the calculation of the electron-phonon coupling energy scale g_0 are listed in Appendix F.

Averaging the dimensionless electron-phonon coupling strength $\lambda_{\mathbf{k}}$ over the Fermi surface at chemical potential μ gives the result shown in Fig. 7. The inset shows the same electron-phonon coupling λ as function of the charge doping n corresponding to each chemical potential μ for both boron nitride and graphene.

Unlike the graphene electron-phonon coupling strength shown in Fig. 2, the electron-phonon coupling strength of boron nitride is qualitatively different from the electronic density of states. At the valence band edge, the electron density of states has a discontinuous jump, whereas λ increases linearly. Due to the direct onset of a large density of states in boron nitride, it is tempting to assert that even small charge dopings could quickly give rise to appreciable electron-phonon coupling strengths. This is not the case. The electron-phonon coupling matrix element $|g_{\mathbf{k}\mathbf{k}'}^{-,v}|^2$ in Eq. (5) also plays an essential role for the overall value of the electron-phonon coupling strength, and is suppressed when the Fermi surface is small. As a result of this, graphene and boron nitride have similar electron-phonon coupling strengths at a given charge doping.

In light of these results, we would expect the difficulty of realizing intrinsic phonon-mediated superconductivity in boron nitride to be similar to that for graphene. Furthermore, the importance of the electron-phonon coupling matrix element underlines the importance of treating the electron-phonon coupling in a detailed manner.

VIII. SUMMARY

In summary, we have studied electron-phonon coupling in graphene and hexagonal boron nitride based on an electron tight binding and a phonon force constant model giving

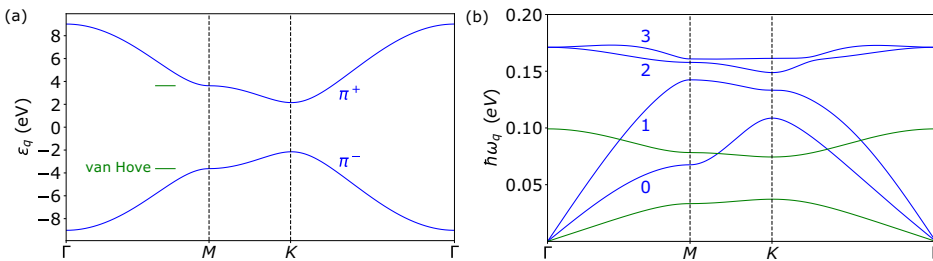


FIG. 6. (a) Electron spectrum for the π band of hexagonal boron nitride (h -BN) in a tight binding hopping model. Contrary to graphene, the band structure is gapped due to sublattice asymmetry. (b) Phonon spectrum for freestanding h -BN in force constant model. In-plane modes are shown in blue, with out-of-plane modes in green.

realistic electron and phonon spectra. The ability to tune the relevant system parameters in this detailed model provides a platform for investigating the superconducting properties of graphene and graphene-like systems.

In graphene, our results indicate that superconductivity may be possible at sufficiently large doping. We have identified the phonon modes which couple most strongly to π -band electrons, which are the electronic states of most relevance for realistic doping levels in graphene. These modes are the high-energy in-plane phonon modes. Solving the gap equation assuming singlet pairing, we find the critical temperature and the superconducting gap structure in the Brillouin zone. The gap has small modulations along the Fermi surface, but is surprisingly uniform even for highly anisotropic Fermi surfaces. Introducing the Coulomb interaction gives a dramatic suppression in the critical temperature, in contrast with the moderate reduction in most normal superconductors. We understand this in terms of the Morel-Anderson model, where the calculated electron-phonon coupling strength and estimates for the renormalization are of the same order. Enhancing the electron-phonon coupling strength is important

to realize phonon-mediated superconductivity in monolayer graphene, but the effect of the Coulomb interaction also has to be discussed in detail.

Motivated by the direct onset of a large density of states in the gapped hexagonal boron nitride, we also calculate the dimensionless electron-phonon coupling there within the same framework. In spite of the large density of states, however, the charge doping required to obtain a sizable electron-phonon coupling is similar to the doping required in graphene since the electron-phonon coupling matrix element is suppressed due to the small Fermi surface at small charge doping.

ACKNOWLEDGMENTS

We thank H. G. Hugdal, E. Erlandsen, V. Saroka, B. Hellsing, and T. Frederiksen for valuable discussions. The Delaunay triangulation procedure was performed using the C++ library delaunator-cpp [74] by V. Bilonenko, copyrighted with an MIT license (2018). We acknowledge financial support from the Research Council of Norway, Grant No. 262633, “Center of Excellence in Quantum Spintronics.” A.S. and J.W.W. also acknowledge financial support from the Research Council of Norway, Grant No. 250985, “Fundamentals of Low-Dissipative Topological Matter.”

APPENDIX A: ELECTRON BAND STRUCTURE

To calculate the graphene electron band structure, we use the nearest neighbor tight binding Hamiltonian [4],

$$H_{el} = -t_1 \sum_{(ij),\sigma} (c_{i\sigma}^\dagger c_{j\sigma} + \text{H.c.}), \quad (\text{A1})$$

as our starting point. By introducing the Fourier-transformed operators, this model becomes

$$H_{el} = \sum_{\mathbf{k},\sigma} (c_{\mathbf{k}\sigma A}^\dagger \quad c_{\mathbf{k}\sigma B}^\dagger) M_{\mathbf{k}} \begin{pmatrix} c_{\mathbf{k}\sigma A} \\ c_{\mathbf{k}\sigma B} \end{pmatrix}, \quad (\text{A2})$$

where the matrix $M_{\mathbf{k}}$ is given by

$$M_{\mathbf{k}} = \begin{pmatrix} 0 & -t_1 \sum_{\delta_A} e^{i\mathbf{k}\cdot\delta_A} \\ -t_1 \sum_{\delta_A} e^{-i\mathbf{k}\cdot\delta_A} & 0 \end{pmatrix}, \quad (\text{A3})$$

and δ_A are the nearest neighbor vectors from sublattice A to sublattice B . Diagonalizing this matrix, we get eigenvectors $F_{D\eta}(\mathbf{k})$ for the two eigenvalues $\epsilon_{\mathbf{k}\eta}$ corresponding to the two

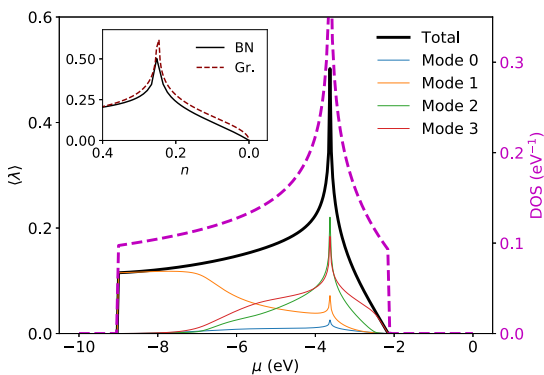


FIG. 7. Electron-phonon coupling strength λ for boron nitride averaged over the Fermi surface at chemical potential μ . The contributions to the total electron-phonon coupling (black) from the various phonon modes are shown in colors. The density of states is shown in magenta. A given energy doping μ corresponds to a charge doping n per site, and the inset shows the electron-phonon coupling as a function of this charge doping for graphene and boron nitride.

π bands, where η is the band index. Thus, the D -sublattice Fourier mode is given by

$$c_{\mathbf{k}\sigma D} = \sum_{\eta} F_{D\eta}(\mathbf{k}) c_{\mathbf{k}\sigma\eta}, \quad (\text{A4})$$

where η denotes the band and an eigenvector of the matrix $M_{\mathbf{k}}$. This provides the definition of the factors $F_{D\eta}(\mathbf{k})$ appearing in the main text.

APPENDIX B: PHONON MODEL DIAGONALIZATION

The phonon dispersion relation calculation in this paper follows Refs. [63,64], where the phonon excitation spectrum is calculated for graphene. We take the same approach, and use a force constant model with up to third nearest neighbor interactions to calculate the dispersion relations for graphene and boron nitride. Since boron nitride has a broken sublattice symmetry, we have to account for the different sublattice masses, and the intersublattice force constants become sublattice dependent. In this Appendix, we discuss how the force constant model can be diagonalized, leaving the discussion of the force constants and their symmetry relations to Appendix C.

We write the phonon Hamiltonian in the form

$$H_{\text{ph}} = \sum_j \frac{\mathbf{P}_j^2}{2M_j} + \frac{1}{2} \sum_{i,j} \sum_{\mu\nu} \Phi_{\mu\nu}^{\kappa_i\kappa_j}(\delta_{ij}) u_{i\mu}^{\kappa_i} u_{j\nu}^{\kappa_j}, \quad (\text{B1})$$

where i, j are lattice site indices on the honeycomb lattice, κ_i, κ_j are the corresponding sublattices, μ, ν are Cartesian indices, and $u_{i\mu}^{\kappa_i}$ is the deviation of site i on the sublattice κ_i (uniquely determined by i) in direction μ . The deviation coupling constants are $\Phi_{\mu\nu}^{\kappa_i\kappa_j}(\delta_{ij})$. In the kinetic term, \mathbf{P}_j is the momentum of the particle at site j , and M_j is the mass.

We next express the phonon Hamiltonian in terms of uncoupled harmonic oscillators. To do this, we first symmetrize the sublattice sectors of the kinetic term. Introducing effective mass $\tilde{M} = \sqrt{M_A M_B}$ and relative masses μ_D given by $M_D = \mu_D \tilde{M}$, we introduce rescaled deviations and momenta

$$\tilde{\mathbf{P}}^D = \mathbf{P}_D / \sqrt{\mu_D}, \quad \tilde{\mathbf{u}}^D = \mathbf{u}^D \sqrt{\mu_D}, \quad (\text{B2})$$

where the rescaling of the deviations is chosen to retain the canonical commutation relations $[u_{i\mu}, P_{j\nu}] = i\hbar\delta_{ij}\delta_{\mu\nu}$. To proceed, we rewrite the Hamiltonian in Fourier space, obtaining

$$H_{\text{ph}} = \frac{1}{2\tilde{M}} \sum_{\mathbf{q}, \mathbf{q}'} \tilde{\mathbf{P}}_{-\mathbf{q}}^{\kappa} \tilde{\mathbf{P}}_{\mathbf{q}}^{\kappa} + \frac{1}{2} \sum_{\kappa\kappa'} \sum_{\mu\nu} \sum_{\mathbf{q}} D_{\mu\nu}^{\kappa\kappa'}(\mathbf{q}) \tilde{u}_{-\mathbf{q}, \mu}^{\kappa} \tilde{u}_{\mathbf{q}, \nu}^{\kappa'}, \quad (\text{B3})$$

where κ, κ' are sublattice indices and the matrix elements $D_{\mu\nu}^{\kappa\kappa'}(\mathbf{q})$ are given by

$$D_{\mu\nu}^{\kappa\kappa'}(\mathbf{q}) = \frac{1}{\sqrt{\mu_{\kappa}\mu_{\kappa'}}} \sum_{j \in \kappa'} \Phi_{\mu\nu}^{\kappa\kappa'}(\delta_j^{\kappa}) e^{i\mathbf{q}\cdot\delta_j^{\kappa}}, \quad (\text{B4})$$

where δ_j^{κ} is the vector from a lattice site on sublattice κ to lattice site j on sublattice κ' .

Using the symmetries of the system, as discussed further in Appendix C, the number of independent real-space coupling constants can be reduced drastically. Here, we only point out the effect of the mirror symmetry under $z \rightarrow -z$. Considering

the lattice deviation coupling term in the phonon Hamiltonian, this symmetry implies that there cannot be any coupling between the in-plane and the out-of-plane modes, and hence that the phonon eigenmodes are either purely in-plane or out-of-plane. The potential energy term can thus be written in the form $V_{\text{ph}} = V_{\text{ph}}^z + V_{\text{ph}}^{xy}$, where

$$V_{\text{ph}}^{xy} = \frac{1}{2} \sum_{\mathbf{q}} (\tilde{u}_{\mathbf{q}}^{xy})^{\dagger} M_{\mathbf{q}}^{xy} \tilde{u}_{\mathbf{q}}^{xy}, \quad (\text{B5})$$

$$V_{\text{ph}}^z = \frac{1}{2} \sum_{\mathbf{q}} (\tilde{u}_{\mathbf{q}}^z)^{\dagger} M_{\mathbf{q}}^z \tilde{u}_{\mathbf{q}}^z,$$

and the deviations $\tilde{u}_{\mathbf{q}}$ are given by

$$\tilde{u}_{\mathbf{q}}^z = (\tilde{u}_{\mathbf{q},z}^A \quad \tilde{u}_{\mathbf{q},z}^B)^T, \quad (\text{B6})$$

$$\tilde{u}_{\mathbf{q}}^{xy} = (\tilde{u}_{\mathbf{q},x}^A \quad \tilde{u}_{\mathbf{q},y}^A \quad \tilde{u}_{\mathbf{q},x}^B \quad \tilde{u}_{\mathbf{q},y}^B)^T.$$

The matrices $M_{\mathbf{q}}^z$ and $M_{\mathbf{q}}^{xy}$ are 2×2 and 4×4 matrices, and the matrix elements for graphene are given in Ref. [63]. For the boron nitride case, similar expressions are derived by inserting values for the coupling constants using the symmetry relations and force constants in Appendix C.

To obtain a system of uncoupled harmonic oscillators, we introduce a new basis $v_{\mathbf{q}}^{\nu}$ given by

$$\tilde{u}_{\mathbf{q}\mu}^D = \sum_{\nu} [\mathbf{e}_{\nu}^D(\mathbf{q})]_{\mu} v_{\mathbf{q}}^{\nu}, \quad (\text{B7})$$

in which the phonon potential energy is diagonal. Here, $[e_{\nu}^D(\mathbf{q})]_{\mu}$ is given by the eigenvectors of $M_{\mathbf{q}}$, v is an eigenvector label, $\mathbf{e}_{\nu}^D(\mathbf{q})$ is the phonon polarization vector on sublattice D at quasimomentum \mathbf{q} , and the index μ picks out a Cartesian component. This relation provides a definition for the phonon polarization vectors occurring in the electron-phonon coupling in the main text.

Since the kinetic term remains diagonal in the new basis, the system is reduced to a system of uncoupled harmonic oscillators, from which we obtain [75] the excitation spectrum through $\omega_{\mathbf{q}\nu}^2 = d_{\mathbf{q}\nu}/\tilde{M}$, where $d_{\mathbf{q}\nu}$ are the eigenvalues of $D(\mathbf{q})$.

In our paper, the phonon spectrum and associated polarization vectors $\mathbf{e}_{\nu}^D(\mathbf{q})$ are determined using numerical diagonalization. At the high-symmetry point K , one may derive reasonably simple expressions for the eigenfrequencies.

APPENDIX C: FORCE CONSTANTS AND SYMMETRIES

The discussion in this Appendix is a generalization of the graphene force constant model in Refs. [63,64] to the case of honeycomb lattices without sublattice symmetry. We provide an overview of how the symmetries of the system impose relations between the force constants in the model, and determine the force constants by fitting the force constant dispersion relation to density functional theory results in Ref. [60].

1. Chiral basis and double counting

The phonon Hamiltonian can be written in the form

$$H_{\text{ph}} = \sum_j \frac{\mathbf{P}_j^2}{2M_j} + \frac{1}{2} \sum_{i,j} \sum_{\mu\nu} \Phi_{\mu\nu}^{\kappa_i\kappa_j}(\delta_{ij}) u_{i\mu}^{\kappa_i} u_{j\nu}^{\kappa_j},$$

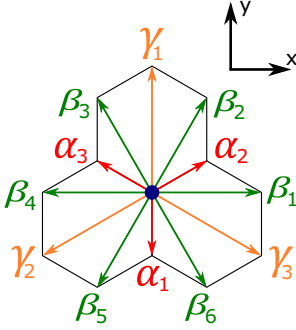


FIG. 8. Labeling of vectors to neighboring sites on the honeycomb lattice.

where \sum_i denotes the sum over all lattice sites on the honeycomb lattice, and all bonds (i, j) are being double counted. To symmetrize these contributions, we may therefore impose

$$\Phi_{\mu\nu}^{K_i K_j}(\delta_{ij}) = \Phi_{\nu\mu}^{K_j K_i}(\delta_{ji}), \quad (C1)$$

where the indices μ, ν are initially considered to be Cartesian. We may however also introduce the chiral basis

$$\xi = x + iy, \quad \eta = x - iy, \quad (C2)$$

so that $\mu, \nu \in \{\xi, \eta, z\}$. Under rotation with angle ϕ around the z axis, the new coordinates do not mix, and transform according to

$$\xi \rightarrow \xi e^{i\phi}, \quad \eta \rightarrow \eta e^{-i\phi}. \quad (C3)$$

In terms of the old coupling coefficients, the coefficients for the deviations in the new basis are given by

$$\begin{aligned} \Phi_{\xi\xi} &= (\Phi_{xx} - \Phi_{yy} - i\Phi_{xy} - i\Phi_{yx})/4, \\ \Phi_{\eta\eta} &= (\Phi_{xx} - \Phi_{yy} + i\Phi_{xy} + i\Phi_{yx})/4, \\ \Phi_{\xi\eta} &= (\Phi_{xx} + \Phi_{yy} + i\Phi_{xy} - i\Phi_{yx})/4, \\ \Phi_{\eta\xi} &= (\Phi_{xx} + \Phi_{yy} - i\Phi_{xy} + i\Phi_{yx})/4. \end{aligned} \quad (C4)$$

Now, both deviations and coupling constant are in general complex.

2. Force constant symmetry relations

The hexagonal boron nitride system has infinitesimal translation symmetry, Bravais lattice translation symmetry, infinitesimal rotation symmetry, lattice C_3 rotation symmetry, σ_z mirror symmetry, and, with the choice of lattice orientation indicated in Fig. 8, σ_x mirror symmetry. We use these symmetries to reduce the number of independent coupling coefficients.

a Translation symmetries

From translation symmetry with a Bravais lattice vector \mathbf{a} , it follows trivially, as already indicated by the force constant notation, that

$$\Phi_{\mu\nu}^{K_i K_j}(\delta_{ij}) = \Phi_{\mu\nu}^{K_i K_j}(\delta_{i+\mathbf{a}, j+\mathbf{a}}). \quad (C5)$$

Due to the infinitesimal translation symmetry of a single graphene sheet under $u_{i\mu}^{K_i} \rightarrow u_{i\mu}^{K_i} + a_\mu$, it furthermore follows that

$$\sum_j \Phi_{\mu\nu}^{K_i K_j}(\delta_{ij}) = 0. \quad (C6)$$

Following Refs. [63,64], we call this the stability condition, and use it to determine the local force constants with $\delta_{ij} = 0$.

Although infinitesimal lattice translation symmetry holds for a freestanding graphene sheet, it breaks down if the monolayer sheet is placed on a substrate. This would give rise to additional free parameters through the force constants $\Phi_{\mu\nu}^{DD}(0)$.

b Rotation symmetries

Application of the C_3 symmetry under 3-fold rotations R_3 gives force constant relations

$$\begin{aligned} \Phi_{\xi\xi}^{K_i K_j}(R_3 \delta_{ij}) &= \Phi_{\xi\xi}^{K_i K_j}(\delta_{ij}) e^{+i2\pi/3}, \\ \Phi_{\eta\eta}^{K_i K_j}(R_3 \delta_{ij}) &= \Phi_{\eta\eta}^{K_i K_j}(\delta_{ij}) e^{-i2\pi/3}, \end{aligned} \quad (C7)$$

whereas $\Phi_{\mu\nu}^{K_i K_j}(R_3 \delta_{ij}) = \Phi_{\mu\nu}^{K_i K_j}(\delta_{ij})$ if μ and ν are not equal chiral in-plane components, as in the two cases listed above.

We also note that the infinitesimal rotation symmetry does not give restrictions on the force constants in addition to the ones we have already discussed.

c Mirror symmetries and complex conjugation

The mirror symmetry σ_z implies that there cannot be any coupling between the in-plane and the out-of-plane deviations, i.e.,

$$\Phi_{\xi z} = \Phi_{\eta z} = \Phi_{z\xi} = \Phi_{z\eta} = 0. \quad (C8)$$

As already discussed in Appendix B, this completely decouples the in-plane and the out-of-plane phonon modes.

The σ_x mirror symmetry implies

$$\Phi_{\mu\nu}^{K_i K_j}(\delta_{ij}) = \Phi_{\bar{\mu}\bar{\nu}}^{K_i K_j}(\sigma_x \delta_{ij}), \quad (C9)$$

where $\bar{\xi} = \eta$, $\bar{\eta} = \xi$, and $\bar{z} = z$.

Finally, we note that the requirement of a real potential gives the relation

$$\Phi_{\mu\nu}^{K_i K_j}(\delta_{ij}) = \Phi_{\bar{\mu}\bar{\nu}}^{K_i K_j}(\delta_{ij})^*, \quad (C10)$$

and this can be combined with the above mirror symmetry σ_x to obtain

$$\Phi_{\mu\nu}^{K_i K_j}(\delta_{ij}) = \Phi_{\mu\nu}^{K_i K_j}(\sigma_x \delta_{ij})^*. \quad (C11)$$

For the case of neighbor vectors parallel to the y axis, invariance of the neighbor vector under the mirror symmetry σ_x implies that the coupling constant has to be real.

3. Boron nitride force constants

Applying the above symmetry relations, the independent force constants in the system are listed in Table I along the bonds illustrated in Fig. 8. The graphene force constants are taken from Ref. [63], and the boron nitride force constants have been obtained by fitting the phonon frequencies at the high-symmetry points to density functional theory results

TABLE I. Force constants for graphene and boron nitride phonons up to next-to-nearest neighbor for graphene and third nearest neighbor for boron nitride. The graphene force constants are taken from Ref. [63]. The tabulated values give Φ/\bar{M} in spectroscopic units of 10^5 cm^{-2} , related to frequency through factors of $2\pi c$, where c is the speed of light.

Parameter	Coupling	\mathbb{R}/\mathbb{C}	Graphene	<i>h</i> -BN
α	$\Phi_{\xi\eta}^{AB}(\alpha_1)$	\mathbb{R}	-4.046	-3.15
β	$\Phi_{\xi\xi}^{AB}(\alpha_1)$	\mathbb{R}	1.107	1.69
γ_A	$\Phi_{\xi\eta}^{AA}(\beta_1)$	\mathbb{C}	-0.238	$-0.32 + 0.05i$
γ_B^*	$\Phi_{\xi\eta}^{BB}(\beta_1)$	\mathbb{C}	-0.238	$-0.36 - 0.07i$
δ_A	$\Phi_{\xi\xi}^{AA}(\beta_1)$	\mathbb{R}	-1.096	-0.68
δ_B	$\Phi_{\xi\xi}^{BB}(\beta_1)$	\mathbb{R}	-1.096	-0.66
α'	$\Phi_{\xi\eta}^{AB}(\gamma_1)$	\mathbb{R}		0.00
β'	$\Phi_{\xi\xi}^{AB}(\gamma_1)$	\mathbb{R}		-0.23
α_z	$\Phi_{zz}^{AA}(\alpha_1)$	\mathbb{R}	-1.176	-1.06
γ_z^A	$\Phi_{zz}^{AA}(\beta_1)$	\mathbb{R}	0.190	0.00
γ_z^B	$\Phi_{zz}^{BB}(\beta_1)$	\mathbb{R}	0.190	0.24

in Ref. [60]. Other force constants in the system can be determined from the force constant symmetry relations listed above.

Note that contrary to what Refs. [63,64] claim, the force constants γ_D are in general complex, whereas the other independent force constants up to third nearest neighbors, including δ_D , are real. This can be seen from the symmetry relation in Eq. (C11) and the double counting symmetrization relation in Eq. (C1), as well as the mirror symmetry σ_x in combination with the Cartesian component expressions in Eq. (C4).

APPENDIX D: COULOMB INTERACTION MODEL

The Coulomb interaction in a lattice model such as ours can be modeled with the Hubbard type interaction

$$V^C = u_0 \sum_i n_{i\uparrow} n_{i\downarrow} + \sum_{(i,j)} u_{ij} n_i n_j. \quad (\text{D1})$$

In this Appendix, we discuss how one may model the doping dependence of the nonlocal interaction strength parameters. The doping dependence of the on-site repulsion is discussed in the main text.

The on-site and two nearest neighbor interaction strength parameters were calculated for pristine graphene in Ref. [54] based on density functional theory and the constrained random phase approximation. Any pristine interaction strength parameter can therefore be modeled through the combination of these values and Coulombic decay [76].

At finite doping, we expect the onset of π -band screening to reduce the interaction coefficients $u_{ij}(\mu)$. To obtain an estimate for the nonlocal interaction parameters, one may write

$$u_{ij}(\mu) = \frac{V_\mu^{\text{sc}}(r_{ij})}{V_0(r_{ij})} u_{ij}(0), \quad (\text{D2})$$

where $V_0(r)$ is the potential screened only by the σ bands and the substrate, and $V_\mu^{\text{sc}}(r)$ is the potential screened also by π -band Dirac electrons. In the long-wavelength limit, the

screened interaction is [42,53]

$$V_\mu^{\text{sc}}(q) = \frac{1}{2\epsilon_0} \left(\frac{e^2}{q + q_0} \right), \quad (\text{D3})$$

where the Thomas-Fermi momentum q_0 is given by [42]

$$q_0 = \frac{e^2 |\mu|}{\pi \hbar^2 v^2 \epsilon_r \epsilon_0}. \quad (\text{D4})$$

Here, v is the Dirac cone velocity, and ϵ_r a relative permittivity depending on the substrate [53]. Inserting parameter values, we obtain the screening length $1/q_0 d = 0.43 \epsilon_r \text{ eV}/|\mu|$.

In real space, the screened interaction takes the form

$$V_\mu^{\text{sc}}(r) = \frac{1}{4\pi \epsilon_r \epsilon_0} \left\{ \frac{1}{r} - \frac{\pi}{2} q_0 [H_0(q_0 r) - N_0(q_0 r)] \right\}, \quad (\text{D5})$$

where $H_0(x)$ is the Struve function and $N_0(x)$ the Bessel function of the second kind [77]. Through asymptotic expansion of the Struve and Bessel functions [78], one may show that the screened potential has long-distance behavior $V_\mu^{\text{sc}}(r) \sim 1/r^3$. The screening length $1/q_0$ determines the crossover point to this rapidly decaying long-distance behavior from the Coulombic small-distance behavior.

Since the screening length is a small fraction of the lattice constant for significant doping of order 2 eV, we keep only the on-site Hubbard interaction. For this on-site term, Eq. (D2) can no longer be used, and as discussed in Sec. III of the main paper, we instead use the direct polarization bubble renormalization.

APPENDIX E: SOLVING THE GAP EQUATION

The gap equation is given by

$$\Delta_{\mathbf{k}} = - \frac{1}{A_{\text{BZ}}} \int d^2 k' \tilde{V}_{\mathbf{k}\mathbf{k}'}^{\text{symm}} \chi_{\mathbf{k}'} \Delta_{\mathbf{k}'}, \quad (\text{E1})$$

where A_{BZ} is the Brillouin zone area and we let $\tilde{V}_{\mathbf{k}\mathbf{k}'}^{\text{symm}} = N_A V_{\mathbf{k}\mathbf{k}'}^{\text{symm}}$.

To find a proper solution to the discretized version of this gap equation, it is important to have sufficiently good resolution in the important regions of the Brillouin zone. The factor $\chi_{\mathbf{k}}$ is peaked around the Fermi surface with a peak width $\propto T$ and necessitates a good resolution there. Furthermore, good resolution is also required in the regions around the corners of the triangle-like Fermi surface at significant doping. To make sure of this, we select points on a uniform grid in the Brillouin zone, add additional points close to the Fermi surface, and further additional points close to the Fermi surface corners.

To solve the gap equation, we rewrite the gap equation in the integral form of Eq. (E1) in terms of a weighted sum over the points described in the previous paragraph. To find the appropriate weights $w_{\mathbf{k}}$, we split the Brillouin zone into triangles $\{t\}$ with the points $\{\mathbf{k}\}$ as vertices using Delaunay triangulation. Denote the area of a triangle t by A_t . The weight of a single point then becomes one third of the sum of the areas of all the triangles that has the point as a vertex, i.e.,

$$w_{\mathbf{k}} = \sum_t A_t \delta_{\mathbf{k} \in t} / 3, \quad (\text{E2})$$

where $\delta_{\mathbf{k} \in t}$ is 1 if \mathbf{k} is a vertex in the triangle t and 0 otherwise.

The gap equation then becomes

$$\Delta_{\mathbf{k}} = -\frac{1}{A_{\text{BZ}}} \sum_{\mathbf{k}'} \tilde{V}_{\mathbf{k}\mathbf{k}'}^{\text{symm}} w_{\mathbf{k}'} \chi_{\mathbf{k}'} \Delta_{\mathbf{k}'}. \quad (\text{E3})$$

The symmetrized potential $\tilde{V}_{\mathbf{k}\mathbf{k}'}^{\text{symm}}$ is symmetric under the exchange of incoming and outgoing momenta, but to symmetrize the eigenvalue problem in this exchange, we multiply this equation with $\sqrt{w_{\mathbf{k}} \chi_{\mathbf{k}}}$ on both sides, to obtain a gap equation in the form

$$\tilde{\Delta}_{\mathbf{k}} = \sum_{\mathbf{k}'} M_{\mathbf{k}\mathbf{k}'}(\beta) \tilde{\Delta}_{\mathbf{k}'}, \quad (\text{E4})$$

where we introduced the weighted gap $\tilde{\Delta}_{\mathbf{k}} = \sqrt{w_{\mathbf{k}} \chi_{\mathbf{k}}} \Delta_{\mathbf{k}}$, and the matrix

$$M_{\mathbf{k}\mathbf{k}'} = -\frac{1}{A_{\text{BZ}}} (\sqrt{w_{\mathbf{k}} \chi_{\mathbf{k}}} \tilde{V}_{\mathbf{k}\mathbf{k}'}^{\text{symm}} \sqrt{w_{\mathbf{k}'} \chi_{\mathbf{k}'}}). \quad (\text{E5})$$

is symmetric in the interchange of \mathbf{k} and \mathbf{k}' .

To reduce the size of the matrix M and improve computational efficiency, we split the Brillouin zone into small triangles similar to the shaded red triangle in Fig. 4(a), and assume that the gap takes the same value at corresponding points in all the triangles. The effective potential corresponding to a scattering process within the shaded red triangle is then the sum of contributions for scatterings to outgoing momenta in all the small triangles which correspond to the outgoing momentum within the shaded triangle. This reduction of the problem excludes gap equation solutions without the full symmetry of graphene, but we have checked that we obtain the same solutions by solving the gap equation in the full Brillouin zone.

We now have a matrix eigenvalue problem linear in the eigenvectors and nonlinear in the eigenvalue. We find the gap structure at the superconducting instability by determining the smallest β , i.e., the largest temperature, for which the largest eigenvalue of $M_{\mathbf{k}\mathbf{k}'}$ becomes 1. The corresponding eigenvector must be a solution of our eigenvalue problem. The critical temperature $T_c = 1/\beta_c$ is located using the bisection algorithm.

APPENDIX F: PARAMETER VALUES

The parameter values used in the electron tight binding model and the electron-phonon coupling for graphene and boron nitride are listed in Table II. The electron-phonon coupling scale g_0 can be written as

$$g_0 = \gamma t_1 \sqrt{\left(\frac{\hbar^2}{2m_e a_0^2}\right) \frac{1}{\hbar \omega_{\Gamma}} \left(\frac{m_e}{M}\right) \left(\frac{a_0}{d}\right)^2}, \quad (\text{F1})$$

where m_e is the electron mass, and a_0 the Bohr radius. This quantity is calculated based on the listed parameter values, and also given in the table.

APPENDIX G: MOREL-ANDERSON MODEL

The Morel-Anderson model is a simple model describing the effect of a repulsive potential in the entire Brillouin zone on top of an attractive potential in a small region around the Fermi surface giving rise to superconductive pairing [52].

TABLE II. Values for the quantities involved in the calculation of the electron-phonon coupling amplitude strength g_0 , where the A sublattice of boron nitride is assumed to host boron and the B sublattice nitrogen.

Quantity	Graphene	h -BN	Description
d	1.42 Å	1.45 Å	NN distance
t_1	2.8 eV	2.92 eV	Hopping amplitude
Δ	0	4.30 eV	Band gap
$\hbar \omega_{\Gamma}$	0.20 eV	0.17 eV	Phonon energy scale
\bar{M}	12.0 u	12.3 u	Effective mass
μ_A	1	0.88	Relative mass, A subl.
μ_B	1	1.14	Relative mass, B subl.
γ	2.5	2.5	$-d \ln t_1 / d \ln d$
m_e	5.49×10^{-4} u		Electron mass
1 Ry	13.6 eV		Rydberg energy
a_0	0.53 Å		Bohr radius
g_0	0.15 eV	0.16 eV	El-ph coupling scale

This model illustrates why there can be a superconducting instability even though the interaction potential is repulsive even close to the Fermi surface.

In the Morel-Anderson model, one assumes that the potential $V_{\mathbf{k}\mathbf{k}'}$ occurring in the gap equation takes the form $V_{\mathbf{k}\mathbf{k}'} = V_{\mathbf{k}\mathbf{k}'}^{\text{rep}} + V_{\mathbf{k}\mathbf{k}'}^{\text{attr}}$ with

$$V_{\mathbf{k}\mathbf{k}'}^{\text{rep}} = \begin{cases} u, & \text{for } -W \leq \xi_{\mathbf{k}}, \xi_{\mathbf{k}'} \leq W, \\ 0, & \text{otherwise,} \end{cases} \quad (\text{G1})$$

$$V_{\mathbf{k}\mathbf{k}'}^{\text{attr}} = \begin{cases} -v, & \text{for } -\epsilon_D \leq \xi_{\mathbf{k}}, \xi_{\mathbf{k}'} \leq \epsilon_D, \\ 0, & \text{otherwise,} \end{cases}$$

where $u, v \geq 0$, W is the bandwidth cutoff, and $\epsilon_D = \hbar \omega_D$ represents the size of the region with attractive interactions around the Fermi surface. In the case of phonon-mediated superconductivity, this is the phonon Debye frequency.

The gap equation for singlet BCS pairing can now be solved by turning the momentum integral into an energy integral, approximating the density of states by the density of states N_F at the Fermi surface, and assuming the gap to take on two different constant values close to ($|\xi_{\mathbf{k}}| \leq \epsilon_D$) and far away from ($|\xi_{\mathbf{k}}| > \epsilon_D$) the Fermi surface.

This gives a critical temperature given by

$$k_B T_c = 1.14 \epsilon_D \exp\left(-\frac{1}{\lambda - \mu^*}\right), \quad (\text{G2})$$

where $\lambda = N_F v$ is the potential strength of the attractive potential, and

$$\mu^* = \frac{N_F u}{1 + N_F u \ln(W/\hbar \omega_D)} \quad (\text{G3})$$

is the renormalization due to the presence of the repulsive interaction. The effect of the repulsive Coulomb potential is therefore to renormalize the strength λ of the attractive potential in the critical temperature formula. At sufficiently large renormalization ($\mu^* \geq \lambda$), the analysis breaks down, and there is no superconducting instability.

After solving the gap equation with different Coulomb repulsion strengths, we fit the critical temperature to a function

of the form

$$k_B T_c = 1.14 \hbar \omega_D \exp\left(-\frac{1}{\lambda - \frac{au}{1+abu}}\right), \quad (\text{G4})$$

with two fitting parameters a and b in addition to the electron-phonon coupling strength λ , which is fixed by the critical temperature at zero repulsive Coulomb interaction.

- [1] K. S. Novoselov, A. K. Geim, S. V. Morozov, D. Jiang, Y. Zhang, S. V. Dubonos, I. V. Grigorieva, and A. A. Firsov, Electric field effect in atomically thin carbon films, *Science* **306**, 666 (2004).
- [2] K. S. Novoselov, D. Jiang, F. Schedin, T. J. Booth, V. V. Khotkevich, S. V. Morozov, and A. K. Geim, Two-dimensional atomic crystals, *Proc. Natl. Acad. Sci. U.S.A.* **102**, 10451 (2005).
- [3] A. K. Geim and K. S. Novoselov, The rise of graphene, *Nat. Mater.* **6**, 183 (2007).
- [4] A. H. Castro Neto, F. Guinea, N. M. R. Peres, K. S. Novoselov, and A. K. Geim, The electronic properties of graphene, *Rev. Mod. Phys.* **81**, 109 (2009).
- [5] S. Das Sarma, S. Adam, E. H. Hwang, and E. Rossi, Electronic transport in two-dimensional graphene, *Rev. Mod. Phys.* **83**, 407 (2011).
- [6] M. I. Katsnelson, Zitterbewegung, chirality, and minimal conductivity in graphene, *Eur. Phys. J. B* **51**, 157 (2006).
- [7] M. I. Katsnelson, K. S. Novoselov, and A. K. Geim, Chiral tunneling and the Klein paradox in graphene, *Nat. Phys.* **2**, 620 (2006).
- [8] P. Kim, Graphene and relativistic quantum physics, in *Dirac Matter*, edited by B. Duplantier, V. Rivasseau, and J.-N. Fuchs (Springer International Publishing, Cham, 2017), p. 1.
- [9] S. P. Kelty, C.-C. Chen, and C. M. Lieber, Superconductivity at 30 K in caesium-doped C₆₀, *Nature (London)* **352**, 223 (1991).
- [10] A. Y. Ganin, Y. Takabayashi, P. Jeglic, D. Arcon, A. Potocnik, P. J. Baker, Y. Ohishi, M. T. McDonald, M. D. Tzirakis, A. McLennan, G. R. Darling, M. Takata, M. J. Rosseinsky, and K. Prassides, Polymorphism control of superconductivity and magnetism in Cs₃C₆₀ close to the Mott transition, *Nature (London)* **466**, 221 (2010).
- [11] N. B. Hannay, T. H. Geballe, B. T. Matthias, K. Andres, P. Schmidt, and D. MacNair, Superconductivity in Graphitic Compounds, *Phys. Rev. Lett.* **14**, 225 (1965).
- [12] M. Calandra and F. Mauri, Theoretical Explanation of Superconductivity in C₆Ca, *Phys. Rev. Lett.* **95**, 237002 (2005).
- [13] G. Csányi, P. B. Littlewood, A. H. Nevidomskyy, C. J. Pickard, and B. D. Simons, The role of the interlayer state in the electronic structure of superconducting graphite intercalated compounds, *Nat. Phys.* **1**, 42 (2005).
- [14] T. E. Weller, M. Ellerby, S. S. Saxena, R. P. Smith, and N. T. Skipper, Superconductivity in the intercalated graphite compounds C₆Yb and C₆Ca, *Nat. Phys.* **1**, 39 (2005).
- [15] N. Emery, C. Hérod, M. d'Astuto, V. Garcia, Ch. Bellin, J. F. Marêché, P. Lagrange, and G. Loupías, Superconductivity of Bulk CaC₆, *Phys. Rev. Lett.* **95**, 087003 (2005).
- [16] I. I. Mazin and A. V. Balatsky, Superconductivity in Ca-intercalated bilayer graphene, *Philos. Mag. Lett.* **90**, 731 (2010).
- [17] E. R. Margine, H. Lambert, and F. Giustino, Electron-phonon interaction and pairing mechanism in superconducting Ca-intercalated bilayer graphene, *Sci. Rep.* **6**, 21414 (2016).
- [18] E. Suárez Morell, J. D. Correa, P. Vargas, M. Pacheco, and Z. Barticevic, Flat bands in slightly twisted bilayer graphene: Tight-binding calculations, *Phys. Rev. B* **82**, 121407(R) (2010).
- [19] R. Bistritzer and A. H. MacDonald, Moiré bands in twisted double-layer graphene, *Proc. Natl. Acad. Sci. U.S.A.* **108**, 12233 (2011).
- [20] Y. Cao, V. Fatemi, S. Fang, K. Watanabe, T. Taniguchi, E. Kaxiras, and P. Jarillo-Herrero, Unconventional superconductivity in magic-angle graphene superlattices, *Nature (London)* **556**, 43 (2018).
- [21] F. Wu, A. H. MacDonald, and I. Martin, Theory of Phonon-Mediated Superconductivity in Twisted Bilayer Graphene, *Phys. Rev. Lett.* **121**, 257001 (2018).
- [22] M. Kociak, A. Yu. Kasumov, S. Guéron, B. Reulet, I. I. Khodos, Yu. B. Gorbatov, V. T. Volkov, L. Vaccarini, and H. Bouchiat, Superconductivity in Ropes of Single-Walled Carbon Nanotubes, *Phys. Rev. Lett.* **86**, 2416 (2001).
- [23] Z. K. Tang, L. Zhang, N. Wang, X. X. Zhang, G. H. Wen, G. D. Li, J. N. Wang, C. T. Chan, and P. Sheng, Superconductivity in 4 angstrom single-walled carbon nanotubes, *Science* **292**, 2462 (2001).
- [24] H. B. Heersche, P. Jarillo-Herrero, J. B. Oostinga, L. M. K. Vandersypen, and A. F. Morpurgo, Bipolar supercurrent in graphene, *Nature (London)* **446**, 56 (2007).
- [25] A. Shailos, W. Nativel, A. Kasumov, C. Collet, M. Ferrier, S. Guéron, R. Deblock, and H. Bouchiat, Proximity effect and multiple Andreev reflections in few-layer graphene, *Europhys. Lett.* **79**, 57008 (2007).
- [26] X. Du, I. Skachko, and E. Y. Andrei, Josephson current and multiple Andreev reflections in graphene SNS junctions, *Phys. Rev. B* **77**, 184507 (2008).
- [27] G.-H. Lee and H.-J. Lee, Proximity coupling in superconductor-graphene heterostructures, *Rep. Prog. Phys.* **81**, 056502 (2018).
- [28] L. S. Panchakarla, K. S. Subrahmanyam, S. K. Saha, A. Govindaraj, H. R. Krishnamurthy, U. V. Waghmare, and C. N. R. Rao, Synthesis, structure, and properties of boron- and nitrogen-doped graphene, *Adv. Mater.* **21**, 4726 (2009).
- [29] C. N. R. Rao, A. K. Sood, K. S. Subrahmanyam, and A. Govindaraj, Graphene: The new two-dimensional nanomaterial, *Angew. Chem., Int. Ed.* **48**, 7752 (2009).
- [30] D. Usachov, O. Vilkov, A. Grüneis, D. Haberer, A. Fedorov, V. K. Adamchuk, A. B. Preobrajenski, P. Dudin, A. Barinov, M. Oehzelt, C. Laubschat, and D. V. Vyalikh, Nitrogen-doped graphene: Efficient growth, structure, and electronic properties, *Nano Lett.* **11**, 5401 (2011).
- [31] H. Liu, Y. Liu, and D. Zhu, Chemical doping of graphene, *J. Mater. Chem.* **21**, 3335 (2011).
- [32] S. Agnoli and M. Favaro, Doping graphene with boron: A review of synthesis methods, physicochemical characterization, and emerging applications, *J. Mater. Chem. A* **4**, 5002 (2016).

- [33] M. Calandra and F. Mauri, Electron-phonon coupling and electron self-energy in electron-doped graphene: Calculation of angular-resolved photoemission spectra, *Phys. Rev. B* **76**, 205411 (2007).
- [34] M. Bianchi, E. D. L. Rienks, S. Lizzit, A. Baraldi, R. Balog, L. Hornekær, and Ph. Hofmann, Electron-phonon coupling in potassium-doped graphene: Angle-resolved photoemission spectroscopy, *Phys. Rev. B* **81**, 041403(R) (2010).
- [35] J. L. McChesney, A. Bostwick, T. Ohta, T. Seyller, K. Horn, J. González, and E. Rotenberg, Extended van Hove Singularity and Superconducting Instability in Doped Graphene, *Phys. Rev. Lett.* **104**, 136803 (2010).
- [36] G. Profeta, M. Calandra, and F. Mauri, Phonon-mediated superconductivity in graphene by lithium deposition, *Nat. Phys.* **8**, 131 (2012).
- [37] N. A. Vinogradov, K. A. Simonov, A. V. Generalov, A. S. Vinogradov, D. V. Vyalikh, C. Laubschat, N. Mårtensson, and A. B. Preobrajenski, Controllable p-doping of graphene on Ir(111) by chlorination with FeCl₃, *J. Phys.: Condens. Matter* **24**, 314202 (2012).
- [38] I. Pletikosić, M. Kralj, M. Milun, and P. Pervan, Finding the bare band: Electron coupling to two phonon modes in potassium-doped graphene on Ir(111), *Phys. Rev. B* **85**, 155447 (2012).
- [39] N. A. Vinogradov, K. A. Simonov, A. A. Zakharov, J. W. Wells, A. V. Generalov, A. S. Vinogradov, N. Mårtensson, and A. B. Preobrajenski, Hole doping of graphene supported on Ir(111) by AlBr₃, *Appl. Phys. Lett.* **102**, 061601 (2013).
- [40] D. Haberer, L. Petaccia, A. V. Fedorov, C. S. Praveen, S. Fabris, S. Piccinin, O. Vilkov, D. V. Vyalikh, A. Preobrajenski, N. I. Verbitskiy, H. Shiozawa, J. Fink, M. Knupfer, B. Büchner, and A. Grüneis, Anisotropic Eliashberg function and electron-phonon coupling in doped graphene, *Phys. Rev. B* **88**, 081401(R) (2013).
- [41] C. Si, Z. Liu, W. Duan, and F. Liu, First-Principles Calculations on the Effect of Doping and Biaxial Tensile Strain on Electron-Phonon Coupling in Graphene, *Phys. Rev. Lett.* **111**, 196802 (2013).
- [42] E. H. Hwang and S. D. Sarma, Dielectric function, screening, and plasmons in two-dimensional graphene, *Phys. Rev. B* **75**, 205418 (2007).
- [43] B. M. Ludbrook, G. Levy, P. Nigge, M. Zonno, M. Schneider, D. J. Dvorak, C. N. Veenstra, S. Zhdanovich, D. Wong, P. Dosanjh, C. Straßer, A. Stöhr, S. Forti, C. R. Ast, U. Starke, and A. Damascelli, Evidence for superconductivity in Li-decorated monolayer graphene, *Proc. Natl. Acad. Sci. U.S.A.* **112**, 11795 (2015).
- [44] E. R. Margine and F. Giustino, Two-gap superconductivity in heavily *n*-doped graphene: *Ab initio* Migdal-Eliashberg theory, *Phys. Rev. B* **90**, 014518 (2014).
- [45] J. Chapman, Y. Su, C. A. Howard, D. Kundys, A. N. Grigorenko, F. Guinea, A. K. Geim, I. V. Grigorieva, and R. R. Nair, Superconductivity in Ca-doped graphene laminates, *Sci. Rep.* **6**, 23254 (2016).
- [46] G. Grimvall, *The Electron-Phonon Interaction in Metals*, Selected Topics in Solid State Physics (North-Holland, New York, 1981).
- [47] B. Hellsing, A. Eiguren, and E. V. Chulkov, Electron-phonon coupling at metal surfaces, *J. Phys.: Condens. Matter* **14**, 5959 (2002).
- [48] F. Mazzola, T. Frederiksen, T. Balasubramanian, P. Hofmann, B. Hellsing, and J. W. Wells, Strong electron-phonon coupling in the σ band of graphene, *Phys. Rev. B* **95**, 075430 (2017).
- [49] R. Meservey and B. B. Schwartz, Equilibrium properties: Comparison of experimental results with predictions of the BCS theory, in *Superconductivity*, Vol. 1, edited by R. D. Parks (Marcel Dekker Inc., New York, 1969), Chap. 2, p. 117.
- [50] C.-H. Park, F. Giustino, J. L. McChesney, A. Bostwick, T. Ohta, E. Rotenberg, M. L. Cohen, and S. G. Louie, Van Hove singularity and apparent anisotropy in the electron-phonon interaction in graphene, *Phys. Rev. B* **77**, 113410 (2008).
- [51] J. C. Johannsen, S. Ulstrup, M. Bianchi, R. Hatch, D. Guan, F. Mazzola, L. Hornekær, F. Fromm, C. Raidel, T. Seyller, and P. Hofmann, Electron-phonon coupling in quasi-free-standing graphene, *J. Phys.: Condens. Matter* **25**, 094001 (2013).
- [52] P. Morel and P. W. Anderson, Calculation of the superconducting state parameters with retarded electron-phonon interaction, *Phys. Rev.* **125**, 1263 (1962).
- [53] V. N. Kotov, B. Uchoa, V. M. Pereira, F. Guinea, and A. H. Castro Neto, Electron-electron interactions in graphene: Current status and perspectives, *Rev. Mod. Phys.* **84**, 1067 (2012).
- [54] T. O. Wehling, E. Şaşıoğlu, C. Friedrich, A. I. Lichtenstein, M. I. Katsnelson, and S. Blügel, Strength of Effective Coulomb Interactions in Graphene and Graphite, *Phys. Rev. Lett.* **106**, 236805 (2011).
- [55] M. Einenkel and K. B. Efetov, Possibility of superconductivity due to electron-phonon interaction in graphene, *Phys. Rev. B* **84**, 214508 (2011).
- [56] N. S. Mishra and P. Saravanan, A review on the synergistic features of hexagonal boron nitride (white graphene) as adsorbent-photo active nanomaterial, *ChemistrySelect* **3**, 8023 (2018).
- [57] C. R. Dean, A. F. Young, I. Meric, C. Lee, L. Wang, S. Sorgenfrei, K. Watanabe, T. Taniguchi, P. Kim, K. L. Shepard, and J. Hone, Boron nitride substrates for high-quality graphene electronics, *Nat. Nanotechnol.* **5**, 722 (2010).
- [58] H. Wang, Y. Zhao, Y. Xie, X. Ma, and X. Zhang, Recent progress in synthesis of two-dimensional hexagonal boron nitride, *J. Semicond.* **38**, 031003 (2017).
- [59] M. Yankowitz, Q. Ma, P. Jarillo-Herrero, and B. J. LeRoy, van der Waals heterostructures combining graphene and hexagonal boron nitride, *Nat. Rev. Phys.* **1**, 112 (2019).
- [60] L. Wirtz, A. Rubio, R. A. de la Concha, and A. Loiseau, *Ab initio* calculations of the lattice dynamics of boron nitride nanotubes, *Phys. Rev. B* **68**, 045425 (2003).
- [61] J. Robertson, Electronic structure and core exciton of hexagonal boron nitride, *Phys. Rev. B* **29**, 2131 (1984).
- [62] N. H. Shimada, E. Minamitani, and S. Watanabe, Theoretical prediction of phonon-mediated superconductivity with $T_c \approx 25$ K in Li-intercalated hexagonal boron nitride bilayer, *Appl. Phys. Express* **10**, 093101 (2017).
- [63] L. A. Falkovsky, Phonon dispersion in graphene, *J. Exp. Theor. Phys.* **105**, 397 (2007).
- [64] L. A. Falkovsky, Phonon dispersion in graphene, *J. Acoust. Soc. Am.* **123**, 3453 (2008).
- [65] Since we consider superconductivity in graphene with Fermi surface doped down toward the van Hove singularity in the π band, only the phonon scattering processes where an electron

is scattered within the π band are of interest. The effect of the mirror symmetry $z \rightarrow -z$ on the sign of the electron-phonon coupling element g is determined by the product of the deviation and the incoming and outgoing electron states. Since all these are antisymmetric under $z \rightarrow -z$, the out-of-plane phonon modes cannot cause electron transitions within the π band.

- [66] G. D. Mahan, *Many-Particle Physics* (Springer, New York, 2000).
- [67] B. Hellsing, T. Frederiksen, F. Mazzola, T. Balasubramanian, and J. W. Wells, Phonon-induced linewidths of graphene electronic states, *Phys. Rev. B* **98**, 205428 (2018).
- [68] R. Heid, Electron-phonon coupling, in *The Physics of Correlated Insulators, Metals and Superconductors*, Modeling and Simulation, Vol. 7, edited by E. Pavarini, E. Koch, R. Scalettar, and R. M. Martin (Verlag des Forschungszentrum Jülich, Jülich, 2017), Chap. 15, pp. 399–427.
- [69] T. Frederiksen (private communication).
- [70] M. I. Katsnelson, *Graphene* (Cambridge University Press, Cambridge, 2012).
- [71] A. S. Alexandrov, *Theory of Superconductivity: From Weak to Strong Coupling* (Institute of Physics Publishing, Bristol, 2003).
- [72] F.-L. Shyu, Electronic and optical properties of boron nitride nanoribbons in electric field by the tight-binding model, *Phys. B (Amsterdam)* **452**, 7 (2014).
- [73] Due to the rescaling of the deviation discussed in Appendix B, the expression for the electron-phonon coupling matrix element $g_{\mathbf{k}\mathbf{k}'}^{n'l',v}$ is modified according to $e_v^D(\mathbf{q}) \rightarrow e_v^D(\mathbf{q})/\sqrt{\mu_D}$.
- [74] V. Bilonenko, Delaunator-cpp, GitHub repository, 2018.
- [75] C. Kittel, *Quantum Theory of Solids* (John Wiley & Sons, New York, 1987).
- [76] M. V. Ulybyshev, P. V. Buividovich, M. I. Katsnelson, and M. I. Polikarpov, Monte Carlo Study of the Semimetal-Insulator Phase Transition in Monolayer Graphene with a Realistic Interelectron Interaction Potential, *Phys. Rev. Lett.* **111**, 056801 (2013).
- [77] F. Stern and W. E. Howard, Properties of semiconductor surface inversion layers in the electric quantum limit, *Phys. Rev.* **163**, 816 (1967).
- [78] M. Abramowitz and I. A. Stegun, *Handbook of Mathematical Functions : With Formulas, Graphs, and Mathematical Tables*, Dover Books on Mathematics (Dover, New York, 1965).

Paper 3

A. Kamra, E. Thingstad, G. Rastelli, R. Duine, A. Brataas, W. Belzig, and
A. Sudbø,

*Antiferromagnetic magnons as highly squeezed Fock states underlying
quantum correlations,*

Phys. Rev. B **100**, 174407 (2019).

Antiferromagnetic magnons as highly squeezed Fock states underlying quantum correlationsAkashdeep Kamra^{1,*}, Even Thingstad,¹ Gianluca Rastelli,^{2,3} Rembert A. Duine,^{4,5,1} Arne Brataas,¹ Wolfgang Belzig,² and Asle Sudbø¹¹*Center for Quantum Spintronics, Department of Physics, Norwegian University of Science and Technology, NO-7491 Trondheim, Norway*²*Department of Physics, University of Konstanz, D-78457 Konstanz, Germany*³*Zukunftskolleg, University of Konstanz, D-78457 Konstanz, Germany*⁴*Institute for Theoretical Physics, Utrecht University, 3584CC Utrecht, The Netherlands*⁵*Department of Applied Physics, Eindhoven University of Technology, Eindhoven, The Netherlands*

(Received 8 April 2019; revised manuscript received 27 August 2019; published 5 November 2019)

Employing the concept of two-mode squeezed states from quantum optics, we demonstrate a revealing physical picture for the antiferromagnetic ground state and excitations. Superimposed on a Néel ordered configuration, a spin-flip restricted to one of the sublattices is called a sublattice magnon. We show that an antiferromagnetic spin-up magnon is composed of a quantum superposition of states with $n + 1$ spin-up and n spin-down sublattice magnons and is thus an enormous excitation despite its unit net spin. Consequently, its large sublattice spin can amplify its coupling to other excitations. Employing von Neumann entropy as a measure, we show that the antiferromagnetic eigenmodes manifest a high degree of entanglement between the two sublattices, thereby establishing antiferromagnets as reservoirs for strong quantum correlations. Based on these insights, we outline strategies for exploiting the strong quantum character of antiferromagnetic (squeezed) magnons and give an intuitive explanation for recent experimental and theoretical findings in antiferromagnetic magnon spintronics.

DOI: [10.1103/PhysRevB.100.174407](https://doi.org/10.1103/PhysRevB.100.174407)**I. INTRODUCTION**

As per the Heisenberg uncertainty principle, the quantum fluctuations of two noncommuting observables cannot simultaneously be reduced to zero. However, it is possible to generate a state with the quantum noise in one observable reduced below its ground-state limit at the expense of enhanced fluctuations in the other observable [1,2]. Considering a single mode or frequency of light, such states, generally called squeezed vacuum [1,2], have proven instrumental in the detection of gravitational waves [3] with a sensitivity beyond the quantum ground-state limit [4–6]. Furthermore, squeezed vacuum states have applications in quantum information [7–11] since they exhibit quantum correlations and entanglement. These are best represented and exploited via the two-mode squeezed vacuum states, where the two participating modes are entangled and correlated [1]. The widely studied [1,2] single- and two-mode squeezed vacuums may be considered a special case, corresponding to zero photon number(s), of a wider class: squeezed Fock states [12,13]. While investigated theoretically, the latter have been largely forgotten, probably owing to the experimental challenge of generating them. The squeezing concept applies to bosonic modes in general, and squeezed states of magnons [14–17] and phonons [18] have also been achieved experimentally.

The concept of squeezed Fock states [12,13] has proven valuable in understanding the spin excitations of ordered magnets [19,20]. Squeezed magnons have been shown to be

the eigenexcitations of a ferromagnet [19,21]. A squeezed magnon is composed of a coherent superposition of the different odd-number states of the spin-1 magnon [19,20,22]. This bestows it a noninteger average spin larger than 1. The relatively weak spin-nonconserving interactions, such as dipolar fields and crystalline anisotropy, underlie the magnon squeezing in ferromagnets. These spin-nonconserving interactions were further found to result in two-sublattice magnets hosting excitations with spin varying continuously between positive and negative values [20]. In contrast, exchange interaction in a two-sublattice magnet leads to a strong squeezing effect, which does not affect the excitation spin and forms a main subject of the present paper. Being eigenexcitations, squeezed magnons are qualitatively distinct in certain ways from the squeezed states of light discussed above, which are nonequilibrium states generated via an external drive. At the same time, the two kinds of states share several similar features on account of their wave functions being mathematically related. To emphasize this difference, we employ terminology in which “squeezed state of a boson” refers to a nonequilibrium state, while a “squeezed boson” is an eigenmode [23].

Instigated by recent experimental breakthroughs [24–29], interest in antiferromagnets (AFMs) for practical applications has been invigorated [30–34]. Due to the well-known strong quantum fluctuations in AFMs, they have also been the primary workhorse of the quantum magnetism community [35]. The Néel ordered configuration, which is consistent with most of the experiments, is not the true quantum ground state of an AFM. Furthermore, quantum fluctuations destroy any order in a one-dimensional isotropic AFM. These and related general ideas applied to AFMs bearing geometrically

*akashdeep.kamra@ntnu.no

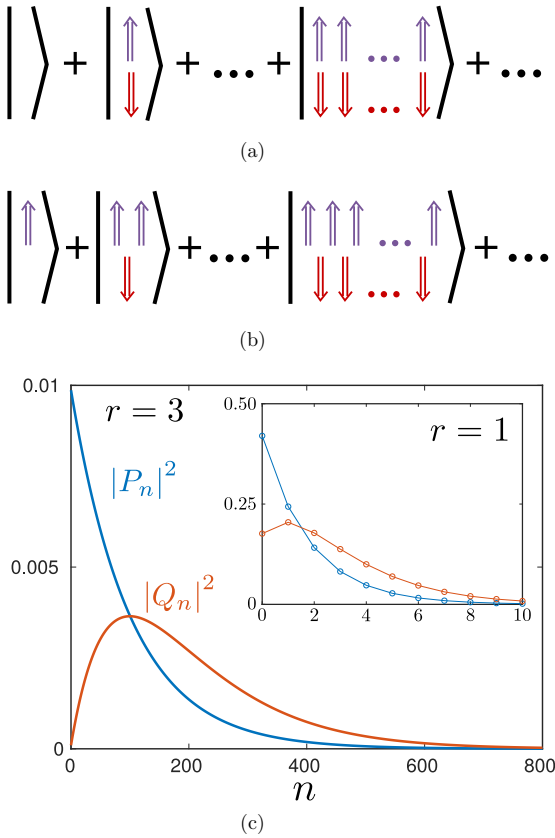


FIG. 1. Schematic depiction of spatially uniform antiferromagnetic (a) vacuum and (b) spin-up eigenmodes. (a) The vacuum mode, represented as $|0\rangle_{\text{sq}} = \sum_n P_n |n, n\rangle_{\text{sub}}$, is a superposition over states with an equal number of spin-up and -down sublattice magnons. (b) The spin-up squeezed magnon, represented as $|\uparrow\rangle_{\text{sq}} = \sum_n Q_n |n+1, n\rangle_{\text{sub}}$, is composed of states with one extra spin-up sublattice magnon. (c) Squared amplitudes corresponding to the sublattice-magnon states constituting the uniform squeezed vacuum and spin-up eigenmodes for squeeze parameters of 3 (main) and 1 (inset).

frustrated interactions underlie quantum spin liquids [36–38], which are devoid of order in the ground state and host exotic, topologically nontrivial excitations embodying massive entanglement.

We here develop the squeezing picture for the ground state and excitations of a simple, two-sublattice AFM. It continuously connects and allows a unified understanding of classical and quantum as well as ordered and disordered antiferromagnetic states. We show that the AFM eigenmodes are obtained by pairwise, two-mode squeezing of sublattice magnons, the spin-1 excitations delocalized over one of the two sublattices. Focusing on spatially uniform modes, the antiferromagnetic ground state is a superposition of states with an equal number of spin-up and -down sublattice magnons [Figs. 1(a) and 1(c)]. The result is a net spin on each sublattice diminished by an

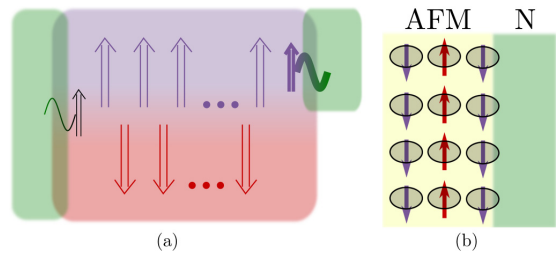


FIG. 2. (a) An external excitation bath (shaded green) interacts weakly with the AFM squeezed magnon if coupled via its unit net spin (left) but strongly if exposed to only one of the sublattices (right). (b) Schematic depiction of a metal (N) coupled to an AFM via a fully uncompensated interface.

amount dictated by the degree of squeezing, parametrized by the non-negative squeeze parameter r . Similarly, a spin-up AFM (squeezed) magnon is composed of a superposition of states with $n+1$ spin-up and n spin-down sublattice magnons [Figs. 1(b) and 1(c)]. Thus, despite its unit net spin, it carries enormous spins on each sublattice, which allows it to couple strongly with other excitations via a sublattice-spin-mediated interaction (Fig. 2). Owing to a perfect correlation between the two sublattice-magnon numbers, AFM squeezed magnons are shown to embody entanglement quantified by von Neumann entropy [1,39] increasing monotonically with r (Fig. 3). The degree of squeezing and entanglement embodied by these eigenmodes is significantly larger than that in hitherto achieved nonequilibrium states. We also comment on existing experiments [40,41] where this squeezing-mediated coupling enhancement (Fig. 2) has been observed and strategies for exploiting the entanglement contained in antiferromagnetic magnons. While the squeezed states of light are generated via external drives and are nonequilibrium states [1], the

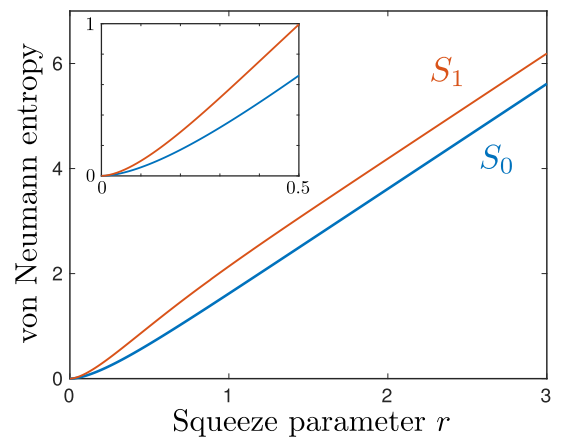


FIG. 3. Entanglement between the two constituent sublattice magnons quantified via von Neumann entropy for the squeezed vacuum (S_0) and magnon (S_1) eigenmodes. The inset shows a zoom of the small- r range.

antiferromagnetic squeezed magnons are eigenmodes of the system with their squeezing being equilibrium in nature and resulting from energy minimization.

II. AFM EIGENMODES AS SQUEEZED FOCK STATES

We consider a Néel ordered ansatz with sublattice A and B spins pointing along \hat{z} and $-\hat{z}$, respectively. The antiferromagnetic Hamiltonian may then be expressed in terms of the corresponding sublattice-magnon ladder operators \tilde{a}_k, \tilde{b}_k as [20,42]

$$\tilde{H} = \sum_k A_k (\tilde{a}_k^\dagger \tilde{a}_k + \tilde{b}_k^\dagger \tilde{b}_k) + C_k (\tilde{a}_k \tilde{b}_{-k} + \tilde{a}_k^\dagger \tilde{b}_{-k}^\dagger), \quad (1)$$

where we assume inversion symmetry and disregard applied magnetic fields for simplicity. Consistent with the assumed Néel order, sublattice B (A) magnons represented by \tilde{b}_k (\tilde{a}_k) are spin up (down). In addition to the general considerations captured by Eq. (1), we will obtain specific results for a uniaxial, easy-axis AFM described by

$$\begin{aligned} \tilde{H}_{\text{uni}} = & \frac{J}{\hbar^2} \sum_{i,\delta} \tilde{S}_A(\mathbf{r}_i) \cdot \tilde{S}_B(\mathbf{r}_i + \boldsymbol{\delta}) \\ & - \frac{K}{\hbar^2} \sum_i [\tilde{S}_{A_z}(\mathbf{r}_i)]^2 - \frac{K}{\hbar^2} \sum_j [\tilde{S}_{B_z}(\mathbf{r}_j)]^2. \end{aligned} \quad (2)$$

Here, the positive parameters J and K account for intersublattice antiferromagnetic exchange and easy-axis anisotropy, respectively. $\tilde{S}_{A,B}$ represent the respective spin operators, \mathbf{r}_i (\mathbf{r}_j) runs over the sublattice A (B), and $\boldsymbol{\delta}$ are vectors to the nearest neighbors. Executing Holstein-Primakoff transformations [43] and switching to Fourier space, Eq. (2) reduces to Eq. (1) apart from a constant-energy offset [20,44], with $A_k = JSz + 2KS$ and $C_k = JSz\gamma_k$. Here, S is the spin on each site, z is the coordination number, and $\gamma_k \equiv (1/z) \sum_{\delta} \exp(i\mathbf{k} \cdot \boldsymbol{\delta})$.

The Hamiltonian [Eq. (1)] is diagonalized to $\tilde{H} = \sum_k \epsilon_k (\tilde{\alpha}_k^\dagger \tilde{\alpha}_k + \tilde{\beta}_k^\dagger \tilde{\beta}_k)$ via a Bogoliubov transformation [43] described by [45]:

$$\tilde{\alpha}_k = u_k \tilde{a}_k + v_k \tilde{b}_{-k}^\dagger, \quad \tilde{\beta}_k = u_k \tilde{b}_k + v_k \tilde{a}_{-k}^\dagger, \quad (3)$$

$$u_k = \sqrt{\frac{A_k + \epsilon_k}{2\epsilon_k}}, \quad v_k = \sqrt{\frac{A_k - \epsilon_k}{2\epsilon_k}}, \quad (4)$$

where $\epsilon_k = \sqrt{A_k^2 - C_k^2}$. $\tilde{\alpha}_k$ and $\tilde{\beta}_k$ represent the spin-down and -up eigenmodes of the AFM, which are subsequently called squeezed magnons. Denoting the resulting antiferromagnetic vacuum or ground-state wave function by $|G\rangle_{\text{sq}}$, we have $\tilde{\alpha}_k |G\rangle_{\text{sq}} = \tilde{\beta}_k |G\rangle_{\text{sq}} = 0$ for all \mathbf{k} .

Let us first consider the spatially uniform modes, i.e., $\mathbf{k} = \mathbf{0}$. We denote states in the corresponding reduced subspaces via $|N_{b_0}, N_{a_0}\rangle_{\text{sub}}$ and $|N_{\tilde{b}_0}, N_{\tilde{a}_0}\rangle_{\text{sq}}$, where N_{b_0} denotes the number of spin-up sublattice magnons and so on. Within the reduced subspaces, the Néel ordered state is thus denoted by $|0, 0\rangle_{\text{sub}}$, while the antiferromagnetic ground state obtained above is represented by $|0, 0\rangle_{\text{sq}}$. We define the relevant two-mode squeeze operator [1]: $\tilde{S}_2(r_0) \equiv \exp(r_0 \tilde{a}_0 \tilde{b}_0 - r_0 \tilde{a}_0^\dagger \tilde{b}_0^\dagger)$, with the non-negative squeeze parameter r_0 given via $u_0 \equiv \cosh r_0$ and $v_0 \equiv \sinh r_0$ [Eq. (4)] [46]. Employing the

identities [1,19]

$$\tilde{\alpha}_0 = \tilde{S}_2(r_0) \tilde{a}_0 \tilde{S}_2^{-1}(r_0), \quad \tilde{\beta}_0 = \tilde{S}_2(r_0) \tilde{b}_0 \tilde{S}_2^{-1}(r_0), \quad (5)$$

where $\tilde{\alpha}_0$ and $\tilde{\beta}_0$ are given by Eq. (3), in the condition $\tilde{\alpha}_0 |0, 0\rangle_{\text{sq}} = \tilde{\beta}_0 |0, 0\rangle_{\text{sq}} = 0$, we obtain

$$|0, 0\rangle_{\text{sq}} = \tilde{S}_2(r_0) |0, 0\rangle_{\text{sub}}. \quad (6)$$

Thus, the uniform modes' antiferromagnetic ground state is a two-mode squeezed vacuum of sublattice magnons. The complementary demonstration of quadrature squeezing is detailed in Appendix A. Working along the same lines as above, it is straightforward to show that $|m, n\rangle_{\text{sq}} = \tilde{S}_2(r_0) |m, n\rangle_{\text{sub}}$, thereby demonstrating the antiferromagnetic eigenmodes are two-mode squeezed sublattice-magnon Fock states. Therefore, the eigenmodes are henceforth called "squeezed magnons."

Based on the analysis above, it becomes evident that the antiferromagnetic ground state is obtained by pairwise, two-mode squeezing of the Néel ordered state:

$$|G\rangle_{\text{sq}} = \left[\prod_k \tilde{S}_2(r_k) \right] |\text{Néel}\rangle_{\text{sub}}, \quad (7)$$

where $\tilde{S}_2(r_k) \equiv \exp(r_k \tilde{a}_k \tilde{b}_{-k} - r_k \tilde{a}_k^\dagger \tilde{b}_{-k}^\dagger)$, with the squeeze parameters r_k given via $u_k = u_{-k} \equiv \cosh r_k$. The $\tilde{\alpha}_k$ eigenmode is thus a two-mode (\tilde{a}_k and \tilde{b}_{-k}) squeezed magnon [Eq. (3)]. Similarly, the $\tilde{\beta}_k$ eigenmode is also a two-mode squeezed magnon formed by \tilde{b}_k and \tilde{a}_{-k} modes [Eq. (3)]. Due to this mathematical equivalence, it suffices to analyze the spatially uniform eigenmodes, which is what we focus on in the following.

III. SPATIALLY UNIFORM EIGENMODES

For ease of notation, we denote the wave functions for a spatially uniform squeezed vacuum by $|0\rangle_{\text{sq}}$ and spin-up squeezed magnon by $|\uparrow\rangle_{\text{sq}}$, while the corresponding squeeze parameter is denoted by r . Considering a uniaxial AFM [Eq. (2)], we obtain $\cosh r \approx (1/2)(Jz/K)^{1/4}$ [Eq. (4)], which translates to $r \approx 3$ for a typical ratio of $J/K \sim 10^4$. To get a feel for numbers, the most squeezed vacuum state of light generated so far corresponds to a squeeze parameter of about 1.7 [2,47]. Furthermore, in the limit $K \rightarrow 0$, the squeeze parameter is found to diverge. This feature is general and a direct consequence [Eq. (4)] of the Goldstone theorem, according to which $\epsilon_0 \rightarrow 0$ in the limit of isotropy.

Employing the relation $\tilde{\alpha}_0 |0\rangle_{\text{sq}} = (\cosh r \tilde{a}_0 + \sinh r \tilde{b}_0^\dagger) |0\rangle_{\text{sq}} = 0$, the squeezed vacuum is obtained in terms of the uniform sublattice-magnons subspace [1]:

$$|0\rangle_{\text{sq}} = \sum_{n=0}^{\infty} \frac{(-\tanh r)^n}{\cosh r} |n, n\rangle_{\text{sub}} \equiv \sum_n P_n |n, n\rangle_{\text{sub}}. \quad (8)$$

The ensuing wave function is schematically depicted in Fig. 1(a), and the distribution over constituent states is plotted in Fig. 1(c). With an increasing r , the number of states that contribute substantially to the superposition increases monotonically. This presence of sublattice magnons in the ground state constitutes quantum fluctuations.

A similar representation for the spin-up squeezed magnon is obtained via $|\uparrow\rangle_{\text{sq}} = \tilde{\beta}_0^\dagger |0\rangle_{\text{sq}} = (\cosh r \tilde{b}_0^\dagger + \sinh r \tilde{a}_0) |0\rangle_{\text{sq}}$

and Eq. (8):

$$\begin{aligned}
 |\uparrow\rangle_{\text{sq}} &= \sum_{n=0}^{\infty} \frac{\sqrt{n+1}(-\tanh r)^n}{\cosh^2 r} |n+1, n\rangle_{\text{sub}} \\
 &\equiv \sum_n Q_n |n+1, n\rangle_{\text{sub}}. \quad (9)
 \end{aligned}$$

A schematic depiction and the distribution over constituent states are shown in Figs. 1(b) and 1(c). In stark contrast to the squeezed vacuum, where the contribution from states decreases monotonically with n , the highest contribution to the superposition here comes from $n \approx \sinh^2 r$. No such peak exists for weak squeezing when $\sinh r < 1$. The average number of spin-up magnons comprising a squeezed magnon is evaluated as $\cosh^2 r + \sinh^2 r$. Thus, a typical AFM squeezed magnon, corresponding to $r \approx 3$ estimated above, is composed of around 200 spin-up magnons on one sublattice and nearly the same number of spin-down magnons on the other. It is thus an enormous excitation, despite its unit net spin.

IV. ENHANCED INTERACTION

This enormous nature of the AFM squeezed magnon reveals an approach to exploit it. When it couples to excitations, such as itinerant electrons or phonons, via its net spin, the interaction strength is proportional to the relatively small unit spin. On the other hand, if an interaction is mediated via the sublattice spin, it will be greatly enhanced (by a factor $\sim \cosh^2 r \approx 100$ for $r \approx 3$) on account of its large sublattice spin content [Fig. 2(a)]. Such a situation arises, for example, when an AFM is exposed to a metal via an uncompensated interface [Fig. 2(b)] [26,48–50]. This effect provides a physical picture for the theoretically encountered enhancement in spin pumping current from AFM into an adjacent conductor coupled asymmetrically to the two sublattices [49]. The same mechanism has also been exploited in predicting an enhanced magnon-mediated superconductivity in a conductor bearing an uncompensated interface with an AFM [51]. Rigorous derivations of electron-magnon and magnon-magnon couplings presented, respectively, in Appendixes B and C demonstrate an enhancement of the interactions consistent with the intuition above, reinforcing the generality of this phenomenon.

V. ENTANGLEMENT

In a two-mode squeezed vacuum, the participating modes are entangled with the degree of entanglement quantified by the von Neumann entropy [1,39] S_0 :

$$\begin{aligned}
 S_0 &= - \sum_n |P_n|^2 \ln(|P_n|^2) \\
 &= 2 \ln(\cosh r) - 2(\sinh^2 r) \ln(\tanh r). \quad (10)
 \end{aligned}$$

Such two-mode squeezed vacuum states of light have been exploited for obtaining useful entanglement [7]. This high von Neumann entropy content of our squeezed-magnon vacuum can be exploited, for example, in entangling two qubits [52] coupled respectively to sublattices A and B. Furthermore, the squeezed magnons themselves embody strong entanglement,

quantified by an even larger von Neumann entropy $S_1 = - \sum_n |Q_n|^2 \ln(|Q_n|^2)$ (Fig. 3), which may be transferred to external excitations. This can be achieved by coupling the systems to be entangled with the opposite sublattices [53–57] via uncompensated interfaces [Fig. 2(b)], for example, as has been detailed further in Appendix D. In comparison, von Neumann entropy [58] of about 1 has been measured in cold-atom systems [59]. This high von Neumann entropy content and the large number of entangled spins ($\sim \cosh^2 r$) that comprise the AFM squeezed magnon make it an entangled excitation complementary to the “massively entangled” excitations hosted by some quantum spin liquids [36–38].

VI. QUANTUM FLUCTUATIONS IN “CLASSICAL” EXPERIMENTS

The interaction enhancement effect [Fig. 2(a)] is rooted in high magnon squeezing and the underlying quantum superposition of a large number of states [Eq. (9)]. It is a direct consequence of the strong quantum fluctuations in the antiferromagnetic ground state, which hosts this excitation, and is thus a quantum fluctuation effect itself. Nevertheless, this coupling enhancement is observed as an increased magnetic damping around the compensation temperature in a compensated ferrimagnet [40], which mimics an AFM [20,60]. Recently, this enhancement was observed and exploited in a compensated ferrimagnet for an ultrastrong magnon-magnon coupling, resulting in hybridization between the two enormous spin-up and -down squeezed magnons [41]. These classical experiments at high temperatures may thus be considered an observation of the antiferromagnetic quantum fluctuations. As detailed in Appendix C, this large squeezing-mediated enhancement ($\sim \sqrt{J/K}$ for our uniaxial AFM), suggested recently in the context of light-matter interaction [61,62], is reproduced by the classical theory of spin dynamics [41,60], where it is termed “exchange enhancement.” This is understandable since the classical dynamics is captured by the quantum system being in a coherent state [49,63,64], which fully accounts for the average effect of these quantum fluctuations.

VII. GENERALIZATIONS

The description in terms of squeezed Fock states developed herein is a mathematical consequence of the Bogoliubov transformation and goes beyond AFMs. It should allow a similar physical picture and subsequent exploitation of quantum effects in other systems such as cold atoms [65–67]. Here, we have disregarded the relatively weak spin-nonconserving interactions. Inclusion of those necessitates a four-dimensional Bogoliubov transform [20], thereby precluding the simple two-mode squeezed Fock state description employed here. Similar complications also arise when considering AFMs lacking inversion symmetry. Nevertheless, an analogous general picture can be developed.

VIII. CONCLUSION

We have developed a description and physical picture of an antiferromagnetic ground state and excitations based on the concept of two-mode squeezed Fock states. Capitalizing

on the tremendous progress in quantum optics, these fresh insights pave the way for exploiting the quantum properties of antiferromagnetic squeezed magnons towards potentially room temperature quantum devices.

ACKNOWLEDGMENTS

A.K. thanks S. Takei, L. Liensberger, M. Weiler, and H. Huebl for valuable discussions. We acknowledge financial support from the Research Council of Norway through its Centers of Excellence funding scheme, Project No. 262633, ‘‘QuSpin,’’ and the DFG through SFB 767. A.S. also acknowledges support from the Research Council of Norway, Grant No. 250985, ‘‘Fundamentals of Low-dissipative Topological Matter.’’

APPENDIX A: DEMONSTRATION OF QUADRATURE SQUEEZING

In this Appendix, we clarify the squeezed nature of the antiferromagnetic ground state by evaluating the quantum fluctuations in the appropriate quadratures. This approach is complementary to the more general discussion in terms of the two-mode squeeze operator [1] presented in the main text. Once again, we focus on the uniform modes, i.e., $\mathbf{k} = \mathbf{0}$, recognizing that the corresponding results for $\mathbf{k} \neq \mathbf{0}$ follow in a similar fashion. We first demonstrate the quadrature squeezing following the standard approach within quantum optics [1] and physically interpret the quadratures later.

For the two-mode squeezing of \tilde{a}_0 and \tilde{b}_0 that is operational here, the relevant quadratures are formed via a combination of both modes’ ladder operators [1]:

$$\tilde{X}_1 \equiv \frac{1}{\sqrt{8}}(\tilde{a}_0 + \tilde{a}_0^\dagger + \tilde{b}_0 + \tilde{b}_0^\dagger), \quad (\text{A1})$$

$$\tilde{X}_2 \equiv \frac{1}{i\sqrt{8}}(\tilde{a}_0 - \tilde{a}_0^\dagger + \tilde{b}_0 - \tilde{b}_0^\dagger). \quad (\text{A2})$$

Employing the bosonic commutation relations of the ladder operators, we obtain $[\tilde{X}_1, \tilde{X}_2] = i/2$, demonstrating that the chosen quadratures of Eqs. (A1) and (A2) represent two non-commuting observables. Denoting the reduced subspace of the uniform modes within the Néel ordered state by $|0\rangle_{\text{sub}}$, the quantum fluctuations in the two quadratures are evaluated as

$$\langle 0|_{\text{sub}}(\delta\tilde{X}_1)^2|0\rangle_{\text{sub}} \equiv \langle 0|_{\text{sub}}(\tilde{X}_1 - \langle\tilde{X}_1\rangle)^2|0\rangle_{\text{sub}} = \frac{1}{4}, \quad (\text{A3})$$

$$\langle 0|_{\text{sub}}(\delta\tilde{X}_2)^2|0\rangle_{\text{sub}} = \frac{1}{4}. \quad (\text{A4})$$

Therefore, the two quadratures host equal quantum noise in the Néel ordered state, that is, $\langle 0|_{\text{sub}}(\delta\tilde{X}_1)^2|0\rangle_{\text{sub}} = \langle 0|_{\text{sub}}(\delta\tilde{X}_2)^2|0\rangle_{\text{sub}}$.

We now consider fluctuations in the antiferromagnetic ground state with the uniform modes’ reduced subspace denoted by $|0\rangle_{\text{sq}}$, as in the main text. Employing the Bogoliubov transformation relations $\tilde{a}_0 = \cosh r \tilde{\alpha}_0 - \sinh r \tilde{\beta}_0^\dagger$ and $\tilde{b}_0 = \cosh r \tilde{\beta}_0 - \sinh r \tilde{\alpha}_0^\dagger$, the two quadratures can be expressed as

$$\tilde{X}_1 = \frac{\cosh r - \sinh r}{\sqrt{8}}(\tilde{\alpha}_0 + \tilde{\alpha}_0^\dagger + \tilde{\beta}_0 + \tilde{\beta}_0^\dagger), \quad (\text{A5})$$

$$\tilde{X}_2 = \frac{\cosh r + \sinh r}{i\sqrt{8}}(\tilde{\alpha}_0 - \tilde{\alpha}_0^\dagger + \tilde{\beta}_0 - \tilde{\beta}_0^\dagger). \quad (\text{A6})$$

Employing the quadrature expressions thus obtained, quantum fluctuations in the antiferromagnetic ground state are conveniently evaluated as

$$\langle 0|_{\text{sq}}(\delta\tilde{X}_1)^2|0\rangle_{\text{sq}} = \frac{(\cosh r - \sinh r)^2}{4} = \frac{e^{-2r}}{4}, \quad (\text{A7})$$

$$\langle 0|_{\text{sq}}(\delta\tilde{X}_2)^2|0\rangle_{\text{sq}} = \frac{(\cosh r + \sinh r)^2}{4} = \frac{e^{2r}}{4}, \quad (\text{A8})$$

thereby demonstrating the quadrature squeezing [1] of the antiferromagnetic ground state, that is, $\langle 0|_{\text{sq}}(\delta\tilde{X}_1)^2|0\rangle_{\text{sq}} < \langle 0|_{\text{sq}}(\delta\tilde{X}_2)^2|0\rangle_{\text{sq}}$.

We now relate the two quadratures [Eqs. (A1) and (A2)] with physical observables of the antiferromagnet (AFM). Employing Fourier relations of the kind

$$\tilde{a}_{\mathbf{k}} = \frac{1}{\sqrt{N}} \sum_i \tilde{a}_i e^{i\mathbf{k}\cdot\mathbf{r}_i}, \quad (\text{A9})$$

in conjunction with the linearized Holstein-Primakoff transformations for the AFM [42,44],

$$\tilde{S}_{A+}(\mathbf{r}_i) = \tilde{S}_{Ax}(\mathbf{r}_i) + i\tilde{S}_{Ay}(\mathbf{r}_i) = \hbar\sqrt{2S}\tilde{a}_i, \quad (\text{A10})$$

$$\tilde{S}_{B+}(\mathbf{r}_j) = \tilde{S}_{Bx}(\mathbf{r}_j) + i\tilde{S}_{By}(\mathbf{r}_j) = \hbar\sqrt{2S}\tilde{b}_j^\dagger, \quad (\text{A11})$$

we obtain

$$\tilde{X}_1 = \frac{1}{2\hbar\sqrt{NS}}(\tilde{S}_{Ax} + \tilde{S}_{Bx}), \quad (\text{A12})$$

$$\tilde{X}_2 = \frac{1}{2\hbar\sqrt{NS}}(\tilde{S}_{Ay} - \tilde{S}_{By}). \quad (\text{A13})$$

Here, N is the total number of sites on each sublattice, S is the spin at each site as defined in the main text, and $\tilde{S}_{Ax} \equiv \sum_i \tilde{S}_{Ax}(\mathbf{r}_i)$ is the x component of the total spin on sublattice A and so on. Thus, the two quadratures are related to the x and y components of the total spin and the Néel order, respectively.

In the qualitatively distinct case of single-mode squeezing manifested by the uniform mode in an anisotropic ferromagnet [19], the two quadratures are simply the x and y components of the total spin, providing a geometrical ‘‘ellipticity’’ interpretation to the squeezing effect [68]. In contrast, the situation is less intuitive for the case of two-mode squeezing as the ellipticity of quantum fluctuations exists in a more abstract space. In the present case, this space is defined by the transverse orthogonal components of the total spin and the Néel order associated with the AFM [Eqs. (A12) and (A13)].

APPENDIX B: ELECTRON-MAGNON COUPLING

Heterostructures with a magnetic insulator layer interfaces with another material hosting conduction electrons have emerged as basic building blocks in a wide range of spintronic concepts and devices. The interfacial exchange-mediated coupling between the magnons in the former and the electrons in the latter have enabled magnon-based information processing schemes, magnon-mediated condensation phenomena, and so on. Thus, an ability to engineer and amplify the electron-magnon coupling is expected to have a strong and broad impact. In this section, we discuss the electron-magnon coupling in an AFM/normal-metal (N) bilayer with the goal of highlighting this tunability and amplification of electron-magnon

coupling by exploiting the squeezing effect, as discussed in the main text. A thorough analysis of this system along with spin transport effects has been provided elsewhere [49]. We here focus on highlighting the amplification effect for an uncompensated AFM with respect to other related systems, providing mathematical expressions complementary to the intuitive physical picture discussed in the main text.

The AFM and N layers are assumed to interact via interfacial exchange, resulting in the following contribution to the Hamiltonian [49] within a continuum model:

$$\tilde{H}_{\text{int}} = -\frac{1}{\hbar^2} \int_{\mathcal{A}} d^2\rho \sum_{G=A,B} \mathcal{J}_G \tilde{S}_G(\boldsymbol{\rho}) \cdot \tilde{S}_N(\boldsymbol{\rho}), \quad (\text{B1})$$

where \mathcal{A} is the interfacial area, $\boldsymbol{\rho}$ is the two-dimensional position vector in the interfacial plane, \tilde{S}_N is the conduction electron spin density operator in N, \tilde{S}_G is the spin density operator in the magnet for sublattice G, and \mathcal{J}_G parametrizes the exchange interaction between the two spin densities, allowing it to be sublattice asymmetric. In terms of the ladder operators for the conduction electrons and magnons, the Hamiltonian above takes the form

$$\tilde{H}_{\text{int}} = \hbar \sum_{\mathbf{q}_1, \mathbf{q}_2, \mathbf{k}} \tilde{c}_{\mathbf{q}_1}^\dagger \tilde{c}_{\mathbf{q}_2} - (W_{\mathbf{q}_1, \mathbf{q}_2, \mathbf{k}}^A \tilde{a}_{\mathbf{k}} + W_{\mathbf{q}_1, \mathbf{q}_2, \mathbf{k}}^B \tilde{b}_{\mathbf{k}}^\dagger) + \text{H.c.}, \quad (\text{B2})$$

where $\tilde{c}_{\mathbf{q}_+}$ denotes the annihilation operator for the N conduction electron with wave vector \mathbf{q} and spin $+\hbar/2$ along the z direction and so on, $\tilde{a}_{\mathbf{k}}$ and $\tilde{b}_{\mathbf{k}}$ are the annihilation operators for the sublattice magnons as discussed in the main text, and $W_{\mathbf{q}_1, \mathbf{q}_2, \mathbf{k}}^A$ is the appropriate amplitude given by the overlap integral between the participating excitation wave functions [49]. With the aim of focusing on the key ingredient in enhancing the coupling, we henceforth consider the relevant and simplified part of the Hamiltonian [enclosed by parentheses in Eq. (B2)] describing electron-magnon coupling:

$$\tilde{P} = W^A \tilde{a}_0 + W^B \tilde{b}_0^\dagger, \quad (\text{B3})$$

where we have again specialized the expression to uniform ($\mathbf{k} = \mathbf{0}$) modes for simplicity and $W^{A,B} \propto \mathcal{J}_{A,IB}$ capture the sublattice-asymmetry in the interfacial coupling.

For comparison, we first consider the case of a single-sublattice isotropic ferromagnet [19] for which the interaction is described simply by $\tilde{P} = W \tilde{a}_0$, with \tilde{a}_0 representing the normal magnon mode. The transition rate Γ for the electron-magnon scattering process is thus simply determined by W , i.e., $\Gamma \propto |W|^2$. For the case of AFMs, in contrast, Eq. (B3) becomes

$$\tilde{P} = (\cosh r W^A - \sinh r W^B) \tilde{a}_0 + (\cosh r W^B - \sinh r W^A) \tilde{b}_0^\dagger \quad (\text{B4})$$

in terms of the normal magnon modes. Now considering $W^A = W^B \equiv W$ for a compensated interface, in which the two sublattices couple equally to the N electrons, we obtain

$$\tilde{P} = W(\cosh r - \sinh r) \tilde{a}_0 + W(\cosh r - \sinh r) \tilde{b}_0^\dagger, \quad (\text{B5})$$

where we see that the transition rate is reduced: $\Gamma \propto (\cosh r - \sinh r)^2 |W|^2 \approx |W|^2 / (4 \cosh^2 r)$, accounting for the large squeezing such that $\cosh r \gg 1$. The electron-magnon coupling for this case is thus suppressed compared to that for ferromagnetic magnons considered above. Arriving

at the crux of this Appendix, as discussed in the main text, when the coupling is mediated by the sublattice spin of the magnon via an uncompensated interface ($W^A = W$, $W^B = 0$), we obtain

$$\tilde{P} = W \cosh r \tilde{a}_0 - W \sinh r \tilde{b}_0^\dagger. \quad (\text{B6})$$

The transition rates for the electron-magnon scattering processes are thus given by $\Gamma \propto \cosh^2 r |W|^2$ for the \tilde{a}_0 mode and $\Gamma \propto \sinh^2 r |W|^2 \approx \cosh^2 r |W|^2$ for the \tilde{b}_0 mode. Thus, we find a squeezing-mediated enhancement in the electron-magnon coupling for the case of sublattice spin-mediated interaction. Furthermore, this is consistent with the simple picture discussed in the main text, and the interaction enhancement factor is related to the sublattice spin associated with a single eigenexcitation: the antiferromagnetic squeezed magnon.

APPENDIX C: MAGNON-MAGNON COUPLING

In this Appendix, we investigate coupling between the two opposite-spin antiferromagnetic eigenmodes caused by a spin-nonconserving interaction [20]. In particular, we demonstrate that a sublattice spin-mediated magnon-magnon coupling is amplified via the squeezing effect, in agreement with the general picture discussed in the main text. This also provides a derivation, within the quantum picture, for the recently observed ‘‘exchange-enhanced’’ ultrastrong magnon-magnon coupling in a compensated ferrimagnet [41] without accounting for all the experimental complexities therein.

In the main text, we considered only interactions that conserve the z -projected spin of the AFM. The diagonalized Hamiltonian therefore assumes the form

$$\tilde{H} = \sum_{\mathbf{k}} \epsilon_{\mathbf{k}} (\tilde{\alpha}_{\mathbf{k}}^\dagger \tilde{\alpha}_{\mathbf{k}} + \tilde{\beta}_{\mathbf{k}}^\dagger \tilde{\beta}_{\mathbf{k}}), \quad (\text{C1})$$

with the two opposite-spin squeezed magnons as degenerate excitations of the system, in the absence of an applied field. However, breaking the spin conservation [69] in the system allows us to couple these opposite-spin excitations, resulting in a lifting of degeneracy and the concomitant hybridization [20]. As discussed in the main text, accounting for such spin-nonconserving terms necessitates a four-dimensional Bogoliubov transform for an exact diagonalization of the Hamiltonian [20]. Here, we circumvent this mathematical complexity by describing the mode coupling in a perturbative manner, treating Eq. (C1) and squeezed magnons as our unperturbed Hamiltonian and eigenexcitations, respectively. This allows us to obtain an analytic expression for the coupling rate while appreciating and justifying the typical approximations employed in such descriptions [1].

For concreteness, we consider the following spin-nonconserving and sublattice spin-mediated contribution to the Hamiltonian that may stem from the magnetocrystalline anisotropy [41]:

$$\tilde{H}_{\text{coup}} = \frac{K_a}{\hbar^2} \sum_i [\tilde{S}_{Ax}(\mathbf{r}_i)]^2 + \frac{K_a}{\hbar^2} \sum_j [\tilde{S}_{Bx}(\mathbf{r}_j)]^2, \quad (\text{C2})$$

where K_a parametrizes this axial-symmetry-breaking anisotropy and the rest of the notation was already introduced in the main text. Employing the Holstein-Primakoff

transformation and switching to Fourier space, the coupling Hamiltonian above is brought to the following form:

$$\tilde{H}_{\text{coup}} = \frac{K_a S}{2} \sum_{\mathbf{k}} \tilde{a}_{\mathbf{k}}^\dagger \tilde{a}_{-\mathbf{k}}^\dagger + \tilde{b}_{\mathbf{k}}^\dagger \tilde{b}_{-\mathbf{k}}^\dagger + \tilde{a}_{\mathbf{k}} \tilde{a}_{-\mathbf{k}} + \tilde{b}_{\mathbf{k}} \tilde{b}_{-\mathbf{k}}. \quad (\text{C3})$$

In writing Eq. (C3), we have neglected terms of the type $\sim \tilde{a}_{\mathbf{k}}^\dagger \tilde{a}_{\mathbf{k}}$ since they can be absorbed into Eq. (C1), leading to a small renormalization of the unperturbed squeezed-magnon energies. We again focus on the uniform modes ($\mathbf{k} = \mathbf{0}$) as they are also the ones observed experimentally [41]:

$$\tilde{H}_{\text{coup}}(\mathbf{k} = \mathbf{0}) = \frac{K_a S}{2} (\tilde{\alpha}_0^2 + \tilde{\beta}_0^2 + \text{H.c.}). \quad (\text{C4})$$

Employing the Bogoliubov transformation relations $\tilde{\alpha}_0 = \cosh r \tilde{\alpha}_0 - \sinh r \tilde{\beta}_0^\dagger$ and $\tilde{\beta}_0 = \cosh r \tilde{\beta}_0 - \sinh r \tilde{\alpha}_0^\dagger$, the coupling Hamiltonian may be expressed in terms of the unperturbed eigenexcitations:

$$\begin{aligned} \tilde{H}_{\text{coup}}(\mathbf{k} = \mathbf{0}) &= -\cosh r \sinh r 2K_a S (\tilde{\alpha}_0 \tilde{\beta}_0^\dagger + \tilde{\alpha}_0^\dagger \tilde{\beta}_0) \\ &+ \frac{K_a S (\cosh^2 r + \sinh^2 r)}{2} (\tilde{\alpha}_0^2 + \tilde{\beta}_0^2 + \text{H.c.}) \end{aligned} \quad (\text{C5})$$

$$\approx -\cosh r \sinh r 2K_a S (\tilde{\alpha}_0 \tilde{\beta}_0^\dagger + \tilde{\alpha}_0^\dagger \tilde{\beta}_0). \quad (\text{C6})$$

In the last simplification above, we have employed the rotating wave approximation [1] and disregarded terms which merely cause rapid oscillations.

Equation (C6) constitutes the main result of this Appendix, where the coupling rate can be read off as $\cosh r \sinh r 2K_a S$. The squeezing-mediated enhancement in the coupling of $\cosh r \sinh r \approx \cosh^2 r \sim \sqrt{J/K}$ is evident and consistent with the intuitive picture presented in the main text. In comparison, if we consider a net spin-mediated magnon-magnon coupling via, for example,

$$\tilde{H}_{\text{coup}} = \frac{K_a}{\hbar^2} \sum [\tilde{S}_{A_x}(\mathbf{r}_i) + \tilde{S}_{B_x}(\mathbf{r}_j)]^2, \quad (\text{C7})$$

an analogous procedure yields a suppressed coupling rate of $K_a S / (4 \cosh^2 r)$, in agreement with the electron-magnon coupling considerations discussed above.

Thus, these two instances (electron-magnon and magnon-magnon couplings) of detailed calculations reinforce the generality of the intuitive picture discussed in the main text. This also suggests these coupling properties are intrinsic to the antiferromagnetic squeezed magnons and therefore applicable to a yet wider class of phenomena involving antiferromagnets. We further note that the squeezing-mediated coupling enhancement that we describe here is mathematically analogous to similar nonequilibrium enhancements suggested recently in the context of light-matter interaction [61,62]. Our suggestion for magnets bears advantages such as stronger enhancement, an equilibrium nature of the effect, tunability via temperature

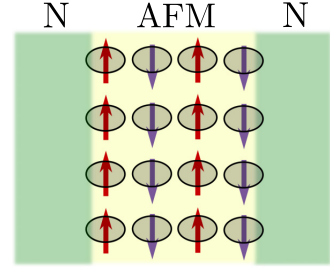


FIG. 4. Schematic depiction of a trilayer heterostructure that allows coupling the two antiferromagnetic sublattices to two different normal metals.

[41], and the recent experimental observation [41] along with the concomitant proof of concept.

APPENDIX D: ACCESSING ENTANGLED SUBSYSTEMS

The von Neumann entropy is widely employed as a measure to quantify entanglement between two subsystems. Thus, its value depends on how a larger system is partitioned into its entangled constituents. In the case of quantum spin liquids, it is common to draw an imaginary boundary and partition the magnet spatially into inside and outside regions. The entanglement entropy may then be evaluated between these two spatial regions and allows us to determine the entangled and/or topological nature of the ground state as well as excitations. On the other hand, in the case of two-mode squeezed states, the participating modes provide a natural partitioning for entanglement [1]. The participating modes are entangled, which may be exploited for useful protocols [1]. However, to this end, it is crucial to access the two entangled modes separately.

As discussed in the main text, antiferromagnetic squeezed magnons are composed of the two-mode squeezing of the sublattice magnons. Therefore, in order to utilize the squeezing-mediated intrinsic entanglement between the sublattice magnons, it is important to access the sublattice magnons individually. This can be achieved by employing AFMs with two uncompensated interfaces in a trilayer structure as depicted in Fig. 4. Similar heterostructures have also been proposed to host magnon-mediated indirect exciton condensation [56]. The experimental methods and relevant materials for achieving uncompensated interfaces have been discussed elsewhere [50]. Furthermore, the recently discovered layered van der Waals AFMs [57] provide another promising route towards achieving the desired coupling to the two sublattices. While Fig. 4 depicts an example of coupling two normal metals to the antiferromagnetic sublattices, the general objective is to couple the two systems to be entangled, which are not necessarily metals, to the opposite sublattices.

[1] C. Gerry and P. Knight, *Introductory Quantum Optics* (Cambridge University Press, Cambridge, 2004).

[2] R. Schnabel, Squeezed states of light and their applications in laser interferometers, *Phys. Rep.* **684**, 1 (2017).

- [3] B. P. Abbott *et al.* (LIGO Scientific Collaboration and Virgo Collaboration), Observation of Gravitational Waves from a Binary Black Hole Merger, *Phys. Rev. Lett.* **116**, 061102 (2016).
- [4] The LIGO Scientific Collaboration, A gravitational wave observatory operating beyond the quantum shot-noise limit, *Nat. Phys.* **7**, 962 (2011).
- [5] The LIGO Scientific Collaboration, Enhanced sensitivity of the LIGO gravitational wave detector by using squeezed states of light, *Nat. Photonics* **7**, 613 (2013).
- [6] H. Grote, K. Danzmann, K. L. Dooley, R. Schnabel, J. Slutsky, and H. Vahlbruch, First Long-Term Application of Squeezed States of Light in a Gravitational-Wave Observatory, *Phys. Rev. Lett.* **110**, 181101 (2013).
- [7] Z. Y. Ou, S. F. Pereira, H. J. Kimble, and K. C. Peng, Realization of the Einstein-Podolsky-Rosen Paradox for Continuous Variables, *Phys. Rev. Lett.* **68**, 3663 (1992).
- [8] T. C. Ralph, Continuous variable quantum cryptography, *Phys. Rev. A* **61**, 010303(R) (1999).
- [9] G. J. Milburn and S. L. Braunstein, Quantum teleportation with squeezed vacuum states, *Phys. Rev. A* **60**, 937 (1999).
- [10] F. Furrer, T. Franz, M. Berta, A. Leverrier, V. B. Scholz, M. Tomamichel, and R. F. Werner, Continuous Variable Quantum Key Distribution: Finite-Key Analysis of Composable Security Against Coherent Attacks, *Phys. Rev. Lett.* **109**, 100502 (2012).
- [11] A. Eddins, S. Schreppler, D. M. Toyli, L. S. Martin, S. Hachengourgy, L. C. G. Govia, H. Ribeiro, A. A. Clerk, and I. Siddiqi, Stroboscopic Qubit Measurement with Squeezed Illumination, *Phys. Rev. Lett.* **120**, 040505 (2018).
- [12] P. Král, Displaced and squeezed Fock states, *J. Mod. Opt.* **37**, 889 (1990).
- [13] M. M. Nieto, Displaced and squeezed number states, *Phys. Lett. A* **229**, 135 (1997).
- [14] J. Zhao, A. V. Bragas, D. J. Lockwood, and R. Merlin, Magnon Squeezing in an Antiferromagnet: Reducing the Spin Noise Below the Standard Quantum Limit, *Phys. Rev. Lett.* **93**, 107203 (2004).
- [15] J. Zhao, A. V. Bragas, R. Merlin, and D. J. Lockwood, Magnon squeezing in antiferromagnetic MnF_2 and FeF_2 , *Phys. Rev. B* **73**, 184434 (2006).
- [16] D. Bossini, S. D. Conte, Y. Hashimoto, A. Secchi, R. V. Pisarev, T. Rasing, G. Cerullo, and A. V. Kimel, Macrospin dynamics in antiferromagnets triggered by sub-20 femtosecond injection of nanomagnons, *Nat. Commun.* **7**, 10645 (2016).
- [17] D. Bossini, S. Dal Conte, G. Cerullo, O. Gomonay, R. V. Pisarev, M. Borovsak, D. Mihailovic, J. Sinova, J. H. Mentink, T. Rasing, and A. V. Kimel, Laser-driven quantum magnonics and terahertz dynamics of the order parameter in antiferromagnets, *Phys. Rev. B* **100**, 024428 (2019).
- [18] S. L. Johnson, P. Beaud, E. Vorobeva, C. J. Milne, É. D. Murray, S. Fahy, and G. Ingold, Directly Observing Squeezed Phonon States with Femtosecond X-Ray Diffraction, *Phys. Rev. Lett.* **102**, 175503 (2009).
- [19] A. Kamra and W. Belzig, Super-Poissonian Shot Noise of Squeezed-Magnon Mediated Spin Transport, *Phys. Rev. Lett.* **116**, 146601 (2016).
- [20] A. Kamra, U. Agrawal, and W. Belzig, Noninteger-spin magnonic excitations in untextured magnets, *Phys. Rev. B* **96**, 020411(R) (2017).
- [21] A. Kamra and W. Belzig, Magnon-mediated spin current noise in ferromagnet | nonmagnetic conductor hybrids, *Phys. Rev. B* **94**, 014419 (2016).
- [22] The “spin-1” magnon is a quasiparticle that carries a spin of \hbar along the z direction [42]. It is not an actual $S = 1$ bosonic particle.
- [23] Within the adopted terminology convention, if one were to generate a nonequilibrium squeezed state of spin excitations in an anisotropic ferromagnet, it would be called the “squeezed state of squeezed magnons.”
- [24] E. Saitoh, M. Ueda, H. Miyajima, and G. Tatara, Conversion of spin current into charge current at room temperature: Inverse spin-Hall effect, *Appl. Phys. Lett.* **88**, 182509 (2006).
- [25] X. He, Y. Wang, N. Wu, A. N. Caruso, E. Vescovo, K. D. Belashchenko, P. A. Dowben, and C. Binek, Robust isothermal electric control of exchange bias at room temperature, *Nat. Mater.* **9**, 579 (2010).
- [26] W. Zhang and K. M. Krishnan, Epitaxial exchange-bias systems: From fundamentals to future spin-orbitronics, *Mater. Sci. Eng., R* **105**, 1 (2016).
- [27] P. Wadley, B. Howells, J. Železný, C. Andrews, V. Hills, R. P. Campion, V. Novák, K. Olejník, F. Maccherozzi, S. S. Dhesi, S. Y. Martin, T. Wagner, J. Wunderlich, F. Freimuth, Y. Mokrousov, J. Kuneš, J. S. Chauhan, M. J. Grzybowski, A. W. Rushforth, K. W. Edmonds, B. L. Gallagher, and T. Jungwirth, Electrical switching of an antiferromagnet, *Science* **351**, 587 (2016).
- [28] T. Kosub, M. Kopte, R. Hühne, P. Appel, B. Shields, P. Maletinsky, R. Hübner, M. O. Liedke, J. Fassbender, O. G. Schmidt, and D. Makarov, Purely antiferromagnetic magneto-electric random access memory, *Nat. Commun.* **8**, 13985 (2017).
- [29] R. Lebrun, A. Ross, S. A. Bender, A. Qaiumzadeh, L. Baldrati, J. Cramer, A. Brataas, R. A. Duine, and M. Kläui, Tunable long-distance spin transport in a crystalline antiferromagnetic iron oxide, *Nature (London)* **561**, 222 (2018).
- [30] E. V. Gomonay and V. M. Loktev, Spintronics of antiferromagnetic systems (review article), *Low Temp. Phys.* **40**, 17 (2014).
- [31] T. Jungwirth, X. Marti, P. Wadley, and J. Wunderlich, Antiferromagnetic spintronics, *Nat. Nanotechnology* **11**, 231 (2016).
- [32] O. Gomonay, V. Baltz, A. Brataas, and Y. Tserkovnyak, Antiferromagnetic spin textures and dynamics, *Nat. Phys.* **14**, 213 (2018).
- [33] V. Baltz, A. Manchon, M. Tsoi, T. Moriyama, T. Ono, and Y. Tserkovnyak, Antiferromagnetic spintronics, *Rev. Mod. Phys.* **90**, 015005 (2018).
- [34] L. Šmejkal, Y. Mokrousov, B. Yan, and A. H. MacDonald, Topological antiferromagnetic spintronics, *Nat. Phys.* **14**, 242 (2018).
- [35] S. Sachdev, *Quantum Phase Transitions* (Cambridge University Press, Cambridge, 2001).
- [36] C. Castelnovo, R. Moessner, and S. L. Sondhi, Spin liquids in frustrated magnets, *Nature (London)* **451**, 42 (2008).
- [37] L. Balents, Spin liquids in frustrated magnets, *Nature (London)* **464**, 199 (2010).
- [38] L. Savary and L. Balents, Quantum spin liquids: A review, *Rep. Prog. Phys.* **80**, 016502 (2017).
- [39] T. Nishioka, Entanglement entropy: Holography and renormalization group, *Rev. Mod. Phys.* **90**, 035007 (2018).

- [40] G. P. Rodrigue, H. Meyer, and R. V. Jones, Resonance measurements in magnetic garnets, *J. Appl. Phys.* **31**, S376 (1960).
- [41] L. Liensberger, A. Kamra, H. Maier-Flaig, S. Geprägs, A. Erb, S. T. B. Goennenwein, R. Gross, W. Belzig, H. Huebl, and M. Weiler, Exchange-Enhanced Ultrastrong Magnon-Magnon Coupling in a Compensated Ferrimagnet, *Phys. Rev. Lett.* **123**, 117204 (2019).
- [42] C. Kittel, *Quantum Theory of Solids* (Wiley, New York, 1963).
- [43] T. Holstein and H. Primakoff, Field dependence of the intrinsic domain magnetization of a ferromagnet, *Phys. Rev.* **58**, 1098 (1940).
- [44] A. I. Akhiezer, V. G. Bar'iahtar, and S. V. Peletminski, *Spin Waves* (North-Holland, Amsterdam, 1968).
- [45] We assume C_k is positive.
- [46] In defining the squeeze operator, we have implicitly assumed positive C_k . If C_k is negative, we obtain the same non-negative squeeze parameter with a squeezing phase of π [1]. The phenomena studied herein remain unaffected under such a phase shift.
- [47] H. Vahlbruch, M. Mehmet, K. Danzmann, and R. Schnabel, Detection of 15 db Squeezed States of Light and their Application for the Absolute Calibration of Photoelectric Quantum Efficiency, *Phys. Rev. Lett.* **117**, 110801 (2016).
- [48] P. K. Manna and S. M. Yusuf, Two interface effects: Exchange bias and magnetic proximity, *Phys. Rep.* **535**, 61 (2014).
- [49] A. Kamra and W. Belzig, Spin Pumping and Shot Noise in Ferrimagnets: Bridging Ferro- and Antiferromagnets, *Phys. Rev. Lett.* **119**, 197201 (2017).
- [50] A. Kamra, A. Rezaei, and W. Belzig, Spin Splitting Induced in a Superconductor by an Antiferromagnetic Insulator, *Phys. Rev. Lett.* **121**, 247702 (2018).
- [51] E. Erlandsen, A. Kamra, A. Brataas, and A. Sudbø, Enhancement of superconductivity mediated by antiferromagnetic squeezed magnons, *Phys. Rev. B* **100**, 100503(R) (2019).
- [52] J. Zou, S. K. Kim, and Y. Tserkovnyak, Tuning entanglement by squeezing magnons in anisotropic magnets, [arXiv:1909.09653](https://arxiv.org/abs/1909.09653).
- [53] L. J. Cornelissen, J. Liu, R. A. Duine, J. B. Youssef, and B. J. van Wees, Long-distance transport of magnon spin information in a magnetic insulator at room temperature, *Nat. Phys.* **11**, 1022 (2015).
- [54] S. T. B. Goennenwein, R. Schlitz, M. Pernpeintner, K. Ganzhorn, M. Althammer, R. Gross, and H. Huebl, Non-local magnetoresistance in YIG/Pt nanostructures, *Appl. Phys. Lett.* **107**, 172405 (2015).
- [55] S. A. Bender, A. Kamra, W. Belzig, and R. A. Duine, Spin Current Cross-Correlations as a Probe of Magnon Coherence, *Phys. Rev. Lett.* **122**, 187701 (2019).
- [56] Ø. Johansen, A. Kamra, C. Ulloa, A. Brataas, and R. A. Duine, Magnon-Mediated Indirect Exciton Condensation through Antiferromagnetic Insulators, *Phys. Rev. Lett.* **123**, 167203 (2019).
- [57] D. MacNeill, J. T. Hou, D. R. Klein, P. Zhang, P. Jarillo-Herrero, and L. Liu, Gigahertz Frequency Antiferromagnetic Resonance and Strong Magnon-Magnon Coupling in the Layered Crystal CrCl_3 , *Phys. Rev. Lett.* **123**, 047204 (2019).
- [58] Strictly speaking, second-order Rényi entropy, which provides a lower bound on von Neumann entropy, was measured.
- [59] R. Islam, R. Ma, P. M. Preiss, M. E. Tai, A. Lukin, M. Rispoli, and M. Greiner, Measuring entanglement entropy in a quantum many-body system, *Nature (London)* **528**, 77 (2015).
- [60] A. Kamra, R. E. Troncoso, W. Belzig, and A. Brataas, Gilbert damping phenomenology for two-sublattice magnets, *Phys. Rev. B* **98**, 184402 (2018).
- [61] C. Leroux, L. C. G. Govia, and A. A. Clerk, Enhancing Cavity Quantum Electrodynamics via Antisqueezing: Synthetic Ultrastrong Coupling, *Phys. Rev. Lett.* **120**, 093602 (2018).
- [62] W. Qin, A. Miranowicz, P.-B. Li, X.-Y. Lü, J. Q. You, and F. Nori, Exponentially Enhanced Light-Matter Interaction, Cooperativities, and Steady-State Entanglement Using Parametric Amplification, *Phys. Rev. Lett.* **120**, 093601 (2018).
- [63] R. J. Glauber, The quantum theory of optical coherence, *Phys. Rev.* **130**, 2529 (1963).
- [64] E. C. G. Sudarshan, Equivalence of Semiclassical and Quantum Mechanical Descriptions of Statistical Light Beams, *Phys. Rev. Lett.* **10**, 277 (1963).
- [65] I. Bloch, J. Dalibard, and W. Zwerger, Many-body physics with ultracold gases, *Rev. Mod. Phys.* **80**, 885 (2008).
- [66] V. Galitski and I. B. Spielman, Spin-orbit coupling in quantum gases, *Nature (London)* **494**, 49 (2013).
- [67] V. Galitski, G. Juzeliūnas, and I. B. Spielman, Artificial gauge fields with ultracold atoms, *Phys. Today* **72(1)**, 38 (2019).
- [68] Quadrature squeezing, however, comments on the ellipticity in the quantum fluctuations and not the expectation values of the spins in the coherent state, as is the case with the ellipticity in the classical spin wave picture. The two kinds of ellipticities, although interrelated in equilibrium for the case under discussion, do not need to be identical in general.
- [69] In the following discussion, we are concerned with the z -projected spin without specifying this directional preference explicitly.

Paper 4

E. Thingstad, E. Erlandsen, and A. Sudbø,

Eliashberg study of superconductivity induced by interfacial coupling to antiferromagnets,

Preprint, arXiv:2105.02235 (2021).

Accepted in Physical Review B.

Eliashberg study of superconductivity induced by interfacial coupling to antiferromagnets

Even Thingstad,^{*} Eirik Erlandsen,^{*} and Asle Sudbø[†]

Center for Quantum Spintronics, Department of Physics, Norwegian University of Science and Technology,
NO-7491 Trondheim, Norway

(Dated: June 30, 2021)

We perform Eliashberg calculations for magnon-mediated superconductivity in a normal metal, where the electron-magnon interaction arises from interfacial coupling to antiferromagnetic insulators. In agreement with previous studies, we find p -wave pairing for large doping when the antiferromagnetic interfaces are uncompensated, and d -wave pairing close to half-filling when the antiferromagnetic interfaces are compensated. However, for the p -wave phase, we find a considerable reduction in the critical temperature compared to previous weak-coupling results, as the effective frequency cutoff on the magnon propagator in this case is found to be much smaller than the cutoff on the magnon spectrum. The d -wave phase, on the other hand, relies less on long-wavelength magnons, leading to a larger effective cutoff on the magnon propagator. Combined with a large density of states close to half-filling, this might allow the d -wave phase to survive up to higher critical temperatures. Based on our findings, we provide new insight into how to realize interfacially induced magnon-mediated superconductivity in experiments.

I. INTRODUCTION

For conventional superconductors, the fluctuations responsible for Cooper-pairing of electrons are provided by phonons [1]. As the role of the phonons is simply to introduce attractive interaction between electrons, superconductivity can in principle arise from exchange of any bosonic quasiparticle that is able to provide a similar attractive interaction [2–5]. One alternative that has received much attention is exchange of paramagnetic spin-fluctuations [6, 7]. The idea is that the spins in a paramagnet, close to magnetic ordering, can act like a medium that can be polarized by the spin of an electron. Another electron can then interact with the polarized medium, giving rise to an effective interaction between the electrons. The quasiparticle mediating the interaction, the paramagnon, represents a damped spin-wave propagating in an ordered patch of the paramagnet [8, 9].

The paramagnon exchange mechanism has been proposed to be closely related to the superconductivity of heavy fermion materials [10–12] and high- T_c cuprates [13, 14]. In the context of the Hubbard model, paramagnon exchange has been found to give rise to p -wave superconductivity for small isotropic Fermi surfaces, and d -wave superconductivity closer to half-filling [11]. This d -wave superconductivity arises from antiferromagnetic fluctuations, so that the interaction is peaked at finite momentum. Although the spin-singlet s -wave channel is repulsive, the d -wave channel is then able to become attractive by taking advantage of sign changes in the gap function [6].

In these systems, superconductivity arises from interactions between fermions due to their own collective spin excitations [13–15]. Spin-fluctuation mediated superconductivity may also occur in heterostructures with itinerant fermions proximity coupled to the spins of insulating materials [16–24]. Since the spins and the itinerant fermions are then separate degrees of freedom, this provides a simpler context to study

superconductivity mediated by spin-fluctuations.

Magnon-mediated superconductivity induced in a normal metal (NM) due to proximity-coupling to a magnetic insulator has so far been investigated within a weak-coupling BCS framework [18, 20–22]. The first case to be considered was a NM coupled to ferromagnetic insulators, which was found to give rise to p -wave pairing [18]. Similarly, for a NM coupled to an antiferromagnetic insulator (AFMI), p -wave solutions were obtained for large dopings by exploiting the inherent squeezing of antiferromagnetic magnons [25] by coupling the conduction electrons in the NM asymmetrically to the two sublattices of the AFMI [21]. This sublattice coupling asymmetry suppresses sublattice interferences in the pairing potential, which are very unfavorable for the p -wave phase. A general asymmetry of this type can be realized by employing an antiferromagnetic interface where both sublattices are exposed (compensated interface), but further breaking the sublattice symmetry by using an antiferromagnetic material with two different atoms on the two sublattices. The particularly relevant case of coupling to only one of the two sublattices is, however, achieved through an uncompensated antiferromagnetic interface where only one of the two sublattices is exposed [26–28].

For the case of a compensated antiferromagnetic interface, the magnons live in a Brillouin zone which is reduced compared to the electron Brillouin zone. This introduces electron-magnon scattering processes of two types: regular and Umklapp [29, 30]. In the regular processes, the electrons are scattered with a momentum within the first magnon Brillouin zone. In the Umklapp processes, on the other hand, the outgoing electron receives an additional momentum corresponding to a magnon reciprocal space lattice vector. The Umklapp processes are of little relevance for the small Fermi surfaces considered in Ref. [21], but closer to half-filling they have been predicted to give rise to d -wave superconductivity in a normal metal sandwiched between two compensated antiferromagnetic interfaces [20]. Analogously to the case of paramagnon exchange in the Hubbard model, the d -wave pairing arises from a repulsive s -wave channel and an interaction that is peaked at finite momentum.

^{*} These authors contributed equally to this work

[†] Corresponding author: asle.sudbo@ntnu.no

We also note that a normal metal coupled to a compensated antiferromagnetic interface is similar to a single material with antiferromagnetically ordered localized spins and itinerant electrons treated as separate degrees of freedom, considered e.g. in Refs. [31–33]. While Ref. [31] simply found the spin singlet s -wave channel to be repulsive for magnon-mediated pairing, Ref. [32] also considered the spin triplet channel and found p -wave superconductivity due to their treatment not probing the interference effects discussed in Ref. [21]. Ref. [33], on the other hand, found that two-magnon scattering processes were dominant for small Fermi surfaces due to the strong destructive interference for one-magnon processes, while spin singlet d -wave pairing driven by one-magnon processes could be possible for larger Fermi surfaces.

A notable difference between the electron-phonon coupling in common weak-coupling superconductors and the electron-magnon coupling considered in the present study, is the behaviour of the coupling matrix element in the limit of small momentum transfers. Since the electron-phonon coupling represents a coupling between electrons and spatial fluctuations of ion densities, it vanishes at zero momentum. In contrast, the coupling between the spins of itinerant electrons and the localized spins of the magnetic insulator is local, and therefore constant in momentum space. For the magnon-mediated superconductivity discussed in the above references, this allows processes with small scattering momentum and small magnon frequencies to dominate the superconducting pairing. In turn, these small momentum processes can compensate for the relatively small interfacial coupling strength of order 10 meV [18, 34], which is typically smaller than the energy scale for the electron-phonon coupling giving rise to phonon-mediated superconductivity [35, 36].

When the dominant contributions to the pairing arise from long-wavelength magnons, one should expect that it may no longer be reasonable to use the cutoff on the boson spectrum as the characteristic boson energy setting the energy scale for the critical temperature. This is not captured in simple BCS theory, which does not consider the frequency dependence of the bosonic fluctuation spectrum responsible for pairing. Furthermore, renormalization of both electrons and bosons is neglected in BCS theory, and these effects could turn out to play a more essential role here. Although BCS theory explains phonon-mediated superconductivity in weak-coupling superconductors reasonably well, a more detailed analysis may be required when other pairing mechanisms are involved.

In this paper, we therefore investigate superconductivity induced in a NM by interfacial coupling to antiferromagnetic insulators using an Eliashberg theory framework. In addition to exploring how the existing results change when the electron renormalization and the proper frequency dependence of the electron-magnon interaction are taken into account, we also study the effect of magnon renormalization and discuss the importance of vertex corrections. Instead of focusing only on regular [21] or Umklapp processes [20], we simultaneously take both types of processes into account and examine how the superconductivity varies with both chemical potential and asymmetry in the coupling to the two sublattices of the antiferromagnet.

In agreement with earlier results, we find a p -wave phase for large sublattice coupling asymmetry and large doping, and a d -wave phase for small sublattice coupling asymmetry and small doping. For the p -wave phase, the critical temperature is considerably reduced compared to previous weak-coupling studies due to the reduction of the effective magnon frequency cutoff. However, the d -wave phase is found to be less reliant on exchange of long-wavelength magnons. This leads to a larger effective cutoff. Near half-filling, the reduction in the contributions from long-wavelength magnons for the d -wave phase can be compensated by a larger density of states, opening up for the possibility of larger critical temperatures. For a strongly nested Fermi-surface, however, one needs to consider e.g. the possibility of a competing spin-density wave instability. Moreover, while a sufficiently large gap in the magnon spectrum may be necessary to protect the ordering of the magnet upon inclusion of magnon renormalization, the net effect on possible critical temperatures is found to be small.

In Sec. II, we present the model of our system. In III, we outline the Eliashberg theory for magnon-mediated superconductivity. We further derive the Fermi surface averaged Eliashberg equations in Sec. IV, and present results for these equations in Sec. V. In Sec. VI we move on to the effect of renormalization of the magnons. Finally, we discuss the validity of the results, as well as additional neglected effects in VII, and experimental considerations in VIII, before we summarize in Sec. IX. Additional details, as well as a discussion of the role of vertex corrections can be found in the appendices.

II. MODEL

We consider a trilayer heterostructure consisting of a normal metal sandwiched between two antiferromagnets, as shown in Fig. 1. The experimental realization of the system would consist of a thin NM layer between two thicker AFMI layers. For simplicity, we model the system using two-dimensional lattice models for the three distinct layers. We assume that the antiferromagnets have staggered magnetic order along the z -direction in spin space, and that this order is opposite in the two antiferromagnets. In general, the spin space z -direction can be either in-plane or out-of-plane in real space for our model.

We model the system with the Hamiltonian $H = H_{\text{NM}} + H_{\text{AFMI}} + H_{\text{int}}$, where

$$H_{\text{NM}} = - \sum_{ij,\sigma} t_{ij} c_{i\sigma}^\dagger c_{j\sigma} - \mu \sum_{i\sigma} c_{i\sigma}^\dagger c_{i\sigma}, \quad (1a)$$

$$H_{\text{AFMI}} = \sum_{ij,\eta} J_{ij} \mathbf{S}_{i\eta} \cdot \mathbf{S}_{j\eta} - K \sum_{i,\eta} (S_{i\eta}^z)^2, \quad (1b)$$

$$H_{\text{int}} = -2\bar{J} \sum_{\eta,\Upsilon} \sum_{i \in \Upsilon} \Omega_{\Upsilon}^2 c_i^\dagger \boldsymbol{\sigma} c_i \cdot \mathbf{S}_{i\eta}, \quad (1c)$$

and the terms describe the normal metal, the antiferromag-

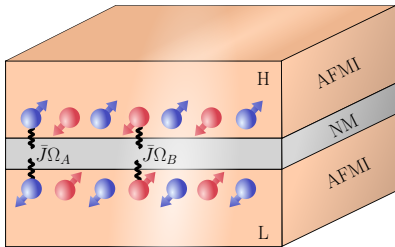


FIG. 1. A trilayer consisting of a normal metal (NM) layer sandwiched between two antiferromagnetic insulator (AFMI) layers. The A and B sublattices of the AFMIs consist of the blue and red lattice sites, respectively. The two AFMIs are oppositely ordered so that the spins associated with a specific sublattice are oppositely oriented for the highest (H) and lowest (L) AFMI. The coupling to the A sublattices of both AFMIs is taken to be of equal strength ($\bar{J}\Omega_A$), and similarly for the B sublattices, so that the itinerant electrons in the NM experience no net magnetic field. The coupling to the A sublattices is however allowed to differ from the coupling to the B sublattices.

netic insulators, and the interfacial coupling between the materials. The sums over i, j denote sums over lattice sites, the sum over $\eta \in \{H, L\}$ denotes a sum over the two antiferromagnetic insulators, and the sum over $\Upsilon \in \{A, B\}$ denotes a sum over the sublattices. All three layers are modelled by square lattices with periodic boundary conditions. In the normal metal, our model describes spinful electrons with annihilation and creation operators $c_{i\sigma}$ and $c_{i\sigma}^\dagger$ for an electron on site i with spin σ . The electron chemical potential is expressed as μ , and t_{ij} is the hopping amplitude, which we set to t for nearest neighbours and zero otherwise. The AFMIs in our model consist of localized lattice site spins, where $S_{i\eta}$ denotes the spin on site i in antiferromagnet η . The exchange coupling between the spins on lattice sites i and j is J_{ij} , which we assume to take the value $J_1 > 0$ for nearest neighbour and J_2 for next-nearest neighbour sites. Moreover, $K > 0$ denotes the easy axis anisotropy. The interfacial coupling between the materials is included as an effective exchange interaction \bar{J} between the lattice site spins in the antiferromagnets and the spins of the conduction band electrons that are confined to the normal metal [18, 20, 34, 37, 38]. We use the notation $c_i = (c_{i\uparrow}, c_{i\downarrow})^T$, and have taken σ to denote the Pauli matrix vector in spin space. In order to be able to introduce asymmetry in the coupling between the normal metal and the two sublattices of the antiferromagnets, we have included a dimensionless, sublattice- and layer-dependent, parameter Ω_Υ^η in the interaction Hamiltonian [21–23]. In order to eliminate any magnetic fields, we will focus on equal coupling to the two antiferromagnets [20], and therefore let $\Omega_\Upsilon^\eta \equiv \Omega_\Upsilon$. In the following, we set $\hbar = a = 1$, with a being the lattice constant.

The normal metal Hamiltonian can be diagonalized to obtain

$$H_{\text{NM}} = \sum_{\mathbf{k} \in \square, \sigma} \xi_{\mathbf{k}} c_{\mathbf{k}\sigma}^\dagger c_{\mathbf{k}\sigma}, \quad (2)$$

where the quasimomentum sum runs over the full Brillouin zone, we have defined $\xi_{\mathbf{k}} = \epsilon_{\mathbf{k}} - \mu$, and the single particle electron dispersion relation is given by $\epsilon_{\mathbf{k}} = -2t(\cos k_x + \cos k_y)$.

To determine the eigenexcitations of the antiferromagnetic insulator, we introduce the linearized Holstein-Primakoff transformation to represent the spins in terms of bosons $a_{i\eta}$ and $b_{i\eta}$ on the two sublattices of the system. Further, introducing the Fourier transformed operators $a_{\mathbf{q}\eta}$ and $b_{\mathbf{q}\eta}$, one may diagonalize the AFMI Hamiltonian using a Bogoliubov transformation

$$a_{\mathbf{q}\eta} = u_{\mathbf{q}} \alpha_{\mathbf{q}\eta} + v_{\mathbf{q}} \beta_{-\mathbf{q}\eta}^\dagger, \quad (3a)$$

$$b_{-\mathbf{q}\eta}^\dagger = u_{\mathbf{q}} \beta_{-\mathbf{q}\eta}^\dagger + v_{\mathbf{q}} \alpha_{\mathbf{q}\eta}, \quad (3b)$$

as detailed in Appendix A. By suitable choice of coherence factors $u_{\mathbf{q}}$ and $v_{\mathbf{q}}$, the AFMI Hamiltonian takes the form

$$H_{\text{AFMI}} = \sum_{\mathbf{q} \in \diamond, \eta} \omega_{\mathbf{q}} (\alpha_{\mathbf{q}\eta}^\dagger \alpha_{\mathbf{q}\eta} + \beta_{\mathbf{q}\eta}^\dagger \beta_{\mathbf{q}\eta}), \quad (4)$$

with eigenmagnon operators $\alpha_{\mathbf{q}\eta}$ and $\beta_{\mathbf{q}\eta}$, magnon dispersion $\omega_{\mathbf{q}}$, and where the quasimomentum \mathbf{q} runs over the reduced Brillouin zone, as illustrated in Fig. 2 (a).

As shown in Refs. [21, 23], the electron-magnon coupling in this system in general consists of staggered and net magnetic fields, as well as electron scattering processes of both regular and Umklapp type. In our case, all net and staggered magnetic fields from the two opposing antiferromagnetic layers cancel.

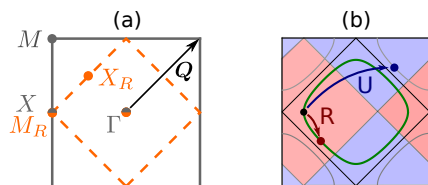


FIG. 2. (a) Electron (grey) and magnon (orange) Brillouin zones with labelling of high symmetry points. We refer to the magnon Brillouin zone as the reduced Brillouin zone (RBZ). The antiferromagnetic ordering vector \mathbf{Q} is also indicated. (b) Fermi surface (green) at moderate doping. Electrons can be scattered from \mathbf{k} (black) to points $\mathbf{k} + \mathbf{q}$ inside the shaded red part of the Brillouin zone through regular processes, and to points $\mathbf{k} + \mathbf{q} + \mathbf{Q}$ in the shaded blue part of the Brillouin zone through Umklapp processes.

The interaction Hamiltonian then takes the form

$$H_{\text{int}} = V \sum_{\substack{\mathbf{k} \in \square \\ \mathbf{q} \in \diamond}} \left[M_{\mathbf{q}}^R c_{\mathbf{k}+\mathbf{q},\downarrow}^\dagger c_{\mathbf{k},\uparrow} + M_{\mathbf{q}}^U c_{\mathbf{k}+\mathbf{q},\downarrow}^\dagger c_{\mathbf{k},\uparrow} \right. \\ \left. + (M_{-\mathbf{q}}^R)^\dagger c_{\mathbf{k}+\mathbf{q},\uparrow}^\dagger c_{\mathbf{k},\downarrow} + (M_{-\mathbf{q}}^U)^\dagger c_{\mathbf{k}+\mathbf{q},\uparrow}^\dagger c_{\mathbf{k},\downarrow} \right], \quad (5)$$

where we have defined the magnon operators $M_{\mathbf{q}}^\kappa = M_{\mathbf{q}H}^\kappa + M_{\mathbf{q}L}^\kappa$ with

$$M_{\mathbf{q}H}^\kappa = \Omega_A a_{\mathbf{q}H} + \kappa \Omega_B b_{-\mathbf{q}H}^\dagger, \quad (6a)$$

$$M_{\mathbf{q}L}^\kappa = \Omega_A a_{-\mathbf{q}L}^\dagger + \kappa \Omega_B b_{\mathbf{q}L}. \quad (6b)$$

Here, $\kappa \in \{R, U\}$ is an index characterizing whether the corresponding electron scattering process is of regular or Umklapp type, which we associate with the values $R \rightarrow +1$ and $U \rightarrow -1$ in the definition of $M_{\mathbf{q}}^\kappa$. Examples of regular and Umklapp scattering processes are shown Fig. 2 (b). We have also defined the momentum shift vector $\mathbf{Q} = \pi(\hat{x} + \hat{y})$ occurring in the Umklapp scattering processes, and the interaction strength parameter $V \equiv -2J\sqrt{S/N}$, where S is the spin quantum number of the AFMI lattice site spins, and N the number of lattice sites.

In terms of the eigenmagnon operators $\alpha_{q\eta}, \beta_{q\eta}$, we may also express the magnon operators $M_{\mathbf{q}}^\kappa$ as

$$M_{\mathbf{q}}^\kappa = (\Omega_A u_{\mathbf{q}} + \kappa \Omega_B v_{\mathbf{q}})(\alpha_{\mathbf{q}H} + \alpha_{-\mathbf{q}L}^\dagger) \\ + (\Omega_A v_{\mathbf{q}} + \kappa \Omega_B u_{\mathbf{q}})(\beta_{-\mathbf{q}H}^\dagger + \beta_{\mathbf{q}L}), \quad (7)$$

so that we may think of the magnon operators $M_{\mathbf{q}}^\kappa$ as linear combinations of antiferromagnetic eigenmagnon operators with a given spin and momentum.

III. ELIASHBERG THEORY

A. Magnon propagators

Since the magnon operators in the electron-magnon interaction only occur in the particular linear combinations $M_{\mathbf{q}}^\kappa$, the propagators of $M_{\mathbf{q}}^\kappa$ will be key building blocks in our Eliashberg theory. In the imaginary time formalism, we therefore define the magnon propagator

$$\mathcal{D}^{\kappa\kappa'}(\mathbf{q}, \tau) = -\langle T_\tau M_{\mathbf{q}}^\kappa(\tau) (M_{\mathbf{q}}^{\kappa'})^\dagger(0) \rangle, \quad (8)$$

where T_τ is the time-ordering operator and the expectation value is computed with the full Hamiltonian. In the non-interacting theory, one may utilize the eigenmagnon propagators to show that

$$\mathcal{D}_0^{\kappa\kappa'}(\mathbf{q}, i\nu_m) = -2A_e^{\kappa\kappa'}(\mathbf{q}) \frac{2\omega_{\mathbf{q}}}{\nu_m^2 + \omega_{\mathbf{q}}^2}, \quad (9)$$

where $\nu_m = 2m\pi/\beta$ is a bosonic Matsubara frequency, and β the inverse temperature. The boosting factors $A_e^{\kappa\kappa'}(\mathbf{q})$ are given by

$$A_e^{RR}(\mathbf{q}) = \frac{1}{2} [(\Omega_A u_{\mathbf{q}} + \Omega_B v_{\mathbf{q}})^2 + (\Omega_A v_{\mathbf{q}} + \Omega_B u_{\mathbf{q}})^2], \quad (10a)$$

$$A_e^{UU}(\mathbf{q}) = \frac{1}{2} [(\Omega_A u_{\mathbf{q}} - \Omega_B v_{\mathbf{q}})^2 + (\Omega_A v_{\mathbf{q}} - \Omega_B u_{\mathbf{q}})^2], \quad (10b)$$

$$A_e^{RU}(\mathbf{q}) = A_e^{UR}(\mathbf{q}) = \frac{1}{2} (\Omega_A^2 - \Omega_B^2) (u_{\mathbf{q}}^2 + v_{\mathbf{q}}^2). \quad (10c)$$

Here, $u_{\mathbf{q}}$ and $v_{\mathbf{q}}$ are the magnon coherence factors, arising from the Bogoliubov transformation, discussed in Appendix A. Inspecting the boosting factor corresponding to regular scattering processes, we see that it coincides with the boosting factor occurring from the canonical transformation used to obtain the effective interaction potential in Ref. [21].

From the expressions for the regular and Umklapp boosting factors $A_e^{RR}(\mathbf{q})$ and $A_e^{UU}(\mathbf{q})$, it is clear that in addition to contributions from only the A and B sublattices proportional to factors of Ω_A^2 and Ω_B^2 , there are in general also interferences between contributions from the two sublattices. Since $u_{\mathbf{q}}$ is typically positive and $v_{\mathbf{q}}$ is typically negative, as discussed in Appendix A, we typically expect destructive interference in the regular process boosting factor $A_e^{RR}(\mathbf{q})$ [21] and constructive interference in the Umklapp process boosting factor $A_e^{UU}(\mathbf{q})$. The significance of these interference effects is controlled by the asymmetry in the coupling to the two sublattices, where we find the strongest sublattice interferences when we couple equally to both sublattices, and that all interference effects are removed when we couple to only one sublattice. The mixed propagator boosting factors A_e^{RU} and A_e^{UR} do not experience similar interferences.

B. Spinor representations

To study magnon-mediated superconductivity, we now construct the Eliashberg theory for the system. To do this, we first introduce the Nambu spinor

$$\psi_{\mathbf{k}} = \begin{pmatrix} c_{\mathbf{k}\uparrow} \\ c_{\mathbf{k}\downarrow} \\ c_{-\mathbf{k}\uparrow}^\dagger \\ c_{-\mathbf{k}\downarrow}^\dagger \\ c_{\mathbf{k}+\mathbf{Q}\uparrow} \\ c_{\mathbf{k}+\mathbf{Q}\downarrow} \\ c_{-\mathbf{k}-\mathbf{Q}\uparrow}^\dagger \\ c_{-\mathbf{k}-\mathbf{Q}\downarrow}^\dagger \end{pmatrix}. \quad (11)$$

The corresponding Green's function can then in general be written as the 8×8 matrix

$$G(\mathbf{k}, \mathbf{k}', \tau) = -\langle T_\tau \psi_{\mathbf{k}}(\tau) \psi_{\mathbf{k}'}^\dagger(0) \rangle, \quad (12)$$

where we will also be using the notation $G(\mathbf{k}, \mathbf{k}, \tau) = G(\mathbf{k}, \tau)$. After a Fourier transform, the imaginary time propagators can be expressed through the Fourier coefficients $G(\mathbf{k}, i\omega_n)$, with fermionic Matsubara frequencies $\omega_n = (2n + 1)\pi/\beta$. The 8×8 matrix can in general be spanned by the Pauli matrix outer products

$$\rho_\alpha \otimes \tau_\beta \otimes \sigma_\gamma, \quad (13)$$

where $\alpha, \beta, \gamma \in \{0, 1, 2, 3\}$ and the Pauli matrix ρ_α acts on the momentum sector degree of freedom, τ_β on the particle/hole degree of freedom, and σ_γ on the spin degree of freedom.

We also introduce the magnon spinor

$$B_{\mathbf{q}} = \left(M_{\mathbf{q}}^R \quad (M_{-\mathbf{q}}^R)^\dagger \quad M_{\mathbf{q}}^U \quad (M_{-\mathbf{q}}^U)^\dagger \right)^T, \quad (14)$$

where each magnon operator in the spinor corresponds to the destruction of an excitation with momentum \mathbf{q} and spin -1 , or the creation of an excitation with momentum $-\mathbf{q}$ and spin $+1$. The magnon operator propagators can now be collected in the magnon propagator matrix

$$D_{\gamma\gamma'}(\mathbf{q}, \tau) = -\langle T_\tau B_{\mathbf{q}}^\gamma(\tau) B_{-\mathbf{q}}^{\gamma'}(0) \rangle. \quad (15)$$

After a Fourier transform, the propagator matrix takes the form

$$D(q) = \begin{pmatrix} 0 & \mathcal{D}^{RR}(q) & 0 & \mathcal{D}^{RU}(q) \\ \mathcal{D}^{RR}(-q) & 0 & \mathcal{D}^{UR}(-q) & 0 \\ 0 & \mathcal{D}^{UR}(q) & 0 & \mathcal{D}^{UU}(q) \\ \mathcal{D}^{RU}(-q) & 0 & \mathcal{D}^{UU}(-q) & 0 \end{pmatrix}, \quad (16)$$

in terms of the previously introduced propagators $\mathcal{D}^{\kappa\kappa'}$. Here, $q = (\mathbf{q}, i\nu_m)$ is a three-vector containing both momentum and the Matsubara frequency. As the magnon propagators respect time-reversal and inversion symmetry, we have $\mathcal{D}^{\kappa\kappa'}(-q) = \mathcal{D}^{\kappa\kappa'}(q)$. Further, the magnon propagators also satisfy $\mathcal{D}^{RU}(q) = \mathcal{D}^{UR}(q)$.

In spinor notation for the magnon and electron operators, the interaction Hamiltonian can be written on the form

$$H_{\text{int}} = \frac{V}{4} \sum_{\substack{\mathbf{k} \in \square \\ \mathbf{q} \in \diamond}} \sum_{\alpha\beta\gamma} g_\gamma^{\alpha\beta} B_{\mathbf{q}}^\gamma \psi_{\mathbf{k}+\mathbf{q}\alpha}^\dagger \psi_{\mathbf{k}\beta}, \quad (17)$$

where the sum over \mathbf{k} runs over the full Brillouin zone, the sum over \mathbf{q} runs over the reduced Brillouin zone, and the index γ corresponds to the various operators in the magnon spinor $B_{\mathbf{q}}^\gamma$. The matrices g_γ are given by

$$g_1 = f_1 \otimes \rho_0, \quad g_2 = f_2 \otimes \rho_0, \quad (18a)$$

$$g_3 = f_1 \otimes \rho_1, \quad g_4 = f_2 \otimes \rho_1, \quad (18b)$$

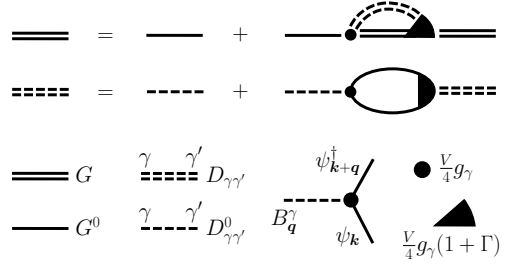


FIG. 3. Feynman diagram expansion for interacting electron and magnon propagators. Each vertex is associated with a factor $Vg_\gamma/4$, and electron and magnon propagators G and D are represented by solid and dashed lines.

where we have introduced the 4×4 matrices

$$f_1 = \frac{1}{2}(\sigma_1\tau_0 - i\sigma_2\tau_3), \quad (19a)$$

$$f_2 = \frac{1}{2}(\sigma_1\tau_0 + i\sigma_2\tau_3), \quad (19b)$$

acting on the spin and particle/hole degrees of freedom to simplify the notation.

C. S -matrix expansion

Starting from the non-interacting electron Hamiltonian and the spinor form of the interaction, we may now apply the S -matrix expansion and use Wicks theorem to obtain a Feynman diagram expansion for the electron Green's function $G(\mathbf{k}, i\omega_n)$, as shown in Fig. 3.

The resulting equation can be solved for the electron Green's function to obtain the Dyson equation

$$G^{-1}(k) = G_0^{-1}(k) - \Sigma(k), \quad (20)$$

where $\Sigma(k)$ is the self-energy, and $G_0(k)$ is the non-interacting electron Green's function given by

$$G_0^{-1}(\mathbf{k}, i\omega_n) = i\omega_n\rho_0\tau_0\sigma_0 - \epsilon_{\mathbf{k}}\rho_3\tau_3\sigma_0 + \mu\rho_0\tau_3\sigma_0. \quad (21)$$

In the following, we neglect vertex corrections, which are discussed more in Appendix D. We may then consider only sunset type diagrams in the self-energy. Performing the S -matrix expansion, we extract the self-energy

$$\Sigma(k) = -\frac{V^2}{2\beta} \sum_{k'} \sum_{\gamma\gamma'} \theta_{\mathbf{k}-\mathbf{k}'} D_{\gamma\gamma'}(k-k') g_\gamma G(k') g_{\gamma'}, \quad (22)$$

as evident from the diagrammatic representation in Fig. 3 up to signs and prefactors. Here, $\theta_{\mathbf{q}}$ is defined by

$$\theta_{\mathbf{q}} = \begin{cases} 1, & \mathbf{q} \in \text{RBZ} \\ 0, & \mathbf{q} \in \text{QBZ} \end{cases}, \quad (23)$$

and ensures that the magnon propagator momentum $\mathbf{q} = \mathbf{k} - \mathbf{k}'$ is restricted to the reduced Brillouin zone (RBZ) [39]. Here, QBZ refers to the conjugate Brillouin zone which, together with the RBZ, comprises the full electron Brillouin zone.

In the discussion so far, we have been using a Nambu spinor $\psi_{\mathbf{k}}$ containing electrons at both \mathbf{k} and $\mathbf{k} + \mathbf{Q}$. Thus, the 8×8 matrix Green's function $G(k)$ may in general have correlations between electrons at momenta \mathbf{k} and $\mathbf{k} + \mathbf{Q}$. In the following, we assume that the processes close to the Fermi surface dominate the self-energy. Away from half-filling, we may then neglect the correlations which are off-diagonal in the momentum sector, as they are suppressed by the large electronic energy at momentum $\mathbf{k} + \mathbf{Q}$ when \mathbf{k} is close to the Fermi surface. This is discussed in more detail in Appendix C. The Green's function $G(k)$ and the self-energy $\Sigma(k)$ then reduce to two uncoupled blocks of size 4×4 which are related by $\mathbf{k} \rightarrow \mathbf{k} + \mathbf{Q}$. In the following, we therefore consider only one of the two blocks.

D. Eliashberg equations

To derive the Eliashberg equations, we decompose the self-energy matrix into contributions corresponding to the various basis matrices $\sigma_{\alpha} \otimes \tau_{\beta}$ for Hermitian 4×4 matrices. We set

$$\Sigma = (1 - Z)i\omega_n\sigma_0\tau_0 + \chi\sigma_0\tau_3 + \phi_s\sigma_2\tau_2 + \phi_t\sigma_1\tau_1, \quad (24)$$

where Z is the electron renormalization, χ is the quasiparticle energy shift, ϕ_s is the spin singlet pairing amplitude, and ϕ_t the amplitude for unpolarized spin triplet pairing.

Among the 16 possible terms on the form $\sigma_{\alpha} \otimes \tau_{\beta}$, we have kept only 4. Of the remaining 12 combinations, the 8 which do not conserve spin cannot occur because they are incompatible with the spin structure of the self energy diagram. The combinations $\tau_3\sigma_3$ and $\tau_0\sigma_3$ are disregarded because they introduce spin-dependent quasiparticle renormalization, which is not expected to be present due to the spin symmetry of the fermions in the system. Finally, we could have introduced terms $\tilde{\phi}_s\tau_1\sigma_2$ and $\tilde{\phi}_t\sigma_1\tau_2$. However, the associated fields $\tilde{\phi}_s$ and $\tilde{\phi}_t$ would play exactly the same roles as ϕ_s and ϕ_t , and we therefore set them to zero.

Due to symmetry relations between the electron correlations in the Nambu spinor Green's function matrix $G(k)$ [40], the normal Green's function fields satisfy

$$Z(-k) = Z(k), \quad Z(\mathbf{k}, i\omega_n) = Z(\mathbf{k}, -i\omega_n)^*, \quad (25)$$

$$\chi(-k) = \chi(k), \quad \chi(\mathbf{k}, i\omega_n) = \chi(\mathbf{k}, -i\omega_n)^*, \quad (26)$$

and the anomalous correlations satisfy

$$\phi_s(-k) = +\phi_s(k), \quad \phi_s(\mathbf{k}, i\omega_n) = \phi_s(\mathbf{k}, -i\omega_n)^*, \quad (27)$$

$$\phi_t(-k) = -\phi_t(k), \quad \phi_t(\mathbf{k}, i\omega_n) = \phi_t(\mathbf{k}, -i\omega_n)^*. \quad (28)$$

We may now derive equations for the fields Z, χ, ϕ_s, ϕ_t by inserting the form for Σ into the Dyson equation, inverting the inverse $G^{-1}(k)$ and inserting $G(k)$ into the self-energy in Eq. (22). Comparing term by term, we then obtain the equations

$$[1 - Z(k)]i\omega_n = -V^2 \frac{1}{\beta} \sum_{k'} \mathcal{D}(k - k') \frac{i\omega_n Z(k')}{\Theta(k')}, \quad (29a)$$

$$\chi(k) = -V^2 \frac{1}{\beta} \sum_{k'} \mathcal{D}(k - k') \frac{\xi_{k'} + \chi(k')}{\Theta(k')}, \quad (29b)$$

$$\phi_s(k) = -V^2 \frac{1}{\beta} \sum_{k'} \mathcal{D}(k - k') \frac{\phi_s(k')}{\Theta(k')}, \quad (29c)$$

$$\phi_t(k) = +V^2 \frac{1}{\beta} \sum_{k'} \mathcal{D}(k - k') \frac{\phi_t(k')}{\Theta(k')}, \quad (29d)$$

under the assumption that a single symmetry channel dominates, so that either $\phi_s = 0$ or $\phi_t = 0$ [41]. We have also introduced the combined magnon propagator

$$\mathcal{D}(\mathbf{q}) = \theta_{\mathbf{q}} \mathcal{D}^{RR}(\mathbf{q}, i\nu_m) + \theta_{\mathbf{q}+\mathbf{Q}} \mathcal{D}^{UU}(\mathbf{q} + \mathbf{Q}, i\nu_m), \quad (30)$$

where the argument \mathbf{q} can now take on values in the full electron Brillouin zone. The submatrix determinant $\Theta(k)$ is given by

$$\Theta(k) = [i\omega_n Z(k)]^2 - \tilde{\xi}_k^2 - |\phi_{s,t}(k)|^2, \quad (31)$$

with anomalous correlation $\phi_{s,t}$ depending on whether we consider a singlet or triplet instability, and where we have introduced $\tilde{\xi}_k = \xi_k + \chi(k)$. In the following, we will assume that the quasiparticle energy shift χ is small compared to the electron bandwidth, and that it can be neglected. Note the opposite signs on the right hand side of the equations for ϕ_s and ϕ_t . This occurs because the spin flips in the vertices of the self-energy diagrams introduce a sign change for the spin singlet amplitude, but not for the spin triplet amplitude.

IV. FERMI SURFACE AVERAGED EQUATIONS

When the electron energy scale is large compared to the magnon energy scale, the regions close to the Fermi surface dominate the momentum sums in the Eliashberg equations. We assume that the quasiparticle renormalization field close to the Fermi surface is weakly dependent on momentum, so that we may write $Z(\mathbf{k}, i\omega_n) = Z(i\omega_n)$. Furthermore, for a single dominant pairing symmetry channel, we assume that the anomalous correlations can be written in the product form $\phi_{s,t}(\mathbf{k}, i\omega_n) = \psi(\mathbf{k})\phi_{s,t}(i\omega_n)$, where we assume some simple functional form $\psi(\mathbf{k})$ for the momentum dependence of

the relevant anomalous correlation.

Since we expect regions close to the Fermi surface to dominate the momentum sum, we may split it into a perpendicular and a parallel part, and neglect the perpendicular momentum dependence of the magnon propagator. Close to the critical temperature, one may furthermore linearize the Eliashberg equations in the anomalous correlations. Converting the perpendicular momentum integration into an energy integral, one then obtains

$$(1 - Z)i\omega_n = \frac{1}{\beta N_F} \sum_{\omega_{n'}} \lambda_1(i\omega_n - i\omega_{n'}) i\omega_{n'} Z' \int d\xi \frac{N(\xi)}{\Theta(\xi, i\omega_{n'})}, \quad (32a)$$

$$\phi_{s,t} = -\frac{1}{\beta N_F} \sum_{\omega_{n'}} \lambda_2^{s,t}(i\omega_n - i\omega_{n'}) \phi'_{s,t} \int d\xi \frac{N(\xi)}{\Theta(\xi, i\omega_{n'})}. \quad (32b)$$

We have here introduced the dimensionless electron-magnon coupling strength $\lambda_1(i\omega_n - i\omega_{n'})$ occurring in the quasiparticle renormalization equations and the modified coupling strength $\lambda_2^{s,t}(i\omega_n - i\omega_{n'})$ occurring in the anomalous correlation equations. We have further denoted $Z(k)$ by Z and $Z(k')$ by Z' , with similar notation also for the remaining fields, and denoted the electron density of states by $N(\xi)$, which takes on the value N_F at the Fermi level. The dimensionless coupling strengths are given by

$$\lambda_1(i\omega_n - i\omega_{n'}) = -\frac{V^2}{N_F} \sum_{\mathbf{k}\mathbf{k}'} \delta(\xi_{\mathbf{k}}) \delta(\xi_{\mathbf{k}'}) \mathcal{D}(k - k'), \quad (33)$$

$$\lambda_2^{s,t}(i\omega_n - i\omega_{n'}) = -\zeta_{s,t} \frac{1}{\langle \psi^2(\mathbf{k}) \rangle_{FS}} \frac{V^2}{N_F} \sum_{\mathbf{k}\mathbf{k}'} \delta(\xi_{\mathbf{k}}) \delta(\xi_{\mathbf{k}'}) \psi(\mathbf{k}) \mathcal{D}(k - k') \psi(\mathbf{k}'), \quad (34)$$

where $\zeta_s = -1$ for spin singlet and $\zeta_t = +1$ for spin triplet is the sign associated with a spin flip in the anomalous pairing. The brackets $\langle \rangle_{FS}$ denote a Fermi surface average.

In the following, we assume that the density of states can be approximated by a constant in the dominant region close to the Fermi surface. We may then perform the energy integral analytically to obtain

$$(1 - Z)i\omega_n = -\frac{i\pi}{\beta} \sum_{\omega_{n'}} \lambda_1(i\omega_n - i\omega_{n'}) \text{sgn}(\omega_{n'}), \quad (35)$$

$$\phi_{s,t} = +\frac{\pi}{\beta} \sum_{\omega_{n'}} \lambda_2^{s,t}(i\omega_n - i\omega_{n'}) \frac{\phi'_{s,t}}{|\omega_{n'} Z'|}. \quad (36)$$

We next assume that the magnon propagator \mathcal{D} can be replaced by the non-interacting propagator \mathcal{D}_0 . Solving the Eliashberg equations is then reduced to calculating dimensionless coupling strengths $\lambda_{1,2}$, and solving eigenvalue problems in the Matsubara frequencies. In Sec. VI, we investigate the effect of including the magnon self-energy.

In addition to introducing the dimensionless coupling strengths $\lambda_{1,2}$, we may follow the conventional routine and also introduce frequency dependent functions $\alpha_{1,2}^2 F(\omega)$ defined such that

$$\lambda_{1,2}(i\omega_n - i\omega_{n'}) = \int d\omega \alpha_{1,2}^2 F(\omega) \frac{2\omega}{(\omega_n - \omega_{n'})^2 + \omega^2}. \quad (37)$$

Comparing with the definition of $\lambda_{1,2}$, this gives

$$\alpha_1^2 F(\omega) = \frac{V^2}{N_F} \sum_{\mathbf{k}\mathbf{k}'} \delta(\xi_{\mathbf{k}}) \delta(\xi_{\mathbf{k}'}) \delta(\omega - \omega_{\mathbf{k}-\mathbf{k}'}) \mathcal{A}_e(\mathbf{k} - \mathbf{k}'), \quad (38)$$

$$\alpha_2^2 F(\omega) = \zeta_{s,t} \frac{1}{\langle \psi^2(\mathbf{k}) \rangle_{FS}} \frac{V^2}{N_F} \sum_{\mathbf{k}\mathbf{k}'} \delta(\xi_{\mathbf{k}}) \delta(\xi_{\mathbf{k}'}) \delta(\omega - \omega_{\mathbf{k}-\mathbf{k}'}) \psi(\mathbf{k}) \mathcal{A}_e(\mathbf{k} - \mathbf{k}') \psi(\mathbf{k}'), \quad (39)$$

where the boosting factor

$$\mathcal{A}_e(\mathbf{q}) = \theta_{\mathbf{q}} A_e^{RR}(\mathbf{q}) + \theta_{\mathbf{q}+\mathbf{Q}} A_e^{UU}(\mathbf{q} + \mathbf{Q}), \quad (40)$$

has been defined analogously to $\mathcal{D}(q)$.

The Eliashberg functions $\alpha_{1,2}^2 F(\omega)$ and the electron-magnon coupling strengths $\lambda_{1,2}(i\nu_m)$ are central quantities in the Fermi surface averaged Eliashberg equations. Through the approximate formula

$$T_c^{\text{AD}} = \frac{\omega_{\log}}{1.2} \exp\left(-\frac{1.04[1 + \lambda_1(0)]}{\lambda_2(0)}\right), \quad (41)$$

they can therefore be used to qualitatively understand the critical temperatures resulting from actually solving the Eliashberg equations. The above formula was suggested by Allen and Dynes [42] for weak and intermediate electron-boson coupling. We have set the Coulomb pseudo-potential to zero, and use the logarithmic average

$$\omega_{\log} = \omega_a \exp\left[\frac{2}{\lambda_2(0)} \int d\omega \ln\left(\frac{\omega}{\omega_a}\right) \frac{\alpha_2^2 F(\omega)}{\omega}\right] \quad (42)$$

as the effective cutoff frequency, where ω_a is an arbitrary frequency scale.

V. SOLVING THE ELIASHBERG EQUATIONS

We now solve the Fermi surface averaged equations using realistic material parameters, as detailed in Appendix E. We set $\Omega_A = 1$, and use $\Omega_B \equiv \Omega \in [0, 1]$ to tune the sublattice coupling asymmetry.

In order to compute the dimensionless coupling strengths $\lambda_{1,2}$, the momentum sums are transformed into integrals over

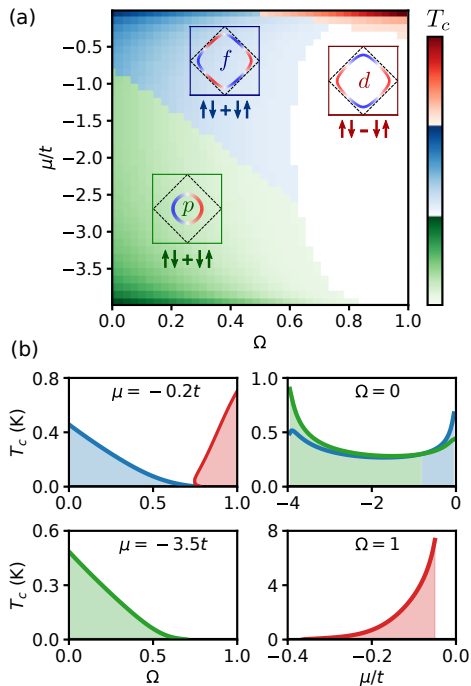


FIG. 4. (a) Phase diagram in terms of sublattice coupling asymmetry $\Omega = \Omega_B/\Omega_A$ and chemical potential μ below half filling. We find spin triplet p -wave, spin triplet f -wave, and spin singlet d -wave phases. The phase diagram is colored according to the critical temperature normalized to the largest value in the phase diagram within the same phase. Parameter regimes supporting multiple superconducting instabilities are colored according to the phase with the largest critical temperature. The insets show the spin structure and momentum structure on the Fermi surface for the various phases. The various subfigures in (b) show the critical temperature T_c as function of Ω (left) and μ (right) along different lines in the phase diagram.

momenta on the Fermi surface. The quasiparticle renormalization field $Z(i\omega_n)$ can then be calculated using Eq. (35). Subsequently, we use Eq. (36) to determine the critical temperature for the superconducting instability by finding the temperature for which the largest eigenvalue of the eigenvalue problem becomes 1 [43, 44]. This gives the critical temperature T_c of the superconducting instability. We consider three different Ansätze for the superconducting pairing, namely even frequency spin triplet p -wave pairing, even frequency spin triplet f -wave pairing and even frequency spin singlet d -wave pairing. These pairings dominate in different parts of the parameter space of our model. Other pairing symmetries like even frequency spin singlet s -wave and different odd frequency variants were not found to give rise to superconductivity. Fig. 4 (a) presents the phase diagram for our model in the Ω - μ -plane, where critical temperature normalized to the maximum value within each phase is indicated by

color intensity. The type of pairing is indicated by choice of color (green/blue/red), where regimes supporting multiple solutions are colored according to the phase with the largest critical temperature.

In the following, we discuss the different superconducting phases in the phase diagram in more detail.

A. Spin triplet p -wave and f -wave pairing

For the even frequency spin triplet p -wave and f -wave pairings, we consider anomalous pairing momentum dependence on the form

$$\psi_p(\mathbf{k}) = \cos \phi_{\mathbf{k}}, \quad (43a)$$

$$\psi_f(\mathbf{k}) = \cos 3\phi_{\mathbf{k}}, \quad (43b)$$

where $\phi_{\mathbf{k}}$ is the polar angle between the quasimomentum \mathbf{k} on the Fermi surface and the x -axis. These momentum dependencies are shown in the insets of the phase diagram.

As expected, and in agreement with the results of Ref. [21], we find even frequency spin triplet p -wave superconductivity for small Fermi surfaces and large sublattice coupling asymmetry, corresponding to small μ and Ω . For small Fermi surfaces, all processes between points on the Fermi surface are of the regular type. Since the magnon energy is smallest for small \mathbf{q} , minimizing the denominator of the magnon propagator, the dominant contribution to the momentum sums in the Eliashberg equations originate from small \mathbf{q} . Without sublattice coupling asymmetry (i.e. $\Omega = 1$), coherence factor interference effects suppress the boosting factor $A_i^{RR}(\mathbf{q})$, whereas $\Omega = 0$ removes these interference effects completely and makes p -wave superconductivity possible.

Setting $\Omega = 0$, we also find an even frequency spin triplet f -wave solution in the entire chemical potential range we have considered. As shown in Fig. 4 (b), the critical temperature of the p -wave solution is larger than the critical temperature of the f -wave solution for small Fermi surfaces. For Fermi surfaces approaching half filling, however, the situation is reversed due to emergence of subleading Umklapp processes. The interaction providing spin triplet pairing is attractive for scattering processes between \mathbf{k} and \mathbf{k}' only when $\phi(\mathbf{k}, i\omega_n)$ and $\phi(\mathbf{k}', i\omega_n)$ have the same sign. Consider now the scattering processes between points on the Fermi surface where the momentum transfer is closest to \mathbf{Q} , bringing the electron from one side of the Fermi surface to the opposing side. From the f -wave and p -wave momentum structure of the anomalous correlations shown in the insets of Fig. 4 (a), it is clear that these processes are always repulsive in the p -wave phase and typically attractive in the f -wave phase. This explains why the f -wave phase has a higher critical temperature than the p -wave phase upon approaching half-filling. As discussed in more detail in Sec. VIII, the combination of $\Omega = 0$ and the presence of Umklapp processes may, however, be challenging to access experimentally.

Compared with the results of Ref. [21], we find significantly lower critical temperatures for the p -wave phase.

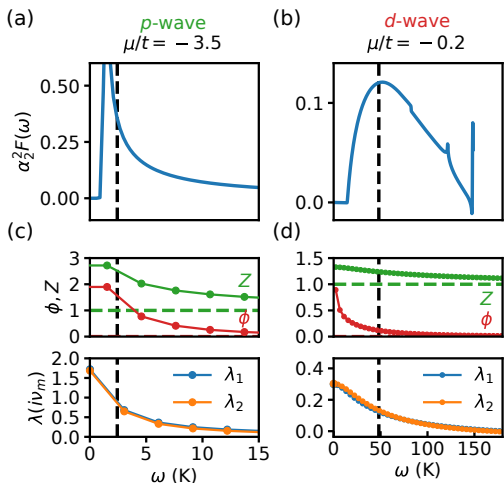


FIG. 5. Eliashberg functions and Eliashberg equation solutions for the p -wave regime ($\mu/t = -3.5$ and $\Omega = 0$) to the left and d -wave regime ($\mu/t = -0.2$ and $\Omega = 1$) to the right. Subfigures (a) and (b) show the Eliashberg function $\alpha_2^2 F(\omega)$. Subfigures (c) and (d) show the dimensionless electron-magnon coupling strengths $\lambda_{1,2}(i\nu_m)$ as well as the Matsubara frequency dependence of the quasiparticle renormalization $Z(i\omega_n)$ and the anomalous correlation $\phi(i\omega_n)$ at the critical temperatures for the respective superconducting instabilities. The logarithmic average ω_{\log} is shown with vertical dashed lines.

We attribute this difference to the magnon energy cutoff. As long-wavelength processes dominate, the characteristic magnon frequency in the pairing interaction is much smaller than the upper cutoff on the magnon spectrum. Since the characteristic frequency serves as the energy scale for the critical temperature, the critical temperature is then significantly reduced, which is captured in the Eliashberg theory analysis.

More quantitatively, this argument can be understood in terms of the Allen-Dynes formula of Eq. (41). Since the boosting factor $A_e^{RR}(\mathbf{q})$ is peaked for small momenta \mathbf{q} , and the electron-magnon coupling strength V is momentum-independent, the electron-magnon coupling function $\alpha_2^2 F(\omega)$ is peaked at small frequencies. This is shown in Fig. 5 (a), where the logarithmic average ω_{\log} is indicated with a dashed line. The effective magnon frequency for the superconducting pairing is therefore significantly reduced compared to the largest magnon frequency in the system. Further, the lower panel of Fig. 5 (b) shows $\lambda_{1,2}(i\nu_m)$, which decays quickly beyond the effective cutoff. Solving the Eliashberg equations gives the solutions for the anomalous correlation $\phi(i\omega_n)$, which also decays quickly beyond the cutoff, and the quasiparticle renormalization $Z(i\omega_n)$, which decays to 1.

B. Spin singlet d -wave pairing

In the Eliashberg equations, the difference between the spin triplet case in Eq. (29d) and the singlet case in Eq. (29c) is the sign. Thus, the small momentum process pairing potential that was attractive for spin triplet pairing becomes repulsive for spin singlet pairing. To obtain singlet pairing attraction, we therefore need to rely on dominant processes with a relative sign between the anomalous pairing $\phi_s(k)$ on the left-hand-side and right-hand-side of the equation. Since small momentum processes cannot provide this sign change, we need to rely on Umklapp processes. As an s -wave Ansatz does not change sign around the Fermi surface, we instead choose the d -wave Ansatz

$$\psi_d(\mathbf{k}) = \frac{1}{2\pi}(\cos k_x - \cos k_y), \quad (44)$$

shown in the inset of the phase diagram in Fig. 4 (a). Since the d -wave phase relies on Umklapp processes, it occurs for chemical potentials μ approaching half-filling in the phase diagram. Furthermore, the Umklapp processes benefit from the coherence factor interference in the boosting factor $A_e^{UU}(\mathbf{q})$, which is maximized for $\Omega = 1$. Crucially, these interferences also suppress the competing regular processes with small momentum \mathbf{q} , which would otherwise prevent spin singlet superconductivity. The d -wave phase therefore occurs only for large Ω in the phase diagram. This picture is also verified in Fig. 4 (b), which shows the critical temperature for the spin singlet d -wave phase as function of coupling asymmetry, and as function of chemical potential at $\Omega = 1$.

The electron-magnon coupling strength function $\alpha_2^2 F(\omega)$ is shown in Fig. 5 (b). With $\Omega = 1$, the regular small momentum processes are suppressed, and away from half-filling, the Umklapp processes between points on the Fermi surface require the magnons to carry momentum which differs from \mathbf{Q} by a finite amount. Therefore, $\alpha_2^2 F(\omega)$ takes on significant values only beyond a relatively large lower frequency cutoff. This cutoff corresponds to the magnon energy associated with the smallest momentum necessary to bring an Umklapp scattered electron with incoming momentum \mathbf{k} from $\mathbf{k} + \mathbf{Q}$ and back to the Fermi surface. Moreover, it should be noted that this smallest momentum depends on where on the Fermi surface the electron was situated to begin with. At the lowest relevant frequencies in $\alpha_2^2 F(\omega)$, only a few momenta \mathbf{k} bring $\mathbf{k} + \mathbf{Q}$ to a position where the momentum transfer necessary to get back to the Fermi surface is associated with a magnon energy that is small enough to match the frequency ω . The function $\alpha_2^2 F(\omega)$ then only obtains contributions from a few points \mathbf{k} that bring $\mathbf{k} + \mathbf{Q}$ close enough to the Fermi surface. As the frequency ω increases, $\alpha_2^2 F(\omega)$ obtains contributions from more points \mathbf{k} as the restriction on how close $\mathbf{k} + \mathbf{Q}$ needs to be to the Fermi surface is relaxed. Therefore, $\alpha_2^2 F(\omega)$ is not peaked at small frequencies. The situation should be contrasted with the p -wave case, where regular scattering on the Fermi surface with vanishing momentum is possible regardless of where on the Fermi surface the initial electron is situated. Denoting the magnon spectrum gap by

ω_0 , $\alpha_2^2 F(\omega \rightarrow \omega_0)$ therefore receives large contributions from $\mathbf{k} - \mathbf{k}' \approx 0$ regardless of where on the Fermi surface \mathbf{k} is situated.

The reduced reliance of the d -wave pairing on processes with small magnon energy gives rise to a larger effective magnon frequency ω_{log} . This larger characteristic magnon frequency suppresses the magnon propagator occurring in $\lambda_{1,2}(i\nu_m)$ for small Matsubara frequencies, but also increases the frequency scale over which the magnon propagator decays compared to the p -wave regime. Together with a large density of states close to half filling, this causes the significant critical temperatures that are observed for the d -wave regime in Fig. 4 (b). As shown in Fig. 5 (d), the dimensionless electron-magnon coupling strength $\lambda_{1,2}(i\nu_m)$ decays to zero beyond the effective cutoff frequency, whereas $\phi(i\omega_n)$ has a crossover from behaviour $1/\omega_n$ to $1/\omega_n^3$.

C. Effect of frustration

Since the superconductivity in our system relies on spin fluctuations, we expect interactions in the AFMI spin model that enhance fluctuations to also enhance the critical temperature. Earlier weak-coupling studies have investigated the effect of a frustrating next-nearest neighbor exchange coupling $J_2 > 0$ in the antiferromagnet on superconductivity dominated by regular fermion-magnon scattering processes [22, 23]. In Fig. 6 (a), we show how the critical temperature increases with J_2 for both the p -wave and d -wave instabilities. The effect of J_2 on the superconductivity can be understood in terms of the magnon excitation energies in Fig. 6 (b), showing that the magnon bands are flattened as J_2 increases. As displayed in Fig. 6 (c) and (d), this shifts weight from large to the more significant small frequencies in the electron-magnon coupling function $\alpha_2^2 F(\omega)$, leading to a higher critical temperature. Notably, increasing J_2 does not affect the gap in the magnon spectrum, meaning that the effective cutoff for the p -wave phase is not much affected. For the d -wave phase, the effective cutoff is somewhat reduced for larger J_2 , but trading some cutoff for a larger dimensionless coupling strength $\lambda_2(0)$ is nevertheless found to be beneficial. As the d -wave phase has a smaller dimensionless coupling strength than the p -wave phase, the increase of the dimensionless coupling strength arising from J_2 leads to a more dramatic increase in critical temperature for the d -wave curve in Fig. 6 (a).

VI. MAGNON RENORMALIZATION

To consider the effect of magnon renormalization, we consider the electron bubble diagram shown in Fig. 3, and once again neglect vertex corrections. Performing the S -matrix expansion, one may show that magnon propagators $D_{\gamma\gamma'}$ satisfy the Dyson equation

$$D^{-1}(q) = D_0^{-1}(q) - \Pi(q), \quad (45)$$

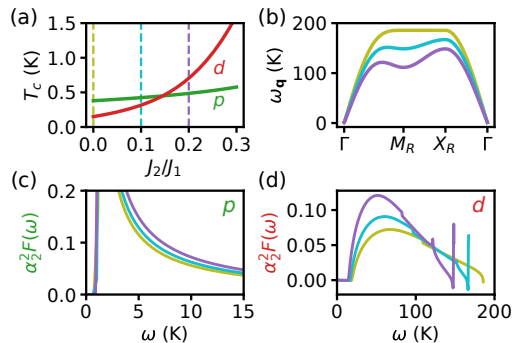


FIG. 6. Effect of frustrating the antiferromagnet with a next-nearest neighbour exchange coupling J_2 . (a) Critical temperature for the p -wave (at $\mu = -3.5t$ and $\Omega = 0$) and d -wave (at $\mu = -0.2t$ and $\Omega = 1$) instabilities as function of J_2 frustrating the antiferromagnet. (b) Magnon spectrum for different values of J_2 , as indicated by the vertical dashed lines in (a), between Brillouin zone high symmetry points as shown in Fig. 2 (a). (c) Electron-magnon coupling function $\alpha_2^2 F(\omega)$ in the p -wave regime. (d) $\alpha_2^2 F(\omega)$ in the d -wave regime. Frustration reduces the magnon excitation energies and enhance the spin fluctuations in the system. Thus, weight is shifted from high magnon energies to low magnon energies in the electron-magnon coupling function $\alpha_2^2 F(\omega)$, and this increases the critical temperature.

where the polarization matrix is given by

$$\Pi_{\gamma\gamma'}(q) = \frac{V^2}{4\beta} \sum_k \text{Tr} [g_\gamma G(k+q) g_{\gamma'} G(k)]. \quad (46)$$

From the matrix structure of the matrices g_γ , it follows that $\Pi_{\gamma\gamma'}$ takes the form

$$\Pi(q) = \begin{pmatrix} 0 & \Pi^{RR}(q) & 0 & \Pi^{RU}(q) \\ \Pi^{RR}(-q) & 0 & \Pi^{UR}(-q) & 0 \\ 0 & \Pi^{UR}(q) & 0 & \Pi^{UU}(q) \\ \Pi^{RU}(-q) & 0 & \Pi^{UU}(-q) & 0 \end{pmatrix}. \quad (47)$$

In principle, we should now solve the coupled equations for the electron and magnon propagators. However, to estimate the effect of magnon renormalization, we use the non-interacting electron Green's functions to calculate the polarizations. Using the previous assumption of neglecting terms in the electron Green's function which are off-diagonal in momentum sector, we may furthermore neglect the mixed process polarizations Π^{UR} and Π^{RU} . This leaves the regular and Umklapp polarizations Π^{RR} and Π^{UU} , which reduce to

$$\Pi_0^{RR}(q) = \frac{V^2}{\beta} \sum_k G_0^{11}(k+q) G_0^{22}(k), \quad (48)$$

$$\Pi_0^{UU}(q) = \frac{V^2}{\beta} \sum_k G_0^{11}(k+q+Q) G_0^{22}(k), \quad (49)$$

where G_0^{11} and G_0^{22} are matrix elements in the non-interacting electron Green's function G_0 corresponding to different spins.

Solving the Dyson equation for the magnon propagator, one may show that the regular and Umklapp propagators become

$$\mathcal{D}^{RR}(q) = \left[\left(\frac{1 - \mathcal{D}_0^{UU} \Pi_0^{UU}}{1 - r \mathcal{D}_0^{UU} \Pi_0^{UU}} \right) - \mathcal{D}_0^{RR} \Pi_0^{RR} \right]^{-1} \mathcal{D}_0^{RR}(q), \quad (50)$$

$$\mathcal{D}^{UU}(q) = \left[\left(\frac{1 - \mathcal{D}_0^{RR} \Pi_0^{RR}}{1 - r \mathcal{D}_0^{RR} \Pi_0^{RR}} \right) - \mathcal{D}_0^{UU} \Pi_0^{UU} \right]^{-1} \mathcal{D}_0^{UU}(q), \quad (51)$$

where we have introduced the quantity

$$r(q) = 1 - \frac{A_e^{UR}(q) A_e^{RU}(q)}{A_e^{RR}(q) A_e^{UU}(q)}. \quad (52)$$

Here, the Umklapp polarization occurs in the regular propagator and vice versa due to the presence of mixed magnon propagators.

We note that in the special case $\Omega = 0$ where we found spin triplet pairing, we have $r = 0$ since all the boosting factors are equal. In the opposite limit of $\Omega = 1$ where we found spin singlet d -wave pairing approaching half-filling, the mixed propagators vanish, so that $r = 1$ and each of the two magnon propagators $\mathcal{D}^{\kappa\kappa}(q)$ are just renormalized by the corresponding polarization $\Pi^{\kappa\kappa}(q)$.

We may now calculate the regular and the Umklapp polarizations. Performing the Matsubara frequency sums in Eqs. (48) and (49), we obtain the standard result

$$\Pi_0^{RR}(\mathbf{q}, i\nu_m) = V^2 \sum_{\mathbf{p}} \left(\frac{n_F(\xi_{\mathbf{p}}) - n_F(\xi_{\mathbf{p}+\mathbf{q}})}{i\nu_m + \xi_{\mathbf{p}} - \xi_{\mathbf{p}+\mathbf{q}}} \right), \quad (53)$$

$$\Pi_0^{UU}(\mathbf{q}, i\nu_m) = V^2 \sum_{\mathbf{p}} \left(\frac{n_F(\xi_{\mathbf{p}}) - n_F(\xi_{\mathbf{p}+\mathbf{q}+\mathbf{Q}})}{i\nu_m + \xi_{\mathbf{p}} - \xi_{\mathbf{p}+\mathbf{q}+\mathbf{Q}}} \right), \quad (54)$$

where the momentum sums are evaluated in the thermodynamic limit through numerical integration [45]. Using that $\xi_{\mathbf{p}} = \xi_{-\mathbf{p}}$, one may show that the imaginary part of the polarization vanishes, so that only the real part remains.

For $\Omega = 0$ and a small Fermi surface, the relevant processes are regular processes. The renormalization of the regular propagator then depends on $\Pi_0^{R+U}(\mathbf{q}, i\nu_m) \equiv \Pi_0^{RR}(\mathbf{q}, i\nu_m) + \Pi_0^{UU}(\mathbf{q}, i\nu_m)$, where the Umklapp polarization Π_0^{UU} is small. In Fig. 7 (a) we present the polarization $\Pi_0^{R+U}(\mathbf{k} - \mathbf{k}', i\nu_m)$ together with the contributions to $\lambda_2(i\nu_m = 0)$ from the various momenta \mathbf{k}' on the Fermi surface given incoming electron momentum \mathbf{k} as shown in the inset. The dominant contributions to $\lambda_2(i\nu_m = 0)$ arise from $\theta \approx 0$, which corresponds to scattering processes with small momentum $\mathbf{q} = \mathbf{k} - \mathbf{k}'$. In this region, the zero frequency polarization is more or less constant. Consistent with what

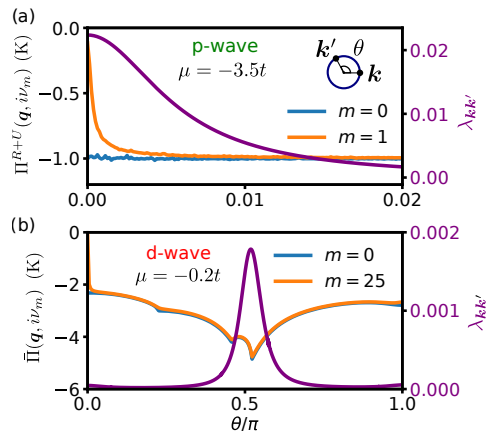


FIG. 7. Polarization renormalizing the magnon propagator for magnon scattering momenta \mathbf{q} between points \mathbf{k} and \mathbf{k}' on the Fermi surface, corresponding to angles 0 and θ , as shown in the inset of (a). The relative contributions $\lambda_{\mathbf{k}\mathbf{k}'}$ from the various points on the Fermi surface to $\lambda_2(i\nu_m = 0)$ is shown in purple. (a) shows the combined polarization $\Pi_0^{R+U}(\mathbf{q}, i\nu_m)$ and the contributions to $\lambda_2(0)$ for $\mu/t = -3.5$ and $\Omega = 0$, where we expect p -wave superconductivity. The dominant contributions to $\lambda_2(0)$ come from small momentum processes close to $\theta = 0$. (b) shows the polarization $\bar{\Pi}(\mathbf{q}, i\nu_m)$, corresponding to Π^{RR} when $\mathbf{k} - \mathbf{k}' = \mathbf{q}$ is inside, and Π^{UU} when $\mathbf{k} - \mathbf{k}' = \mathbf{q}$ is outside the reduced Brillouin zone. Dominant contributions to $\lambda_2(0)$ come from Umklapp processes in vicinity to $\mathbf{k} - \mathbf{k}' = \mathbf{Q}$. The temperature has been set to $T = 1$ K in both subfigures.

we expect from Eq. (53), the finite frequency polarizations approach zero as $\mathbf{q} \rightarrow 0$. The region where the finite frequency polarizations deviate significantly from the zero frequency polarization is, however, small compared to the region over which we expect the dominant contributions to λ_2 [46]. Hence we may approximate the polarization for $\Omega = 0$ and small Fermi surface by a constant value $\Pi_C \approx \Pi_0^{RR}(\mathbf{q} \rightarrow 0, i\nu_m = 0) = -N_F V^2$.

For $\Omega = 1$, the regular and Umklapp propagators are simply renormalized by the regular and Umklapp polarizations, respectively. Fig. 7 (b) therefore presents the polarization $\bar{\Pi}_0(\mathbf{q}, i\nu_m) \equiv \theta_{\mathbf{q}} \Pi_0^{RR}(\mathbf{q}, i\nu_m) + \theta_{\mathbf{q}+\mathbf{Q}} \Pi_0^{UU}(\mathbf{q} + \mathbf{Q}, i\nu_m)$, which is relevant for the d -wave phase. Also shown are the contributions to $\lambda_2(i\nu_m = 0)$ as in Fig. 7 (a). The polarization is now weakly dependent on frequency, but it varies somewhat with momentum in the relevant region. Qualitatively, it should also in this case be possible to extract the effect of magnon renormalization by setting the polarization to a constant value.

In the following, we consider the same two special cases as above. For $\Omega = 0$ and large doping, where we found p -wave superconductivity, the relevant magnon propagator is $\mathcal{D}^{RR}(q)$, which can be written

VII. DISCUSSION

$$\mathcal{D}^{RR}(q) = -\frac{4\omega_{\mathbf{q}}A_e^{RR}(\mathbf{q})}{\nu_m^2 + \omega_{\mathbf{q}}^2 + 4\omega_{\mathbf{q}}A_e^{RR}(\mathbf{q})\Pi_C}. \quad (55)$$

Thus, the magnon frequency in the denominator has been replaced by an effective magnon frequency $\omega_{\mathbf{q}}^{\text{eff}}$, given by

$$(\omega_{\mathbf{q}}^{\text{eff}})^2 = \omega_{\mathbf{q}}^2 + 4\omega_{\mathbf{q}}A_e^{RR}(\mathbf{q})\Pi_C. \quad (56)$$

Since the polarization is negative, the effective magnon frequency may turn imaginary, indicating that it is no longer reasonable to start out from a Néel ordered state. At $\mathbf{q} = 0$, where the magnon energy is the smallest, it happens for

$$|\Pi_C| \geq 2KS \left(\frac{1 + K/2z_1 J_1}{1 + K/z_1 J_1} \right), \quad (57)$$

where z_1 is the number of nearest neighbors.

For $\Omega = 1$ and large Fermi surface, where we found d -wave superconductivity, the two relevant propagators \mathcal{D}^{RR} and \mathcal{D}^{UU} are given by

$$\mathcal{D}^{\kappa\kappa}(q) = -\frac{4\omega_{\mathbf{q}}A_e^{\kappa\kappa}(\mathbf{q})}{\nu_m^2 + \omega_{\mathbf{q}}^2 + 4\omega_{\mathbf{q}}A_e^{\kappa\kappa}(\mathbf{q})\Pi_0^{\kappa\kappa}}, \quad (58)$$

with $\kappa \in \{R, U\}$. Similar to the previous special case, we may now introduce an effective magnon frequency. Since the unrenormalized magnon frequency is the smallest for $\mathbf{q} = 0$ and the regular boosting factor $A_e^{\kappa\kappa}(\mathbf{q} = 0)$ is suppressed due to coherence factor interference, we expect that the effective magnon frequency may primarily turn imaginary for Umklapp processes close to $\mathbf{q} = 0$. One may show that this happens for

$$\left| \Pi_0^{UU} \right| \geq \frac{1}{2}KS. \quad (59)$$

Although the coupling to the electrons may therefore in principle destroy the magnetic order in the antiferromagnet, unsurprisingly, this does not happen as long as the easy axis anisotropy is sufficiently large compared to the polarization.

A picture now emerges where the easy-axis anisotropy and the magnon renormalization play opposite roles stabilizing and destabilizing the magnetic order in the antiferromagnet, respectively. Retaining magnetic order upon inclusion of magnon renormalization requires a larger easy axis anisotropy. The larger easy axis anisotropy has little effect on the numerator of the magnon propagator, but shifts the square of the magnon energies in the denominator upwards by an almost constant value with respect to momentum when J_2/J_1 is small. By choice of the easy-axis anisotropy, the effect of the magnon renormalization on the effective magnon frequencies can then be compensated. Superconductivity may therefore still occur at critical temperatures similar to those obtained by disregarding magnon renormalization.

The Eliashberg equation solutions in this paper are obtained using Fermi surface averaged equations, thus neglecting the dependence of the magnon propagator and the fields appearing in the Eliashberg equations on momentum perpendicular to the Fermi surface. The justification for this is as follows: Although the magnon propagator is momentum dependent, the behaviour of the right-hand-side of the Eliashberg equations when moving \mathbf{k}' away from the Fermi surface is still dominated by the suppression arising from the fermion energies in the denominator due to the large energy scale of the electrons. In this case there are additional variations arising from the momentum dependence of the magnon propagator. Thus, a possible avenue for further work could be to take the full momentum dependence in the Eliashberg equations into account in order to test the accuracy of our approximation.

The results also rely on vertex corrections being small, so that the series of vertex diagrams can be cut off after the zeroth-order contribution. For phonon-mediated superconductivity, the smallness of the higher-order vertex diagrams is ensured by Migdal's theorem [47], which states that higher-order diagrams are smaller by a factor ω_E/E_F , where ω_E is a characteristic phonon frequency. Migdal's theorem is however known to break down for long-wavelength phonons [47, 48] and in systems with strong Fermi surface nesting [49–51]. Moreover, for reduced spatial dimensionality, the reduction of the higher-order diagrams should be expected to be less dramatic [51, 52]. As the superconductivity studied in this work relies on long-wavelength magnons and/or a two-dimensional Fermi surface close to half-filling, it then seems plausible that vertex corrections could be of importance. A discussion of the effect of vertex corrections in the present system is presented in Appendix D. For large doping, we find that vertex corrections can become of relevant magnitude, but that the region in momentum space where the corrections are large might be small enough to limit their effect. Exactly at half-filling, the vertex corrections are expected to be quite large, but their effect can be reduced by moving away from half-filling.

Upon approaching half-filling, we would also at some point expect on-set of spin density wave correlations. Exactly at half-filling, one may straightforwardly generalize the above Eliashberg theory to accommodate the expected commensurate spin density wave instability. Previously, this has been done for the phonon-induced instability [53]. Below half filling, the commensurate wave-vector \mathbf{Q} does not connect points on the Fermi surface. We therefore expect the commensurate spin density wave to be suppressed relative to superconductivity due to the large electronic energy for processes between states which are not on the Fermi surface. However, we may still have incommensurate spin density waves, which are far more challenging to investigate theoretically. In this paper, we have been investigating the properties of the superconducting phases, and the highly non-trivial interplay between superconducting and spin density wave orders that we could potentially obtain is beyond the scope of the present study.

Another effect that could be included is the effect of the

quasiparticle energy shift χ . For the present system, χ was found to be small compared to the Fermi energy for chemical potentials ranging from half-filling and down towards the vicinity of the bottom of the band. Apart from the limit where the Fermi level approaches the bottom of the band, inclusion of χ would typically amount to a small, weakly frequency-dependent, shift of the effective chemical potential in the Eliashberg equations, and it was therefore neglected in the presented calculations.

The effect of Coulomb interactions on the electron self-energy is in general challenging to calculate [48]. Their effect on the Fermi surface averaged Eliashberg equations for the anomalous pairing amplitudes is typically included by neglecting vertex corrections and including an extra repulsive and frequency-independent potential in the equations. The Coulomb repulsion will then have a limited effect on the critical temperatures as long as $\lambda_2(i\nu_m = 0)$ is somewhat larger than the Coulomb pseudopotential μ^* [48]. Moreover, taking the Coulomb interaction to be momentum independent, its contributions to the gap equation will cancel for unconventional pairing symmetries like the ones considered in this work. For a momentum dependent Coulomb potential, the Coulomb contributions to the gap equation no longer cancel identically for unconventional pairing symmetries, but μ^* will still be reduced compared to the s -wave case.

In the system setup we have considered, the antiferromagnetic order and interfacial coupling to the two antiferromagnets has been chosen such that any magnetic fields cancel. If we instead consider a single antiferromagnetic layer and $\Omega \neq 1$, there would be a net magnetic field, as shown in Eqs. (B1c) and (B1d). In addition, there would also be a term in the magnon propagator that is odd in frequency, as shown in Eq. (B4). The odd part of the propagator would renormalize and reduce the magnetic field h , and produce an effective magnetic field \tilde{h} . Together with the odd part of the propagator, this effective magnetic field could in principle give rise to an exotic coexistence of odd- and even frequency superconductivity [54]. For the experimentally most relevant parameters, we would however expect the magnetic field to be too strong to give significant critical temperatures.

We also note that a previously studied system consisting of a normal metal sandwiched between two ferromagnetic insulators [18] gives rise to a p -wave phase that bears many similarities with the p -wave phase considered in the present study. The main difference between the two systems is the absence of the magnon coherence factors in the ferromagnetic case. The numerator of the magnon propagator (or effective potential in a weak-coupling framework) for the ferromagnet therefore scales as $\omega_q^{FM} \sim K$ for long-wavelength magnons, while the numerator of the magnon propagator for the antiferromagnet scales as $A_e^{RR}(\mathbf{q})\omega_q \sim J_1$. For superconductivity dominated by long-wavelength magnons, with $K/J_1 \ll 1$, the dimensionless electron-magnon coupling $\lambda_2(i\nu_m = 0)$ may however still be of the same magnitude in both cases, corresponding to similar dimensionless coupling constants in a weak-coupling framework. This is because the ferromagnet propagator can simply rely on having a smaller gap in the magnon spectrum, making the denominator of the propaga-

tor smaller for the long-wavelength processes. As the critical temperature in a simple weak-coupling framework only depends on the dimensionless coupling constant and the cutoff on the boson spectrum, sizeable critical temperatures can then be obtained for both ferromagnets and antiferromagnets. Within an Eliashberg framework, on the other hand, the effective cutoff frequency is determined by the characteristic magnon energies in the pairing interaction. Since, with ferromagnets, the large values for $\lambda_2(i\nu_m = 0)$ were obtained by relying on smaller magnon energies in the denominator of the propagator, the effective frequency cutoff will be smaller, and the critical temperatures obtainable with ferromagnets should be smaller than with antiferromagnets.

In the current antiferromagnetic case, magnon renormalization was found to have little effect on the available critical temperatures. This is because the larger easy axis anisotropy K , required to protect magnetic order in the AFMIs, is compensated by the magnon energy renormalization in the denominator of the propagator. The larger easy-axis anisotropy has little effect on the numerator of the propagator. For the case of the ferromagnet, on the other hand, increasing K so that it compensates the renormalization would also lead to a larger numerator in the propagator. Magnon renormalization could then open the way for slightly higher critical temperatures.

VIII. EXPERIMENTAL CONSIDERATIONS

The model employed in this study allows us to tune the interfacial coupling between the normal metal and the two different sublattices of the antiferromagnet independently. In principle, such a general asymmetric coupling could be engineered, as discussed in the introduction. However, the experimentally most promising route to realizing superconductivity in systems well described by our model appears to be through fully compensated and uncompensated interfaces, where the conduction band electrons in the normal metal are coupled to only one AFMI sublattice ($\Omega = 0$), or equally to both AFMI sublattices ($\Omega = 1$). There is however a significant difference between our model and the intended realization with an uncompensated interface for the case $\Omega = 0$. In the intended realization, the square lattice of the normal metal matches the exposed sublattice of the antiferromagnet, and not the square lattice of the antiferromagnet itself, as in our model. Thus, the electron Brillouin zone coincides with the Brillouin zone of the antiferromagnet. Although it is possible to imagine a compensated interface where the magnons at the interface live in a smaller Brillouin zone than the electrons, this would not be the typical case.

Within our model, Umklapp processes are included for both $\Omega = 0$ and $\Omega = 1$. In the intended realization for $\Omega = 0$, however, Umklapp processes are absent. For a small Fermi surface, the effect of Umklapp processes in our model is small, since all processes between points on the Fermi surface are of the regular type. The p -wave phase we expect for uncompensated interfaces and large doping is therefore well represented by our model. For small doping, however, the f -wave phase of our model takes precedence over the p -wave phase pre-

cisely because of the Umklapp processes. The f -wave phase is therefore of less experimental relevance, and we expect that the p -wave phase would dominate regardless of doping for a normal metal sandwiched between two uncompensated interfaces.

For the p -wave phase with $\Omega = 0$, having a trilayer heterostructure in order to cancel all magnetic fields seems necessary, as the critical temperature is significantly reduced compared to previous predictions [21]. For the d -wave phase with $\Omega = 1$, the result of coupling to a single antiferromagnet would lead to the presence of a staggered field. As a staggered field might be less detrimental to superconductivity than a uniform spin-splitting [55], a bilayer heterostructure might be a viable option in this case.

When it comes to choice of parameters, it is clear that a strategy of simply taking a very small gap in the magnon spectrum in order to increase the dimensionless coupling strength $\lambda_2(0)$ has its limitations, as this leads to a very small effective cutoff frequency and slow increase in critical temperature with dimensionless coupling strength. In order to realize superconductivity in this system it is then essential that the constant prefactor that appears in the gap equation is sufficiently large. A sizeable interfacial exchange coupling and electron density of states is then preferable. Moreover, as the effective induced interaction experienced by the electrons in the normal metal might be reduced with the thickness of the normal metal [18], the metallic layer should be kept quite thin.

The easy-axis anisotropy governs the size of the gap in the magnon spectrum, and appears to play a crucial role in realizing superconductivity. A sufficiently large gap in the magnon spectrum could be important for both the p -wave and d -wave phases in order to stabilize the antiferromagnet. The p -wave phase does, however, rely more heavily on fine-tuning of the easy-axis anisotropy in order to produce a nonzero, but sufficiently small, effective magnon gap producing a sizeable critical temperature. This could make the p -wave phase more difficult to realize experimentally. The d -wave pairing receives contributions from a wider range of magnon energies, and the critical temperature is therefore more robust to a shift of the magnon energies. For larger Fermi surfaces, a larger easy-axis anisotropy is however needed to preserve magnetic order in the antiferromagnet, which could in itself be an experimental complication. However, using a magnetically more stable three-dimensional antiferromagnet instead of the two-dimensional magnet considered in our model, could potentially lead to a reduction in the easy-axis anisotropy required to stabilize the magnets.

In contrast to earlier results, the present study indicates that the d -wave phase may be able to produce higher critical temperatures than the p -wave phase. However, the d -wave phase is, in our model, dependent on proximity to half-filling, where it e.g. needs to compete with spin-density wave order. This competition may push the superconducting phase down towards lower filling-fractions associated with lower critical temperatures. It should also be noted that since the d -wave phase relies on Umklapp processes, it is more sensitive to the detailed structure of the Fermi surface. In comparison with the p -wave phase, the d -wave phase may therefore place

stricter requirements on the electron band structure of the normal metal in the experimental realization. Compared with the third option of coupling to ferromagnetic insulators, however, both phases considered in the present study seem more promising.

IX. SUMMARY

We use Eliashberg theory to study interfacially induced magnon-mediated superconductivity in a normal metal-antiferromagnet heterostructure. For large doping and uncompensated antiferromagnetic interfaces, we find p -wave superconductivity, while for small doping and compensated antiferromagnetic interfaces, we find d -wave superconductivity. This can be understood in terms of sublattice interferences suppressing and enhancing scattering processes in the system. Although the qualitative results are in accordance with earlier weak-coupling studies, the critical temperature achievable for the p -wave phase is found to be significantly reduced as the characteristic magnon frequency in the pairing interaction is much smaller than the cutoff on the magnon spectrum. The d -wave phase, on the other hand, is found to rely less on long-wavelength magnons and can therefore potentially produce larger critical temperatures when approaching half-filling. Close to half-filling the d -wave instability may however have to compete with a spin-density wave instability, potentially reducing the available critical temperatures. A sufficiently large gap in the magnon spectrum might be necessary to stabilize the magnetic order in the antiferromagnets due to feedback from the electrons, but this is found to have limited effect on the critical temperatures.

X. ACKNOWLEDGEMENTS

We acknowledge useful discussions with J.W. Wells. We acknowledge financial support from the Research Council of Norway Grant No. 262633 “Center of Excellence on Quantum Spintronics” and Grant No. 250985, “Fundamentals of Low-dissipative Topological Matter”.

Appendix A: Antiferromagnetic magnons

Starting from the AFMI Hamiltonian, we introduce the linearized Holstein-Primakoff transformation [56]

$$S_{i \in A, H}^+ = \sqrt{2S} a_{iH} \quad S_{i \in A, L}^+ = \sqrt{2S} a_{iL}^\dagger \quad (\text{A1a})$$

$$S_{j \in B, H}^+ = \sqrt{2S} b_{jH}^\dagger \quad S_{j \in B, L}^+ = \sqrt{2S} b_{jL} \quad (\text{A1b})$$

$$S_{i \in A, H}^- = \sqrt{2S} a_{iH}^\dagger \quad S_{i \in A, L}^- = \sqrt{2S} a_{iL} \quad (\text{A1c})$$

$$S_{j \in B, H}^- = \sqrt{2S} b_{jH} \quad S_{j \in B, L}^- = \sqrt{2S} b_{jL}^\dagger \quad (\text{A1d})$$

$$S_{i \in A, H}^z = S - a_{iH}^\dagger a_{iH} \quad S_{i \in A, L}^z = -S + a_{iL}^\dagger a_{iL} \quad (\text{A1e})$$

$$S_{j \in B, H}^z = -S + b_{jH}^\dagger b_{jH} \quad S_{j \in B, L}^z = S - b_{jL}^\dagger b_{jL}, \quad (\text{A1f})$$

where we have assumed oppositely aligned antiferromagnetic order in the spin space z -direction for the two antiferromagnets.

Inserting this into the AFMI Hamiltonian and expressing it in terms of sublattice magnon Fourier modes $a_{q\eta}$ and $b_{q\eta}$, the AFMI Hamiltonian takes the form

$$H_{\text{AFMI}} = \sum_{q, \eta} C_q (a_{q\eta}^\dagger a_{q\eta} + b_{q\eta}^\dagger b_{q\eta}) + D_q (a_{q\eta} b_{-q\eta} + a_{q\eta}^\dagger b_{-q\eta}^\dagger), \quad (\text{A2})$$

where C_q and D_q are given by

$$C_q = 2z_1 J_1 S - 2z_2 J_2 S (1 - \tilde{\gamma}_q) + 2KS, \quad (\text{A3a})$$

$$D_q = 2z_1 J_1 S \gamma_q, \quad (\text{A3b})$$

and we have defined

$$\gamma_q = \frac{1}{z_1} \sum_{\delta_1} e^{iq \cdot \delta_1}, \quad \tilde{\gamma}_q = \frac{1}{z_2} \sum_{\delta_2} e^{iq \cdot \delta_2}. \quad (\text{A4})$$

Here, z_1 and z_2 are the number of nearest and next-nearest neighbour vectors, which are summed over and denoted by δ_1 and δ_2 . The Hamiltonian is diagonalized through the Bogoliubov transform

$$a_{q\eta} = u_q \alpha_{q\eta} + v_q \beta_{-q\eta}^\dagger, \quad (\text{A5a})$$

$$b_{-q\eta}^\dagger = u_q \beta_{-q\eta}^\dagger + v_q \alpha_{q\eta}, \quad (\text{A5b})$$

where the coherence factors u_q and v_q can be written as

$$u_q = \cosh \theta_q, \quad v_q = \sinh \theta_q, \quad (\text{A6})$$

in terms of the hyperbolic angle

$$\theta_q = -\frac{1}{2} \tanh^{-1} \left(\frac{D_q}{C_q} \right). \quad (\text{A7})$$

The resulting magnon spectrum is

$$\omega_q = \sqrt{C_q^2 - D_q^2}. \quad (\text{A8})$$

By expressing the inverse hyperbolic tangent in terms of a logarithm, one may show the relations

$$u_q^2 + v_q^2 = +C_q / \omega_q, \quad (\text{A9a})$$

$$2u_q v_q = -D_q / \omega_q, \quad (\text{A9b})$$

for the coherence factor combinations which appear in the magnon propagator.

Whereas u_q is positive, v_q is typically negative. Furthermore, we notice that when K and J_2 are small compared to J_1 , $|\theta_q|$ becomes large when $q \rightarrow 0$, as D_q approaches C_q . This causes u_q to grow large and positive and v_q to grow large and negative in this limit.

Appendix B: Interfacial coupling Hamiltonian

In the main text, we presented expressions for the interfacial coupling and the magnon propagators under the assumption that the two antiferromagnets couple to the normal metal with equal strength. In this appendix, we generalize the results beyond this assumption.

The interfacial coupling Hamiltonian describing the coupling to a single antiferromagnetic insulator labelled by η can be written $H_{\text{int}}^\eta = H_{\text{int}}^{h, \eta} + H_{\text{int}}^{v, \eta}$, where the magnetic exchange field contributions $H_{\text{int}}^{h, \eta} = H_{\text{int}}^{h, A, \eta} + H_{\text{int}}^{h, B, \eta}$ from the two sublattices are

$$H_{\text{int}}^{h, A, H} = -\bar{J} \Omega_A^H S \sum_{\mathbf{k} \in \square, \sigma} \sigma \left(c_{\mathbf{k}\sigma}^\dagger c_{\mathbf{k}\sigma} + c_{\mathbf{k}+\mathbf{Q}, \sigma}^\dagger c_{\mathbf{k}\sigma} \right), \quad (\text{B1a})$$

$$H_{\text{int}}^{h, B, H} = +\bar{J} \Omega_B^H S \sum_{\mathbf{k} \in \square, \sigma} \sigma \left(c_{\mathbf{k}\sigma}^\dagger c_{\mathbf{k}\sigma} - c_{\mathbf{k}+\mathbf{Q}, \sigma}^\dagger c_{\mathbf{k}\sigma} \right), \quad (\text{B1b})$$

$$H_{\text{int}}^{h, A, L} = +\bar{J} \Omega_A^L S \sum_{\mathbf{k} \in \square, \sigma} \sigma \left(c_{\mathbf{k}\sigma}^\dagger c_{\mathbf{k}\sigma} + c_{\mathbf{k}+\mathbf{Q}, \sigma}^\dagger c_{\mathbf{k}\sigma} \right), \quad (\text{B1c})$$

$$H_{\text{int}}^{h, B, L} = -\bar{J} \Omega_B^L S \sum_{\mathbf{k} \in \square, \sigma} \sigma \left(c_{\mathbf{k}\sigma}^\dagger c_{\mathbf{k}\sigma} - c_{\mathbf{k}+\mathbf{Q}, \sigma}^\dagger c_{\mathbf{k}\sigma} \right), \quad (\text{B1d})$$

and where the exchange coupling strengths $\bar{J} \Omega_\gamma^\eta$ are in general different for the two antiferromagnets. Coupling to only one antiferromagnet can be realized by e.g. setting $\Omega_\Gamma^L = 0$. Assuming $\Omega_\Gamma^H = \Omega_\Gamma^L$, however, all magnetic fields cancel.

The electron-magnon interaction is given by

$$H_{\text{int}}^{V, \eta} = V \sum_{\substack{\mathbf{k} \in \square \\ \mathbf{q} \in \diamond}} \left[M_{q\eta}^R c_{\mathbf{k}+\mathbf{q}, \downarrow}^\dagger c_{\mathbf{k}, \uparrow} + M_{q\eta}^U c_{\mathbf{k}+\mathbf{q}+\mathbf{Q}, \downarrow}^\dagger c_{\mathbf{k}, \uparrow} + (M_{-q\eta}^R)^\dagger c_{\mathbf{k}+\mathbf{q}, \uparrow}^\dagger c_{\mathbf{k}, \downarrow} + (M_{-q\eta}^U)^\dagger c_{\mathbf{k}+\mathbf{q}+\mathbf{Q}, \uparrow}^\dagger c_{\mathbf{k}, \downarrow} \right], \quad (\text{B2})$$

where we have defined magnon operators $M_{q\eta}^\kappa$ associated with the antiferromagnet η as

$$M_{qH}^\kappa = \Omega_A^H a_{qH} + \kappa \Omega_B^H b_{-qH}^\dagger, \quad (\text{B3a})$$

$$M_{qL}^\kappa = \Omega_A^L a_{-qL}^\dagger + \kappa \Omega_B^L b_{qL}, \quad (\text{B3b})$$

so that the operator M_q^κ introduced in the main text is given by $M_q^\kappa = M_{qH}^\kappa + M_{qL}^\kappa$. Expressing the magnon operators in terms of the eigenmagnon operators resulting from the Bogoliubov transformation, the corresponding magnon propagators are

$$\begin{aligned} \mathcal{D}_{0,\eta}^{\kappa\kappa'}(\mathbf{q}, i\omega_n) = & -A_{e,\eta}^{\kappa\kappa'}(\mathbf{q}) \frac{2\omega_{\mathbf{q}}}{\omega_n^2 + \omega_{\mathbf{q}}^2} \\ & -A_{o,\eta}^{\kappa\kappa'} \frac{2i\omega_n}{\omega_n^2 + \omega_{\mathbf{q}}^2}. \end{aligned} \quad (\text{B4})$$

Here, the first term is even under the three-vector transformation $q \rightarrow -q$, and the second term is odd. The expressions for $A_{e,\eta}^{\kappa\kappa'}(\mathbf{q})$ can be obtained from Eq. (10) in the main text by the simple generalization $A_{e,\eta}^{\kappa\kappa'}(\mathbf{q}) \rightarrow A_{e,\eta}^{\kappa\kappa'}(\mathbf{q})$ and $\Omega_T \rightarrow \Omega_\eta^T$. The odd part prefactor $A_{o,\eta}^{\kappa\kappa'}$ is q -independent, and given by

$$A_{o,\eta}^{\kappa\kappa'} = \frac{1}{2}\eta \left[(\Omega_A^\eta)^2 - \kappa\kappa' (\Omega_B^\eta)^2 \right], \quad (\text{B5})$$

where we associate the index η with the values $H \rightarrow 1$ and $L \rightarrow -1$. We notice that the odd part of the propagator has different signs for the two antiferromagnets, so that their contributions cancel out when we couple equally to the two antiferromagnets.

Appendix C: Suppression of electron correlations which are off-diagonal in momentum

In this appendix, we argue that terms in the electron Green's function which are off-diagonal in momentum are suppressed as long as the electron propagator renormalization is small compared to the difference in electron energies at the momenta \mathbf{k} and $\mathbf{k} + \mathbf{Q}$.

The self-energy is in general an 8×8 matrix in the momentum, particle/hole, and spin degrees of freedom. The self-energy can then be written

$$\Sigma = \begin{pmatrix} \Sigma_{11} & \Sigma_{12} \\ \Sigma_{21} & \Sigma_{22} \end{pmatrix}, \quad (\text{C1})$$

where Σ_{ij} is now a 4×4 submatrix in the particle/hole and spin degrees of freedom corresponding to momentum sector (i, j) . The self-energy is related to the Green's function through the Dyson equation, so that

$$G^{-1}(k) = \begin{pmatrix} G_0^{-1}(k) - \Sigma_{11}(k) & -\Sigma_{12}(k) \\ -\Sigma_{21}(k) & G_0^{-1}(k + Q) - \Sigma_{22}(k) \end{pmatrix}. \quad (\text{C2})$$

Away from half-filling, both \mathbf{k} and $\mathbf{k} + \mathbf{Q}$ cannot both be on the Fermi surface, so one of the submatrices on the diagonal will have a term proportional to the identity matrix and prefactor of the same order as the electron energy scale. We now assume that \mathbf{k} is close to the Fermi surface, so that this applies to $G_0^{-1}(k + Q)$. To obtain the Green's function $G(k)$, we then make use of the following matrix inversion identity [57]: Given a matrix G^{-1} which can be partitioned into submatrices and written on the form

$$G^{-1} = \begin{pmatrix} N_{11} & N_{12} \\ N_{21} & N_{22} \end{pmatrix}, \quad (\text{C3})$$

where N_{11} and N_{22} are invertible matrices [58], the inverse can similarly be expressed

$$G = \begin{pmatrix} M_{11} & M_{12} \\ M_{21} & M_{22} \end{pmatrix}, \quad (\text{C4})$$

with submatrices

$$M_{11} = (N_{11} - N_{12}N_{22}^{-1}N_{21})^{-1}, \quad (\text{C5a})$$

$$M_{12} = -(N_{11} - N_{12}N_{22}^{-1}N_{21})^{-1}N_{12}N_{22}^{-1}, \quad (\text{C5b})$$

$$M_{21} = -N_{22}^{-1}N_{21}(N_{11} - N_{12}N_{22}^{-1}N_{21})^{-1}, \quad (\text{C5c})$$

$$M_{22} = (N_{22} - N_{21}N_{11}^{-1}N_{12})^{-1}. \quad (\text{C5d})$$

In our case, N_{22} can now be thought of as an electronic energy that is much larger than the other submatrices, which have contributions from the self-energy and the non-interacting Green's function close to the Fermi surface. As long as the renormalization is small compared to the electron energy scale in the problem, $N_{22}^{-1}N_{21}$ is then small, and M_{21} and M_{12} are suppressed relative to M_{11} . By similar reasoning, M_{22} is also small, and M_{11} can be approximated by N_{11}^{-1} .

When $\mathbf{k} + \mathbf{Q}$ is close to the Fermi surface, we may similarly neglect M_{11} and the off-diagonal terms, but not $M_{22} \approx N_{22}^{-1}$. For a general \mathbf{k} , we may therefore neglect the off-diagonal terms, which is exactly what we use in the main text.

Appendix D: Vertex corrections

In order to obtain some insight into the importance of vertex corrections, we will attempt to estimate the magnitude of the lowest-order vertex corrections. Focusing on regular processes for the time being, a magnon-equivalent of the lowest-order vertex correction for phonon-mediated superconductivity is presented in Fig. 8 (a). Due to conservation of spin, this diagram vanishes for our system. Starting with the upper vertex of the vertical magnon line, we see that the electron spin is flipped from \uparrow to \downarrow , meaning that the outgoing magnon carries a spin $+1$. In the lower vertex of the vertical magnon line, this spin needs to be returned to the electrons, but the incoming electron already has spin \uparrow instead of spin \downarrow , and spin can therefore not be conserved in this vertex. Including Umklapp

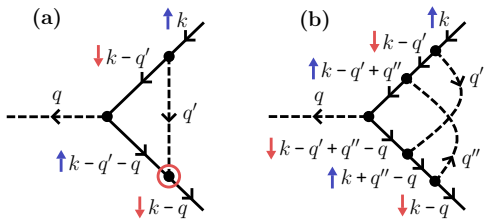


FIG. 8. (a) Typical lowest-order vertex correction, which vanishes in this case due to conservation of spin. (b) Lowest-order vertex correction for our model.

processes, the momentum structure of Fig. 8 (a) will differ, but the spin structure stays the same. The lowest-order vertex corrections are therefore of the type represented by the diagram in Fig. 8 (b). As the diagram in (b) is of higher order, the effect of vertex corrections should then be expected to be smaller than what would have been the case if the diagram in (a) had not vanished.

The diagram in Fig. 8 (b) represents a correction to the electron-magnon vertex $\frac{V}{4}g_\gamma \rightarrow \frac{V}{4}g_\gamma(1 + \Gamma)$, where

$$\begin{aligned} \Gamma(k, q) &\sim \frac{V^4}{\beta^2} \sum_{q', q''} \mathcal{D}_0^{RR}(q') \mathcal{D}_0^{RR}(q'') G_0^{11}(k + q'' - q) \\ &\times G_0^{22}(k - q' + q'' - q) G_0^{11}(k - q' + q'') G_0^{22}(k - q'). \end{aligned} \quad (\text{D1})$$

A quick estimate for Γ can be obtained in the following way [36]. We approximate the magnon propagators as

$$\mathcal{D}_0^{RR}(q) \sim -\frac{A_e^{RR}(0)}{\omega_c}, \quad (\text{D2})$$

for Matsubara frequency q_m less than some cutoff frequency $\omega_c \sim \omega_0$, where ω_0 is the magnon gap. For $q_m > \omega_c$, we take the magnon propagator to be zero. The number of terms that should be included in each of the Matsubara sums is then roughly $\beta\omega_c$. When performing the sums over momentum, the fermions will typically be away from the Fermi surface. We then approximate the momentum sums with the number of lattice sites N , and the electron Green's functions by $G_0^{aa} \sim 1/E_F$, where E_F is the Fermi energy, which is taken as a measure of the electron energy scale ~ 1 eV. We then obtain

$$\Gamma \sim \left(\frac{V^2 N A_e^{RR}(0)}{E_F^2} \right)^2 \sim \left(\frac{1}{100} \right)^2, \quad (\text{D3})$$

where we have inserted typical values for the relevant energy scales, and taken $\Omega = 0$ which is suitable for the case of a relatively small Fermi surface where regular processes dominate. This estimate would indicate that vertex corrections are typically small. It does however not take into account that there

can be large contributions arising from fermions being close to the Fermi surface when $q \rightarrow 0$. In order to pick up such contributions, we need to perform a more detailed estimate.

Starting from Eq. (D1), we can perform the Matsubara sums. Following Ref. [59], we focus on the term that arises from the poles of the boson propagators, limiting the number of factors with fermion energies in the denominator. At zero temperature, this term becomes

$$\begin{aligned} \Gamma_1(k, q) &= -4V^4 \sum_{q', q''} A_e^{RR}(q') A_e^{RR}(q'') \\ &\times \left(\frac{1}{\omega_{q'} + ik_n - \xi_{k-q'}} \right) \left(\frac{1}{\omega_{q''} + \xi_{k+q''-q} - i(k_n - q_m)} \right) \\ &\times \left(\frac{1}{\omega_{q'} + i(k_n - q_m) - \omega_{q''} - \xi_{k-q'+q''-q}} \right) \\ &\times \left(\frac{1}{\omega_{q'} + ik_n - \omega_{q''} - \xi_{k-q'+q''}} \right). \end{aligned} \quad (\text{D4})$$

To estimate this term in the limit of small q , we need to analyze which regions of the Brillouin zone that dominate the momentum sums. The momentum scattering processes in the vertex correction diagram can be represented by a hexagon where opposing sides are parallel and equally long due to conservation of momentum, as shown in Fig. 9. Each vertex in the hexagon represents the momentum of an electron propagator in the Feynman diagram. We consider processes where k and $k - q$ are close to the Fermi surface. Consider the variables q' and $q' - q'' \equiv \pi$ to be the integration variables of our momentum sums. For small q , the vertices 2 and 3 in Fig. 9 are reasonably close to each other. The dominant contributions to the diagram should therefore arise when $k - q' + q''$ is close to the Fermi surface. With $q' - q''$ fixed, the position of the remaining two vertices 1 and 4 is fixed by choosing q' . Taking vertex 1 to be close to the Fermi surface, vertex 4 will now typically end up away from the Fermi surface. The number of terms in the sum over q' where vertex 1 is close to the Fermi

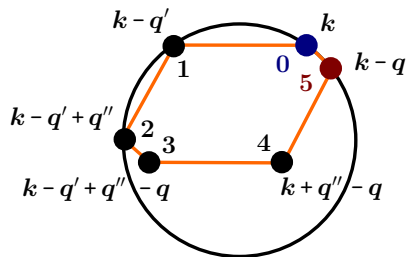


FIG. 9. The momentum scattering processes in the simplest non-vanishing vertex correction of Fig. 8 (b) can be represented as a hexagon. Opposing sides in the hexagon are parallel and equally long due to conservation of momentum. The Fermi surface (assuming large doping) is shown as a circle.

surface is of order $N_F\omega_c$. The Green's functions corresponding to points 1 and 4 in the hexagon can then be approximated by $1/\omega_c$ and $1/E_F$, respectively. By also approximating the boosting factors by their maximum values $A_e^{RR}(\mathbf{0})$ and the remaining magnon energies by ω_c , we may then approximate the vertex correction by

$$\Gamma_1(k, q) = -\frac{4N_F[V^2A_e^{RR}(\mathbf{0})]^2}{E_F} \sum_{\boldsymbol{\pi}} \left(\frac{1}{ik_n - \xi_{\mathbf{k}-\boldsymbol{\pi}}} \right) \times \left(\frac{1}{i(k_n - q_m) - \xi_{\mathbf{k}-\boldsymbol{\pi}-\mathbf{q}}} \right). \quad (\text{D5})$$

Alternatively, one can attempt to further restrict the sum over \mathbf{q}' in order to keep all the fermions close to the Fermi surface, producing a similar result as in Eq. (D5).

Introducing $\mathbf{p} = \mathbf{k} - \boldsymbol{\pi}$, the diagram can now be calculated by Taylor expanding in small \mathbf{q} , using

$$\xi_{\mathbf{p}-\mathbf{q}} \approx \xi_{\mathbf{p}} - (\nabla\xi_{\mathbf{p}}) \cdot \mathbf{q} = \xi_{\mathbf{p}} - v_F q \cos(\theta_{\mathbf{q}}(\mathbf{p})), \quad (\text{D6})$$

where v_F is the Fermi velocity and $\theta_{\mathbf{q}}(\mathbf{p})$ is the angle between $\nabla\xi_{\mathbf{p}}$ and \mathbf{q} . Writing the momentum integral in terms of polar coordinates and integrating out the radial momentum, we then obtain

$$\Gamma_1(k, q) \approx -i \frac{4[N_F V^2 A_e^{RR}(\mathbf{0})]^2}{E_F} \times \left[\Theta(k_n) - \Theta(k_n - q_m) \right] \int_0^{2\pi} d\theta \left(\frac{1}{iq_m - v_F q \cos(\theta)} \right). \quad (\text{D7})$$

Performing also the angular integration, one may show that the vertex correction contribution for nonzero bosonic Matsubara frequency is of order

$$\Gamma_1(k, q) \sim \left(\frac{N_F V^2 A_e^{RR}(\mathbf{0})}{E_F} \right)^2 \left(\frac{E_F}{\sqrt{v_F^2 q^2 + q_m^2}} \right). \quad (\text{D8})$$

In short, this result can be interpreted as follows: Dominant contributions to Eq. (D4) arise from $N_F\omega_c$ terms in each of the momentum sums where two of the electron propagators then are of order $1/\omega_c$ as these electrons are close to the Fermi surface. One of the electron propagators is replaced by a factor $1/E_F$, as the electron in this case is not close to the Fermi surface. The last propagator momentum is reasonably close to the Fermi surface due to the small momentum scattering \mathbf{q} . This propagator is found to be of order $1/\sqrt{(v_F q)^2 + q_m^2}$, where the square root can be interpreted as an interpolation between the frequency and the momentum energy scales for the scattering process with three-momentum (\mathbf{q}, q_m) .

For $\mathbf{q} \rightarrow 0$, $q_m \sim 1$ K, and typical values for the remaining energy scales, the expression in Eq. (D8) is found to be of

order 1, indicating that vertex corrections could become important for long-wavelength magnons. As $v_F q$ in the denominator grows quickly with q , the momentum region where our estimate for the vertex corrections is of importance is quite limited. Whereas the above expression is quickly reduced when q surpasses q_m/v_F , the corresponding momentum cut-off for the magnon propagator depends on the magnon group velocity close to the bottom of the band, meaning that the momentum region where the estimated vertex corrections are of importance is typically significantly smaller than the momentum region where we obtain large contributions to the Eliashberg equations. A more rigorous treatment of the vertex corrections would treat both momentum sums in detail and could potentially give rise to contributions that are larger and/or less quickly reduced with increasing \mathbf{q} .

As the diagram in Fig. 8 (a) vanishes for our model, one might imagine that it could be possible to obtain significant vertex corrections by going to higher-order in magnon operators in the electron-magnon interaction, giving rise to electron-magnon scattering processes without spin flips. Including higher-order terms in the interaction Hamiltonian arising from the z -component of the antiferromagnetic spins, one may construct a diagram like the one in Fig. 8 (a) where the vertical magnon line has been replaced with a magnon loop and the vertices of the magnon loop does not involve an electron spin flip, conserving the electron spin in the diagram. Performing estimates like those presented above, such diagrams are found to be of similar magnitude and displaying a similar suppression with increasing momentum \mathbf{q} as the diagram in Fig. 8 (b).

For larger Fermi surfaces and $\Omega = 1$, the regular processes are of little importance and the physics is dominated by Umklapp processes. Modifying the diagram of Fig. 8 (b) to only include Umklapp processes, all spin- \downarrow electron propagators therefore attain an additional momentum shift \mathbf{Q} . Below half-filling, for \mathbf{k} on the Fermi surface, placing $\mathbf{k} - \mathbf{q} + \mathbf{Q}$ on the Fermi surface now requires a finite momentum \mathbf{q} . Contrary to the case with regular processes and $\mathbf{q} \rightarrow 0$, choosing the hexagon vertex 2 reasonably close to the Fermi surface does therefore not necessarily mean that the hexagon vertex 3 is also reasonably close.

Exactly at half-filling, the Fermi surface is perfectly nested, and the electron momenta can all be chosen reasonably close to the Fermi surface for a wide range of integration momenta and relevant values of \mathbf{q} . Thus, we would get large vertex corrections [49, 50, 60]. Moving away from half-filling, the nesting of the Fermi surface is no longer perfect. Our simplest estimate in Eq. (D3) will then eventually be restored, where $A_e^{RR}(\mathbf{0})$ needs to be replaced with the maximum value of $A_e^{UV}(\mathbf{q})$ for scattering processes on the Fermi surface. Thus, we would expect vertex corrections to become unimportant sufficiently far away from half-filling.

Appendix E: Material parameters

Typical parameter values are shown in Table I. The electron density of states is calculated by numerical evaluation of the elliptical integral in Ref. [61].

TABLE I. Parameter values used in the numerical results. We refer to the main text for an explanation of their meanings.

Quantity	Value
J_1	2 meV
J_2	$0.2 J_1$
K	$1 \times 10^{-4} J_1$
\bar{J}	15 meV
S	1
t	1 eV

- [1] J. Bardeen, L. N. Cooper, and J. R. Schrieffer, *Phys. Rev.* **108**, 1175 (1957).
- [2] F. Schlawin, A. Cavalleri, and D. Jaksch, *Phys. Rev. Lett.* **122**, 133602 (2019).
- [3] A. Kavokin and P. Lagoudakis, *Nature Materials* **15**, 599 (2016).
- [4] F. P. Laussy, A. V. Kavokin, and I. A. Shelykh, *Phys. Rev. Lett.* **104**, 106402 (2010).
- [5] Y. Takada, *Journal of the Physical Society of Japan* **45**, 786 (1978).
- [6] D. J. Scalapino, *Journal of Low Temperature Physics* **117**, 179 (1999).
- [7] T. Moriya and K. Ueda, *Reports on Progress in Physics* **66**, 1299 (2003).
- [8] N. F. Berk and J. R. Schrieffer, *Phys. Rev. Lett.* **17**, 433 (1966).
- [9] S. Doniach and S. Engelsberg, *Phys. Rev. Lett.* **17**, 750 (1966).
- [10] M. Cyrot, *Solid State Communications* **60**, 253 (1986).
- [11] D. J. Scalapino, E. Loh, and J. E. Hirsch, *Phys. Rev. B* **34**, 8190 (1986).
- [12] K. Miyake, S. Schmitt-Rink, and C. M. Varma, *Phys. Rev. B* **34**, 6554 (1986).
- [13] P. Monthoux, A. V. Balatsky, and D. Pines, *Phys. Rev. Lett.* **67**, 3448 (1991).
- [14] P. Monthoux and D. Pines, *Phys. Rev. Lett.* **69**, 961 (1992).
- [15] A. Abanov, A. V. Chubukov, and J. Schmalian, *Advances in Physics* **52**, 119 (2003).
- [16] M. Kargarian, D. K. Efimkin, and V. Galitski, *Phys. Rev. Lett.* **117**, 076806 (2016).
- [17] X. Gong, M. Kargarian, A. Stern, D. Yue, H. Zhou, X. Jin, V. M. Galitski, V. M. Yakovenko, and J. Xia, *Science Advances* **3** (2017).
- [18] N. Rohling, E. L. Fjærby, and A. Brataas, *Phys. Rev. B* **97**, 115401 (2018).
- [19] H. G. Hugdal, S. Rex, F. S. Nogueira, and A. Sudbø, *Phys. Rev. B* **97**, 195438 (2018).
- [20] E. L. Fjærby, N. Rohling, and A. Brataas, *Phys. Rev. B* **100**, 125432 (2019).
- [21] E. Erlandsen, A. Kamra, A. Brataas, and A. Sudbø, *Phys. Rev. B* **100**, 100503 (2019).
- [22] E. Erlandsen and A. Sudbø, *Phys. Rev. B* **102**, 214502 (2020).
- [23] E. Erlandsen, A. Brataas, and A. Sudbø, *Phys. Rev. B* **101**, 094503 (2020).
- [24] H. G. Hugdal and A. Sudbø, *Phys. Rev. B* **102**, 125429 (2020).
- [25] A. Kamra, E. Thingstad, G. Rastelli, R. A. Duine, A. Brataas, W. Belzig, and A. Sudbø, *Phys. Rev. B* **100**, 174407 (2019).
- [26] J. Nogués and I. K. Schuller, *Journal of Magnetism and Magnetic Materials* **192**, 203 (1999).
- [27] J. Nogués, J. Sort, V. Langlais, V. Skumryev, S. Suriñach, J. Muñoz, and M. Baró, *Physics Reports* **422**, 65 (2005).
- [28] R. L. Stamps, *Journal of Physics D: Applied Physics* **33**, R247 (2000).
- [29] S. Takei, B. I. Halperin, A. Yacoby, and Y. Tserkovnyak, *Phys. Rev. B* **90**, 094408 (2014).
- [30] E. L. Fjærby, N. Rohling, and A. Brataas, *Phys. Rev. B* **95**, 144408 (2017).
- [31] S. V. Vonsovskii and Y. A. Izyumov, *Soviet Physics Uspekhi* **5**, 723 (1963).
- [32] G. Chen and W. A. Goddard, *Science* **239**, 899 (1988).
- [33] H. Shimahara, *Journal of the Physical Society of Japan* **63**, 1861 (1994).
- [34] Y. Kajiwara, K. Harii, S. Takahashi, J. Ohe, K. Uchida, M. Mizuguchi, H. Umezawa, H. Kawai, K. Ando, K. Takanashi, S. Maekawa, and E. Saitoh, *Nature* **464**, 262 (2010).
- [35] F. Mazzola, T. Frederiksen, T. Balasubramanian, P. Hofmann, B. Hellsing, and J. W. Wells, *Phys. Rev. B* **95**, 075430 (2017).
- [36] P. Coleman, *Introduction to Many-Body Physics* (Cambridge University Press, 2015).
- [37] S. Takahashi, E. Saitoh, and S. Maekawa, *Journal of Physics: Conference Series* **200**, 062030 (2010).
- [38] S. A. Bender and Y. Tserkovnyak, *Phys. Rev. B* **91**, 140402 (2015).
- [39] In general, the electron can be scattered with any momentum, however, upon explicitly introducing regular (R) and Umklapp (U) magnon operators, all magnon scattering processes can be described within the reduced Brillouin zone.
- [40] J. Linder and A. V. Balatsky, *Rev. Mod. Phys.* **91**, 045005 (2019).
- [41] One may derive equations also when this is not the case, but they will be somewhat more involved, as there will be interference terms in the submatrix determinant Θ .
- [42] P. B. Allen and R. C. Dynes, *Phys. Rev. B* **12**, 905 (1975).
- [43] C. Sanderson and R. Curtin, *Journal of Open Source Software* **1**, 26 (2016).
- [44] C. Sanderson and R. Curtin, in *Mathematical Software – ICMS 2018* (Springer International Publishing, Cham, 2018) pp. 422–430.
- [45] GNU Scientific Library, <https://www.gnu.org/software/gsl/>.
- [46] It should be noted that although the size of the region with significant deviations from the zero frequency polarization increases with Matsubara frequency ν_m , so does also the width of the region over which we expect the dominant contributions to

the corresponding $\lambda_2(i\nu_m)$. Thus, we still expect to be able to approximate the polarization by a constant for larger Matsubara frequencies ν_m .

- [47] A. B. Migdal, *JETP* **34**, 1438 (1958).
- [48] P. B. Allen and B. Mitrović, *Theory of Superconducting Tc*, edited by H. Ehrenreich, F. Seitz, and D. Turnbull, Solid State Physics, Vol. 37 (Academic Press, 1983) pp. 1–92.
- [49] A. Virosztek and J. Ruvalds, *Phys. Rev. B* **42**, 4064 (1990).
- [50] A. Virosztek and J. Ruvalds, *Phys. Rev. B* **59**, 1324 (1999).
- [51] F. Schrodi, P. M. Oppeneer, and A. Aperis, *Phys. Rev. B* **102**, 024503 (2020).
- [52] A. Madhukar, *Solid State Communications* **24**, 11 (1977).
- [53] R. Szczęśniak, *Physics Letters A* **336**, 402 (2005).
- [54] M. Matsumoto, M. Koga, and H. Kusunose, *Journal of the Physical Society of Japan* **81**, 033702 (2012).
- [55] A. Cebula, J. Zieliński, and J. Biesiada, *Journal of Superconductivity* **13**, 479 (2000).
- [56] C. Kittel, *Quantum Theory of Solids* (John Wiley & Sons, 1987).
- [57] R. A. Horn and C. R. Johnson, *Matrix Analysis* (Cambridge University Press, Cambridge, 2012).
- [58] The identity can also be formulated more generally, but this will be sufficient for our purposes.
- [59] B. Roy, J. D. Sau, and S. Das Sarma, *Phys. Rev. B* **89**, 165119 (2014).
- [60] D. Djajaputra and J. Ruvalds, *International Journal of Modern Physics B* **13**, 25 (1999).
- [61] R. Piasecki, (2008), arXiv:0804.1037 [cond-mat.str-el].

ISBN 978-82-326-5820-6 (printed ver.)
ISBN 978-82-326-5514-4 (electronic ver.)
ISSN 1503-8181 (printed ver.)
ISSN 2703-8084 (online ver.)



NTNU

Norwegian University of
Science and Technology